

Determination of Mass Loss and Mass Transfer Rates  
of Algol (Beta Persei) from the Analysis of  
Absorption Lines in the UV Spectra Obtained by the  
IUE Satellite

by

Kristen Wecht

Presented to the Graduate and Research Committee  
of Lehigh University  
in Candidacy for the Degree of  
Doctor of Philosophy

in

Physics

Lehigh University

April 2006

# CERTIFICATE OF APPROVAL

Approved and recommended for acceptance as a dissertation to partial fulfillment of the requirements for the degree of Doctor of Physics.

\_\_\_\_\_  
Date

\_\_\_\_\_  
Accepted Date

\_\_\_\_\_  
George E. McCluskey, Jr. (Advisor)

Special Committee Directing the Doctoral Work of Kristen Wecht

\_\_\_\_\_  
Gary G. DeLeo

\_\_\_\_\_  
A. Peet Hickman

\_\_\_\_\_  
John P. Huennekens

\_\_\_\_\_  
Daniel Zeroka

# CONTENTS

Certificate of Approval	ii
Acknowledgements	iii
Table of Contents	vi
List of Tables	ix
List of Figures	x
Abstract	1
1 Introduction	2
2 Background	5
2.1 Stellar Properties, Evolution and Classification	5
2.2 Binary Star Characteristics and Classification	8
2.3 Observational Indications of Mass Flow	17
2.4 Algol (Beta Persei), Algol-type Systems and the Algol Paradox	22
2.5 Previous Observations and Models for Algol	28
3 IUE Observations	33
3.1 IUE Spacecraft and Database	33
3.2 IUE Observations of Algol	39
3.3 Line-of-sight Geometry for Each Algol IUE Observation	45
3.4 Sample IUE Data for Algol	66
4 Analysis of the Data	68

4.1	Data Analysis Overview	68
4.2	Gas Composition, Excitation, and Ionization	70
4.2.1	Ion Types and Electronic-Transitions	70
4.2.2	Ionization Fractions	73
4.3	Preliminary Considerations	80
4.3.1	Managing the IUE Data	80
4.3.2	Spectral-Line Identification and Systematic Velocity Determination	81
4.3.3	Correction for Influence of Algol C	84
4.4	Determination of UV Light Curves	99
4.4.1	Method for Determining Continuum Flux	99
4.4.2	Continuum Flux and Light Curve Results	100
4.5	Determination of Radial Velocities and Absorbing-Gas Characteristics from Spectral Line Analyses	116
4.5.1	Methods of Spectral Line Analyses	116
4.5.2	Radial Velocity Calculations and Results	118
4.5.3	Line Widths and Asymmetries	132
4.5.4	Residual Intensities	136
4.5.5	Equivalent Widths and Column Densities	145
4.5.6	Difference Spectra	149
4.5.7	Mass Loss Rate	171
5	Discussions and Conclusions	176
5.1	Direct Approach	177

5.2	Difference Approach	187
5.3	Concluding Remarks	190
	Bibliography	191
	Appendices	
A	Published Estimates of Algol Parameters	207
B	Algol Timeline	245
C	Ionization Fractions	257
D	Tabulated Data	
	D.1 Continuum Flux	267
	D.2 Radial Velocities	277
	D.3 Line Widths	286
	D.4 Residual Intensities	296
	D.5 Equivalent Widths	299
	D.6 Difference Spectra Results and Ion Column Densities	302
	Vita	308

## LIST OF TABLES

2.1.1	Role of Mass of a Star .....	7
2.2.1	Orbital Elements of Binary Systems .....	10
2.4.1	Selected Algol Parameters .....	24
2.5.1	Advances in Observational Coverage of Algol.....	28
3.1.1	Science Payload and Cameras.....	36
3.1.2	IUE Spectrograph Parameters .....	38
3.2.1	IUE Observing Runs of Algol.....	40
3.2.2	IUE SWP Observations of Algol .....	41
3.2.3	IUE LWP/LWR Observations of Algol .....	43
3.2.4	Comparison of IUE Phases to Other Work.....	44
3.3.1	Input Parameters for Binary Maker 3.0.....	64
4.2.1.1	Electronic Transitions (SWP) .....	71
4.2.1.2	Electronic Transitions (LWP/LWR) .....	72
4.3.3.1	Initial Algol Properties Adopted for This Comparison.....	90
4.3.3.2	Final Algol Properties Adopted for This Comparison .....	95
4.3.3.3	Final Algol Properties Adopted for IUE Corrections .....	98
4.5.7.1	Phases Used for Mirror Comparison.....	171
4.5.7.2	Properties of Longward Mirror – Difference Component .....	175
5.2.1	Epoch Activity Level Comparison.....	189

## LIST OF FIGURES

2.1.1	Hertzsprung-Russell Diagram (HRD).....	6
2.2.1	Schematic of a Binary System .....	8
2.2.2	Orbital Plane of a Binary Star Inclined .....	9
2.2.3	Visual Binary.....	11
2.2.4	Spectroscopic Binaries .....	12
2.2.5	Radial Velocity Curve.....	13
2.2.6	Light Curve of Partially Eclipsing Binary.....	13
2.2.7	Light Curve of Eclipsing Binary (Primary is Total) .....	14
2.2.8	Shape of Binary Components.....	15
2.2.9	Geometry of Restricted 3-Body Problem.....	16
2.3.1a	Radial Velocity Curve with Rotation Effect only .....	18
2.3.1b	Radial Velocity Curve with Gas Stream and Rotation Effects ....	18
2.3.2	Light Curve of R Canis Majoris.....	19
2.3.3a	U Cep U-band Light Curve of Primary Eclipse Ingress.....	20
2.3.3b	U Cep U-band Light Curve of Primary Eclipse Egress .....	20
2.3.4a	U Cep UV Mg II Resonance Doublet 1986 Oct 22.....	21
2.3.4b	U Cep UV Mg II Resonance Doublet 1986 June 4.....	21
2.3.5	Hypothetical Photometric Distortions from Gas Stream Effects .	22
2.4.1	Scale Diagram of Algol.....	24
2.4.2	Algol Light Curve at 3428 Å.....	25
2.4.3	Crawford's Evolutionary Scenario.....	27
2.5.1	Model of Algol Deduced from H $\alpha$ Observations .....	29

2.5.2	Model for the Circumstellar Material in Algol Deduced from H <sub>α</sub> Observations .....	30
2.5.3a	Radio Model .....	31
2.5.3b	Schematic of Algol with Radio Source .....	31
2.5.4	Soft X-ray Model .....	32
2.5.5	Mg II Absorption Model .....	32
3.1.1	IUE Satellite .....	33
3.1.2	Optical Schematic of the IUE Scientific Instrument .....	35
3.1.3	The First IUE Image .....	37
3.3.1a	Line-of-Sight Geometry for Epoch 1978 Sept. – Nov. SWP Phases .....	46
3.3.1b	Line-of-Sight Geometry for Epoch 1978 Dec. – 1979 Jan. SWP Phases .....	47
3.3.1c	Line-of-Sight Geometry for Epoch 1979 November SWP Phases	48
3.3.1d	Line-of-Sight Geometry for Epoch 1983 November SWP Phases	49
3.3.1e	Line-of-Sight Geometry for Epoch 1984 March SWP Phases .....	50
3.3.1f	Line-of-Sight Geometry for Epoch 1985 July SWP Phases .....	51
3.3.1g	Line-of-Sight Geometry for Epoch 1986 Feb. - March SWP Phases .....	52
3.3.1h	Line-of-Sight Geometry for Epoch 1989 September SWP Phases	53
3.3.2a	Line-of-Sight Geometry for Epoch 1978 Sept.–Nov. LWP/LWR Phases .....	55
3.3.2b	Line-of-Sight Geometry for Epoch 1978 Dec.–1979	



	LWP/LWR Phases.....	56
3.3.2c	Line-of-Sight Geometry for Epoch 1979 November	
	LWP/LWR Phases.....	57
3.3.2d	Line-of-Sight Geometry for Epoch 1983 November .....	
	LWP/LWR Phases.....	58
3.3.2e	Line-of-Sight Geometry for Epoch 1984 March	
	LWP/LWR Phases.....	59
3.3.2f	Line-of-Sight Geometry for Epoch 1985 July LWP/LWR Phases	60
3.3.2g	Line-of-Sight Geometry for Epoch 1986 Feb. – March	
	LWP/LWR Phases.....	61
3.3.2h	Line-of-Sight Geometry for Epoch 1989 September	
	LWP/LWR Phases.....	62
3.3.3	Selected Line-of-Sight Geometries of Algol IUE Observations..	65
3.4.1a	Sample IUE Data at $\phi = 0.9217$ .....	66
3.4.1b	Sample IUE Data $\phi = 0.9388$ .....	66
3.4.2	Line-of-Sight as Viewed from Above for the 1984 Exposure	
	at Phases 0.922 and 0.939 1984 IUE Data .....	67
4.1.1	IUE Spectra Analysis Flow-Chart.....	69
4.2.2.1	Ionization Fraction of Carbon, Nitrogen, and Oxygen at 12,300 K	76
4.2.2.2	Ionization Fraction of Mg, Al, Si, and Fe at 12,300 K.....	76
4.2.2.3	Ionization Fraction of Carbon, Nitrogen, and Oxygen 25,000 K.	77
4.2.2.4	Ionization Fraction of Mg, Al, Si, and Fe at 20,000 K.....	78
4.2.2.5	Ionization Fraction of Carbon, Nitrogen, and Oxygen at 30,000 K	78

4.2.2.6	Ionization Fraction of Carbon, Nitrogen, and Oxygen at 45,000 K	79
4.3.2.1	Wavelength of Local Minima as a Function of Phase.....	81
4.3.2.2	Rest Wavelengths Identified with the Interactive Program Developed in this Paper.....	83
4.3.3.1	Elliptical Geometry .....	85
4.3.3.2	Radial Velocity Comparison of Algol A wrt the Sun vs. Phase of Algol A-B.....	91
4.3.3.3	Radial Velocity Comparison of Algol A wrt the Sun vs. Phase of Algol AB-C.....	92
4.3.3.4	Radial Velocity Comparison of Algol A wrt the Sun vs. Phase of Algol A-B $\omega = \omega(t)$ .....	96
4.3.3.5	Hill's Observed Radial Velocities of Algol A with Corrections Applied for $\omega = \omega(t)$ .....	97
4.4.4.1	Flux vs. Wavelength in the Interval 2000 – 2050 Å. ....	99
4.4.2.1	Selected Algol IUE SWP Continua (Large Aperture Exposures)	101
4.4.2.2	Selected Algol IUE LWP/LWR Continua (Large Aperture Exposures).....	102
4.4.2.3	Algol IUE SWP Continua Epoch Comparison (Large Aperture Exposures).....	106
4.4.2.4	Algol SWP Flux vs Phase (Large Aperture Only) .....	107
4.4.2.5	Algol LWP/LWR Flux vs Phase .....	108
4.4.2.6	Normalized Algol IUE SWP Light Curves.....	109
4.4.2.7a	Normalized Algol IUE LWP/LWR Light Curves.....	110

4.4.2.7b	Normalized Algol IUE LWP/LWR Light Curves.....	111
4.4.2.8	SWP Normalized Average Algol IUE Light Curves 1550-1750 Å .....	112
4.4.2.9	LWP/LWR Normalized Average Algol IUE Light Curves 2425-2825 Å .....	113
4.4.2.10	SWP Normalized Average Algol IUE Light Curves Near Primary Eclipse 1550-1750 Å.....	114
4.4.2.11	LWP/LWR Normalized Average Algol IUE Light Curves Near . Primary Eclipse 2425-2828 Å.....	115
4.5.1.1	Mg II 2796 and Mg II 2798, Symmetric .....	116
4.5.1.2	Mg II 2796 and Mg II 2798, Asymmetric.....	116
4.5.2.1	Radial Velocity vs Phase Al II 1670 .....	119
4.5.2.2	Radial Velocity vs Phase Al III 1854.....	120
4.5.2.3	Radial Velocity vs Phase C II 1334 .....	121
4.5.2.4	Radial Velocity vs Phase Fe II 1640 .....	122
4.5.2.5	Radial Velocity vs Phase Si III 1294 .....	123
4.5.2.6	Radial Velocity vs Phase Si IV 1393 .....	124
4.5.2.7	Radial Velocity vs Phase Si IV 1402 .....	125
4.5.2.8	Radial Velocity vs Phase Fe 2586.....	126
4.5.2.9	Radial Velocity vs Phase Fe II 2600 .....	127
4.5.2.10	Radial Velocity vs Phase Mg II 2796.....	128
4.5.2.11	Radial Velocity vs Phase Mg II 2803.....	129
4.5.3.1	Variation in Line Widths, Symmetrical and Asymmetrical.....	133

4.5.3.2	Line Width as a Function of Phase Al II 1670 .....	134
4.5.3.3	Line width as a function of phase Si IV 1393 .....	135
4.5.4.1	Residual Intensities of Selected IUE SWP& LWP/LWR Lines vs. Phase Al II 1670 .....	138
4.5.4.2	Residual Intensities of Selected IUE SWP& LWP/LWR Lines vs. Phase Al III 1854 .....	139
4.5.4.3	Residual Intensities of Selected IUE SWP& LWP/LWR Lines vs. Phase Al III 1862 .....	140
4.5.4.4	Residual Intensities of Selected IUE SWP& LWP/LWR Lines vs. Phase Si IV 1393.....	141
4.5.4.5	Residual Intensities of Selected IUE SWP& LWP/LWR Lines vs. Phase Si IV 1402.....	142
4.5.4.6	Residual Intensities of Selected IUE SWP& LWP/LWR Lines vs. Phase Mg II 2796.....	143
4.5.4.7	Residual Intensities of Selected IUE SWP& LWP/LWR Lines vs. Phase Mg II 2803 .....	144
4.5.5.1	Equivalent Width Al II 1670 Line.....	146
4.5.5.2	Equivalent Width Si IV 1393 .....	147
4.5.5.3	Equivalent Width Si IV 1402 .....	148
4.5.6.1a	Algol IUE SWP Spectra Si IV 1393, Epochs 1978 - 1983 .....	152
4.5.6.1b	Algol IUE SWP Spectra Si IV 1393, Epochs 1984 - 1986 .....	153
4.5.6.1c	Algol IUE SWP Spectra Si IV 1393, Epoch 1989 .....	154
4.5.6.2a	Algol IUE SWP Spectra Si IV 1402, Epochs 1978 - 1983 .....	155

4.5.6.2b	Algol IUE SWP Spectra Si IV 1402, Epochs 1984 - 1986 .....	156
4.5.6.2c	Algol IUE SWP Spectra Si IV 1402, Epoch 1989 .....	157
4.5.6.3a	Algol IUE SWP Spectra Al III 1854, Epochs 1978 - 1983 .....	158
4.5.6.3b	Algol IUE SWP Spectra Al III 1854, Epochs 1984 - 1986 .....	159
4.5.6.3c	Algol IUE SWP Spectra Al III 1854, Epoch 1989 .....	160
4.5.6.4a	Algol IUE SWP Spectra Al III 1862, Epochs 1978 - 1983 .....	161
4.5.6.4b	Algol IUE SWP Spectra Al III 1862, Epochs 1984 - 1986 .....	162
4.5.6.4c	Algol IUE SWP Spectra Al III 1862, Epoch 1989 .....	163
4.5.6.5a	Algol IUE LWP/LWR Spectra Mg II Near 2800, Epochs 1978 – 1983 .....	164
4.5.6.5b	Algol IUE LWP/LWR Spectra Mg II Near 2800, Epochs 1984 – 1986 .....	165
4.5.6.5c	Algol IUE LWP/LWR Spectra Mg II Near 2800, Epoch 1989 ...	166
4.5.6.6	Vrad Phase Comparison LWP/LWR Mg II 2796 .....	167
4.5.6.7	Ni Difference Phase Comparison LWP/LWR Mg II 2796 .....	168
4.5.6.8	Mg II $\lambda\lambda$ 2796, 2803 .....	169
4.5.6.9	Mg II $\lambda\lambda$ 2796, 2803 Difference Spectra .....	170
4.5.7.1	Difference Spectrum Corresponding Phases Symmetrically ..... Situated About Primary Eclipse .....	172
5.1.1a	Al II 1670 Equivalent Width vs. Phase .....	178
5.1.1b	Al II 1670 Radial Velocity Curve .....	178
5.1.2a	Al III 1854 Equivalent Width vs. Phase .....	179
5.1.2b	Al III 1854 Radial Velocity Curve .....	179

5.1.3a	Mg II 2796 Equivalent Width vs. Phase .....	180
5.1.3b	Mg II 2796 Radial Velocity Curve.....	180
5.1.4a	Mg II 2803 Equivalent Width vs. Phase .....	181
5.1.4b	Mg II 2803 Radial Velocity Curve.....	181
5.1.5a	Si IV 1393 Equivalent Width vs. Phase .....	182
5.1.5b	Si IV 1393 Radial Velocity Curve .....	182
5.1.6a	Si IV 1402 Equivalent Width vs. Phase .....	183
5.1.6b	Si IV 1402 Radial Velocity Curve .....	183
5.1.7	Algol Model .....	185

# ABSTRACT

The International Ultraviolet Explorer (IUE) archive of high-resolution ultraviolet spectra of the eclipsing semi-detached binary star, Algol ( $\beta$  Persei, HD 19356), taken from September 1978 to September 1989, is analyzed in order to characterize the movement of gas within and from this system. Light curves are constructed, using a total of 1647 continuum level measurements. These results support the semidetached status of this interacting binary star. Radial velocities, residual intensities, full width half maxima (FWHM), line asymmetries, and equivalent widths of UV absorption lines for aluminum, magnesium, iron, and silicon in a range of ionization states are determined and analyzed. For selected epochs, we were able to isolate gas stream and photospheric contributions by an examination of the differences between spectral line shapes.

We observed variations in line shape and strength, with orbital phase and epoch, indicating the presence of stable gas streams and circumstellar gas, and periods of increased mass-transfer activity associated with transient gas streams. The 1989 data indicates moderate activity. This epoch was examined most closely since it provides the greatest phase coverage. Spectral line profiles in 1978 and 1984 have the strongest gas-flow absorption components, indicating that these are the epochs of the greatest activity. The dense phase coverage in September 1989 allows us to measure the mass loss rate from Algol B into Algol A which is of order  $\sim 10^{-14} M_{\odot}/\text{yr}$ . Since the highest gas-flow velocities are in the 100 kilometer per second range, well below escape velocity, we conclude that systemic mass loss due to gas flow is small for the Algol system.

# 1. INTRODUCTION

A grain of sand held at arm's length covers a patch of sky that holds 1,000 galaxies (StarGaze DVD 2000). When multiplied across the entire sky, this means the universe contains at least 120 billion galaxies, and each galaxy hosts an average of 100 billion stars.

Our current understanding of stars derives almost entirely from the detection and examination of electromagnetic radiation. The physical and evolutionary properties of stars are revealed when these spectroscopic studies are combined with theoretical models based on applications of fundamental physical laws. In particular, it was in large part the combination of the classification scheme of Annie Jump Cannon, the quantification of temperature-luminosity relationships by Henry Norris Russell, and the development of quantum mechanics that led to our current understanding. We now recognize that nearly all stars are composed mostly of hydrogen and helium, and that differences in color and brightness are related to both mass and evolutionary stage, but ultimately to mass.

It is estimated that 40-60% of the 100 billion stars in each of the 120 billion galaxies are actually gravitationally bound collections of two or more stars – *binary stars* or *multiple stars*. This fact of nature is essential to our understanding of all stars since stellar masses can be directly determined only by observing the motions of binary star components under their mutual gravitational interactions. Of course, once the relationship between mass and other observed properties is established, this scheme can then be used to estimate the masses of stars that are not components of binary systems.



In some cases, the separations between the binary-star components are so small that the stars experience mutual structural disturbances. These interactions lead to some very interesting phenomena not found in systems with greater separations, including orbital perturbations, stellar distortions and mass flow. The characteristics of such *interacting binaries* can be revealed by spectroscopic studies in a variety of wavelength ranges.

In this work we study the ultraviolet light from the variable star Algol, the second brightest star in the constellation of Perseus. This star,  $\beta$  Persei, is actually a multiple star system. Two of its component stars are so close together that there is movement of gas from one star to the other. The orientation of the orbit is such that one star partially eclipses the other every 2.9 days, resulting in the observable variability of total light from the system with the naked eye.

Ultraviolet observations of Algol enable us to study in more detail the hot circumstellar gas moving within and from the system. Instrumentation aboard the International Ultraviolet Explorer (IUE) spacecraft recorded 103 exposures in UV light from Algol between September 1978 and September 1989. Each exposure corresponds to a specific point in time and related configuration of the relative positions of the component stars with respect to our line of sight from Earth. We see the manifestation of mass flow in the UV light variations across these exposures.

A detailed analysis of the ultraviolet spectral lines reveals noticeable variations in spectral features with orbital phase and time frame (epoch) that correspond to the properties of mass flow within and from the Algol system. From the differences in spectral line widths at different phases with and without the gas stream, we estimate the

number of atoms in the gas stream. From the shifts in wavelength from the rest wavelength, we determine the radial velocities as functions of time for each spectral line. From these quantities we estimate the mass loss rate and infer other physical characteristics of this interacting binary system.

## 2. BACKGROUND

### 2.1 *Stellar Properties, Evolution, and Classification*

In order to fully appreciate the strange phenomenon known as the Algol Paradox, we first examine our current understanding of the properties and evolution of non-interacting stars. These include isolated (single) stars and components of multiple-star systems that are well separated.

The classification of stars according to their surface temperature and luminosity is represented by the Hertzsprung-Russell (HR) diagram, FIG. 2.1.1. The physical properties of a star are correlated with position on the diagram. The horizontal axis is labeled in order of decreasing surface temperature (Kelvin) with the letters O, B, A, F, G, K, and M (subtypes 0 and 5 are labeled as space permits). The vertical axis indicates increasing luminosity (in fractions of solar luminosity  $L_{\odot}^*$ ). Fainter stars appear near the bottom, brighter ones near the top. *Diagonal lines* indicate approximate radii in units of solar diameters ( $2R_{\odot}$ ). Broad grey curves indicate the locations of the luminosity classes Ia (Very luminous supergiants), Ib (Less luminous supergiants), II (Luminous giants), III (Giants), IV (Subgiants), V (Main sequence stars or dwarf stars). The position of the Sun indicates its identification as a G2 V star.

---

\*  $L_{\odot} = 3.826 \times 10^{33}$  ergs/s

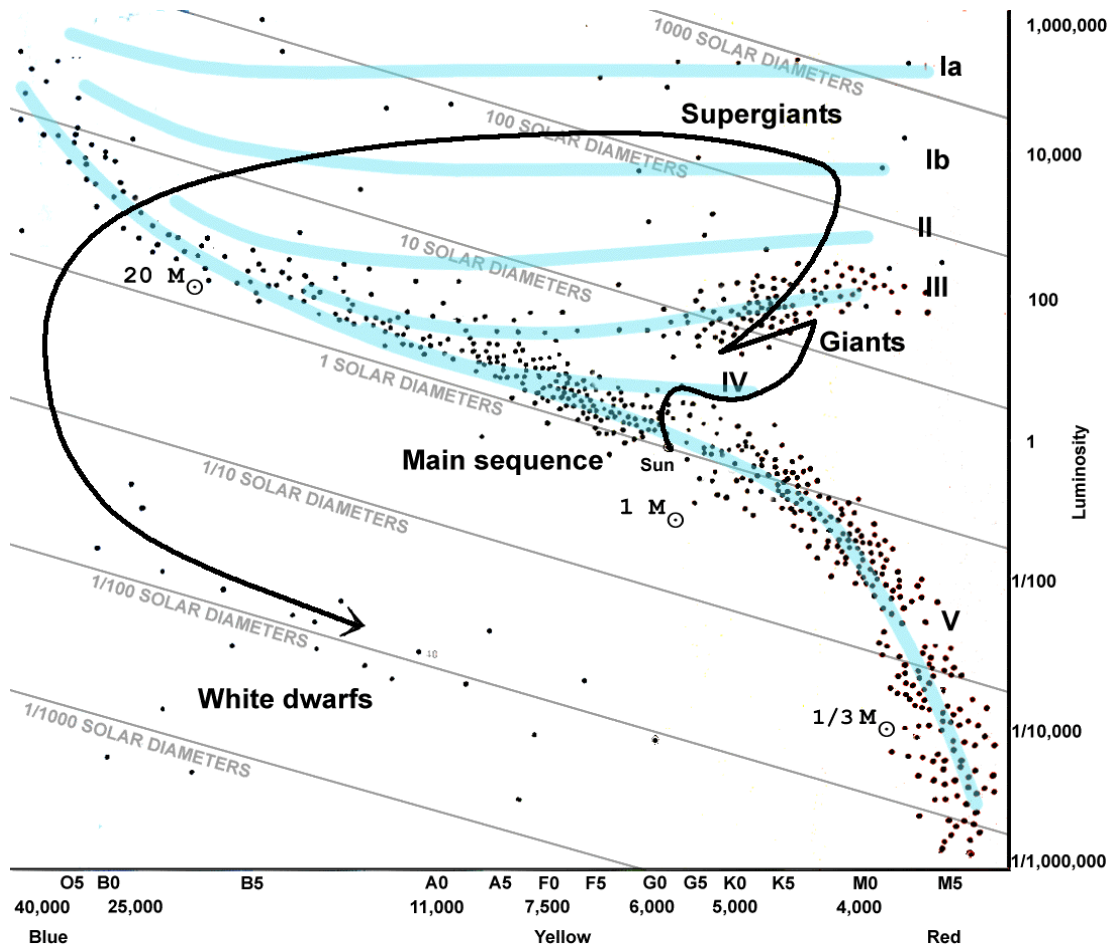


FIG. 2.1.1—*Hertzsprung-Russell Diagram (HRD)*. Adapted from a figure in “The Universe and Beyond, 3rd Ed., T. Dickinson, Firefly, 1999. Also shown is the evolutionary path of the sun.

The broad diagonal band, the main sequence, includes more than 90% of all stars (including our Sun) and associates increasing luminosity with increasing surface temperature. For stars on the main sequence, both temperature and luminosity increase monotonically with increasing mass. The most massive stars, such as O and B stars, are very hot and very bright. The low mass M stars are cooler and dimmer.

Off the main sequence, however, surface area, or size, rather than temperature, is the stronger influence on luminosity. Some red giants and supergiants are only half as hot as the Sun, but they can be a hundred to a million times more luminous. Planet-size

white dwarfs, although generally hotter than the Sun, are much dimmer. Luminous but cool giants fall in the upper right, hot but dim white dwarfs in the lower left.

A star's evolution can be described by its change of position on the diagram, as shown for our sun by the solid line in FIG. 2.1.1. A star of solar mass will spend roughly 10 billion years on the main sequence and an additional 2 billion years along the various stages of becoming a white dwarf. Stellar masses also diminish as the stars evolve beyond the main sequence. For example, by the time the sun completes its evolution, its mass will have diminished to about 2/3 of its current value.

An important element of our understanding of stellar evolution is that the lifetime of a star varies inversely with its main-sequence mass. For example, even with its great mass, an O 5 star burns its fuel so aggressively that it has a main sequence lifetime of only about one million years. Yet a typical M star has a theoretical lifetime of 500 billion years. (see TABLE 2.1.1)

TABLE 2.1.1  
Role of Mass of a Star

Mass	Temperature	Spectral Type	Lifetime (yrs)
40	40,000	O	1 million
7	15,000	B	80 million
2	8,200	A	2 billion
1.3	6,600	F	5 billion
1.0	5,800	G	10 billion
0.8	4,300	K	20 billion
0.2	3,300	M	500 billion

Although FIG. 2.1.1 only shows the evolutionary pathway for a solar-mass star, these pathways and the corresponding elapsed times are known for all main sequence masses. However, these are appropriate to isolated or non-interacting stars. As we shall see, these evolutionary trajectories can be significantly altered by a close binary partner.

## 2.2 Binary Star Characteristics and Classification

The stars that compose binary star systems have a variety of separations, from one to two times the radius of our Sun,<sup>\*</sup> to many times the distance between Sun and Pluto.<sup>†</sup> The components of an interacting binary are so close together that the evolutionary history of each of the two components at some stage begins to depart appreciably from the evolution of single (isolated) stars (Sahade and Wood 1978).

Systems that contain stars with small separations have shorter orbital periods and are difficult or impossible to resolve using current methods. The more widely separated the component, the longer the period. Orbital periods can range from minutes to thousands of years.

FIG. 2.2.1 is a schematic binary system showing the elliptical orbits of components  $S_1$  (the primary star) and  $S_2$  (the secondary star) about their center of mass ( $X$ ) with semimajor axes  $a_1$  and  $a_2$ , and masses  $m_1$  and  $m_2$ . The eccentricity and period of both orbits are the

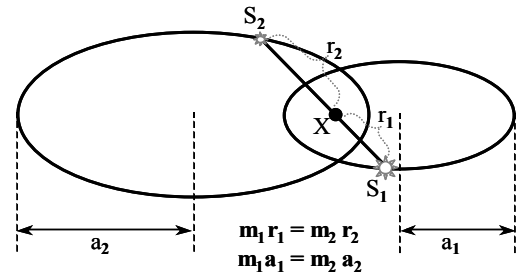


FIG. 2.2.1—Schematic binary system

same. Some systems have eccentric orbits, others are circular. Binary systems where the

<sup>\*</sup> Radius of the Sun:  $R_{\odot} = 6.9599 \times 10^{10}$  cm

<sup>†</sup> Distance between Sun and Pluto: 39.4821 AU, AU =  $1.4960 \times 10^{13}$  cm, the average Earth-Sun distance.

component stars are close together tend to have circularized orbits due to tidal interactions between the two stars.

Seven orbital elements "...define the form and size of the true orbit, the position of the orbit plane, the position of the orbit within that plane, and the position of the companion star in the orbit at any specified time" (Aitken 1935).

FIG. 2.2.2 is a schematic of a binary system inclined with respect to the plane of our sky showing the orbit of  $S_2$  (the secondary star) relative to  $S_1$  (the primary star).

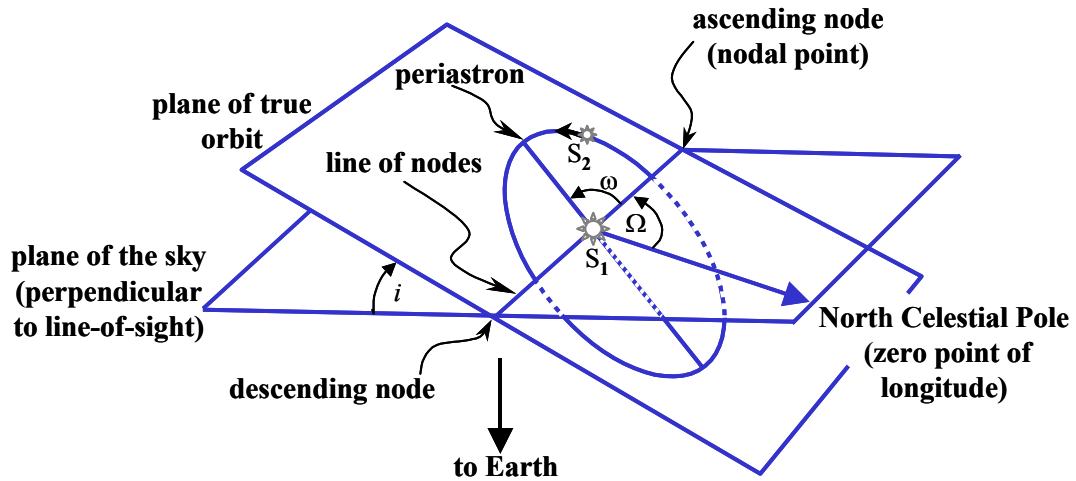


FIG. 2.2.2—Orbital Plane of a Binary Star, Inclined (adapted from Fig. 25 p. 60 Binnendijk 1960, and <http://scienceworld.wolfram.com/physics/OrbitalElements.html>, 2006).

The orbital elements are defined as: (1) the *period* of revolution  $P$ , (2) the *time of periastron passage*  $T$ , (3) the *eccentricity*  $e$  of the true ellipse, (4) the *semimajor axis*  $a$  of the true ellipse, (5) the *position angle of nodal point*  $\Omega$ , (6) the *longitude of periastron*  $\omega$ , and (7) the *orbital inclination*  $i$ . (See TABLE 2.2.1).

TABLE 2.2.1  
Orbital Elements of Binary Systems

P	Period of revolution	Time it takes for one orbit
T	Time of periastron passage	A time at which the body passed through pericenter, the time of maximum orbital velocity
e	Eccentricity of the true ellipse	Eccentricity of the ellipse in the plane of the orbit (not of the projection of the orbit on the sky)
$\Omega$	Position angle of nodal point which lies between $0^\circ$ and $180^\circ$	It is also the position angle of the line of nodes. (The line of nodes is the line of intersection of the orbit plane with the plane perpendicular to the line of sight).
$\omega$	Longitude of periastron, or the angle in the plane of the true orbit between the line of nodes and the major axis	It is measured from the nodal point to the point of periastron passage in the direction of the companion's motion and may have any value from 0 to 360. It should be stated whether the position angles increase or decrease with time.
i	Inclination of the orbit plane	The angle between the orbit plane and the plane at right angles to the line of sight. Its value lies between $0^\circ$ and $\pm 90^\circ$ depending on whether the orbital motion at the nodal point is carrying the companion star away from (+), or toward (-) the observer.

*(Source: Aitken 1935 p.77-78; Binnendijk 1960 p.59-60)*

Binary stars are often classified according to mode of observation and special characteristics. The categories are not mutually exclusive and include visual, astrometric, spectroscopic, eclipsing, and interacting.



A *visual binary* is a bound system that can be resolved into two stars telescopically. If the orbital period is not too long, it is possible to track the motion of each member of the system, though usually only relative motion is observable. The mutual orbits of these stars are observed to have periods ranging from about one year to thousands of years (decades are ideal for observation).

FIG. 2.2.3 is a representation of the motions of Sirius A and B, a visual binary. The left figure (A) shows the apparent motions relative to background stars of Sirius A, its companion B and the center of mass of the system C. The right figure (B) shows the orbital motions of Sirius A and B relative to the system's center of mass.

In an *astrometric binary* only one star is discernible, but its oscillatory motion in the sky reveals the presence of a hidden companion orbiting a common center of mass.

A *spectroscopic binary* is often an unresolved system whose binary nature is revealed by the periodic oscillations of lines in its spectrum. In the case of a *double-lined spectroscopic binary*, two sets of spectral features are observed (one set for each star), oscillating with opposite phases. In the case of a *single-lined spectroscopic binary* one of the stars is

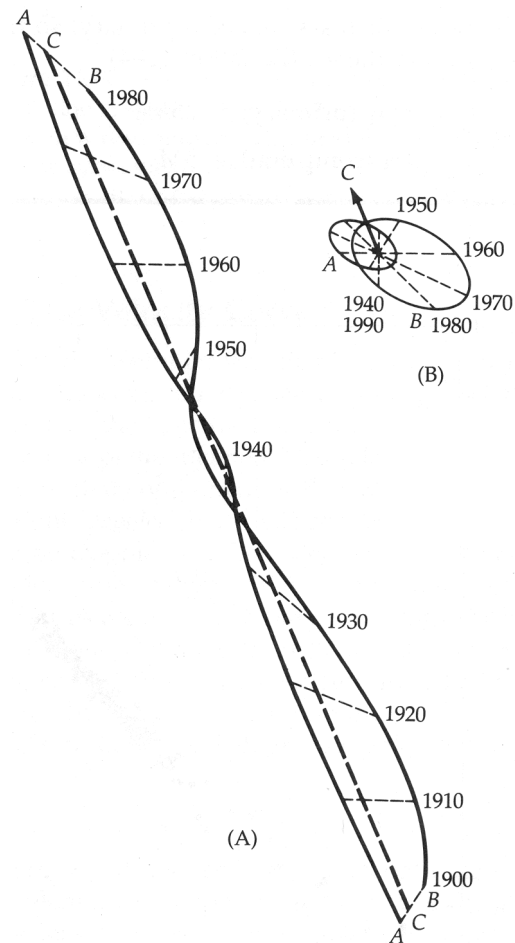


FIG. 2.2.3—Visual Binary  
(Source: Fig. 12-2 p. 237 Zeilik 1998)

comparatively too faint to be detected, and only one set of oscillating spectral lines dominates. Typical orbital periods range from hours to months.

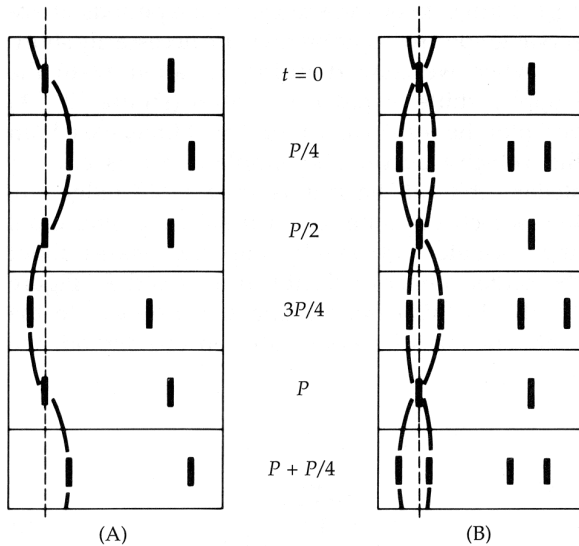


FIG. 2.2.4—Spectroscopic Binaries  
(Source: Fig. 12-4 p. 239 Zeilik 1998)

FIG. 2.2.4 are schematic spectra of spectroscopic binaries. In a single-line system (A), only one set of lines shows an oscillation in wavelength from the Doppler shift. In a double-line system (B), two sets of lines oscillate out of phase as the two stars revolve around their common center of mass.

The degree to which a spectral feature shifts from its rest wavelength (the Doppler shift) is a measure of the velocity of its source along our line of sight, the *radial velocity*. A plot of these line-of-sight velocities as a function of time is called a *radial velocity curve*.

FIG. 2.2.5 is a schematic representation of a radial velocity curve for a double-lined spectroscopic binary system with a circular orbit. The left figure (A) shows the circular path of primary star P and companion star C about the center of mass X, with an orbital inclination of  $90^\circ$  ("edge on" with respect to our line of sight from Earth). The figure on the right (B) shows the component radial velocities, where the center of mass of the system is receding at a constant speed  $CM$  relative to the Sun.  $V$  and  $v$  represent the speeds relative to the CM of the primary and companion (secondary), respectively, as

they move through one orbital period,  $P$ . According to convention, the primary is generally taken as the brightest star in the system.

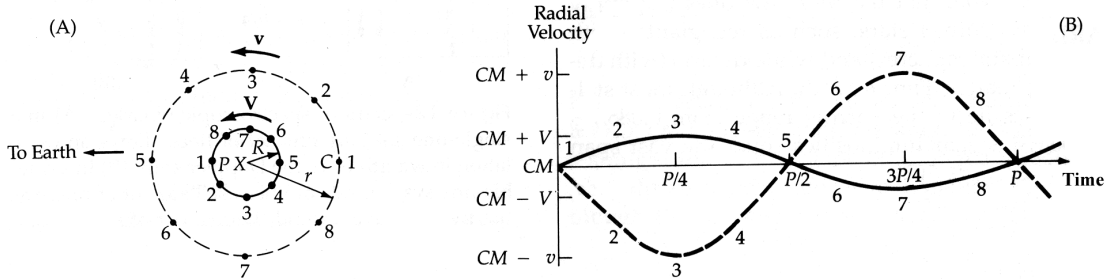


FIG. 2.2.5—Radial Velocity Curve  
(Source: Fig. 12-5 p. 240 Zeilik 1998)

A significant fraction of binary systems have inclinations in the range of about 70-90°; that is, their orbits are almost "edge on" with respect to our line of sight from Earth. If the component separations are sufficiently small, the stars will undergo eclipses, one star blocking all or part of the light from the other as viewed from Earth. FIG. 2.2.6 illustrates the photometric orbit

(or light curve) of a hypothetical partially eclipsing binary. In this illustration, the smaller star is assumed to be the hotter and brighter star. Hence, it is identified as the primary. During the "primary eclipse," the hotter primary star

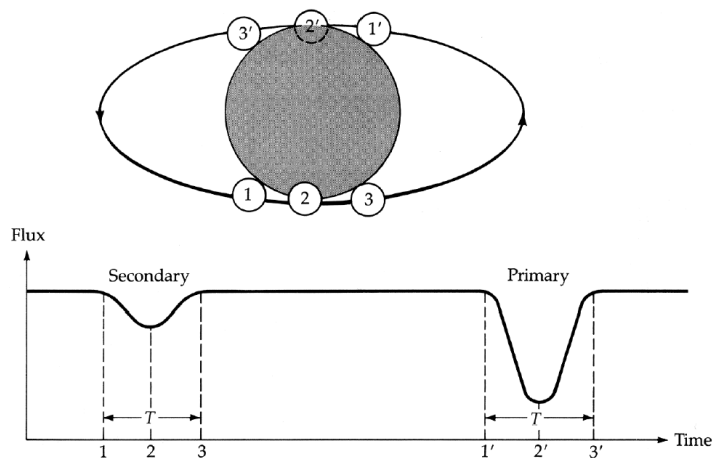


FIG. 2.2.6—Light Curve of Partially Eclipsing Binary  
(Source: Fig. 12-10 p. 244 Zeilik 1998)

is (partially) eclipsed by the secondary star, leading to a large reduction in binary-system flux.

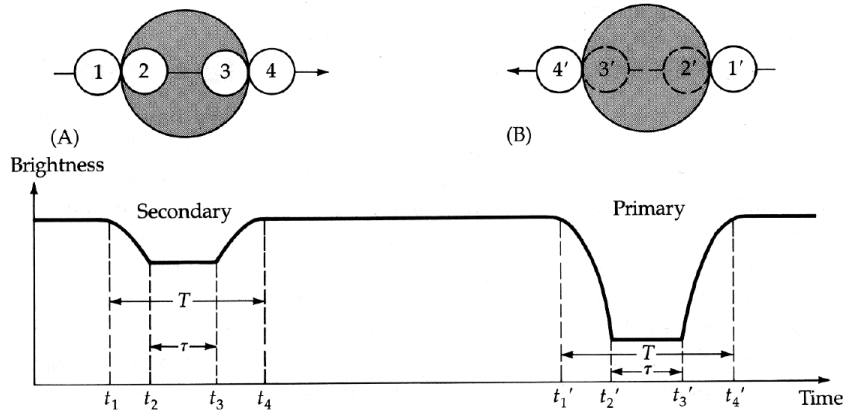


FIG 2.2.7—Light curve of eclipsing binary (primary is total)

FIG. 2.2.7 represents the light curve of an eclipsing system where the small star, the hotter component, is completely eclipsed. The four numbered contact points define the duration of the eclipse. These central eclipses would have flat bottoms if the limb darkening effect were excluded. During secondary eclipse (A), the primary passes in front of the secondary (i.e., the secondary is eclipsed). During primary eclipse (B), one-half an orbital period later, the primary star passes behind the larger secondary.

In close binary systems the gravitational field of one component can distort the shape of its companion. In some cases, the interaction produces a flow of mass out of one star, which either impacts the other star directly, forms an accretion disk or envelope around one or both components (circumstellar or circumbinary, respectively), or leaves the system altogether, resulting in a variety of interesting phenomena. For instance, the components may be so close together, and highly distorted, that they share a common atmosphere.

The shape of the component stars in a binary star system depends on the degree to which limiting equipotential surfaces called Roche lobes (described later in this section) are filled by the stars (for more information, see Hilditch 2001, p. 688). This is shown in FIG. 2.2.8. The components of *detached* systems (A) have radii much less than their separation and are nearly spherical in these cases; the two stars evolve nearly independently. In a *semidetached* system (B) one of the stars is so distorted and distended by its proximity to the companion that mass may flow away from the larger star. If both stars fill or expand beyond their Roche lobes, the two stars will share a common atmosphere bounded by a dumbbell-shaped equipotential surface. These are called *contact* systems (C).

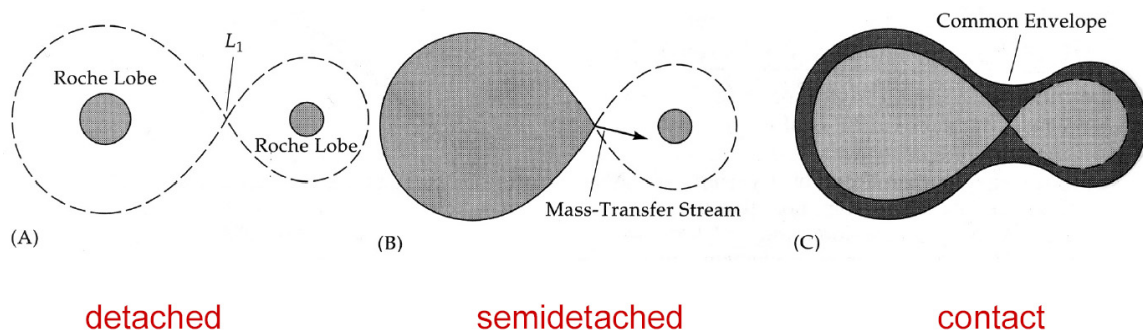


FIG. 2.2.8—Shape of Binary Components (Source: Fig. 12-12 p. 246 Zeilik 1998)

Semidetached and contact systems are *interacting binaries*. *Algol-type* binaries (discussed Section 2.4) belong to the semidetached subclass of interacting binaries. Algol itself, the focus of this work, is the prototype of this class.

Roche lobe geometry is derived from the *Restricted three-body problem*: Two bodies  $m_1$  and  $m_2$  move in circular orbits about their common center of mass, while a third body of infinitesimal mass moves in the gravitational field of the other two bodies

(for further information, see Hilditch 2001, p. 157). Masses  $m_1$  and  $m_2$  are considered centrally condensed or point masses, and are in circular and synchronous orbits so that the orbital period equals the rotational period.

FIG. 2.2.9 illustrates the geometry of the restricted three-body problem. Masses  $m_1$  and  $m_2$  are in orbit about their mutual center of mass,  $X$  (with  $m_1 > m_2$ ). The distances from  $m_1$  and  $m_2$  to the infinitesimal point mass at  $(x, y, z)$  are  $r_1$  and  $r_2$  respectively. The semimajor axis,  $a$ , is the separation of  $m_1$  and  $m_2$ . The Roche equipotentials (indicated by the contours) are equipotential surfaces in this co-rotating

frame of the restricted three-body problem. These effective potential-energy surfaces include both true gravitational and fictitious centrifugal contributions. If we let the semimajor axis  $a = 1$  then the normalized potential  $\phi$  (in the co-rotating frame) experienced at any position  $(x, y, z)$  is the sum of the two point-mass potentials and the rotational potential (*Equation 4.46 p.157 Hilditch 2001*):

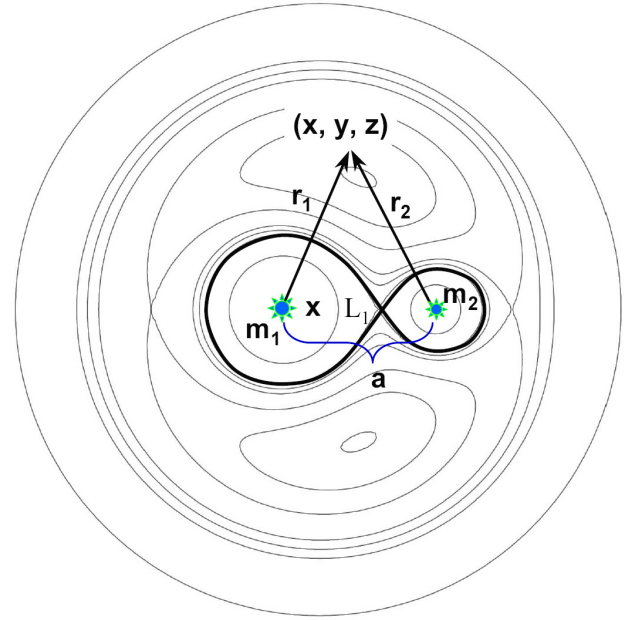


FIG. 2.2.9—Geometry of Restricted 3-body problem

$$\phi = -\frac{Gm_1}{r_1} - \frac{Gm_2}{r_2} - \frac{\omega^2}{2} \left[ \left( x - \frac{m_2}{m_1 + m_2} \right)^2 + y^2 \right] \quad (2.2.1)$$

where  $G$  is the Gravitational constant\* and  $\omega$  is the angular velocity of the co-rotating coordinate system. The equipotentials that intersect (dark, thick teardrop-shaped contours) at a point along the line of centers that joins the two masses are called *Roche lobes*. The point of intersection is called the  $L_1$  point, or the *inner Lagrangian point*.

Initial conditions restrict the third body to a certain volume. This means the particle cannot cross the equipotential surface defined by its initial conditions; that is, a small test mass, viewed within the rotating coordinate system, will move within (not cross) the equipotential surface corresponding to the test particle's total energy (i.e., positions where the test mass would have no kinetic energy – no velocity – with respect to the rotating frame).

The Roche equipotentials provide constraints on the motion of matter moving under the gravitational influence of  $m_1$  and  $m_2$ . In particular, we are concerned with the flow of stellar gases in the case of a semidetached interacting binary. Observational evidence for such mass flow is provided in the following section.

### 2.3 Observational Indications of Mass Flow

The activity levels of Algol-type binaries vary from one system to another and within the same system across epochs. Gas stream effects accompanying periods of higher activity are observed in the radial velocity curves of Algol-type systems. FIG. 2.3.1a is a schematic radial velocity curve of an eclipsing binary *without* the gas stream.

---

\*  $G = 6.67259 \times 10^{-8}$  dyne  $\text{cm}^2/\text{g}^2$

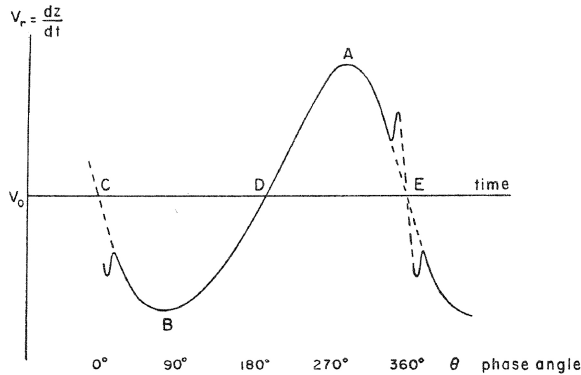


FIG. 2.3.1a—Radial velocity curve with rotation effect only  
(Source: Fig. 88 p.173 Binnendijk 1960)

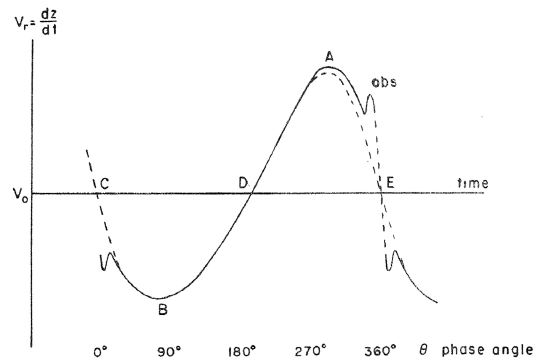


FIG. 2.3.1b—Radial velocity curve with gas stream and rotation effects  
(Source: Fig. 89 p.174 Binnendijk 1960)

Primary eclipse occurs at  $0^\circ$  and  $360^\circ$  (points C and E). The extra oscillation at phase =  $360^\circ$  (primary minimum), is due to the rotation effect.\* FIG. 2.3.1b, on the other hand, is a typical radial velocity curve of an Algol-type system undergoing an epoch of mass transfer. The location (in phase) of the excess radial velocity is indicative of mass flowing from the secondary, through the inner Lagrangian point, toward the facing hemisphere of the primary. This type of asymmetry in radial velocity curves was noted as early as 1908 when Barr described these curves as having an ascending branch of greater length than the descending branch. The explanation of a gas stream, however, was not suggested until Struve (1941) postulated<sup>†</sup> such a gas stream in  $\beta$  Lyrae\*<sup>§</sup>.

\* "When the bright star is entering eclipse, one limb is gradually covered by the eclipsing star and consequently the lines from the bright star are fully broadened on one side only because of the velocity of the one wholly visible limb. When these lines are measured for determination of radial velocity, the center of density of the line will be shifted toward the broadened edge and away from the center of the symmetrical line that would be observed if both lines were visible." (Rossiter 1924)

<sup>†</sup> "...[V]iolet satellites are interpreted as a stream flowing from the B9 star, along the side of the invisible second component which becomes uncovered after minimum light." (Struve 1941)



Epochs of active mass transfer are also evident in the light curves of Algol-type systems. Dugan (1924) was the first to conclude that the "anomalous hump"<sup>†</sup> in the light curve of R Canis Majoris<sup>‡</sup> at the end of primary minimum<sup>§</sup> "has some real significance." He indicates its transient nature when he says, "The constancy of the hump, however, is placed in doubt by the observations of other nights." That is, the hump was not present on other nights. FIG. 2.3.2 is the R CMa light curve containing the "hump," as indicated by the solid circles (between 4-6h on the figure).

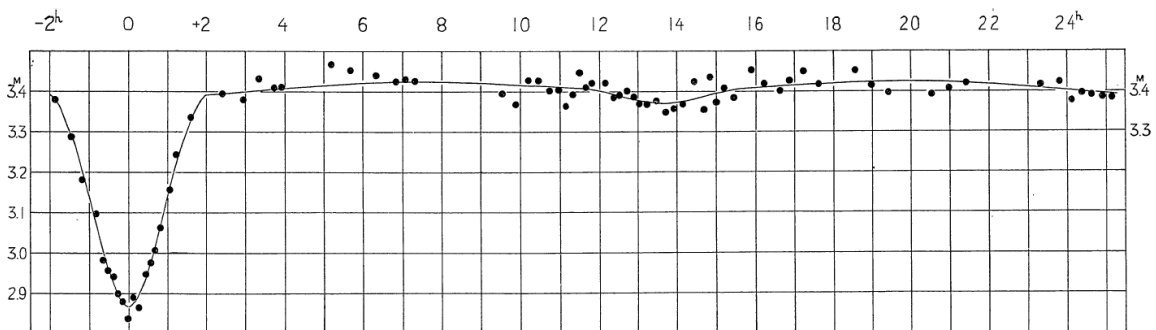


FIG. 2.3.2—Light Curve of R Canis Majoris  
(Source: Fig. 8 p.68 Dugan 1924)

The solid circles are averaged data points. The solid curve on the other hand is the expectation for the light curve in the absence of mass flow effects. Data are from observations in epoch 1898-1899.

Another example of gas stream effects is provided by observations of U Cep.<sup>\*\*</sup>

Olson (1980) compares the light curves of U Cep, from different epochs during ingress

<sup>\*§</sup> "There is weak evidence that  $\beta$  Lyrae is semidetached but often this is simply assumed to be the case" (Sahade, McCluskey, and Kondo 1993 p.40).

<sup>†</sup> This was discovered independently in 1898 by Pickering (1904) and Wendel (1909) according to Sahade and Wood (1978).

<sup>‡</sup> R Canis Majoris (R CMa) is a bright, short period, semidetached eclipsing binary of the Algol type (Verricatt and Ashok, 1999) with the lowest known mass of Algol systems hosting the least massive secondary star (Ribas et al., 2002).

<sup>§</sup> Hump observed 1898-1899.

<sup>\*\*</sup> U Cephei, an eclipsing semidetached binary, is the most active of short period interacting Algol-type binaries. (McCluskey et. al 1988) with a period of 2.49 days (Olson et al.1981).

and egress, which become "... grossly distorted during mass-transfer events." FIG. 2.3.3a is the U Cep U-band light curve of primary eclipse ingress. The solid line is the mean undisturbed egress curve reflected around mid eclipse; *filled circles*, 1978 September 27 (low activity); *squares*, 1976 (moderate activity); *triangles*, October 26 (high activity).

FIG. 2.3.3b is the U Cep U-band light curve of primary eclipse egress. The *filled circles* are data from five nights of low photometric contamination; *triangles*, active night 1975 October 31.

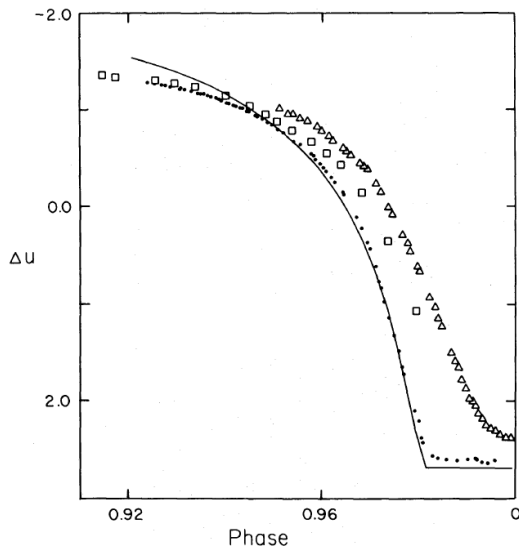


FIG. 2.3.3a—*U Cep U-band light curve of primary eclipse ingress*  
(Source: Fig. 2 p.258 Olson 1980)

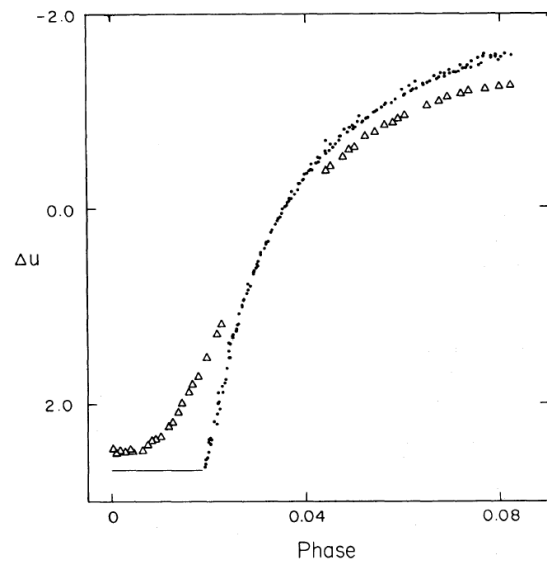


FIG. 2.3.3b—*U Cep U-band light curve of primary eclipse egress*  
(Source: Fig. 1 p. 258 Olson 1980)

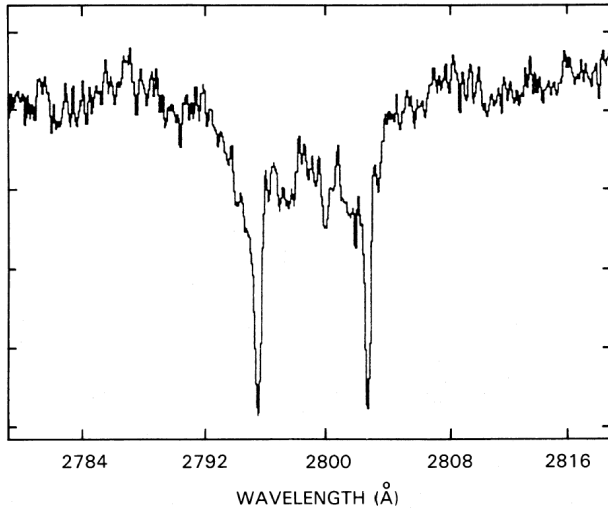


FIG 2.3.4a—*U Cep UV Mg II resonance doublet 1986 Oct 22* (Source: Fig. 2d p.1025 McCluskey et al. 1988)

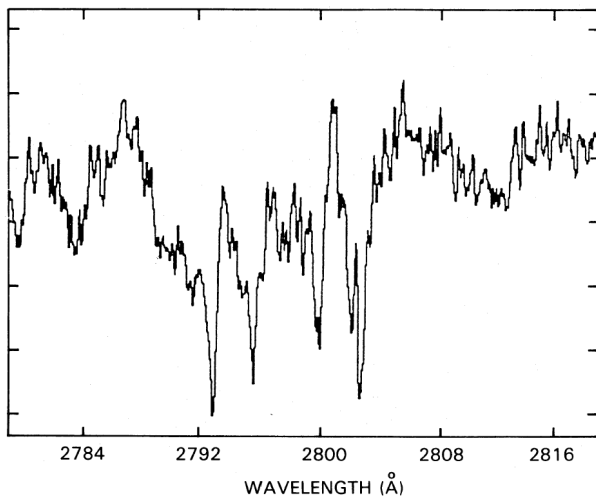


FIG 2.3.4b—*U Cep UV Mg II resonance doublet 1986 Jun 4* (Source: Fig. 2a p.1024 McCluskey et al. 1988)

McCluskey et al. (1988)

detected gas stream effects in *U Cephei* by examining ultraviolet Mg II line profiles from different epochs.

FIG. 2.3.4a shows the Mg II resonance doublet, presumably during a

quiescent period on 22 October 1986 at phase 0.180. The spectral lines at

2796 Å and 2803 Å are well resolved.

FIG. 2.3.4b shows the same spectral range on 4 June 1986 at a similar

phase (0.132). The pair of extra, narrow lines, blueshifted by 2.7 Å at

~2793 Å and ~2800 Å are interpreted as a transient high-mass flow event

with a radial mass velocity of -286

km/s.

Walter (1973) presents a general picture of the gas stream effects. FIG. 2.3.5 illustrates hypothetical distortions of light curves outside primary eclipse caused by absorption (cross-hatched) and emission (dotted) for systems with impact regions of the gas streams near the equator (A and B) and near the poles (D) of the small bright component. These are consistent with the features already discussed of FIGs. 2.3.1 and 2.3.2.

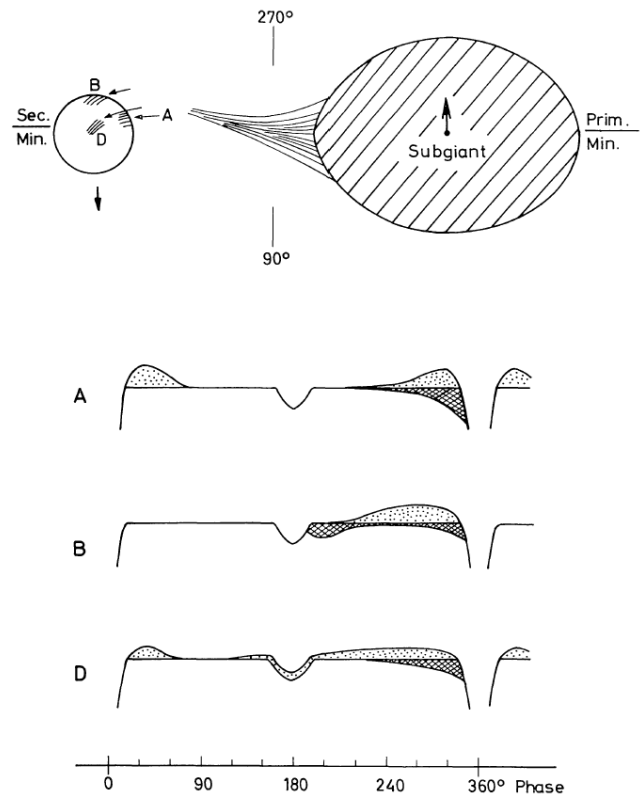


FIG. 2.3.5—Hypothetical photometric distortions from gas stream effects (Source: Fig. 3 p. 292 Walter 1973)

#### 2.4 Algol (Beta Persei), Algol-Type Systems and the Algol Paradox

Algol-type binary star systems have been studied actively since 1783, when Englishman John Goodricke conjectured that the cause of the light variations in Beta

Persei\* "... could hardly be accounted for otherwise than ... by the interposition of a large body revolving round Algol ..." (Goodricke 1783).

Ancient people had already noticed the dramatic decrease in Algol's light (1.2 magnitudes within five hours) that gave rise to the name *Al Ghūl*, which means "changing spirit" to the inhabitants of the Arabian Peninsula. The ancient Hebrews named this bright star *Rōsh-ha-Satan*, which means "Satan's Head," and the Chinese named it *Tseih She*, "the Piled-up Corpses" (Kopal 1959). Other descriptive names include "the eye of the Medusa,"<sup>†</sup> and "the demon star."

Algol (HD 19356)<sup>‡</sup> is the brightest eclipsing binary system in the sky and the prototype of its class (Drake 2003). It is the first variable system to be identified as an eclipsing binary. Algol is actually a triple system where the earliest reference to a third component is credited to Stebbins in 1924 (Sahade and Wood 1978). This ternary stellar system consists of an eclipsing close-binary with a period of 2.87 days, orbiting a main-sequence A7m star in 1.86 years (Lestrade et al. 1993). The primary star of the eclipsing close-binary is a nearly spherical B8 V star and the less massive secondary is a highly distorted K0-3 IV star in contact with its Roche equipotential surface (Guinan et al. 1989). The masses of Algol A, B and C are  $3.7 M_{\odot}$ ,  $0.81 M_{\odot}$ , and  $1.6 M_{\odot}$ , respectively. The Algol system is located a distance of 28 pc from Earth (1pc = 3.25 light years).

A comprehensive set of system parameters, as reported by numerous investigators, is collected in Appendix A, Tables 1-59. A selection of these parameters is provided in TABLE 2.4.1.

---

\* Algol itself is also known as Beta Persei.

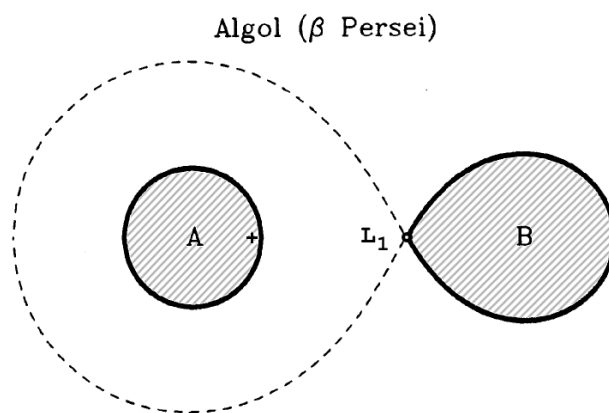
† In Greek mythology Medusa is a Gorgon, a vicious female monster with sharp fangs and hair of living venomous snakes (en.wikipedia.org 2006).

‡ Also designated  $\beta$  Per; 26 Persei; HR 936; SAO 38592; ADS 2362

TABLE 2.4.1  
Selected Algol Parameters

Algol A	Algol B	Algol C
B8 V	K2 IV	F2 V
$T_A = 12500 \pm 500$ K	$T_B = 4500 \pm 300$ K	$T_C = 7000 \pm 200$ K
$M_A = 3.7 \pm 0.3 M_\odot$	$M_B = 0.81 \pm 0.05 M_\odot$	$M_C = 1.7 \pm 0.2 M_\odot$
$R_A = 2.90 \pm 0.04 R_\odot$	$R_B = 3.5 \pm R_\odot$	$R_C = 1.6 \pm 0.2 R_\odot$
$P_{A-B} = 2.8673^d$		$P_{AB-C} = 679.9^d$
$sep_{A-B} = 14.0 R_\odot$		$sep_{AB-C} = 2.67 \pm 0.08$ AU

FIG. 2.4.1 is a diagram of the Algol binary as seen from above the orbital plane. The Roche lobes and components of the system are drawn to scale. The + sign indicates the position of the center of mass of the binary.



The zero-velocity surface passes through the inner Lagrangian point  $L_1$ .

FIG. 2.4.1—Scale diagram of Algol  
(adapted from Fig. 7 p. 335 Richards et al. 1988)

Like Algol itself, Algol-type binaries are composed of an early-type main-sequence (O V - B V) primary that lies well within its Roche lobe, and a less massive late-type subgiant (F IV - K IV) secondary that fills its Roche lobe and loses mass to the primary.

The eclipses of Algol-type binaries are dramatic because the hotter (and brighter) primary star of the eclipsing pair contributes about 90 percent to the total visible light of the system, and most of this light is blocked when the cooler (and fainter) secondary star eclipses the primary. The eclipse of the secondary star produces a small diminution in

the visible light from the pair. The light curve of Algol demonstrates this signature difference in the depths of primary and secondary minimum.

FIG. 2.4.2 is a light curve of Algol at 3428 Å, using Copernicus satellite data (Chen et al. 1977). Secondary minimum occurs at phase = 0.5, when Algol B is partially

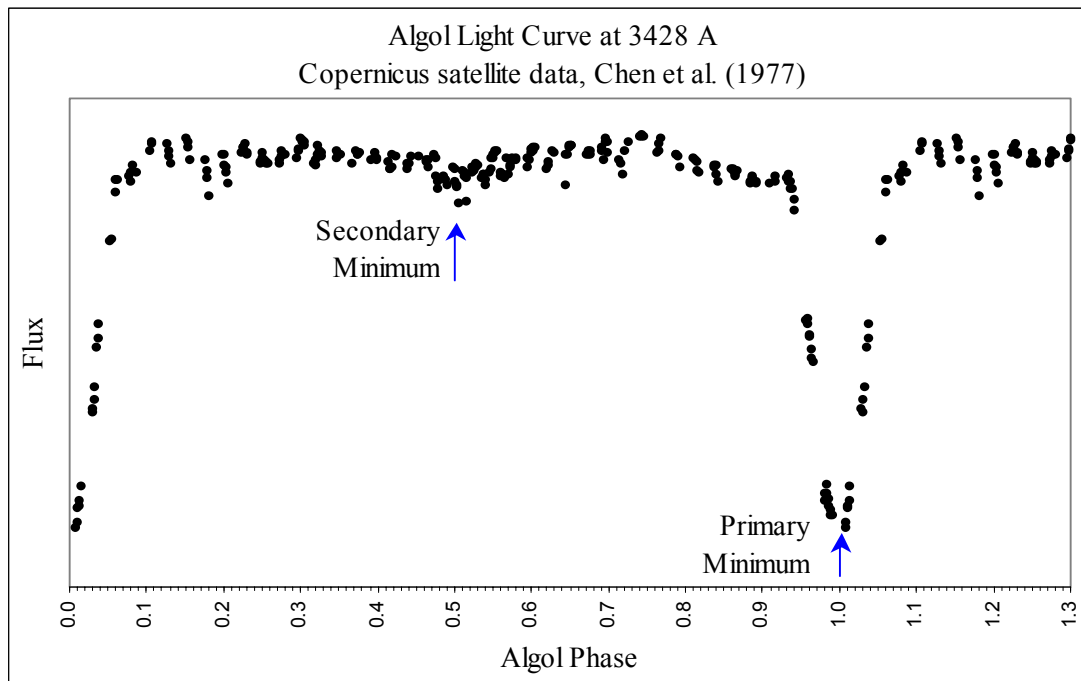


FIG. 2.4.2—Algol light curve at 3428 Å (Source: Copernicus satellite data, Chen et al. 1977)

eclipsed by Algol A. Primary minimum occurs at phase = 0.0 (equivalent to 1.0) and is noticeably deeper since most of the light from the system, which comes from Algol A, is being attenuated by the dimmer Algol B as it passes between us and the primary.

Outside of the eclipses, the spectrum of an Algol-type binary shows absorption lines from the primary, while the spectrum of the fainter secondary star can be detected only during primary eclipse (Richards 2002 Web site ).

The secondaries of Algol-type systems are peculiar because they do not follow the expected mass-luminosity relation; that is, "... the secondary components possess masses

which are as a rule too small for their observed luminosities" (Kopal 1955). Crawford (1955) describes these peculiar secondaries as "... combining subgiant character with small mass ( $<1\odot$ )". This circumstance, the well known *Algol Paradox*, is described by Crawford: "It is not possible to understand how stars with such small mass could have had enough time in five billion years to reach the advanced stage of evolution suggested by their subgiant characteristics..." In Kopal's words, "... as both components are no doubt of equal age (and, presumably, of initially the same chemical composition), the subgiant secondaries cannot manifestly be 'old' on the same time scale."

Crawford explains this seemingly contradictory set of circumstances by relating "the 'advanced age' of these stars to the fact that they fill the inner zero-velocity surface"\*

Kopal, independently, makes this same ingenious connection:

"If ... these stars are secularly expanding, there is a compelling reason why their size cannot exceed that of their Roche limit: for no larger *closed* equipotential exists which would contain the whole mass of the respective configuration. ...[O]nce this maximum distension permissible on dynamical grounds has been attained, a continuing tendency to expand is bound to bring about a *secular loss of mass* ... [T]here remains but little room for doubt that the relative smallness of their present masses is but the consequence of a secular loss caused by continued expansion."

Crawford's evolutionary scenario, which solves the Algol paradox, is illustrated in FIG.

2.4.3.

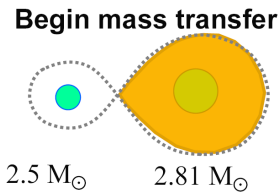
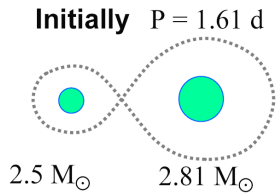
---

\* This is equivalent to filling the Roche lobe.

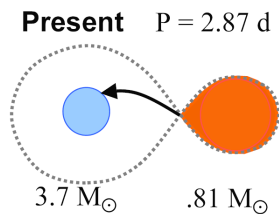
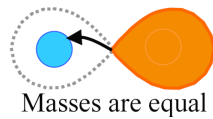


**Algol "A"      Algol "B"**

Crawford (1955) p.75



**Begin reversal of mass ratio**



"Let us consider in a general way the evolution of a close binary system subsequent to its formation at a given date by some unknown mechanism. One of the stars will, in general, be more massive than the other."

"The more massive star will, from the mass-luminosity relation, be much more luminous and will evolve more rapidly. At a certain point, it will acquire an unstable depleted core (Schöberg and Chandrasekhar 1942) and begin to move very rapidly to the right in the H-R diagram (Sandage and Schwarzschild 1952), expanding its radius as it does so. It is then very probable that this expansion will continue until the star fills the inner zero-velocity surface."

"The star will then continue to expand, but will not be able to hold on to the mass that passes out of the surface. This mass will either be collected by the companion or be ejected from the system by centrifugal force, probably depending on whether or not fairly violent ejection mechanisms, such as prominences, dominate. The material lost, lying at the surface of the star, will be rich in hydrogen; and, as mass is lost, the ratio of the mass contained in the depleted core to the total mass of the star will increase. This ratio is a measure of the "biological age" of the star. As this age increases, the expansion will continue."

"By this mechanism, the star can gradually become less massive than its companion and eventually less luminous, becoming the secondary component."

FIG. 2.4.3 - Crawford's Evolutionary Scenario (1955, p.75) illustrated using Algol (Beta Persei)

## 2.5 Previous Observations and Models for Algol

Algol was first studied in the visual range, then in other wavelength ranges as technologies became available. Budding (1986) compiled a table of “advances in observational coverage” of Algol (see TABLE 2.5.1).

TABLE 2.5.1

Some advances in observational coverage of Algol

Year	Authors	Innovation	Result
1966	Chen and Reuning	IR (1.6 $\mu$ ) light curve	Pronounced secondary minimum; photometric peculiarities
1966	Cristaldi <i>et al.</i>	H $\alpha$ photometry	Evidence of spectral instabilities
1967	Glushneva and Esipov	IR (0.7–1.1 $\mu$ ) spectroscopy	Transient emission features
1972	Hjellming <i>et al.</i>	Radio observations (2695 and 8085 MHz)	Emission with short time variations discovered
1973	Ryle and Elsmore	Radio-interferometry	Accurate location of barycentre
1974	Labeyrie <i>et al.</i>	Speckle interferometry	Resolution of Algol C.
1975	Chen and Wood	UV spectroscopy	Detailed scans of L $\alpha$ at different orbital phases
1975	Eaton	UV light curves	Physical parameter values in UV
1975	Smyth <i>et al.</i>	IR (2.2 $\mu$ ) light curves	Apparent discrepancies with models
1975	Longmore and Jameson	IR (2.2, 3.6, 4.8, 8.6 $\mu$ ) light curves	IR excess – attributed to gas stream
1975	Bachmann and Hershey	Inclusion of accurate astrometry	More confident element specification
1975	Gibson <i>et al.</i>	Radio observations (1400, 2695, 6000, and 8085 MHz)	Large flare (> 1 Jy) detected.
1976	Guinan <i>et al.</i>	H $\alpha$ and H $\beta$ index monitoring	Presence of circumstellar emission region revealed
1976	Schnopper <i>et al.</i>	X-ray observation	Emission in 2–6 keV band detected
1978	Rudy and Kemp	Polarimetry	Independent determination of orbital inclination
1978	Tomkin and Lambert	Reticon spectroscopy	Detection of Na II D lines of secondary
1978	Nadeau <i>et al.</i>	IR (10 $\mu$ ) data	Anomalous shape of secondary minimum
1979	Bonneau	Speckle interferometry	Revised absolute elements of triple system
1979	White <i>et al.</i>	X-ray spectrometry	No eclipses. Active corona of sub-giant inferred
1980	Zeilik <i>et al.</i>	IR (JHKLM) light curves	IR luminosity ratios
1979	Cugier	UV Spectrometry	High resolution Mg II line profiles
1981	Chen <i>et al.</i>	(Copernicus)	allow detailed modelling
1981	Kemp <i>et al.</i>	Upgraded polarimetry	Perpendicularity of AB and AC orbit planes inferred
1982	Zirin and Liggett	IR coude spectrometry	Deep absorption at $\lambda$ 10830 due to Algol B
1983	Kemp <i>et al.</i>	Polarimetry	Discovery of eclipse polarization effect

(Source: Budding 1986, Table 1 page 244)

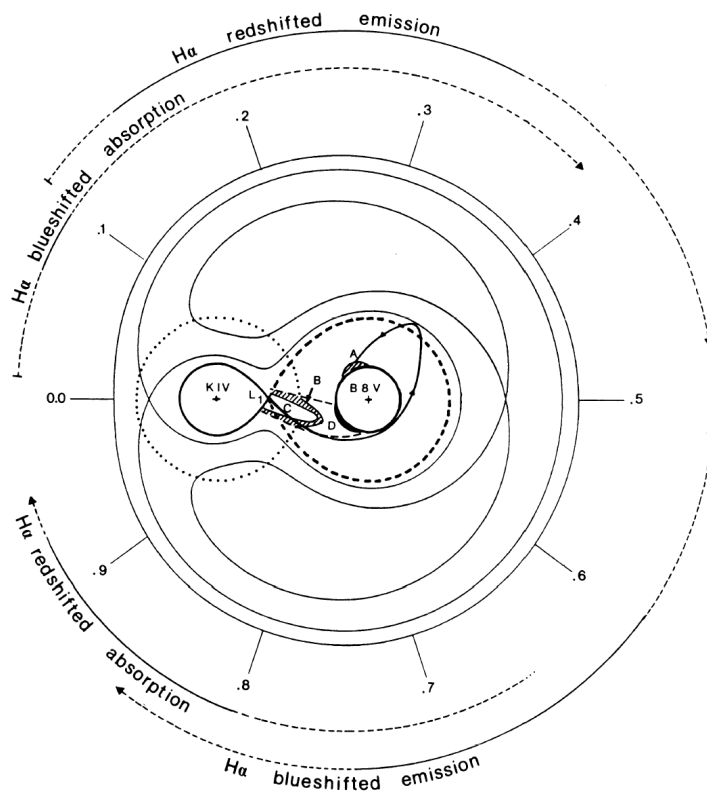


FIG. 2.5.1—Model of Algol deduced from  $H_{\alpha}$  observations  
(Source: Fig. 3 p. 225 Gillet et al. 1989)

FIG. 2.5.1 is a model of Algol (Gillet et al. 1989) deduced from  $H_{\alpha}$  (6562.8 Å) observations in 1985 and 1986. They observed the greatest blueshifted  $H_{\alpha}$  emission between phases 0.6 and 0.75. The greatest redshifted  $H_{\alpha}$  emission is between phases 0.13 and 0.34. These phase regions are identified by the outer circular segments in FIG. 2.5.1. Gillet

et al. (1989) explained the two emission regions as (1) the stream itself (region B in the figure) and (2) a localized region near the photosphere of Algol A (region A). The thin continuous lines are the Roche equipotentials. The two thin dashed lines mark the extension of the stream of gas from Algol B near the  $L_1$  point to Algol A (deduced from the hydrodynamic model of Prendergast and Taam 1974). These trajectories create the first shock, a hot spot on the photosphere of Algol A. The surrounding region, identified by “D” on the figure, is completely ionized by the hot spot. The second shock is created by the impact of the stream that passes around the primary. This hot spot is identified as

“A.” The dotted circle is the approximate position of the corona associated with the cool secondary star (as assumed by White et al. 1986; and Lestrade et al. 1988).

FIG. 2.5.2 is a model for the circumstellar material in Algol. Like the 1989 model of FIG. 2.5.1, this 1993 model is also developed from an analysis of  $H_\alpha$  difference

profiles. The 1993 analysis, however, used observations made in 1972, 1976, 1977, and 1985. According to this study, Richards (1993) observed strong single-

peaked emission features outside of primary eclipse and

absorption features during primary eclipse which she interpreted as a transient, high density ( $N_e \geq 10^{11} / \text{cm}^3$ ), low mass ( $M \sim 10^{-13} M_\odot$ ), localized region situated close to the photosphere of the primary but high above the orbital plane. She interpreted the weak double-peaked emission profiles seen outside of primary eclipse and the emission seen during primary eclipse as a transient rotating accretion disk which surrounded the primary. She observed broad, shallow absorption features, in the late 1976 to early 1977 data, at phases throughout the orbit of the binary and attributed this to a high-velocity component of the disk which surrounded the primary at that time. The region  $lr$  is the "localized region,"  $hrvr$  is the "high-rotational-velocity region." Both regions are part of

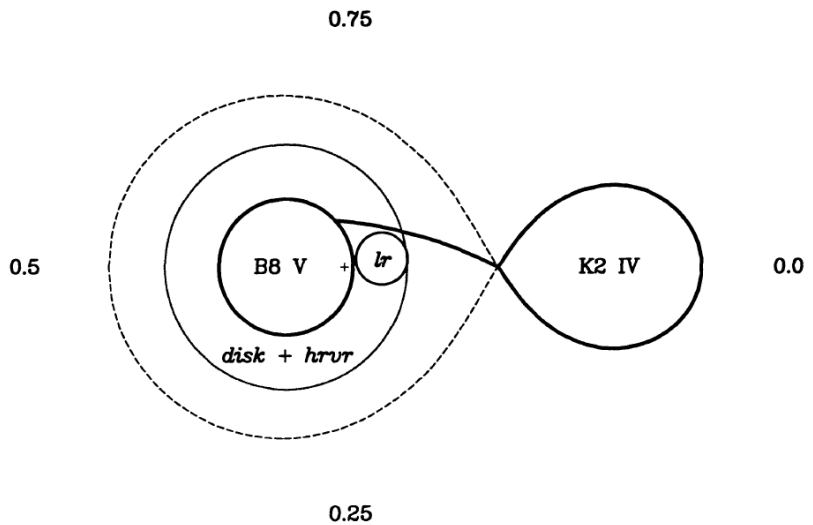


FIG. 2.5.2—Model for the circumstellar material in Algol deduced from  $H_\alpha$  observations (Source: Fig. 20 p. 290, Richards 1993)

a "weak transient rotating accretion disk." The arced line drawn between the secondary (K2 IV star) and the primary (B8 V star) is the Lubow-Shu (1975, 1976) gas stream.

The VLBA (Radio) observations presented by Mutel and Molner (1998) provided "...the first evidence for double-lobed structure in the radio corona of an active late-type star in the quiescent (basal) state." FIG. 2.5.3a is a schematic drawing of their "simple polar cap model." The basal components fill the extended region above the polar caps, while the flare emission regions are concentrated in the smaller regions of the higher magnetic field closer to the stellar surface. The lobes are separated by  $1.6 \text{ mas}^*$ , or  $2.8 R_B$ . FIG. 2.5.3b contains a scale drawing of the binary system with respect to the radio source. It is assumed that the centroid of the radio emission is coincident with the center of the K star.

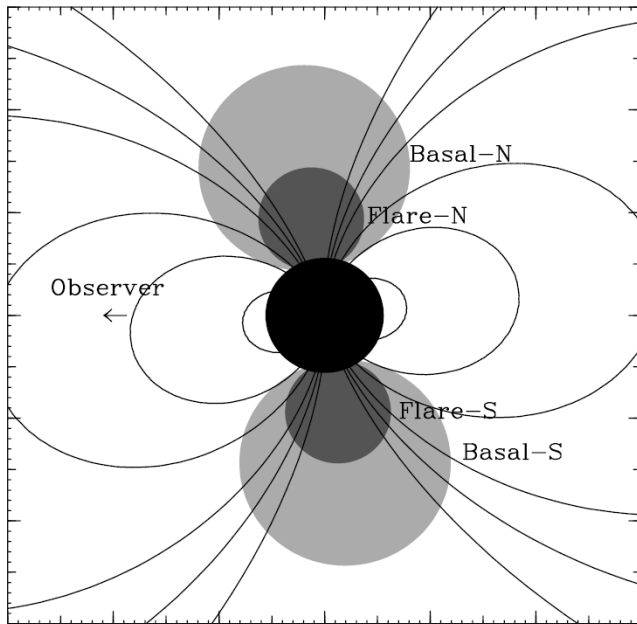


FIG. 2.5.3a—Radio Model  
(Source: Fig.3 p. 373 Mutel and Molner 1998)

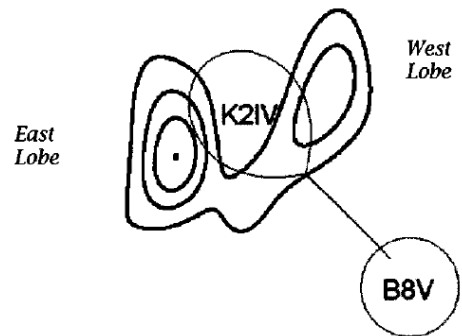


FIG. 2.5.3b—Schematic of Algol with radio source (Source: Fig. 13 p. 381 Mutel and Molner 1998)

\* An angular measurement. There are 60 arc-seconds in one arc-minute, 60 arc-minutes in one degree, and 360 degrees in a full circle. One thousandth of an arc-second = 1 milliarc-second (mas)

Harnden et al. (1977) detected Algol in the soft X-ray region and interpreted the X-ray flux as "...thermal emission produced by the direct accretion of mass from the K

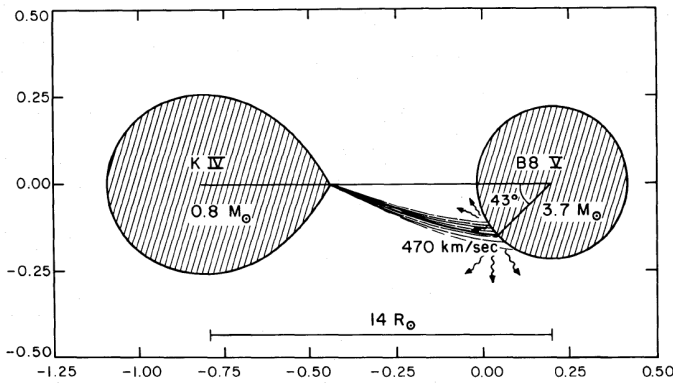


FIG. 2.5.4—Soft X-ray Model  
(Source: Fig. 2 p. 420 Harnden et al. 1977)

star to the B8 member of the triple star system." The 0.15 to 2 KeV X-ray luminosity is  $\sim 10^{30}$  ergs/s. FIG. 2.5.4 shows a simulated restricted three-body trajectory corresponding to Roche lobe overflow in Algol for gas leaving the surface of the K

star at a thermal velocity  $\sim 7 \text{ km/s}$  from the inner Lagrangian point  $L_1$ . The stream intercepts the B8 V star at an angle of  $43^{\circ}$  with respect to the line of centers and with a velocity of  $470 \text{ km/s}$ .

Cugier (1982) analyzed UV observations of Algol from the Copernicus satellite. From the additional absorption components of Mg II near  $2800 \text{ \AA}$ , he concludes that "...the absorbing region in which these components originate is optically thick and covers at least 20 per cent of the disc of the primary star, Algol A."

FIG. 2.5.5 is the geometry of the region of effective formation of the additional absorption components. The regions indicated as (1) and (2) correspond to Mg II  $2795.5 \text{ \AA}$  and Mg II  $2802.7 \text{ \AA}$  lines, respectively.

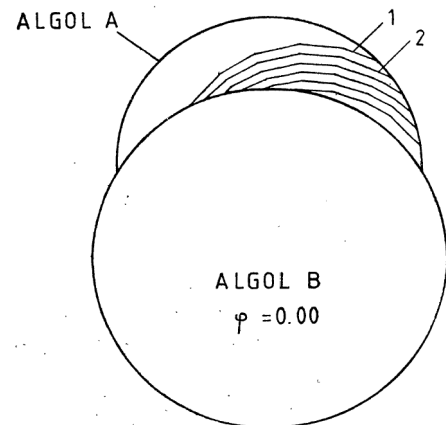


FIG. 2.5.5—Mg II Absorption Model  
(Source: Fig. 10 p.397 Cugier 1982)

## 3. IUE OBSERVATIONS

### 3.1 *IUE Spacecraft and Database*

The IUE satellite,<sup>\*</sup> launched on January 26, 1978 and shown in FIG. 3.1.1, was the first observatory type satellite totally dedicated to ultraviolet astronomy (Boggess et al. 1978).

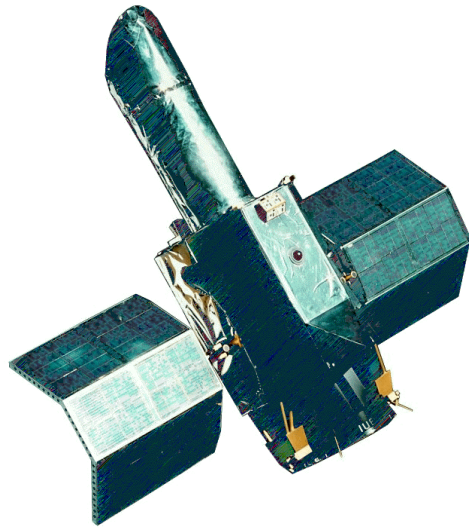


FIG. 3.1.1—*IUE Satellite*. (Source: [http://sp.dext.estec.esa.nl/content/doc/af/2479\\_.htm](http://sp.dext.estec.esa.nl/content/doc/af/2479_.htm))

Guest astronomers were able to operate the satellite in real time (with a joystick) similar to the operation of a ground-based observatory (IUE, a). Initially, these remote operations were performed 16 hours a day from NASA/GSFC<sup>†</sup> and eight hours a day from VILSPA<sup>‡</sup> (IUE, b). Later, scientists could make their observations remotely from their

home institutions (IUE, c). Although scheduling was facilitated by placing the spacecraft in a geosynchronous orbit, the demand for observation time consistently exceeded availability (by two to three times) during its 18.5 years of operation (IUE, b). (It's interesting to note that IUE's estimated lifetime was 3 to 5 years) (IUE, d). Currently IUE is considered to be the most productive and successful satellite in the history of space astronomy (IUE, e). IUE made, on average, one one-hour observation every 90

---

<sup>\*</sup> International Ultraviolet Explorer (IUE) satellite

<sup>†</sup> Goddard Space Flight Center (GSFC), Greenbelt, Maryland

<sup>‡</sup> Villafranca Satellite Tracking Station (VILSPA), Villanueva de la Canada, Madrid, Spain.

minutes, around the clock (IUE, a). The durability of IUE enabled astronomers to monitor longer term changes by revisiting many targets. IUE remained operational until 30 September 1996 (IUE, b). The 104,000 images obtained by IUE were transformed into 111,000 spectral files, available to scientists throughout the world (IUE, e). “The IUE Data Archive remains the most heavily used astronomical archive in existence.” (IUE, f)

The five mission goals are (IUE, g): (1) to obtain high-resolution spectra of stars of all spectral types to determine their physical characteristics, (2) to study gas streams in and around binary star systems, (3) to observe faint stars, galaxies and quasars, (4) to observe the spectra of planets and comets, and (5) to make repeated observations of objects with variable spectra. (6) This work addresses goals (1), (2), and (5) above.

Here are just a few "firsts" (selected from the 27 listed) (IUE, h): (a) the first evidence for strong magnetic fields in chemically peculiar stars, (a) the first observational evidence for semi-periodic mass loss in high mass stars, (b) the first discovery of high velocity winds in stars other than the Sun, (c) the discovery of starspots on late type stars through the Doppler mapping techniques, (d) the discovery of large scale motions in the transition regions of low gravity stars, (e) the discovery of the effect of chemical abundance on the mass loss rate of stars, (f) the first determination of a temperature and density gradient in a stellar corona outside the Sun, and (g) the creation of the first worldwide astronomical reduced-data archive delivering 44,000 spectra per year (5 spectra per hour) to astronomers in 31 countries.



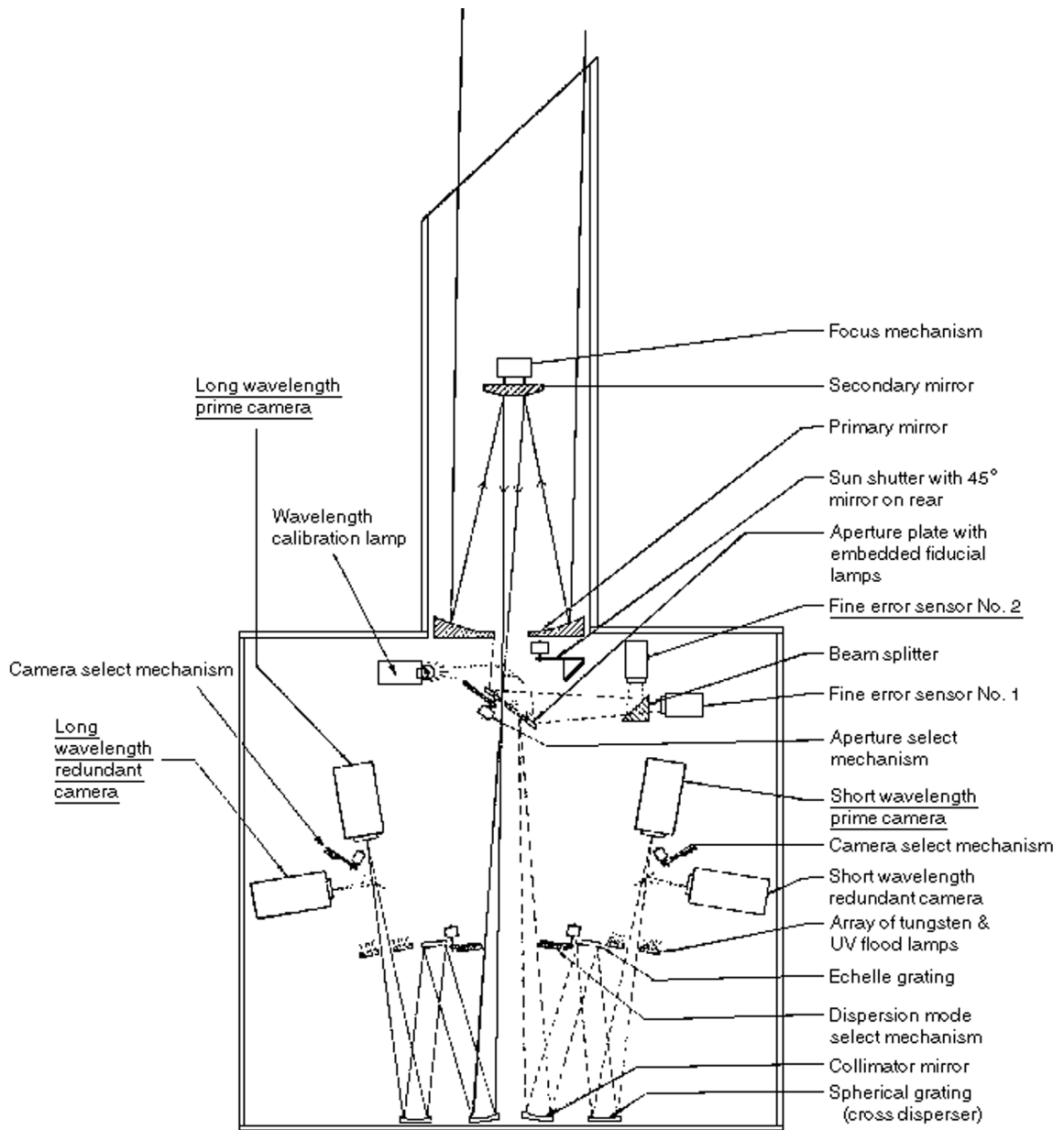


FIG. 3.1.2—Optical Schematic of the IUE Scientific Instrument. (Source: online document cited 4/22/06 [http://archive.stsci.edu/iue/instrument/obs\\_guide/fig2.1.gif](http://archive.stsci.edu/iue/instrument/obs_guide/fig2.1.gif))

The IUE scientific instrument consists of a telescope, acquisition camera, two ultraviolet spectrographs, and four cameras. (See FIG. 3.1.2 and TABLE 3.1.1.) The telescope is a 45-cm aperture, f/15 telescope of Ritchey-Chretien design. The Fine Error Sensor (FES), is used in camera mode to obtain a visual star field image for target identification and acquisition. It is then used in tracking mode for guiding, providing a pointing stability of about 1/2 arcsec.

TABLE 3.1.1  
SCIENCE PAYLOAD AND CAMERAS

Science Payload	Description <sup>m,n,o</sup>
Telescope	45 cm, f/15 Ritchey-Chretien Cassegrain
Spectrographs	Echelle (1150 - 1980 Å and 1800 - 3200 Å)
Apertures	SMALL (3 arcsec diameter) circle LARGE (10 x 20 arcsec) slot
Resolution	HIGH 0.08 Å @ 1400 Å (17 km/s) HIGH 0.17 Å @ 2600 Å (20 km/s) LOW 2.7 Å @ 1500 Å (600 km/s) LOW 14.0 Å @ 2700 Å (1500 km/s)
Cameras	Description <sup>m,n,o</sup>
SWP (1097-2097 Å)	Short Wavelength Prime (sensitivity: $2 \times 10^{-15}$ ergs/s/cm <sup>2</sup> /Å)
LWP (1808-3359 Å)	Long Wavelength Prime (sensitivity: $1 \times 10^{-15}$ ergs/s/cm <sup>2</sup> /Å)
LWR (1810-3456 Å)	Long Wavelength Redundant (sensitivity: $2 \times 10^{-15}$ ergs/s/cm <sup>2</sup> /Å)
SWR	Short Wavelength Redundant (Never operational)
FES #1	Fine Error Sensor #1 (Has not been used in operations.)
FES #2	Fine Error Sensor #2 (16 arcmin field of view and effective image resolution of about 8 arcsec)

Each spectrograph may be used with either of two apertures. The large aperture is a slot (approximately 10 by 20 arcsec) and the small aperture is a circle about 3 arcsec in diameter. The image quality of the IUE telescope's optics yields a roughly 3 arcsec image, so observations using the small aperture result in some light loss (IUE, h). The large aperture is used most frequently since it gives photometric reliability with little or no loss of resolution (IUE, d). Approximately 27% of the IUE exposures of Algol are taken in the small aperture mode.

The spectrograph design permits operation of each spectrograph in either of two modes: high dispersion/high resolution and low dispersion /low resolution (IUE, d). These produce an approximate velocity resolution between 10 and 25 km/sec for high resolution and between 600 and 1500 km/sec for low resolution (IUE, d). The long-wavelength spectrograph (LWP/LWR) operates in a wavelength range of 1850 to 3300 Å. The short-wavelength spectrograph (SWP) operates in a wavelength range of 1150 to 2000 Å (IUE, d). See TABLE 3.1.2 for the IUE spectrograph parameters. The high dispersion mode was used for all IUE exposures of Algol.

There are four cameras, two for each spectrograph. One is designated prime and the other backup (or redundant). Both the prime (LWP) and redundant

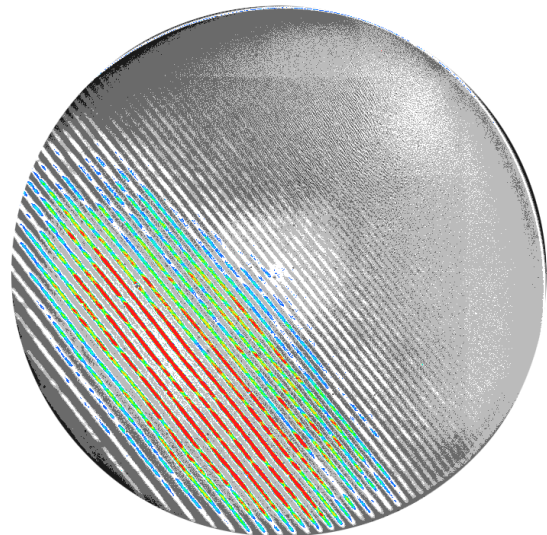


FIG. 3.1.3—*The First IUE Image*. High dispersion LWP image of Capella taken on February 9, 1978. (Source: <http://www.vilspa.esa.es/iue/last/first.html>)

(LWR) cameras were used during the mission. In the short wavelength range, only the prime camera (SWP) was fully functional. Each camera consists of an SEC Vidicon with an ultraviolet converter. The signal is digitized and transmitted to the ground via the spacecraft telemetry stream. FIG. 3.1.3 is a sample raw image. (Notice the parallel lines which are the echelle orders that have been spacially separated via the cross disperser).

TABLE 3.1.2

IUE SPECTROGRAPH PARAMETERS

Parameter	LWP	LWR	SWP
Wavelength Range (Å)	1808-3359	1810-3456	1097-2097
Order Range	69-127	67-127	66-125
Abs. Calib. Wavelength Range (Å)	1850-3350	1850-3350	1150-1980
Abs. Calib. Order Range	69-125	69-125	70-120
Coll. Focal Length (mm)	950	950	950
Cam. Focal Length (mm)	684	684	684
Coll.-to-Cam. Angle (deg.)	20.42	20.42	20.37
Image Scale ( $\mu\text{m pix}^{-1}$ )	36.4	36.4	35.7
X-Disp. Ruling Freq. ( $\text{gr mm}^{-1}$ )	241.50	241.50	369.233
X-Disp. Order	1	1	1
Ech. Ruling Freq. ( $\text{gr mm}^{-1}$ )	63.207	63.207	101.947
Ech. Blaze Wavel. ( $\mu\text{m}$ )	23.19	23.19	13.76
Ech. Blaze Angle (deg.)	48.126	48.126	45.449
Ech. Grating Angle (deg.)	0	0	0

*(Source of Table 3.1.2: cited 4/22/06  
<http://archive.stsci.edu/iue/manual/newsips/node94.html>)*

The main data product that now resides in the final archive has been processed with the New Spectral Image Processing System (NEWSIPS). The resulting downloadable files have the extension MXHI (for high dispersion spectra) or MXLO (for low

dispersion spectra). Since all IUE spectra of Algol were taken in the high dispersion mode the archived spectra of Algol are in the MXHI format only.

In order to extract the wavelength and flux vectors from these files we processed the MXHI files with an IDL (Interactive Data Language) subroutine written by Jess Johnson (February 2004). This custom program exports each MXHI file as a text file that is easily imported into commonly used software packages and manipulated.

### 3.2 *IUE Observations of Algol*

We present here the complete list of Algol IUE observations from the online MAST\* IUE archive, 103 in all, 59 SWP images in the far-ultraviolet (1150-1900 Å) and 44 LWP/LWR images in the mid-ultraviolet (1900-3200 Å). Algol IUE observations were made during intermittent observing runs, the first starting on September 13, 1978, and the last ending on September 4, 1989 (or HJD<sup>†</sup> 2,443,765.24896 – 2,447,783.64315). The 1989 September data are especially useful in this work since the density of orbital coverage is the highest. TABLE 3.2.1 is a summary of the observing runs of Algol with their corresponding densities of orbital coverage.

---

\* Multimission Archive at Space Telescope (MAST), <http://archive.stsci.edu/>

<sup>†</sup> Julian date, or JD is the number of days since 12:00 on 1 January, 4713 BC; the basis of time for astrodynamics. HJD, or the heliocentric Julian date, is the JD at the Sun. In this work JD is assumed to be heliocentric and is used interchangeably with HJD.

TABLE 3.2.1  
IUE OBSERVING RUNS OF ALGOL

Year 1900+	# of LWP spectra per observing run	Approx. span of days	# of SWP spectra per observing run	Approx. span of days	Approx. density of data points
78 Sept.	1	-	1	-	1/(orbit)
78 Nov.	3	3	6	3	4.3/orbit
78 Dec-79 Jan	6	7	5	7	2.3/orbit
79 Nov.	3	< 1 (~2 hr)	3	< 1 (~2 hr)	3/(<1/3 orbit)
83 Nov.	6	< 1 (~6 hr)	7	< 1 (~6 hr)	6.5/(<1/3 orbit)
84 Mar.	1	-	4	2	5/(2/3 orbit)
85 Jul.	7	< 1 (~6.5 hr)	7	< 1 (~6.5 hr)	7/(<1/3 orbit)
86 Feb.-Mar.	2	6	9	7	4.5/orbit
89 Sept.	15	3.3	17	3.3	13.9/orbit

The orbital phase,  $\phi$ , of each image was calculated using the equation

$$\phi = NP - \text{INT}(NP) \quad (3.2.1)$$

where NP is the number of orbital periods since the time of primary minimum,

$$NP = \frac{\text{HJD}_{\text{MIDEXP}} - t_{\text{Pr.Min A-B}}}{P_{\text{A-B}}}, \quad (3.2.2)$$

and INT (NP) is the integer part of NP.  $\text{HJD}_{\text{MIDEXP}}$  is the heliocentric Julian date of mid exposure,  $t_{\text{Pr.Min A-B}} = 2,445,641.5135$  days (Al-Naimiy et al. 1984) is the time of a reference primary minimum of the eclipsing pair, and  $P_{\text{A-B}} = 2^{\text{d}}.86731077$  is the orbital period (Gillet et al. 1989).

The entire set of Algol IUE exposures were taken in the high-resolution mode ( $\lambda/\Delta\lambda \approx 10^4$ ). Of the 59 SWP images and 44 LWP/LWR images, 15 and 13 were taken in the small aperture modes, respectively. Tables 3.2.2 and 3.2.3 list the pertinent information for each SWP and LWP/LWR exposure in order of increasing phase.

TABLE 3.2.2

## IUE SWP Observations of Algol

SWP ID	Data ID	Aper	Month	Day	Year	Hour	min	JD at mid exposure	Phase
1	SWP03772	SMALL	1	1	1979	18	5	2,443,875.2543	0.0015
2	SWP03262	SMALL	11	8	1978	6	42	2,443,820.7800	0.0031
3	SWP36983	LARGE	9	11	1989	1	0	2,447,780.5423	0.0052
4	SWP07111	SMALL	11	7	1979	10	23	2,444,184.9348	0.0053
5	SWP37019	LARGE	9	13	1989	22	26	2,447,783.4350	0.0141
6	SWP07112	SMALL	11	7	1979	11	17	2,444,184.9720	0.0183
7	SWP36984	LARGE	9	11	1989	2	3	2,447,780.5858	0.0204
8	SWP36985	LARGE	9	11	1989	3	15	2,447,780.6356	0.0378
9	SWP03303	SMALL	11	11	1978	8	56	2,443,823.8726	0.0816
10	SWP37021	LARGE	9	14	1989	3	21	2,447,783.6397	0.0855
11	SWP36989	LARGE	9	11	1989	9	43	2,447,780.9050	0.1317
12	SWP22417	LARGE	3	5	1984	17	58	2,445,765.2489	0.1538
13	SWP22418	LARGE	3	5	1984	18	34	2,445,765.2739	0.1625
14	SWP36992	LARGE	9	11	1989	13	39	2,447,781.0689	0.1889
15	SWP36996	LARGE	9	11	1989	22	44	2,447,781.4474	0.3209
16	SWP03752	SMALL	12	30	1978	19	52	2,443,873.3282	0.3297
17	SWP37001	LARGE	9	12	1989	9	37	2,447,781.9008	0.4790
18	SWP03818	SMALL	1	6	1979	0	43	2,443,879.5302	0.4927
19	SWP37003	LARGE	9	12	1989	14	11	2,447,782.0911	0.5454
20	SWP27781	LARGE	2	24	1986	19	36	2,446,486.3168	0.6326
21	SWP02643	SMALL	9	13	1978	17	58	2,443,765.2490	0.6361
22	SWP27782	LARGE	2	24	1986	20	28	2,446,486.3529	0.6452
23	SWP27783	LARGE	2	24	1986	20	57	2,446,486.3731	0.6522
24	SWP27784	LARGE	2	24	1986	21	27	2,446,486.3939	0.6595
25	SWP27785	LARGE	2	24	1986	22	12	2,446,486.4251	0.6704
26	SWP27786	LARGE	2	24	1986	22	40	2,446,486.4446	0.6772
27	SWP03794	SMALL	1	3	1979	22	48	2,443,877.4504	0.7674
28	SWP37011	LARGE	9	13	1989	6	13	2,447,782.7592	0.7784
29	SWP27830	LARGE	3	2	1986	23	51	2,446,492.4939	0.7869
30	SWP27831	LARGE	3	3	1986	0	47	2,446,492.5328	0.8005
31	SWP27832	LARGE	3	3	1986	1	16	2,446,492.5529	0.8075
32	SWP37014	LARGE	9	13	1989	13	18	2,447,783.0543	0.8813
33	SWP26472	LARGE	7	25	1985	11	55	2,446,271.9967	0.8866
34	SWP21452	LARGE	11	5	1983	13	35	2,445,644.0665	0.8904
35	SWP26473	LARGE	7	25	1985	12	54	2,446,272.0376	0.9009
36	SWP21453	LARGE	11	5	1983	14	44	2,445,644.1142	0.9070
37	SWP26474	LARGE	7	25	1985	13	52	2,446,272.0779	0.9149
38	SWP22411	LARGE	3	5	1984	2	0	2,445,764.5835	0.9217
39	SWP21454	LARGE	11	5	1983	15	45	2,445,644.1565	0.9218
40	SWP37016	LARGE	9	13	1989	16	17	2,447,783.1786	0.9247
41	SWP26475	LARGE	7	25	1985	14	54	2,446,272.1210	0.9299
42	SWP21455	LARGE	11	5	1983	16	43	2,445,644.1968	0.9358
43	SWP22439	LARGE	3	7	1984	23	59	2,445,767.4996	0.9388
44	SWP36979	LARGE	9	10	1989	20	30	2,447,780.3543	0.9397
45	SWP26476	LARGE	7	25	1985	16	5	2,446,272.1703	0.9471
46	SWP21456	LARGE	11	5	1983	18	11	2,445,644.2578	0.9571
47	SWP36980	LARGE	9	10	1989	21	43	2,447,780.4050	0.9573
48	SWP26477	LARGE	7	25	1985	17	13	2,446,272.2175	0.9636

TABLE 3.2.2 – *continued*

SWP ID	Data ID	Aper	Month	Day	Year	Hour	min	JD at mid exposure	Phase
49	SWP03298	SMALL	11	11	1978	1	2	2,443,823.5436	0.9669
50	SWP21457	LARGE	11	5	1983	19	9	2,445,644.2983	0.9712
51	SWP36981	LARGE	9	10	1989	23	7	2,447,780.4634	0.9777
52	SWP03259	SMALL	11	8	1978	5	3	2,443,820.7111	0.9791
53	SWP26478	LARGE	7	25	1985	18	17	2,446,272.2621	0.9791
54	SWP21458	LARGE	11	5	1983	19	44	2,445,644.3226	0.9797
55	SWP03260	SMALL	11	8	1978	5	37	2,443,820.7349	0.9874
56	SWP03771	SMALL	1	1	1979	17	9	2,443,875.2158	0.9880
57	SWP07110	SMALL	11	7	1979	9	28	2,444,184.8953	0.9915
58	SWP36982	LARGE	9	11	1989	0	17	2,447,780.5122	0.9947
59	SWP03261	SMALL	11	8	1978	6	9	2,443,820.7572	0.9951

In each of these tables, the first column identifies for use in this work an abbreviated designation used for cross-referencing and indexing. The second column is the unique identifying label assigned by the IUE mission. The third column indicates the aperture (large or small). Columns 4-8 are the month, day, year, hour, and minute of the exposure. Column 9 is the heliocentric JD at mid exposure, which is a simple average of the JD's representing the start and end times of each exposure. The last column is the phase, calculated using equations (3.2.1) and (3.2.2) above.

TABLE 3.2.4 is a comparison of our calculated phases with those calculated in other work. The differences in phases stem from the use of different ephemerides; i.e., slightly different values of orbital parameters, such as time of primary minimum and period.



TABLE 3.2.3  
IUE LWP/LWR Observations of Algol

LWP/LWR ID	Data ID	Aper	Month	Day	Year	Hour	min	JD at mid exposure	Phase
1	LWR03350	SMALL	1	1	1979	18	12	2,443,875.2588	0.0030
2	LWP16323	LARGE	9	11	1989	0	53	2,447,780.5371	0.0034
3	LWR06047	SMALL	11	7	1979	10	17	2,444,184.9295	0.0034
4	LWR02856	SMALL	11	8	1978	6	50	2,443,820.7851	0.0049
5	LWR06048	SMALL	11	7	1979	11	11	2,444,184.9668	0.0165
6	LWP16324	LARGE	9	11	1989	2	10	2,447,780.5905	0.0220
7	LWP16325	LARGE	9	11	1989	3	20	2,447,780.6390	0.0390
8	LWR02911	SMALL	11	11	1978	8	50	2,443,823.8683	0.0801
9	LWP16356	LARGE	9	14	1989	3	26	2,447,783.6432	0.0867
10	LWP16327	LARGE	9	11	1989	9	37	2,447,780.9008	0.1303
11	LWP02895	LARGE	3	5	1984	18	2	2,445,765.2514	0.1547
12	LWP16329	LARGE	9	11	1989	13	45	2,447,781.0730	0.1903
13	LWP16333	LARGE	9	11	1989	22	39	2,447,781.4438	0.3196
14	LWR03328	SMALL	12	30	1978	19	12	2,443,873.3003	0.3200
15	LWR03329	SMALL	12	30	1978	19	45	2,443,873.3231	0.3280
16	LWP16338	LARGE	9	12	1989	9	32	2,447,781.8973	0.4778
17	LWR03398	SMALL	1	6	1979	0	48	2,443,879.5335	0.4939
18	LWP16340	LARGE	9	12	1989	14	15	2,447,782.0939	0.5463
19	LWP07717	LARGE	2	24	1986	19	43	2,446,486.3216	0.6343
20	LWR02345	SMALL	9	13	1978	19	4	2,443,765.2946	0.6520
21	LWR03374	SMALL	1	3	1979	22	53	2,443,877.4536	0.7685
22	LWP16347	LARGE	9	13	1989	6	19	2,447,782.7633	0.7798
23	LWP07738	LARGE	3	2	1986	23	57	2,446,492.4980	0.7884
24	LWP16350	LARGE	9	13	1989	13	23	2,447,783.0577	0.8825
25	LWP06484	LARGE	7	25	1985	12	0	2,446,272.0001	0.8878
26	LWP02226	LARGE	11	5	1983	13	40	2,445,644.0698	0.8915
27	LWP06485	LARGE	7	25	1985	12	58	2,446,272.0404	0.9018
28	LWP02227	LARGE	11	5	1983	14	49	2,445,644.1176	0.9082
29	LWP06486	LARGE	7	25	1985	13	59	2,446,272.0827	0.9166
30	LWP02228	LARGE	11	5	1983	15	49	2,445,644.1591	0.9227
31	LWP16352	LARGE	9	13	1989	16	22	2,447,783.1820	0.9259
32	LWP06487	LARGE	7	25	1985	15	4	2,446,272.1279	0.9323
33	LWP02229	LARGE	11	5	1983	16	47	2,445,644.1994	0.9367
34	LWP16320	LARGE	9	10	1989	20	35	2,447,780.3577	0.9409
35	LWP06488	LARGE	7	25	1985	16	12	2,446,272.1751	0.9488
36	LWP02230	LARGE	11	5	1983	18	15	2,445,644.2605	0.9581
37	LWP16321	LARGE	9	10	1989	21	50	2,447,780.4098	0.9590
38	LWP06489	LARGE	7	25	1985	17	19	2,446,272.2216	0.9650
39	LWR02906	SMALL	11	11	1978	1	8	2,443,823.5476	0.9683
40	LWP02231	LARGE	11	5	1983	19	13	2,445,644.3009	0.9721
41	LWP16322	LARGE	9	10	1989	23	14	2,447,780.4682	0.9794
42	LWP06490	LARGE	7	25	1985	18	21	2,446,272.2647	0.9801
43	LWR03349	SMALL	1	1	1979	17	16	2,443,875.2199	0.9895
44	LWR06046	SMALL	11	7	1979	9	23	2,444,184.8913	0.9901

TABLE 3.2.4  
Comparison of IUE Phases to Other Work

SWP Exposure Information					SWP Phase			
SWP ID	Data ID	Aper	Month	Year	Cugier & Molaro (1984)	Sahade & Hernandez (1985)	Brandi et al. (1989)	This work (2006)
1	SWP03772	SMALL	1	1979	0.00216	0.018	...	0.0015
2	SWP03262	SMALL	11	1978	0.00424	...	...	0.0031
4	SWP07111	SMALL	11	1979	0.00636	...	...	0.0053
6	SWP07112	SMALL	11	1979	0.01920	...	...	0.0183
9	SWP03303	SMALL	11	1978	0.08298	...	...	0.0816
16	SWP03752	SMALL	12	1978	0.33060	0.346	...	0.3297
18	SWP03818	SMALL	1	1979	0.49347	0.509	...	0.4927
20	SWP27781	LARGE	2	1986	...	...	0.63	0.6326
21	SWP02643	SMALL	9	1978	0.63637	...	...	0.6361
22	SWP27782	LARGE	2	1986	...	...	0.64	0.6452
23	SWP27783	LARGE	2	1986	...	...	0.65	0.6522
24	SWP27784	LARGE	2	1986	...	...	0.65	0.6595
25	SWP27785	LARGE	2	1986	...	...	0.66	0.6704
26	SWP27786	LARGE	2	1986	...	...	0.67	0.6772
27	SWP03794	SMALL	1	1979	0.76818	0.784	...	0.7674
29	SWP27830	LARGE	3	1986	...	...	0.78	0.7869
30	SWP27831	LARGE	3	1986	...	...	0.79	0.8005
31	SWP27832	LARGE	3	1986	...	...	0.80	0.8075
49	SWP03298	SMALL	11	1978	0.96818	...	...	0.9669
52	SWP03259	SMALL	11	1978	0.98026	...	...	0.9791
55	SWP03260	SMALL	11	1978	0.98849	...	...	0.9874
56	SWP03771	SMALL	1	1979	0.98860	0.004	...	0.9880
57	SWP07110	SMALL	11	1979	0.99280	...	...	0.9915
59	SWP03261	SMALL	11	1978	0.99624	...	...	0.9951

LWP/LWR Exposure Information					LWP/LWR Phase			
LWP/LWR ID	Data ID	Aper	Month	Year	Cugier & Molaro (1984)	Sahade & Hernandez (1985)	Brandi et al. (1989)	This work (2006)
1	LWR03350	SMALL	1	1979	0.00386	0.019	...	0.0030
3	LWR06047	SMALL	11	1979	0.99280	...	...	0.0034
4	LWR02856	SMALL	11	1978	0.00617	...	...	0.0049
5	LWR06048	SMALL	11	1979	0.01775	...	...	0.0165
8	LWR02911	SMALL	11	1978	0.08153	...	...	0.0801
14	LWR03328	SMALL	12	1978	0.32092	0.336	...	0.3200
15	LWR03329	SMALL	12	1978	0.32891	0.344	...	0.3280
17	LWR03398	SMALL	1	1979	0.49463	0.510	...	0.4939
20	LWR02345	SMALL	9	1978	0.65235	...	...	0.6520
21	LWR03374	SMALL	1	1979	0.76939	0.785	...	0.7685
39	LWR02906	SMALL	11	1978	0.96964	...	...	0.9683
43	LWR03349	SMALL	1	1979	0.99030	0.006	...	0.9895
44	LWR06046	SMALL	11	1979	0.99159	...	...	0.9901

### 3.3 *Line-of-sight Geometry for Each Algol IUE Observation*

The IUE spectra contain two types of changing features: those associated with periodic changes in our line of sight and identified by phase, and others related to actual changes in binary system activity, identified by time period, or “epoch.” Each IUE observation of Algol is correlated with a specific date and time which is in turn related to a specific orbital phase (see Section 3.2). It is therefore important to visualize the line-of-sight geometry of each phase as well as the phases observed during each epoch.

FIGs. (3.3.1a-h) and FIGs. (3.3.2a-h) illustrate the line-of-sight geometry for each Algol IUE SWP and LWP/LWR observation, respectively, grouped by epoch. The epochs are grouped as follows: 1978 Sept. - 1978 Nov., 1978 Dec. -1979 Jan., 1979 Nov., 1983 Nov., 1984 March, 1985 July, 1986 Feb. - March, and 1989 Sept. where we have combined the lone 1978 September observation (in each of the wavelength ranges) with the 1978 November observations, keeping in mind that marked changes can (and did) occur in the system across that time span.

The vertical dashed line in each figure is the axis of rotation, the sense of which is up, and passes through the center of mass of the system. The large dark spot on Algol A marks the impact region of the stream of gas according to the model of Harnden et al. 1977 (See FIG. 2.5.4). It is located at an angle of  $43^\circ$  from a line connecting the centers of the two components, originating from Algol A. The four smaller spots on Algol A are simply markers to help the eye keep track of which parts of the hemispheres are visible at each phase. These four markers are located on the equator at  $0^\circ$ ,  $90^\circ$ ,  $180^\circ$ , and  $270^\circ$  with respect to a line connecting the center of Algol A to the center of Algol B. The + marks indicate the positions of the center of mass of Algol A, Algol B, and Algol A-B.

**SWP**

**1978 Sep - Nov**

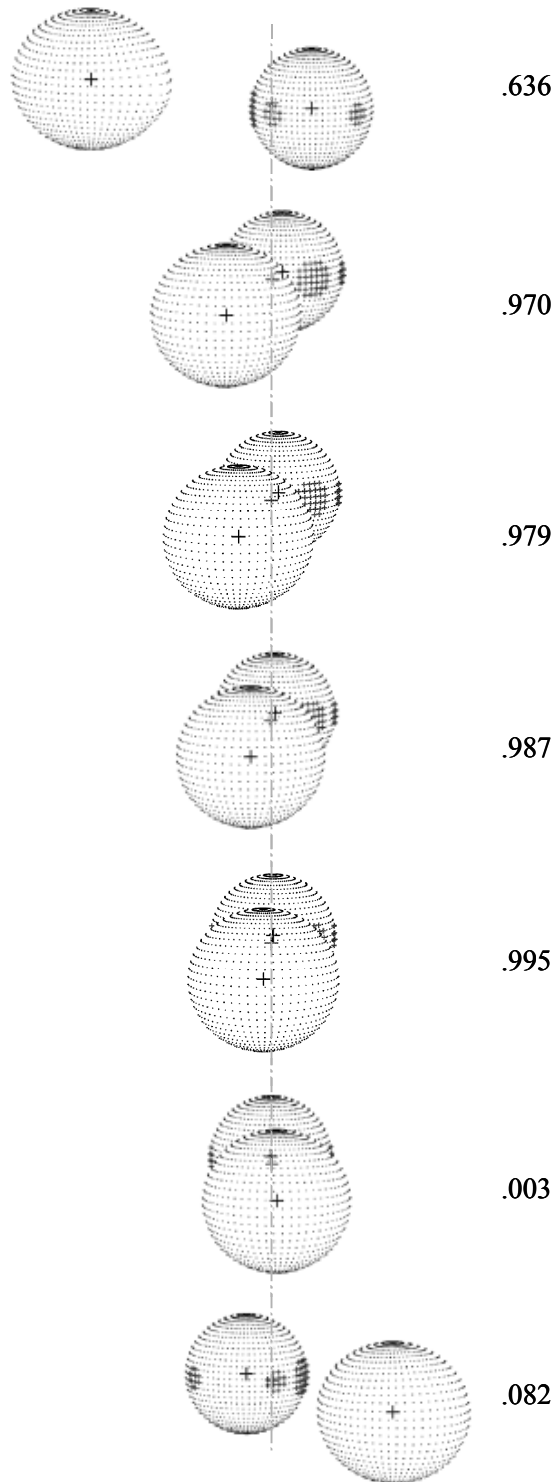


FIG. 3.3.1a—Line-of-sight Geometry for Epoch 1978 Sept. – Nov. SWP phases

**SWP**

**1978 Dec - 1979 Jan**

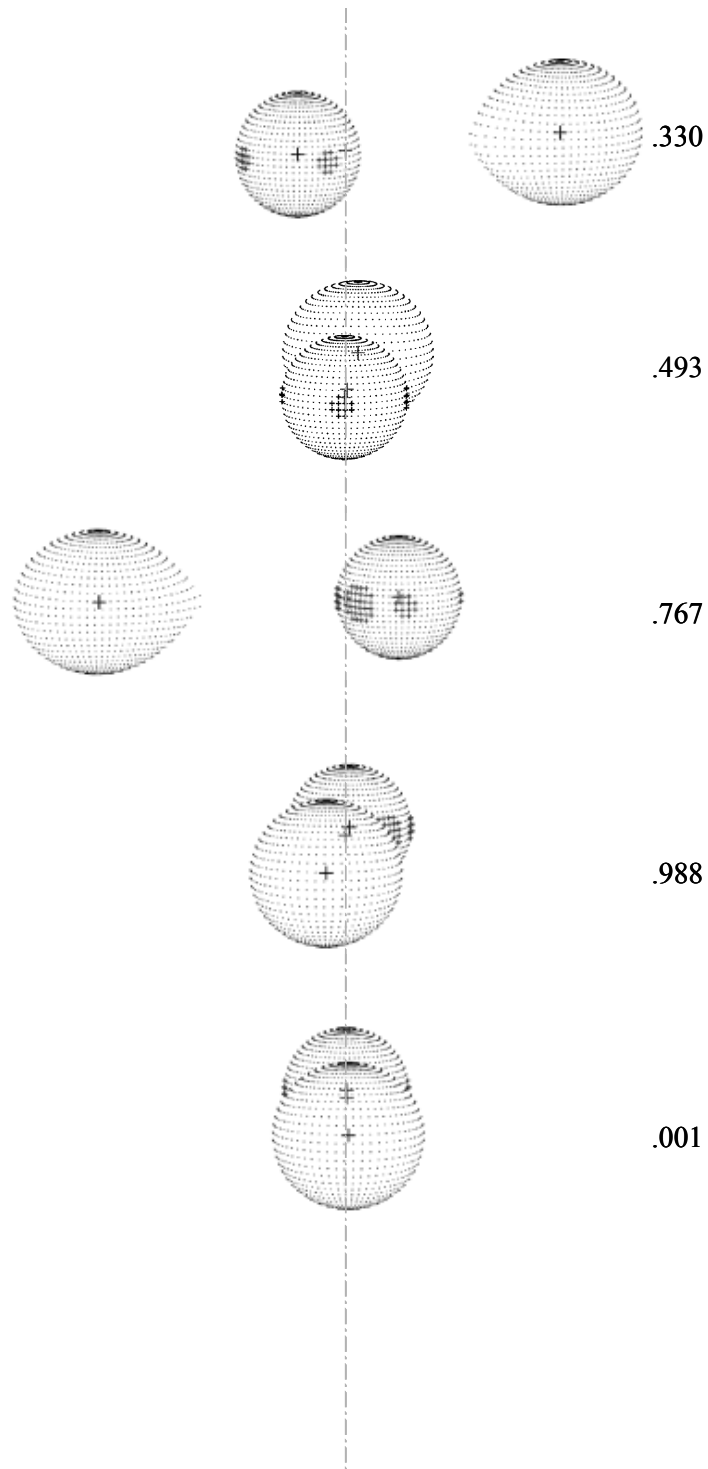


FIG. 3.3.1b—Line-of-sight Geometry for Epoch 1978 Dec. – 1979 Jan. SWP phases

**SWP**

**1979 Nov**

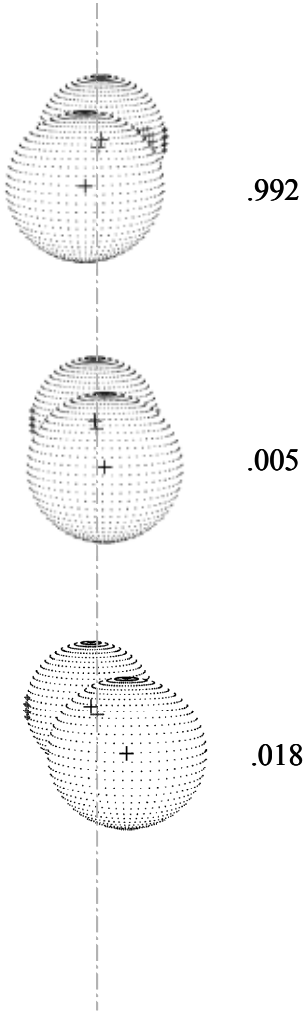


FIG. 3.3.1c—Line-of-sight Geometry for Epoch 1979 November SWP phases

**SWP**

**1983 Nov**

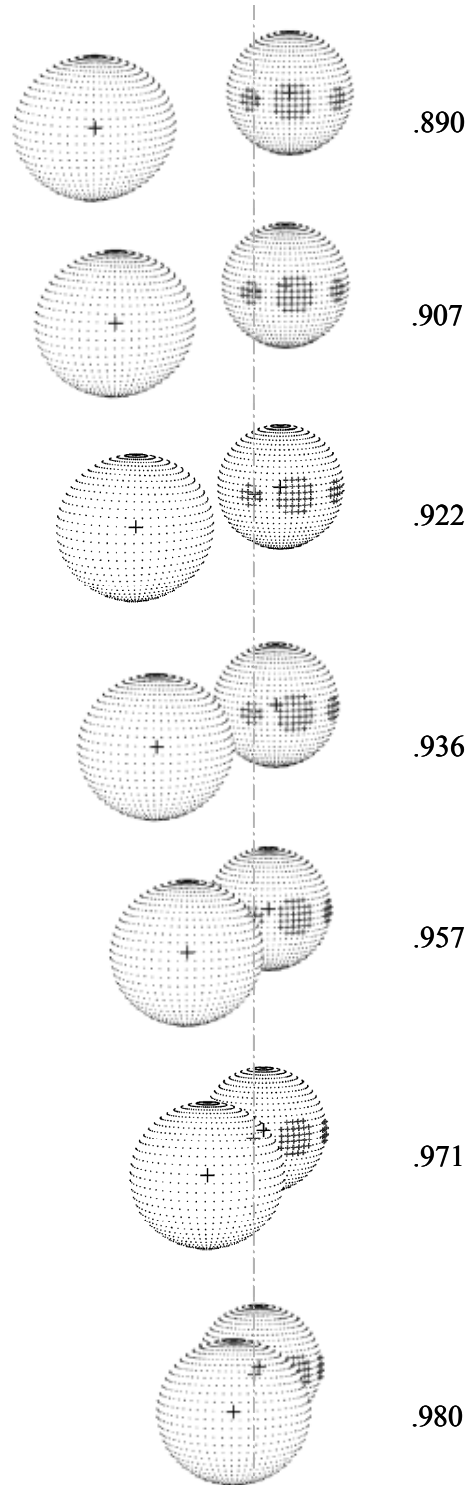


FIG. 3.3.1d—Line-of-sight Geometry for Epoch 1983 November SWP phases

**SWP**

**1984 Mar**

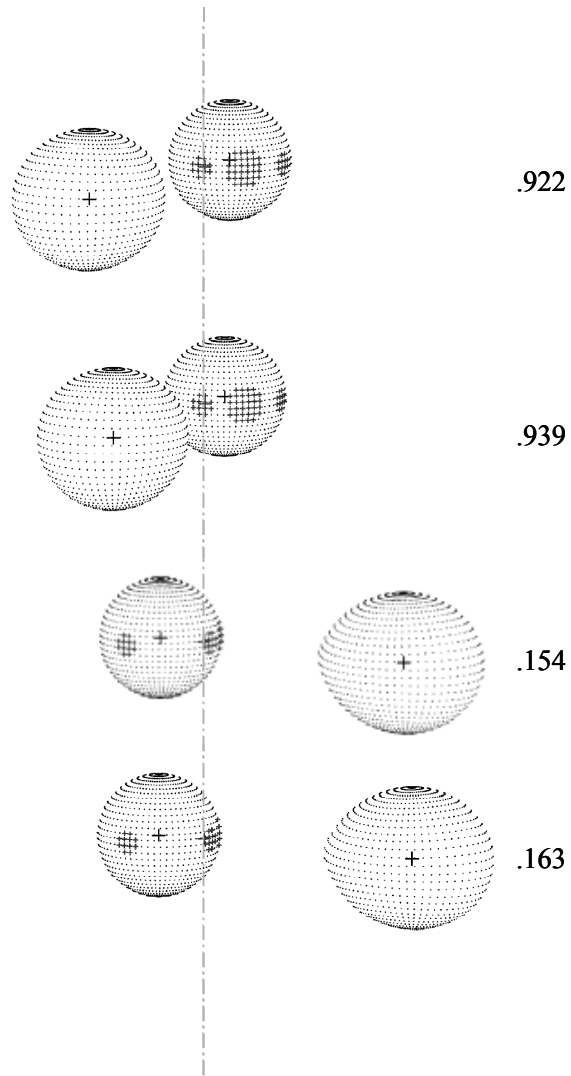


FIG. 3.3.1e—Line-of-sight Geometry for Epoch 1984 March SWP phases



**SWP**

**1985 Jul**

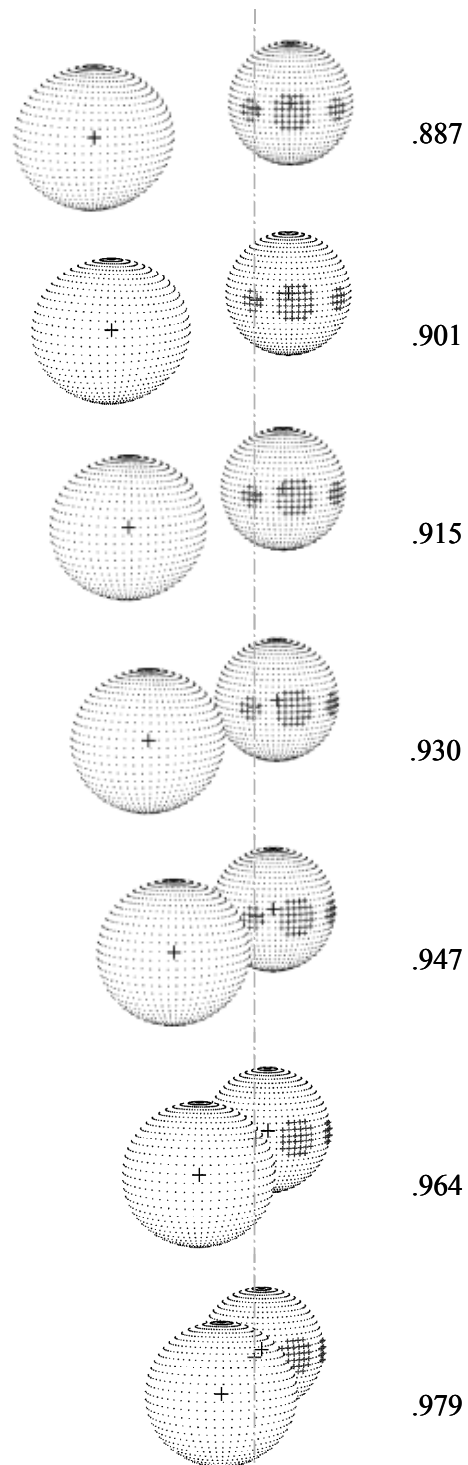
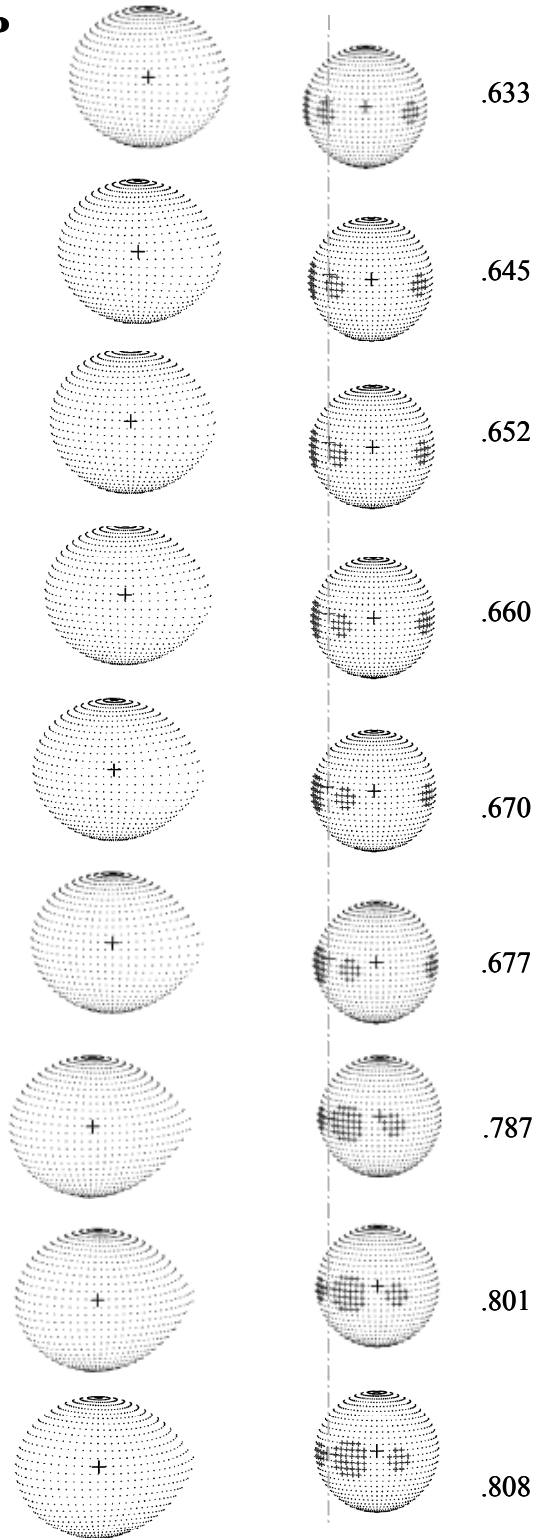


FIG. 3.3.1f—Line-of-sight Geometry for Epoch 1985 July SWP phases

**SWP**



**1986 Feb-Mar**

.633

.645

.652

.660

.670

.677

.787

.801

.808

FIG. 3.3.1g—Line-of-sight Geometry for Epoch 1986 Feb. - March SWP phases

**SWP**

**1989 Sep**

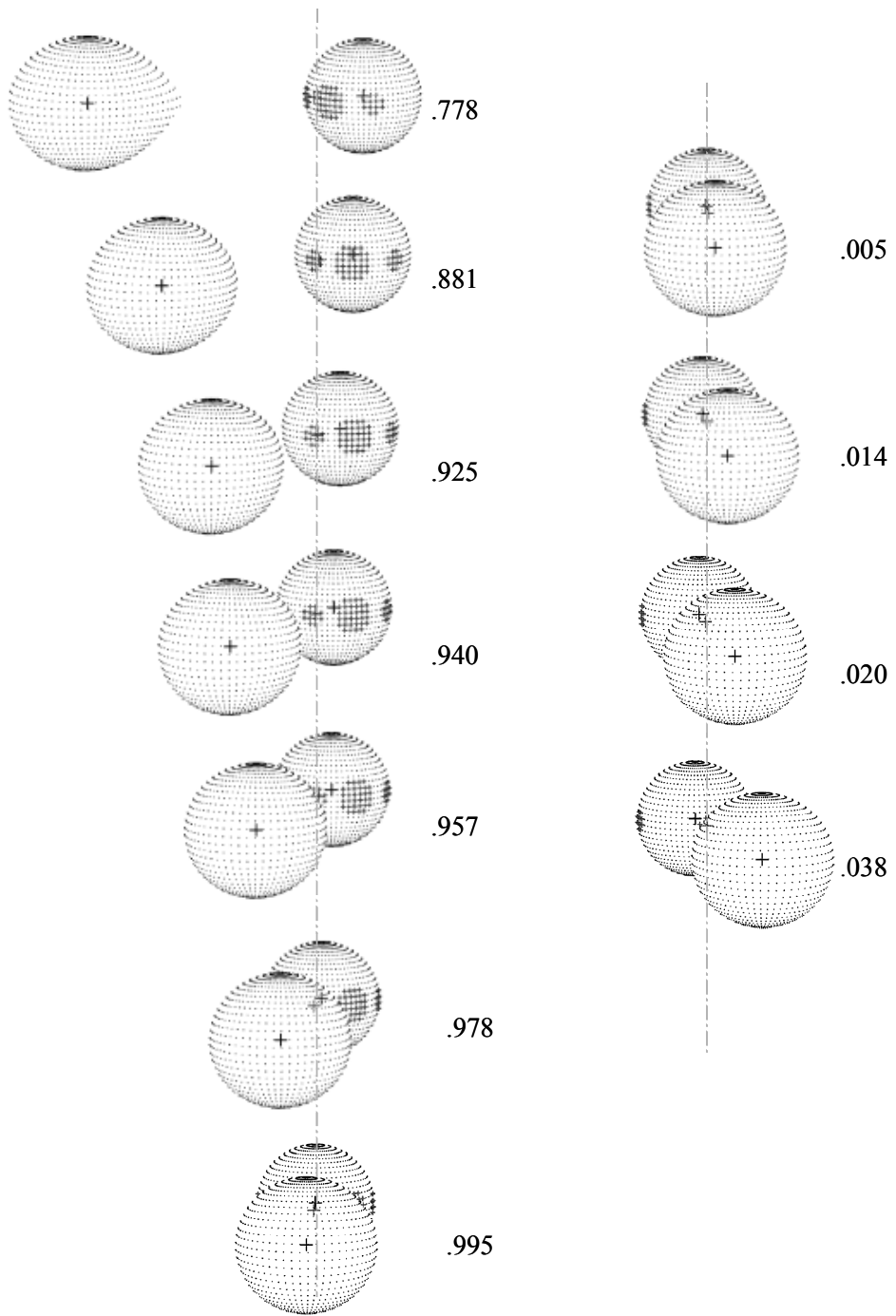


FIG. 3.3.1h—Line-of-sight Geometry for Epoch 1989 September SWP phases

**SWP**

**1989 Sep**

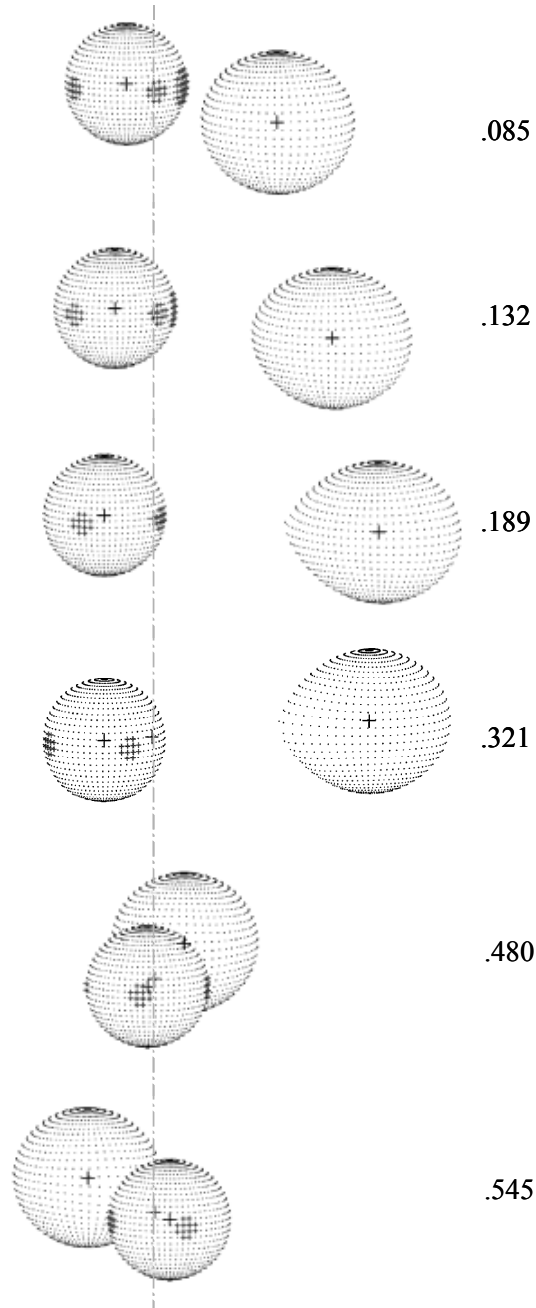


FIG 3.3.1h—*continued*

**LWP/LWR**

**1978 Sep - Nov**

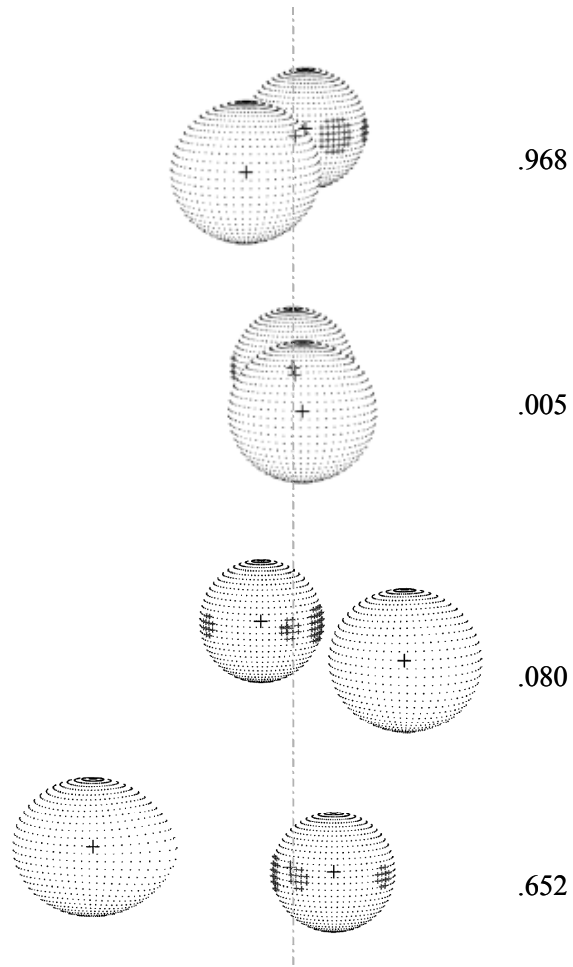


FIG. 3.3.2a—Line-of-sight Geometry for Epoch 1978 Sept. – Nov. LWP/LWR phases

**LWP/LWR**

**1978 Dec - 1979 Jan**

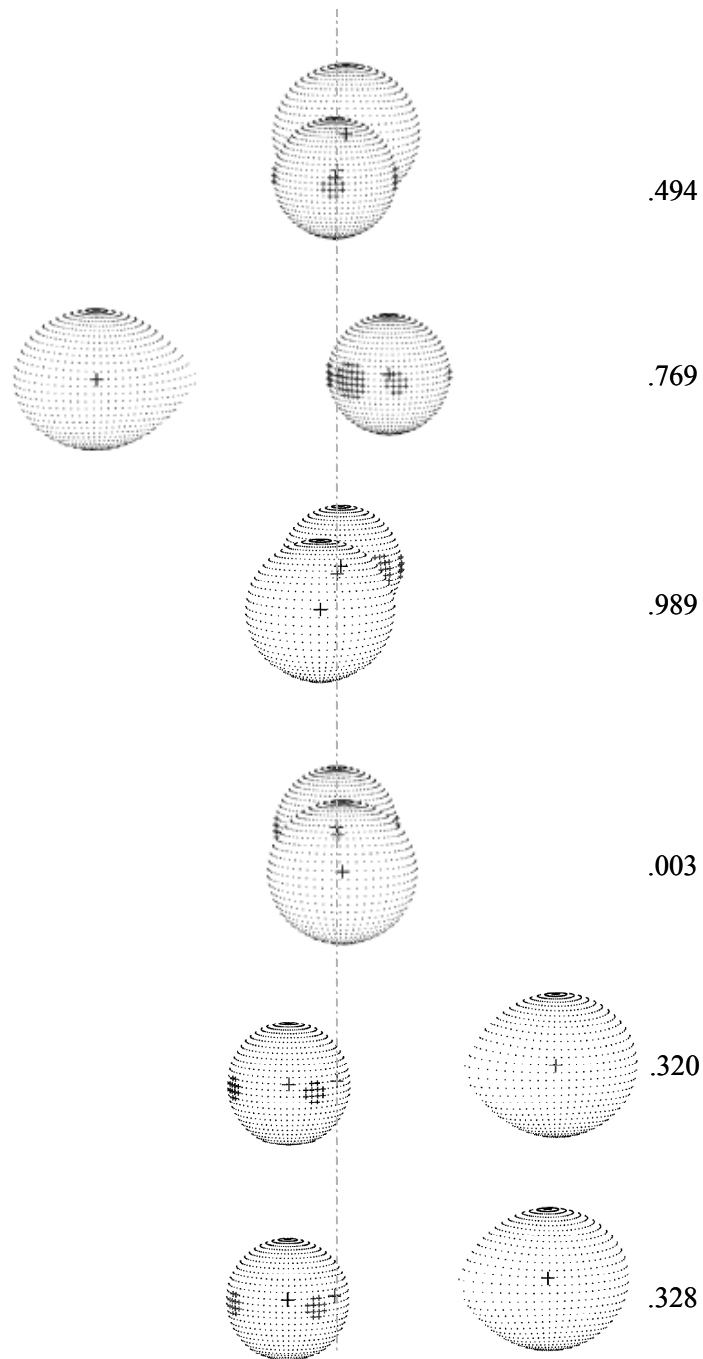


FIG. 3.3.2b—Line-of-sight Geometry for Epoch 1978 Dec. – 1979 LWP/LWR phases

LWP/LWR

1979 Nov

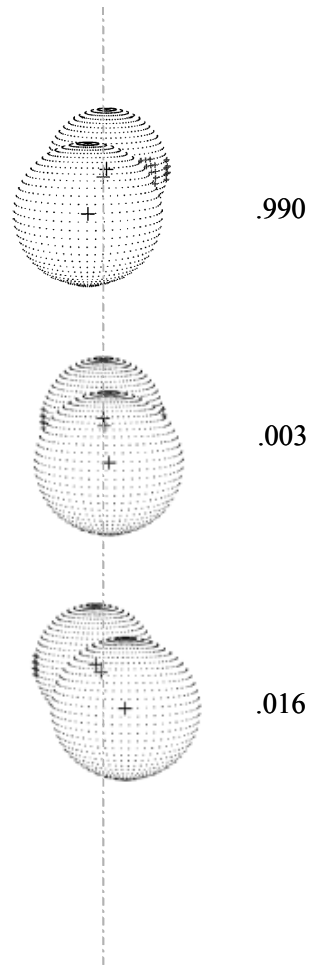


FIG. 3.3.2c—Line-of-sight Geometry for Epoch 1979 November LWP/LWR phases

LWP/LWR

1983 Nov

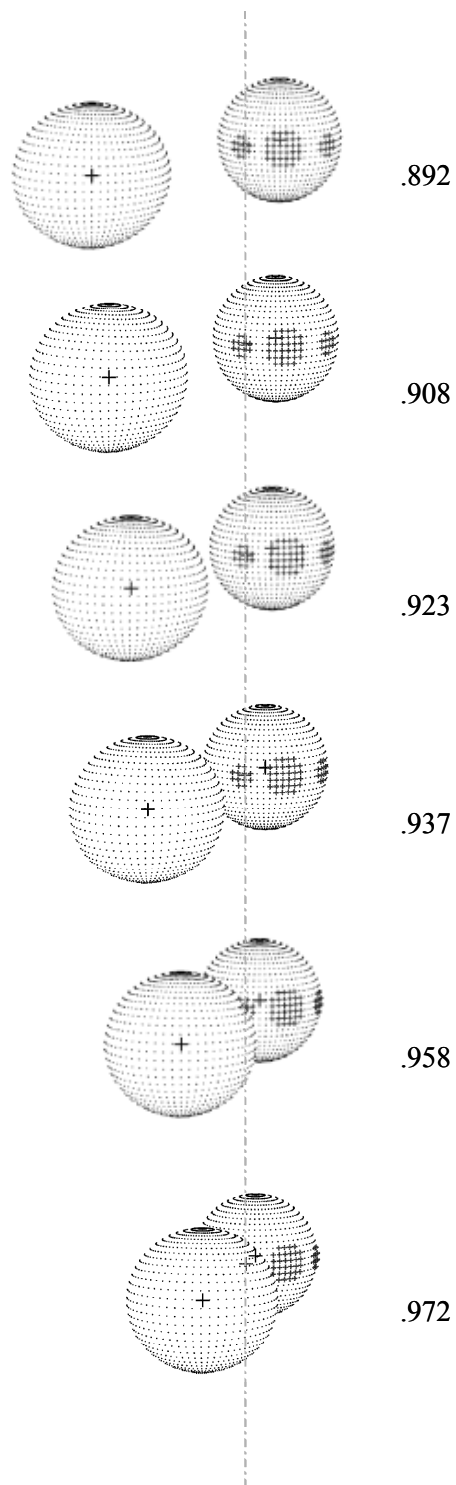


FIG. 3.3.2d—Line-of-sight Geometry for Epoch 1983 November LWP/LWR phases



**LWP/LWR**

**1984 Mar**

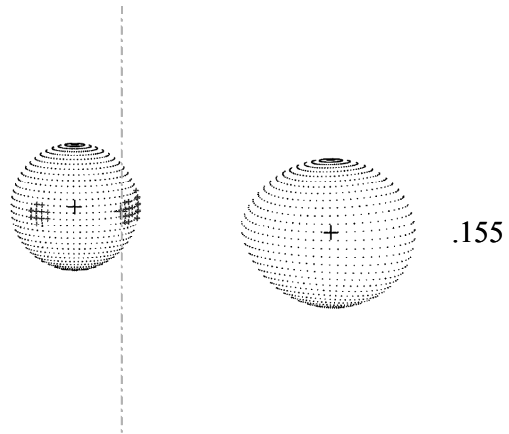


FIG. 3.3.2e—*Line-of-sight Geometry for Epoch 1984 March LWP/LWR phases*

LWP/LWR

1985 Jul

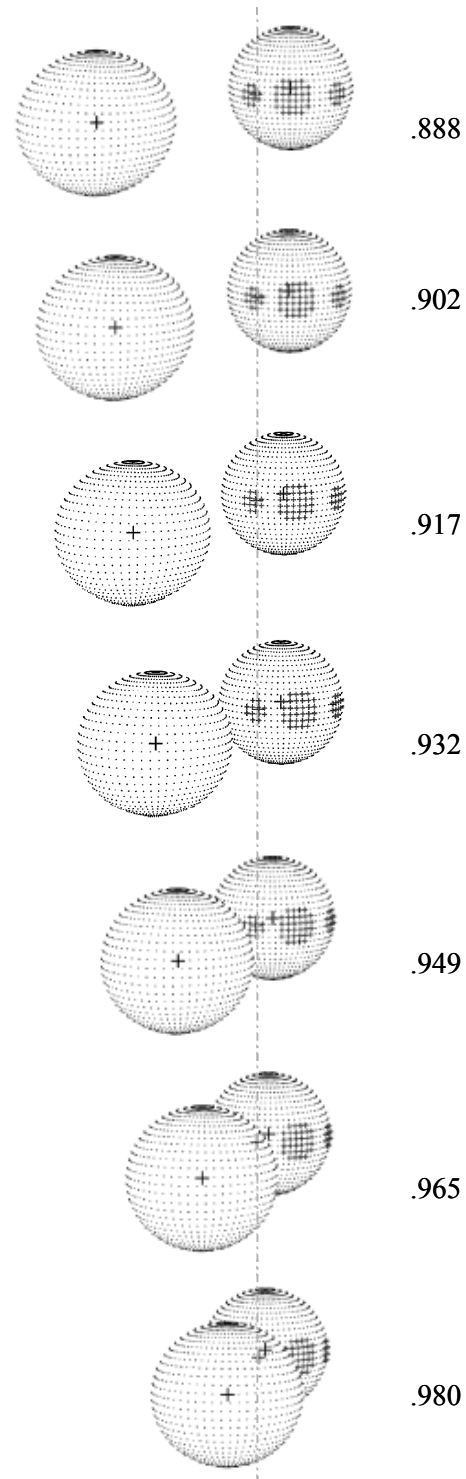


FIG. 3.3.2f—Line-of-sight Geometry for Epoch 1985 July LWP/LWR phases

**LWP/LWR**

**1986 Feb - Mar**

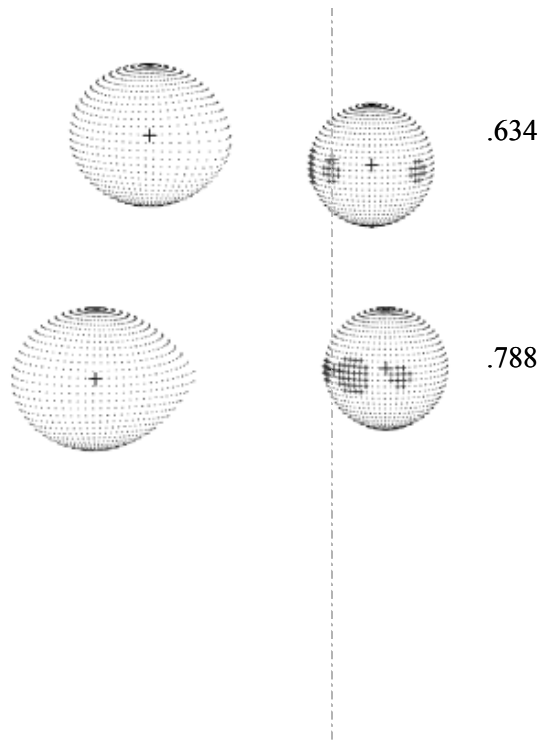


FIG. 3.3.2g—Line-of-sight Geometry for Epoch 1986 Feb. - March LWP/LWR phases

**LWP/LWR**

**1989 Sep**

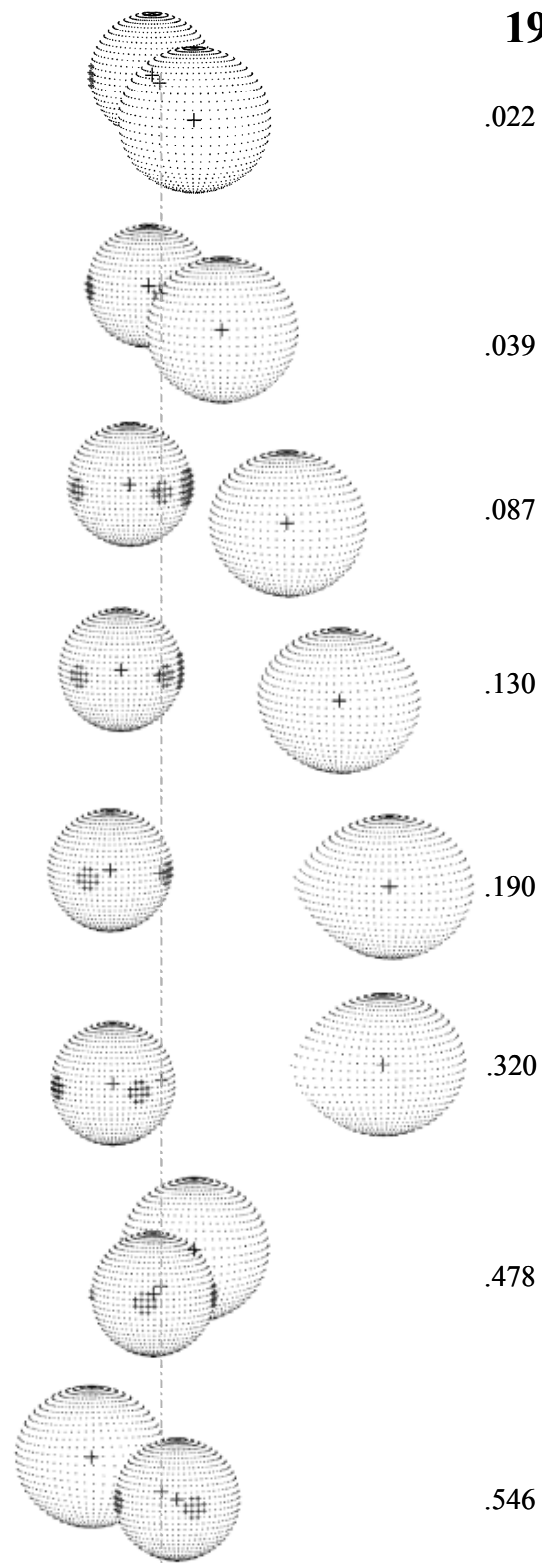


FIG. 3.3.2h—*Line-of-sight Geometry for Epoch 1989 September LWP/LWR phases*

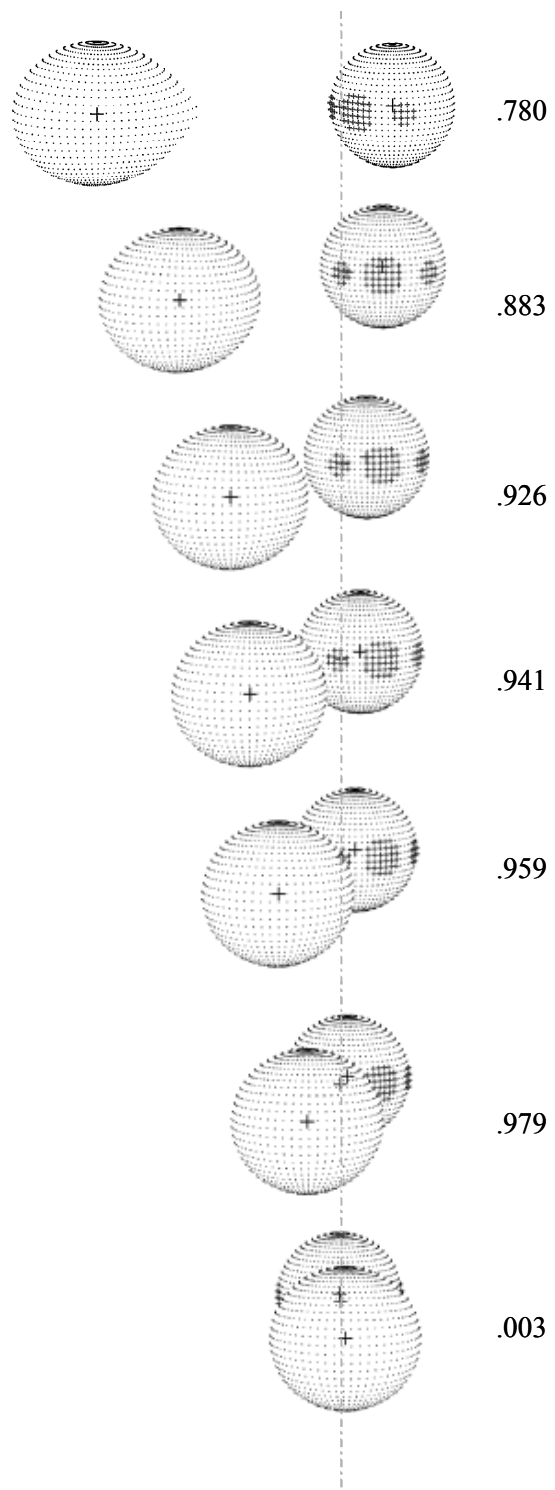


FIG. 3.3.2h—continued

These figures (FIGS. 3.3.1a-h and 3.3.2a-h) were generated using a software package called Binary Maker 3.0.\* Its engine is based on the Wilson-Divnney code†. This program outputs light curves, radial velocity curves, and orbit geometry. We varied the input parameters, selecting combinations of the values listed in the Tables in Appendix A, until the simulated radial velocity curve from the program matched our best measured radial velocity curve, that of Al II  $\lambda$ 1670 (discussed in Section 4). The final input parameters are listed in TABLE 3.3.1. (These values are provided in this table for completeness, but play no role in this work other than the generation of the figures.)

TABLE 3.3.1  
INPUT PARAMETERS FOR BINARY MAKER 3.0

mass ratio input = 0.218900	mass ratio < 1 = 0.218900
Omega 1 = 5.088680	Omega 2 = 2.279096
Omega inner = 2.279097	Omega outer = 2.140058
C 1 = 8.381879	C 2 = 3.771847
C inner = 3.771848	C outer = 3.543710
Fillout 1 = -0.550000	Fillout 2 = 0.000002
Lagrangian L1 = 0.650349	Lagrangian L2 = 1.451217
AG = r1(back) = 0.206784	AS = r2(back) = 0.281108
BG = r1(side) = 0.206255	BS = r2(side) = 0.248632
CG = r1(pole) = 0.205160	CS = r2(pole) = 0.238990
DG = r1(point) = 0.206960	DS = r2(point) = 0.349510
Surface area 1 = 0.533939	Surface area 2 = 0.839262
Volume 1 = 0.036403	Volume 2 = 0.070632
Mean radius 1 = 0.206066	Mean radius 2 = 0.256243
Mean radius 1 (vol) = 0.205597	Mean radius 2 (vol) = 0.256431
Eccentricity = 0.00000	Longitude of Periastron = 133.0000
Phase of periastron = 0.00000	Phase of conjunction = 0.00000
Angular Rotation F1 = 1.0000	Angular Rotation F2 = 1.0000
Normalization Phase = 0.25000	Normalization Factor = 1.00000
inclination = 81.400	wavelength = 2000.00
temperature 1 = 12500.00	temperature 2 = 5000.00
luminosity 1 = 0.9997	luminosity 2 = 0.0003
gravity coefficient 1 = 0.250	gravity coefficient 2 = 0.080
limb darkening 1 = 0.850	limb darkening 2 = 0.560
reflection 1 = 1.000	reflection 2 = 0.500
Third light = 0.0000	Period = 2.86731000
K1 = 44.000000	K2 = 201.000000
V0 = 0.000000	
Absolute Parameters	
Mass 1 = 3.721372 solar masses	Mass 2 = 0.814629 solar masses
Semi-major axis = 9.769090 million km	Semi-major axis = 14.036050 solar radii
Mean radius 1 = 2.013081 million km	Mean radius 1 = 2.892357 solar radii
Mean radius 2 = 2.503266 million km	Mean radius 2 = 3.596646 solar radii
Mean density 1 = 0.218199 grams/cm <sup>3</sup>	Mean density 2 = 0.024618 grams/cm <sup>3</sup>

\* © Contact Software, Binary Maker 3, D.H. Bradstreet, D.P. Steelman, dbradstr@eastern.edu

† R. E. Wilson and E. J. Divnney (1971)

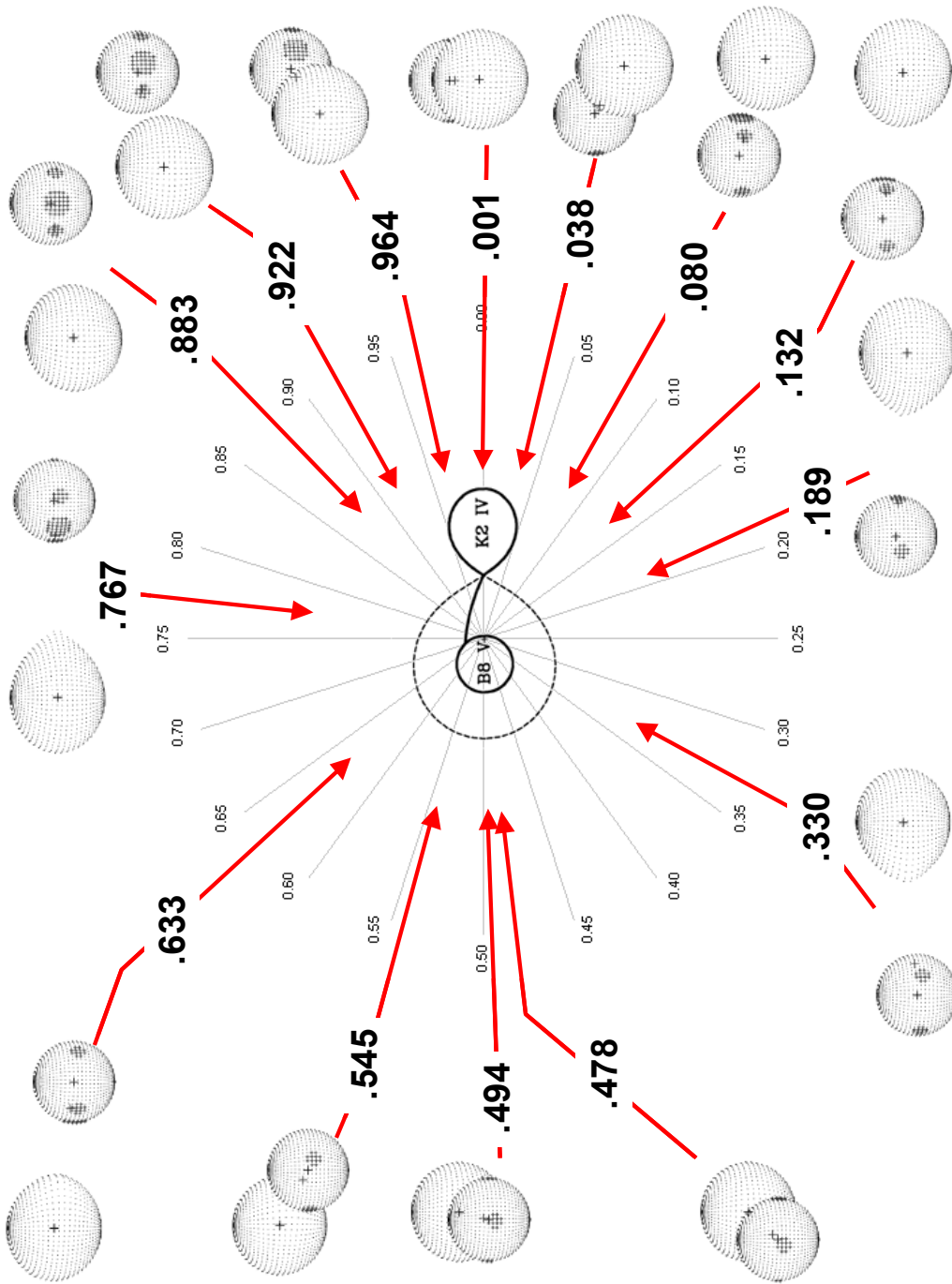


FIG. 3.3.3—Selected Line of Sight Geometries of Algot IUE Observations

### 3.4 Sample IUE Data for Algol

Before proceeding into a detailed analysis of the IUE data in the following chapter, we present a sample of the data in order to clarify the meaning of essential features, especially in the context of the phases described above. The samples in FIG. 3.4.1a and FIG. 3.4.1b represent spectra in the SWP UV range 1390 Å to 1405 Å

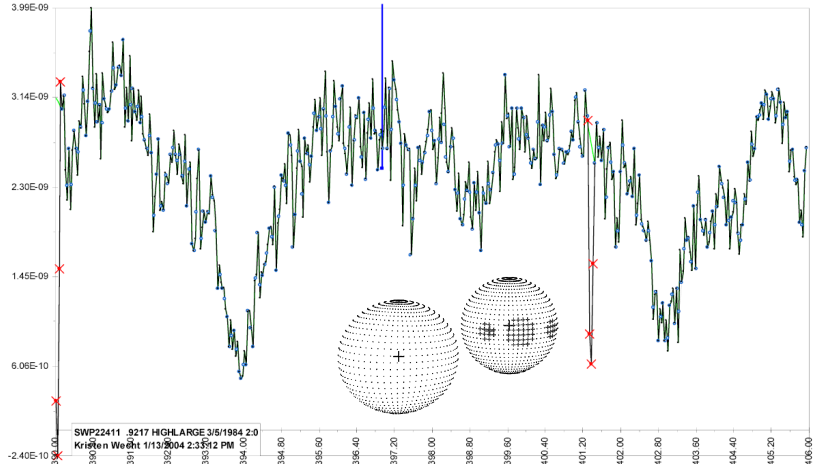


FIG. 3.4.1a—Sample IUE data SWP 22411 Si IV 1393 Å and Si IV 1402 Å ( $\phi=0.9217$   $\beta$  Per 3/5/1984)

taken 1.1 orbits apart, on 3/5/1984 ( $\phi = 0.922$ ) and 3/7/1984 ( $\phi = 0.939$ ) respectively. In each of the figures the binary-system orientations at the corresponding phases

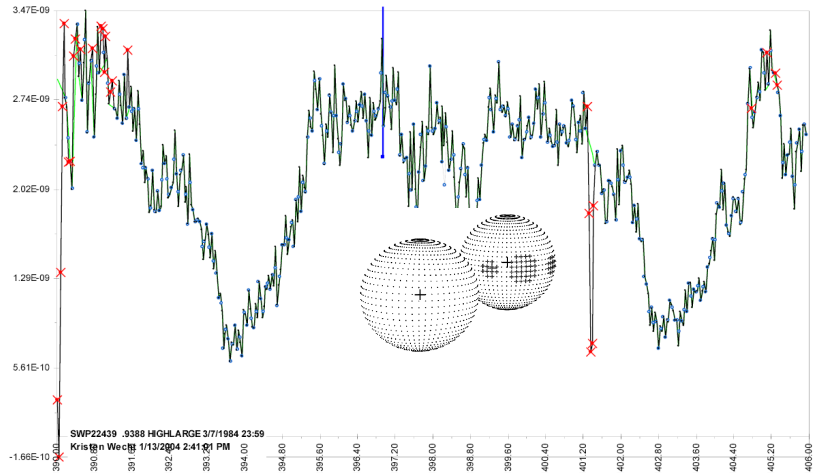


FIG. 3.4.1b—Sample IUE data SWP 22439 Si IV 1393 Å and Si IV 1402 Å ( $\phi=0.9388$   $\beta$  Per 3/7/1984)

are shown as viewed along our line of sight from the Earth. (These orientations are just those presented in the previous section.) The small x's mark the flagged points. The



small dots mark the "preview" data points. The black thin jagged line is the best output product from the NEWSIPS processing.

These spectra primarily show absorption features, the strongest of which is the resonance absorption doublet of Si IV at 1393 and 1402 Å. These 1984 line profiles of Si IV become increasingly asymmetric, (additional red absorption) in going from phase 0.922 to 0.939. (This phase interval is the beginning of primary eclipse.) The increasing red absorption is due to a change in our viewing angle of the gas stream, from looking diagonally across the stream to looking more along the stream.

It is important to understand that only the B8 V (primary) star is emitting significantly in the UV spectral range. Hence, the spectral features represent the absorption of ultraviolet light emitted from the primary by constituents located between the B8 V star and the Earth. Therefore, the change in phase (orientation) alters

(i) the quantity of intervening gas located in a cylinder between the primary and Earth, and (ii) the radial components of the

corresponding gas velocities. Both of these effects contribute to the spectral line change in going from FIG. 3.4.1a to FIG. 3.4.1b which is due to gas

flowing from the secondary to the primary. FIG. 3.4.2 shows the

direction of the gas stream as well as

the lines of site, as viewed from above.

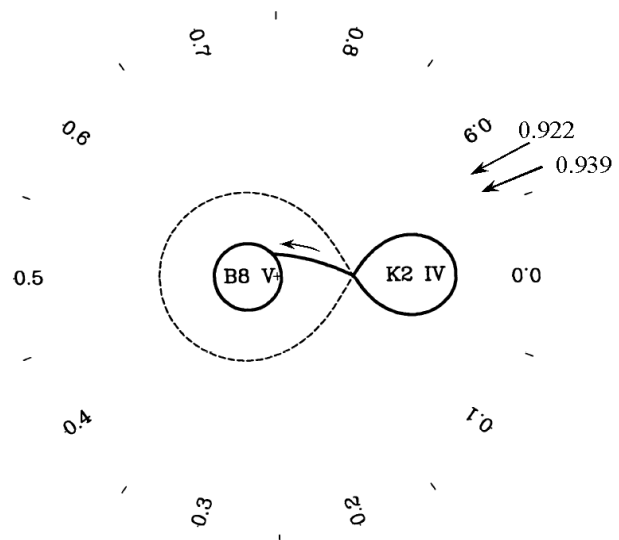


FIG. 3.4.2—Lines of sight as viewed from above for the 1984 exposures at phases 0.922 and 0.939 (Adapted from Fig. 16 p. 285 Richards 1993)

## 4. ANALYSIS OF THE DATA

### 4.1 *Data Analysis Overview*

Spectra from the MAST IUE archive (see Section 3.1) are processed and analyzed in a series of stages, and described in detail in the following sections. An overview of the process is described here and supported by a flow-chart representation in FIG. 4.1.1.

Numerical results generated by the various levels of data analysis are identified by rectangular boxes in the figure. Operations are identified by ovals and circles. The titles appearing in the rectangular and oval shapes are italicized in the description below.

Data from the MAST IUE archive (“IUE Spectra” for our purposes) suffer from several deficiencies, including a jaggedness that renders them poorly suited for certain types of mathematical processing and flagged data points indicative of suspected errors. We subject the IUE Spectra to a *Preliminary Processing* step to deal with these issues, thereby producing our *Smoothed Spectra*. This is described in Section 4.3.1.

By *Identifying the Continuum* levels in small UV ranges, as described in Section 4.4.1, we generate the *Continuum Flux and Light Curves* reported in Section 4.4.2. Continuum flux curves represent UV intensities as functions of wavelength, whereas light curves display these intensities as functions of phase.

The remaining analyses involve the examination of spectral line features. In order to facilitate those treatments, two preliminary steps are taken. Our methods for *Spectral-Line Identification and Systematic Velocity Determination* and a *Correction for the Influence of Algol C* are described in Sections 4.3.2 and 4.3.3, respectively.

*Line Feature Analyses* are then performed, as described in Section 4.5.1, resulting in *Line Positions*, *Line Depths*, *Line Widths*, and *Line Asymmetries*. The latter two results are described in Section 4.5.3. A straightforward calculation results in our reported *Radial Velocity Curves*, described in Section 4.5.2. Further calculations produce the *Residual Intensities* described in Section 4.5.4 and the *Equivalent Widths* and *Gas Densities* described in Section 4.5.5.

The use of *Difference Spectra* to remove photosphere effects is explored in Section 4.5.6. The *Mass Loss Rate* from Algol B is computed in Section 4.5.7.

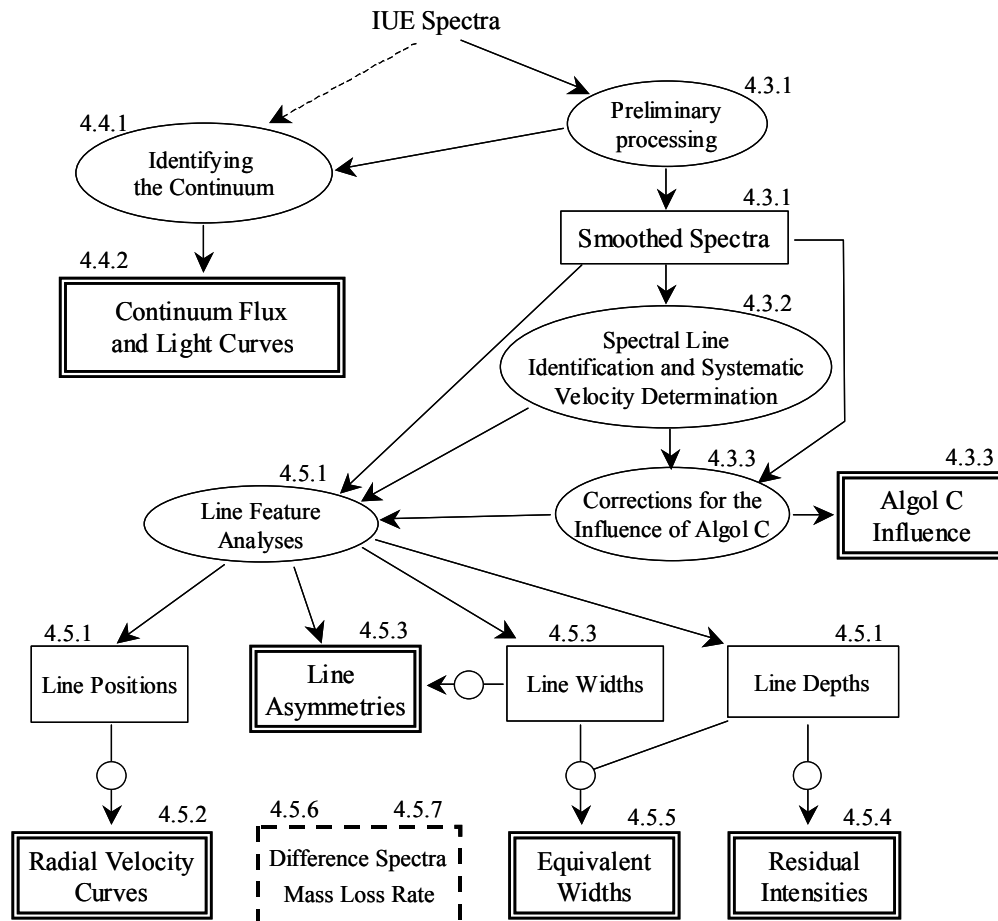


FIG. 4.1.1—*IUE Spectra Analysis Flow-Chart*

## 4.2 *Gas Composition, Excitation, and Ionization*

### 4.2.1 *Ion Types and Electronic-Transitions*

The IUE spectral features are produced mostly by the selective absorption of UV light, emitted by the primary, due to intervening gases. The atoms and ions constituting the intervening gas could be located at the photosphere of the primary, associated with Algol-system gas flow, or present in the interstellar region between Algol and Earth. Gases occupying the various regions are generally characterized by different constituent atoms, temperatures, electron pressures, and radial velocities. In some cases, the transitions are sufficiently strong and isolated so that definitive identifications are straightforward. In other cases, however, the transitions may be weak and/or “blended” with nearby and perhaps unrelated spectra features.

We developed an algorithm to facilitate the identification of electronic transitions corresponding to various absorption features. This procedure, described in Section 4.3.2, provides an additional benefit by producing an estimate of the center of mass velocity of the Algol system, called the “systematic velocity.”

Using this algorithm along with experiences based upon previous examinations of similar stellar systems, we identified many spectral lines with ion type and electronic transition. Characteristics of these ions and transitions are provided in TABLE 4.2.1.1.

TABLE 4.2.1.1 – Electronic Transitions (Source: NIST and Kurucz online databases)

SWP Line ID	$\lambda_{\text{obs}}$ Vac (Å)	Configurations	Terms	$J_i$	$J_k$	$g_i$	$g_k$	$f_{ik}$	$\log(gf_{ik})$	$A_{ki}$ (s <sup>-1</sup> )
Al II 1670	1670.7867	$2p^6 3s^2 \rightarrow 3s 3p$	$^1S \rightarrow ^1P^\circ$	0 → 1	1 → 3	1	3	1.83e+00	0.263	1.46e+09
Al III 1854	1854.7164	$2p^6 3s \rightarrow 2p^6 3p$	$^2S \rightarrow ^2P^\circ$	$1/2 \rightarrow 3/2$	2 → 4	2	4	5.57e-01	0.047	5.40e+08
Al III 1862	1862.7895	$2p^6 3s \rightarrow 2p^6 3p$	$^2S \rightarrow ^2P^\circ$	$1/2 \rightarrow 1/2$	2 → 2	2	2	2.77e-01	-0.256	5.33e+08
C II 1334	1334.532	$2s^2 2p \rightarrow 2s 2p^2$	$2P^\circ \rightarrow ^2D$	$1/2 \rightarrow 3/2$	2 → 4	2	4	1.27e-01	-0.597	2.37e+08
C II 1335	1335.708	$2s^2 2p \rightarrow 2s 2p^2$	$2P^\circ \rightarrow ^2D$	$3/2 \rightarrow 5/2$	4 → 6	4	6	1.14e-01	-0.341	2.84e+08
C IV 1548	1548.185	$1s^2 2s \rightarrow 1s^2 2p$	$^2S \rightarrow ^2P^\circ$	$1/2 \rightarrow 3/2$	2 → 4	2	4	1.90e-01	-0.419	2.65e+08
C IV 1550	1550.774	$1s^2 2s \rightarrow 1s^2 2p$	$^2S \rightarrow ^2P^\circ$	$1/2 \rightarrow 1/2$	2 → 2	2	2	9.52e-02	-0.720	2.64e+08
Fe II 1608	1608.45106	$(5D)4s a6D \rightarrow (6S)sp y6P$		4.5 → 3.5					-0.145	2.31E+08
Fe II 1635	1635.4010	$3d^6(^5D)4s \rightarrow 3d^6(^6S)4s 4p(^3P^\circ)$	$a^4D \rightarrow x^4P^\circ$	$7/2 \rightarrow 5/2$	8 → 6	8	6	7.2e-02	-0.24	2.4e+08
Fe II 1639	1639.40124	$(5D)4s a6D \rightarrow (6S)sp y6P$		0.5 → 1.5					-0.874	8.29E+07
Fe II 1640	1640.15205	$D7 a4F \rightarrow (3F)4p y4G$		1.5 → 2.5					-0.717	7.93E+07
Fe III 1895	1895.456	$(6S)4s 7S \rightarrow (6S)4p 7P$		3 → 4					0.461	5.96E+08
Fe III 1914	1914.056	$(6S)4s 7S \rightarrow (6S)4p 7P$		3 → 3					0.344	5.74E+08
Si II 1260	1260.42	$3s^2 3p \rightarrow 3s^2 3d$	$2P^\circ \rightarrow ^2D$	$1/2 \rightarrow 3/2$	2 → 4	2	4	9.5e-01	0.28	2.0e+09
Si II 1264	1264.737	$3s^2 3p \rightarrow 3s^2 3d$	$2P^\circ \rightarrow ^2D$	$3/2 \rightarrow 5/2$	4 → 6	4	6	8.3e-01	0.52	2.3e+09
Si II 1304	1304.37	$3s^2 3p \rightarrow 3s 3p^2$	$2P^\circ \rightarrow ^2S$	$1/2 \rightarrow 1/2$	2 → 2	2	2	9.2e-02	-0.74	3.6e+08
Si II 1305	1305.592	$s3p2 2D \rightarrow 3d^1 2F$		2.5 3.5					0.71	2.51E+09
Si II 1309	1309.277	$3s^2 3p \rightarrow 3s 3p^2$	$2P^\circ \rightarrow ^2S$	$3/2 \rightarrow 1/2$	4 → 2	4	2	9.0e-02	-0.44	7.0e+08
Si II 1526	1526.708	$3s^2 3p \rightarrow 3s^2 4s$	$2P^\circ \rightarrow ^2S$	$1/2 \rightarrow 1/2$	2 → 2	2	2	1.30e-01	-0.584	3.73e+08
Si II 1533	1533.432	$3s^2 3p \rightarrow 3s^2 4s$	$2P^\circ \rightarrow ^2S$	$3/2 \rightarrow 1/2$	4 → 2	4	2	1.3e-01	-0.28	7.4e+08
Si II 1808	1808.012	$3s^2 3p \rightarrow 3s 3p^2$	$2P^\circ \rightarrow ^2D$	$1/2 \rightarrow 3/2$	2 → 4	2	4	3.6e-03	-2.14	3.7e+06
Si II 1816	1816.98	$3s^2 3p \rightarrow 3s 3p^2$	$2P^\circ \rightarrow ^2D$	$3/2 \rightarrow 5/2$	4 → 6	4	6	5.9e-03	-1.63	7.9e+06

TABLE 4.2.1.1 SWP - continued

SWP Line ID	$\lambda_{\text{vac}}^{\text{obs}}$ (Å)	Configurations	Terms	$J_i$	$J_k$	$g_i$	$g_k$	$f_{ik}$	$\log(gf_{ik})$	$A_{ki}$ ( $s^{-1}$ )
Si III 1294	1294.545	$3s3p \rightarrow 3p^2$	$3p^o \rightarrow 3p$	1 → 2		3 → 5	2.27e-01	-0.167	5.42e+08	
Si III 1296	1296.726	$3s3p \rightarrow 3p^2$	$3p^o \rightarrow 3p$	0 → 1		1 → 3	5.44e-01	-0.265	7.19e+08	
Si III 1298	1298.89	$3s3p \rightarrow 3p^2$	$3p^o \rightarrow 3p$	1 → 1		3 → 3	1.36e-01	-0.391	5.36e+08	
Si III 1301	1301.149	$3s3p \rightarrow 3p^2$	$3p^o \rightarrow 3p$	1 → 0		3 → 1	1.80e-01	-0.267	2.13e+09	
Si III 1302	1302.2									
Si III 1303	1303.323	$3s3p \rightarrow 3p^2$	$3p^o \rightarrow 3p$	2 → 1		5 → 3	1.35e-01	-0.170	8.85e+08	
Si IV 1393	1393.755	$2p^63s \rightarrow 2p^63p$	$2^2S \rightarrow 2^2P^o$	$1/2 \rightarrow 3/2$		2 → 4	4.50e-01	-0.046	7.73e+08	
Si IV 1402	1402.77	$2p^63s \rightarrow 2p^63p$	$2^2S \rightarrow 2^2P^o$	$1/2 \rightarrow 1/2$		2 → 2	2.24e-01	-0.349	7.58e+08	

TABLE 4.2.1.2 – LWP/LWR

LWP/LWR Line ID	b.l.	$\lambda_{\text{vac}}^{\text{obs}}$ (Å)	Configurations	Terms	$J_i$	$J_k$	$g_i$	$g_k$	$f_{ik}$	$\log(gf_{ik})$	$A_{ki}$ ( $s^{-1}$ )
<b>LWP/LWR</b>											
Fe II 2586		2586.6500	$3d^6(^5D)4s \rightarrow 3d^6(^5D)4p$	$a^6D \rightarrow z^6D^o$	$9/2 \rightarrow 7/2$		10 → 8	6.5e-02	-0.19	8.1e+07	
Fe II 2599		2599.147	$3d^6(^5D)4s \rightarrow 3d^6(^5D)4p$	$a^6D \rightarrow z^6D^o$	$7/2 \rightarrow 5/2$		8 → 6	9.9e-02	-0.10	1.3e+08	
Fe II 2600		2600.173	$3d^6(^5D)4s \rightarrow 3d^6(^5D)4p$	$a^6D \rightarrow z^6D^o$	$9/2 \rightarrow 9/2$		10 → 10	2.2e-01	0.35	2.2e+08	
Fe II 2750 (a)		2750.13	$3d^6(^5D)4s \rightarrow 3d^6(^5D)4p$	$a^4D \rightarrow z^4F^o$	$5/2 \rightarrow 7/2$		6 → 8	3.2e-01	0.28	2.1e+08	
Fe II 2750 (b)		2750.29	$3d^6(^5D)4s \rightarrow 3d^6(^5D)4p$	$a^4D \rightarrow z^4D^o$	$1/2 \rightarrow 1/2$		2 → 2	1.2e-01	-0.60	1.1e+08	
Mg II 2796		2796.352	$2p^63s \rightarrow 2p^63p$	$2^2S \rightarrow 2^2P^o$	$1/2 \rightarrow 3/2$		2 → 4	6.08e-01	0.085	2.60e+08	
Mg II 2803		2803.531	$2p^63s \rightarrow 2p^63p$	$2^2S \rightarrow 2^2P^o$	$1/2 \rightarrow 1/2$		2 → 2	3.03e-01	-0.218	2.57e+08	
Mg II 2791		2791.599	$2p^63p \rightarrow 2p^63d$	$2^2P^o \rightarrow 2^2D$	$1/2 \rightarrow 3/2$		2 → 4	9.37e-01	0.273	4.01e+08	
Mg II 2798 (a)		2798.823	$2p^63p \rightarrow 2p^63d$	$2^2P^o \rightarrow 2^2D$	$3/2 \rightarrow 5/2$		4 → 6	8.44e-01	0.528	4.79e+08	
Mg II 2798 (b)		2798.754	$3p \ 2P \rightarrow 3d \ 2D$		1.5	1.5			-0.42	8.09E+07	

Since we are concerned with gas flow associated with the Algol system, it is important to distinguish the Algol gas-flow contributions from the photospheric absorption. Since the photospheric conditions of the primary are relatively well understood, we can, to some extent, distinguish photospheric contributions by examining the predicted ionization fractions as functions of temperature and electron pressure. This analysis is described in the following section.

#### 4.2.2 Ionization Fractions

In our preliminary examination of the spectra, we noticed several lines that are known to be indicators of hot plasma and circumstellar material, (Kempner and Richards, 1999); namely, Si IV  $\lambda\lambda 1393.755, 1402.770$  and C IV  $\lambda 1548.85$ . “The presence of Si IV and C IV indicates the existence of regions considerably hotter than a normal B8V photosphere,” (McCluskey and Kondo, 1984).

The Saha equation can be used to estimate the ionization fraction of each atomic species as functions of temperature and electron pressure, assuming conditions of thermodynamic equilibrium. The Saha equation is given below in ordinary and logarithmic forms

$$\frac{N^{(r+1)}}{N^{(r)}} = \frac{2kT}{P_e} \left( \frac{2\pi m_e kT}{h^2} \right)^{\frac{3}{2}} \frac{Z^{(r+1)}}{Z^{(r)}} e^{-\chi^{(r)}/kT} \quad (4.2.2.1)$$

$$\log \frac{N^{(r+1)}}{N^{(r)}} = \log \frac{Z^{(r+1)}}{Z^{(r)}} + \frac{5}{2} \log T - \frac{5040}{T} \chi^{(r)} - \log P_e - 0.179 \quad (4.2.2.2)$$

The terms in these equations are defined as follows:

$r$	ionization state, where $r = 0$ indicates un-ionized
$N^{(r)}$	number of atoms in ionization state $r$
$Z^{(r)}$	atomic partition function for ionization state $r$
$\chi^{(r)}$	ionization energy in eV for ionization state $r$
$P_e$	electron pressure, in dynes/cm <sup>2</sup>
$T$	temperature in Kelvin

The partition functions are given by

$$Z^{(r)} = \sum_{i=1}^{i_{\max}} g_i^{(r)} e^{-\varepsilon_i^{(r)}/kT} \quad (4.2.2.3)$$

where

$i$	atomic energy level
$g_i^{(r)}$	statistical weight (degeneracy) of the $i^{\text{th}}$ level for ionization state $r$
$i_{\max}$	last bound level for ionization state $r$ (depends on $T$ and $P_e$ )
$\varepsilon_i^{(r)}$	energy of $i^{\text{th}}$ level for ionization state $r$ , relative to the ground state (i.e., $\varepsilon_i = 0$ )

The ionization fraction is the ratio of  $N^{(r)}$  to the total number of atoms of that type;

hence,

$$X^{(r)} = \frac{N^{(r)}}{N^{(0)} + N^{(1)} + \dots + N^{(r)} + \dots + N^{(r_{\max})}} \quad (4.2.2.4)$$

or

$$X^{(r)} = \frac{1}{\frac{N^{(0)}}{N^{(r)}} + \frac{N^{(1)}}{N^{(r)}} + \dots + 1 + \dots + \frac{N^{(r_{\max})}}{N^{(r)}}} \quad (4.2.2.5)$$



Since the Saha equation gives ratios of consecutive ionization stages, terms such as

$\frac{N^{(2)}}{N^{(5)}}$  were constructed as follows:

$$\frac{N^{(2)}}{N^{(5)}} = \left( \frac{N^{(2)}}{N^{(3)}} \right) \left( \frac{N^{(3)}}{N^{(4)}} \right) \left( \frac{N^{(4)}}{N^{(5)}} \right) \quad (4.2.2.6)$$

We developed a Visual Basic for Application to automate this process. The input parameter values are from the NIST\* and Kurucz† online databases.

The effective temperature  $T_e$  of Algol is  $\sim 12,300$  K with an electron pressure  $P_e \sim 316.2$  dynes/cm<sup>2</sup>, or  $\log(P_e) \sim 2.5$  (Aller 1953; Underhill 1972, Table 8, gives a value of  $P_e = 3.9709 \times 10^2$  dynes/cm<sup>2</sup> for  $T_e = 12370$  K). The solutions of the Saha equation for the B8 V component of Algol are plotted in FIGs. 4.2.2.1 and 4.2.2.2. We see in the primary's photosphere the presence of C II, N II, and O II; and silicon is almost evenly split between Si II and Si III.

---

\* [http://physics.NIST.gov/cgi-bin/AtData/main\\_asd](http://physics.NIST.gov/cgi-bin/AtData/main_asd)

† <http://cfa-www.harvard.edu/amdata/Kurucz23/sekur.html>

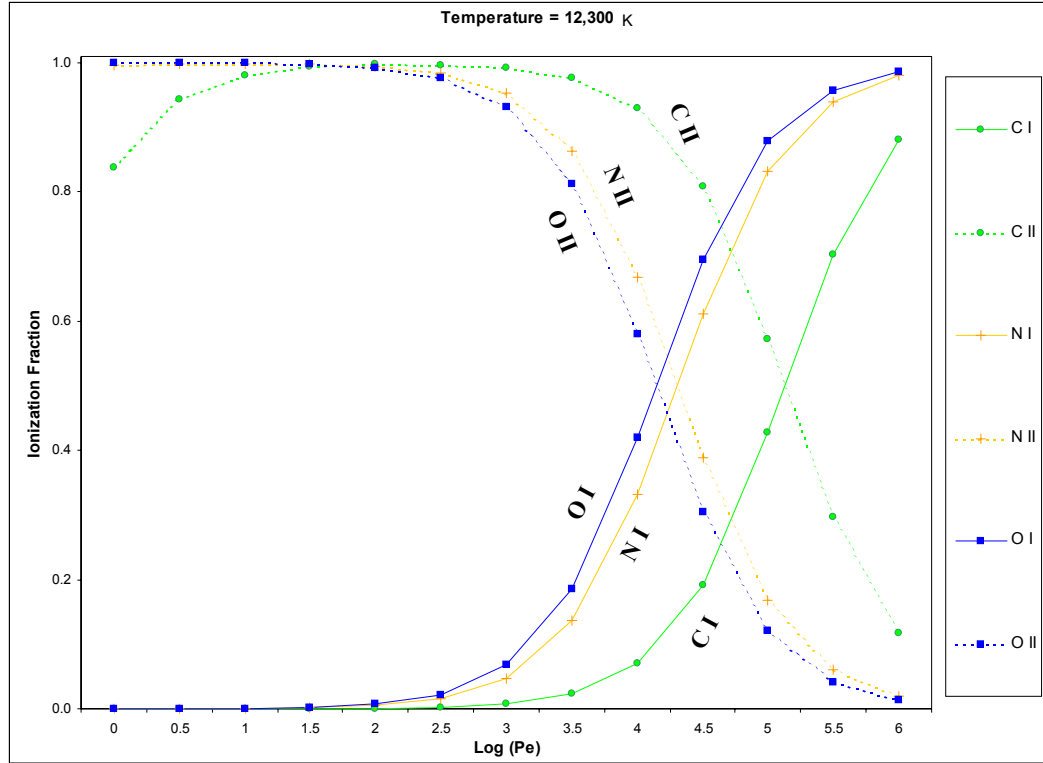


FIG. 4.2.2.1 - Ionization Fraction of Carbon, Nitrogen, and Oxygen at 12,300 K

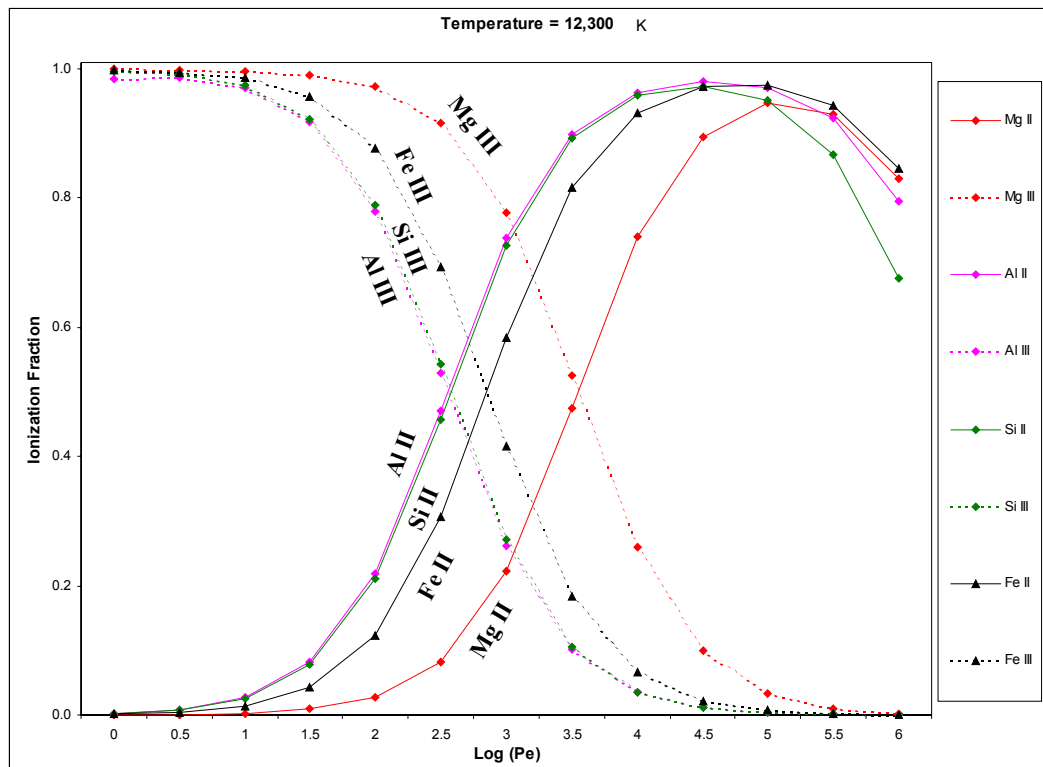


FIG. 4.2.2.2 - Ionization Fraction of Mg, Al, Si, and Fe at 12,300 K

Anticipating the presence of gases at non-photospheric temperatures, we examine additional solutions of the Saha equation, revealing the formation of C IV at  $\sim 25,000$  K (for electron pressures  $\leq 1000$  dynes/cm<sup>2</sup>; see FIG. 4.2.2.3), Si IV at  $\sim 20,000$  K (FIG. 4.2.2.4), O IV at  $\sim 30,000$  K (FIG. 4.2.2.5), and N V at  $\sim 45,000$  K (FIG. 4.2.2.6).

For completeness, a set of these figures corresponding to temperatures of 8,000 K, 10,000 K, 12,300 K, 15,000 K, 20,000 K, 25,000 K, 28,500 K, 30,000 K, 35,000 K, 45,000 K, and 50,000 K are provided in Appendix D.1.

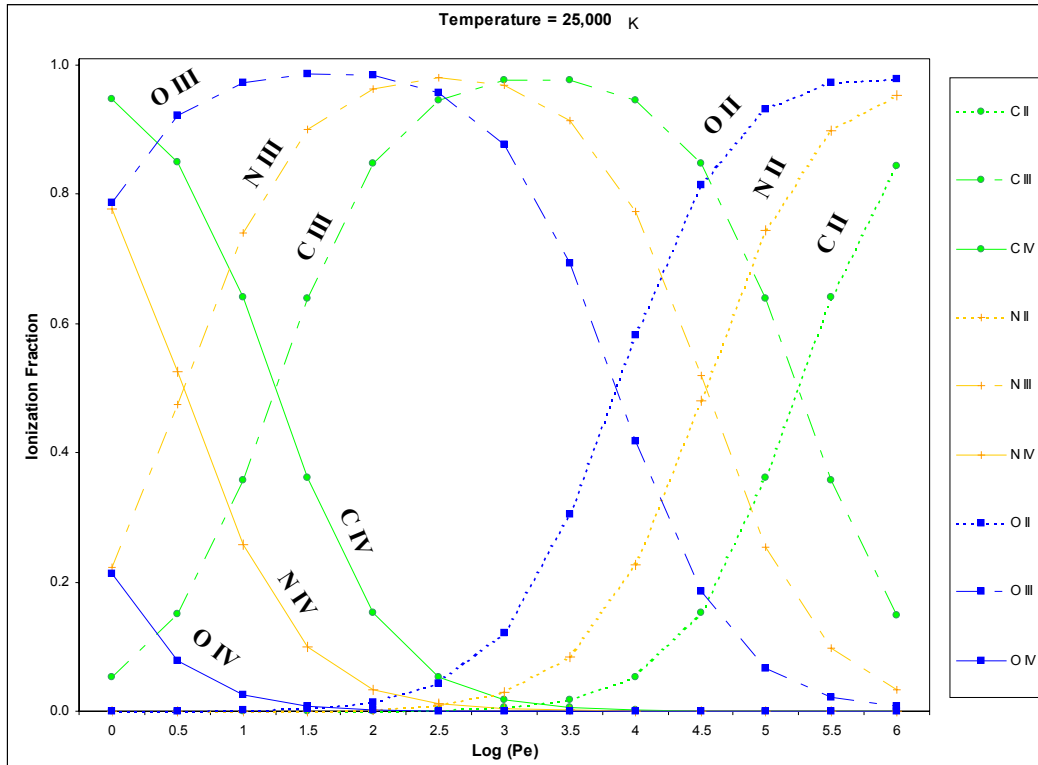


FIG. 4.2.2.3 - Ionization Fraction of Carbon, Nitrogen, and Oxygen at 25,000 K

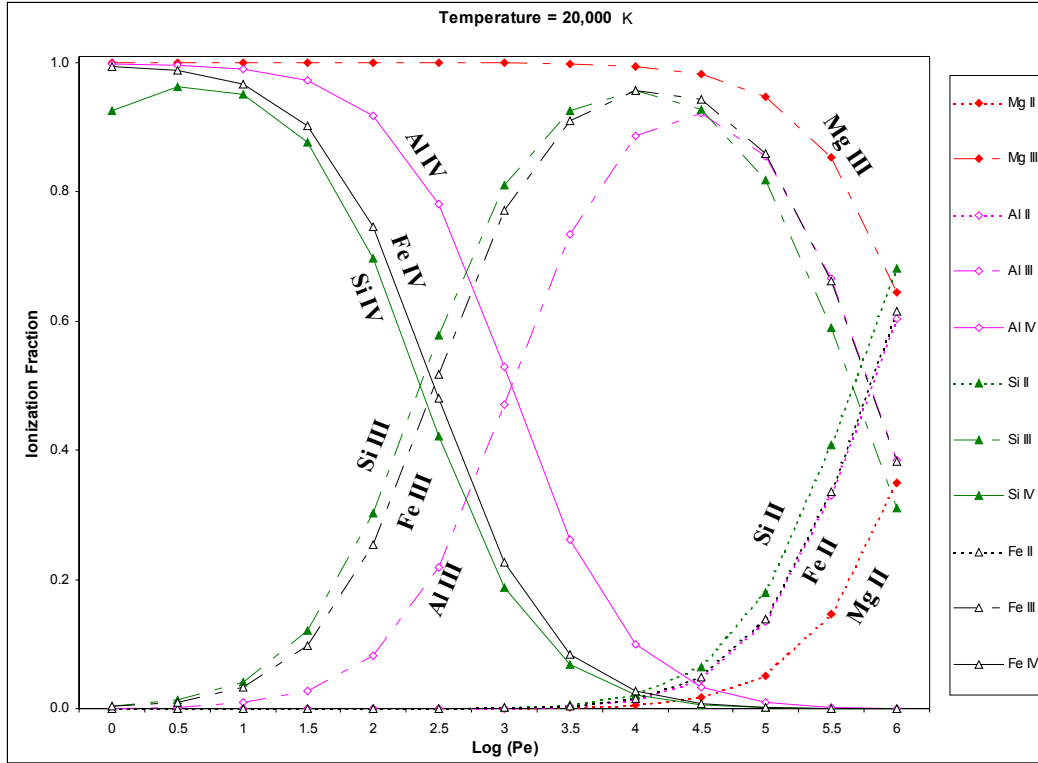


FIG. 4.2.2.4 - Ionization Fraction of Mg, Al, Si, and Fe at 20,000 K

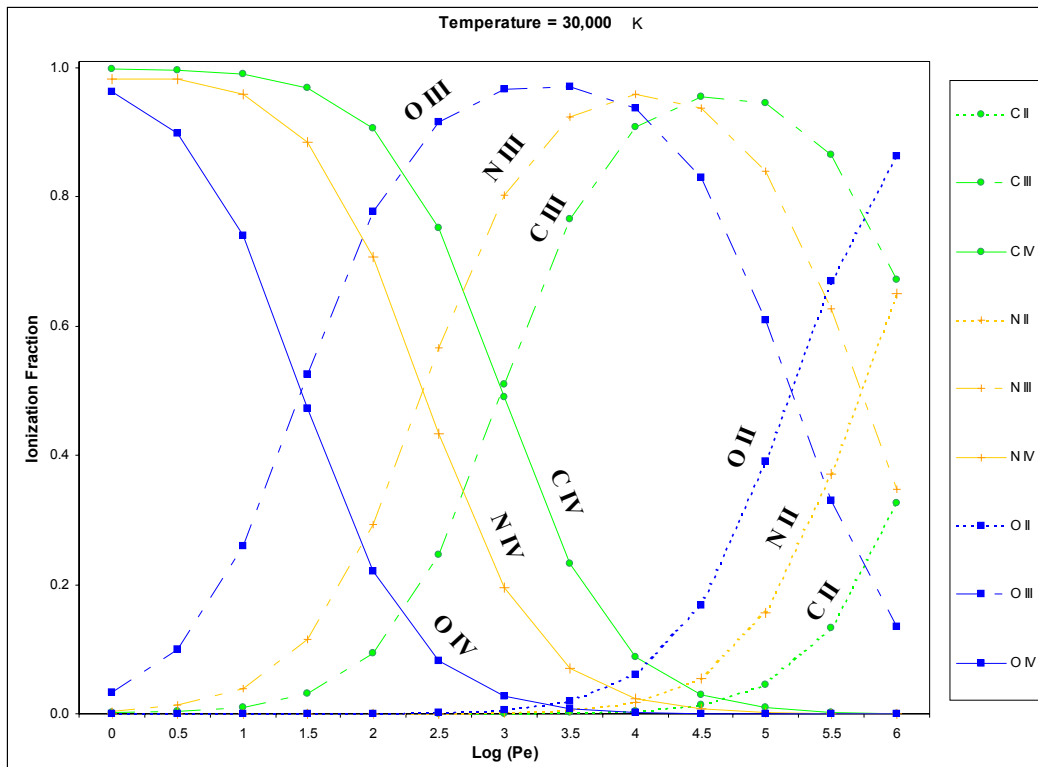


FIG. 4.2.2.5 - Ionization Fraction of Carbon, Nitrogen, and Oxygen at 30,000 K

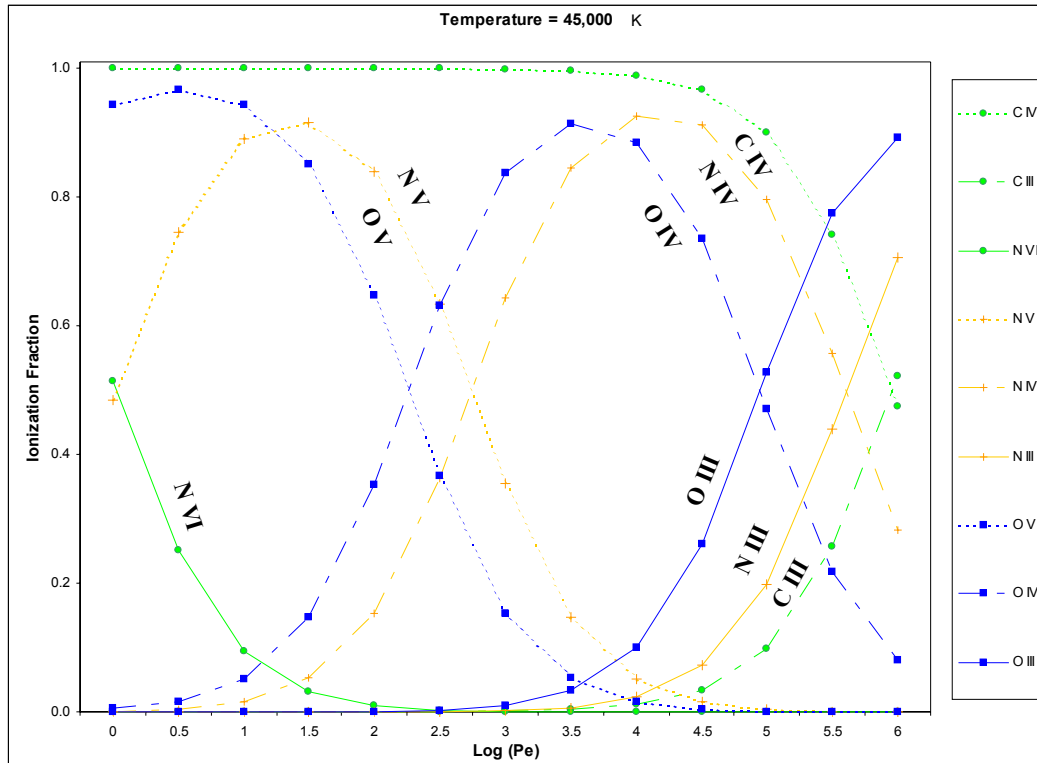


FIG. 4.2.2.6 - Ionization Fraction of Carbon, Nitrogen, and Oxygen at 45,000 K

We did not see definitive evidence for the presence of C IV  $\lambda 1550.7742$ , N V  $\lambda \lambda 1238.821, 1242.804$ , or O IV  $\lambda 1397.20$  in any of the Algol spectra, which indicate plasma temperatures ranging from  $2 \times 10^4$  to  $5 \times 10^4$  K. These were too blended or too weak to detect. Chemical depletion was previously suggested. The Si IV doublet is relatively strong, compared to the C IV  $\lambda 1548$  line, which is quite weak and difficult to measure accurately. In the SWP analysis, we focus on the Si IV lines since they show a nice variation across the orbital phases, as well as across the epochs.

### 4.3. Preliminary Considerations

#### 4.3.1 Managing the IUE Data

The IUE dataset contains many points that have been flagged to indicate suspected measurement or recording errors. We replaced these values with numbers computed by a simple linear interpolation using the first point on either side of the flagged point(s). Symbols (“x”) were retained in our plots to denote the locations of flagged data points. We did not use regions of spectra characterized by large sequences of contiguous flagged data points.

These adjusted datasets were further processed to remove the jaggedness that renders them poorly suited for certain types of mathematical processing. In order to accomplish this, we used a moving average procedure with Pascal Triangle weighting, which is commonly used for this application.

A 12-step Pascal Triangle scheme ( $N = 12$ ) was applied to each vector of 21,000 data points for the SWP measurements and 23,000 data points for LWP/LWR. Hence, a vector of smoothed data points  $F$  was constructed from the corresponding IUE vector  $F'$  as follows (for even  $N$ ):

$$F_i = \frac{1}{2^N} \sum_{n=0}^N \left[ \frac{N!}{(N-n)!n!} \right] F'_{-\frac{N}{2}+n+i} \quad (4.3.1.1)$$

This approach is particularly appropriate when one wishes to reduce noise while preserving Gaussian features.

### 4.3.2 Spectral-Line Identification and Systematic Velocity

The smoothed spectra show many absorption features, even over wavelength ranges of only several Angstroms. In order to facilitate the process of identifying the spectral features with ion types and transitions, we developed a custom interactive visualization program using VBA (Visual Basic for Applications). The program connects to our smoothed-spectra database and automatically locates the wavelengths of local minima. Upon specifying a wavelength range, all of the local minima in that range are plotted as a function of orbital phase. An illustration of the output is shown by the data circles of FIG. 4.3.2.1, which was computed for a wavelength range of 1636.76 –

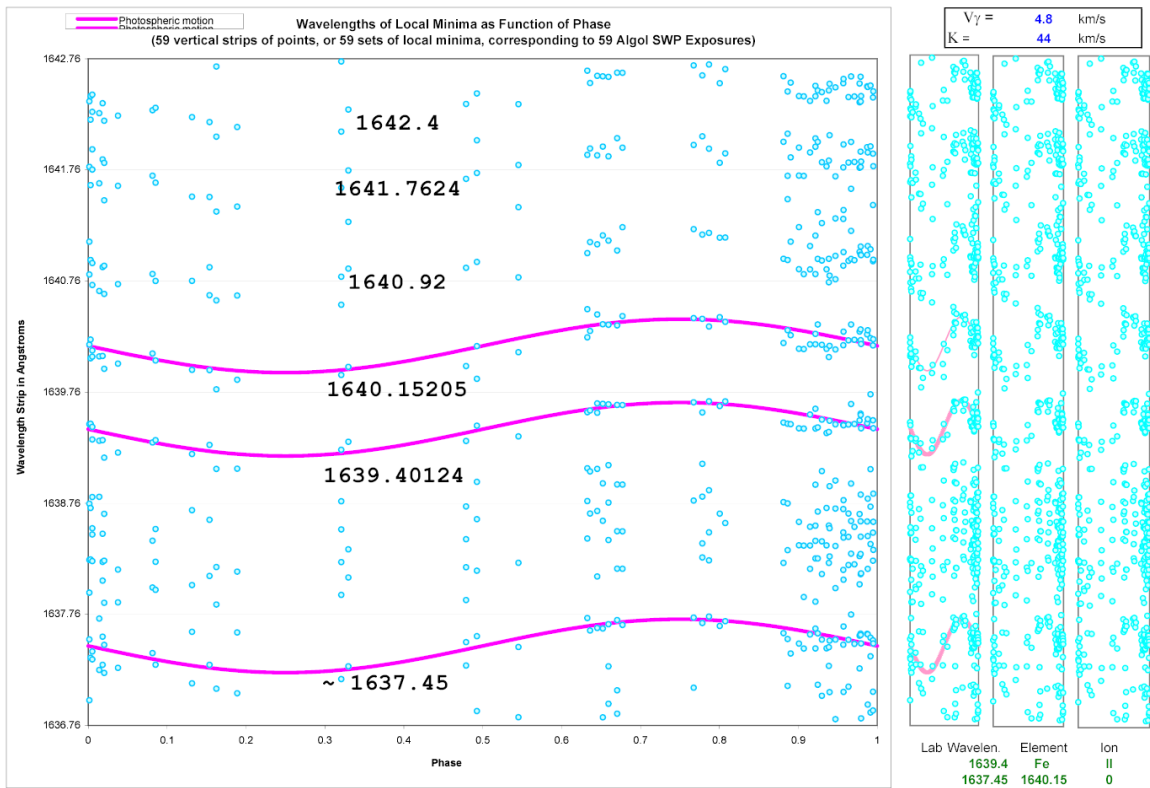


FIG. 4.3.2.1. — *Wavelength of local minima as a function of phase.* The 59 vertical strips of points, or 59 sets of local minima, correspond to the 59 Algol IUE SWP exposures.

1642.76 Å. The three strips on the right are duplicates of the left-hand plot, but compressed and periodically reproduced so as to assist the eye in detecting patterns. A variety of sinusoidal patterns are easily seen.

These patterns represent Doppler shifts associated with the most fundamental motions of the gases producing the absorptions, for instance (1) the photospheric motion of Algol A relative to the center of mass of the Algol A-B system, and (2) the motion of the center of mass of the Algol system relative to the Sun. The factors leading to the scatter in the data (and broadening of the spectral lines) include the rotation of Algol A, the revolution of the Algol A-B system about Algol C, and gas flow relative to the photosphere of Algol A. The effect of Algol C is addressed in the next section, and non-photospheric gas flow in all subsequent sections.

This first order analysis allows us to identify prominent spectral lines, and also refine previous measurements of the systematic velocity,  $V_0$ , and the semiamplitude,  $K_A$ , which represents the maximum radial velocity of Algol A relative to the center of mass. In the simple model described above, Algol A moves at radial velocity  $V(\varphi)$  with respect to the Sun, where  $\varphi$  is the orbital phase and:

$$V(\varphi) = V_0 - K_A \sin(2\pi\varphi) \quad (4.3.2.1)$$

Accordingly, the predicted absorption wavelengths can be expressed in terms of  $V_0$ ,  $K_A$ , and the vacuum wavelength,  $\lambda_0$ :

$$\lambda(\varphi) = \lambda_0 + \frac{1}{c} \lambda_0 V(\varphi) \quad (4.3.2.2)$$

Three of these lines are shown in FIG. 4.3.2.1 for the vacuum rest wavelengths indicated and values of  $K_A = 44$  km/s and  $V_0 = 4.8$  km/s. These values represent best fits



to our data, and we include them in Table 9 and Table 1, respectively, of Appendix A as a contribution from this work.

The process of identifying spectral lines is illustrated for the spectral range of 1636.76 – 1642.76 Å. The corresponding smooth spectra are shown in FIG. 4.3.2.2 for phase 0.0015 corresponding to one of the 59 SWP exposures. Compressed plots, such as those shown on the right side of FIG. 4.3.2.1 are used to identify strong photospheric features. The sinusoidal lines of FIG. 4.3.2.1 (left figure) are then interactively adjusted by varying the rest wavelength until a best fit to the data points is achieved. This method has in some cases allowed us to predict the wavelength of a line to within 0.001 Å even before we have identified it.

In the spectrum of FIG. 4.3.2.2 the local minima (hollow triangles) correspond to the first vertical strip of points, at phase 0.0015, in FIG. 4.3.2.1. Our program automatically outputs 59 such plots, each containing a set of local minima. This

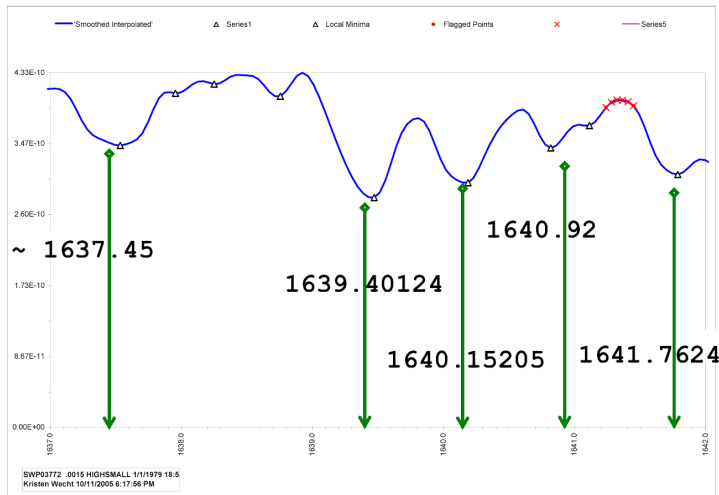


FIG. 4.3.2.2. —Rest wavelengths identified with the interactive program we developed. Fe II 1639.40124 and Fe II 1640.15205 are the strongest. Hollow triangles indicate the local minima. The arrows locate the positions of the lab vacuum wavelengths of the identified lines.

collection of 59 plots enables us to select the strongest lines, at a glance, in the wavelength range of interest. The strongest lines are the ones we want to measure since there will be less effects from blending and less scatter in the measurements.

Fe II  $\lambda\lambda$ 1639.40124,

1640.15205 are consistently the strongest across the 59 exposures in this wavelength range. The 59 sets of minima correspond to the 59 vertical strips of points that are automatically plotted against phase in FIG 4.3.2.1.

### 4.3.3. *Correction for Influence of Algol C*

The binary motions of Algol A and B are complicated by the presence of a third component, Algol C. Since the Algol A, B, and C masses are  $3.7M_{\odot}$ ,  $0.81M_{\odot}$ , and  $1.6M_{\odot}$ , respectively, none of the components are sufficiently small to justify ignoring their effect on the others. However, an approximate solution is suggested by the small separation of A and B compared to the distance from either of those to Algol C. The A-B system is characterized by separation  $14 R_{\odot}$  (Richards et al. 2003) and orbital period 2.86731077 days (Gillet et al. 1989), and the AB-C system has separation 2.67 AU (Pan et al. 1993) and orbital period 680.08 days. (Hill et al. 1971)

Our goal here is to correct the radial velocities of Algol A to account for the presence of Algol C. We accomplish this by treating the three stars as point masses. The motion of Algol A and B about their common center of mass is taken to be independent of Algol C. Algol C is assumed to influence Algol A and B equally; hence, motion involving Algol C is treated as a two-body problem, where Algol A and B are replaced by a fictitious mass equal to the sum of the A and B masses located at the A-B center of mass. Hence, the three-body problem is divided into two, two-body problems and the radial velocity of Algol A is given by:

$$V_{A: \odot} = V_o + V_{A-B:AB-C} + V_{A:A-B} \quad (4.3.3.1)$$

where we use the following notation:

The center of mass (c.m.) of A with respect to the sun  $\equiv A: \odot$ .

The c.m. of AB-C with respect to the sun  $\equiv AB-C: \odot \equiv V_0$

The c.m. of A-B with respect to the c.m. AB-C  $\equiv A-B:AB-C$

The c.m. of A with respect to the c.m. of A-B  $\equiv A:A-B$

Although the trajectories of binary star components can be determined analytically, no one has succeeded in developing an analytical expression for the time dependences of the coordinates. Hence, this must be solved numerically.

As described in Section 2.2, the true orbit is characterized by semimajor axis  $a$  and eccentricity,  $e$ . The position of one binary component relative to the other is identified by the two time-dependent quantities, separation  $r$  and true anomaly (angle)  $\theta$ , as shown in FIG. 4.3.3.1.  $r(\theta)$  traces the well known elliptical shape, where

$$r(\theta) = \frac{a(1 - e^2)}{1 + e \cos \theta} \quad (4.3.3.2)$$

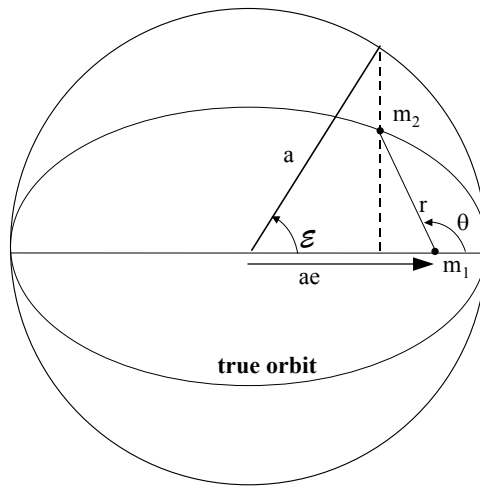


FIG. 4.3.3.1 – *Elliptical Geometry (Source: original work)*

The time dependence of the true anomaly can be calculated in principle from the following equation:

$$t(\theta) - T = \frac{P(1 - e^2)^{3/2}}{2\pi} \int_0^\theta \frac{d\theta'}{(1 + e \cos \theta')^2} \quad (4.3.3.3)$$

where  $T$  is the time of periastron passage (time when  $\theta = 0$ , when the components are closest) and  $P$  is the period.

This equation was reformulated by Kepler so that it could be written

$$\mathcal{E} - e \sin \mathcal{E} = \mathcal{M} \quad (4.3.3.4)$$

(See, for example, Escobal, 1976)

The mean anomaly,  $\mathcal{M}$ , is proportional to time (Eq. 4.3.3.5), and the eccentric anomaly,  $\mathcal{E}$ , is related to the true anomaly (Eq. 4.3.3.6).

$$\mathcal{M} = \left( \frac{2\pi}{P} \right) (t - T) \quad (4.3.3.5)$$

$$\tan \frac{\mathcal{E}}{2} = \left[ \frac{1 - e}{1 + e} \right]^{1/2} \tan \theta / 2 \quad (4.3.3.6)$$

A geometric interpretation of  $\mathcal{E}$  is provided in FIG. 4.3.3.1

Since  $\mathcal{E}$  cannot be determined analytically, we apply the Newton-Raphson iterative procedure (Hilditch 2001, p. 38), according to which a solution of  $f(x) = 0$  is given by

$$x_n = x_{n-1} - \frac{f(x_{n-1})}{f'(x_{n-1})} \quad (4.3.3.7)$$

When applied to Kepler's equation, we construct

$$f(\mathcal{E}) = \mathcal{E} - e \sin \mathcal{E} - \frac{2\pi}{P}(t - T) \quad (4.3.3.8)$$

Taking the derivative with respect to  $\mathcal{E}$  we have

$$f'(\mathcal{E}) = 1 - e \cos \mathcal{E} \quad (4.3.3.9)$$

Substituting into the Newton-Raphson iterative solution (Molnar and Mutel 1998), we have

$$\mathcal{E}_n = \mathcal{E}_{n-1} - \frac{f(\mathcal{E}_{n-1})}{f'(\mathcal{E}_{n-1})} \quad (4.3.3.10)$$

$$\mathcal{E}_n = \mathcal{E}_{n-1} - \frac{\mathcal{E}_{n-1} - e \sin \mathcal{E}_{n-1} - \frac{2\pi}{P}(t - T)}{1 - e \cos \mathcal{E}_{n-1}} \quad (4.3.3.11)$$

The iterative solutions of Eq. 4.3.3.11 are calculated separately for the A-B and AB-C motions, yielding solutions  $\mathcal{E}_{A-B}$  and  $\mathcal{E}_{AB-C}$  which satisfy

$$\mathcal{E}_{A-B} - e_{A-B} \sin \mathcal{E}_{A-B} = \mathcal{M}_{A-B} \quad (4.3.3.12)$$

and

$$\mathcal{E}_{AB-C} - e_{AB-C} \sin \mathcal{E}_{AB-C} = \mathcal{M}_{AB-C} \quad (4.3.3.13)$$

where

$$\mathcal{M}_{A-B} = 2\pi \frac{(t - T_{A-B})}{P_{A-B}} \quad (4.3.3.14)$$

$$\mathcal{M}_{AB-C} = 2\pi \frac{(t - T_{AB-C})}{P_{AB-C}} \quad (4.3.3.15)$$

and  $e_{x-y}$  is the eccentricity and  $T_{x-y}$  is the period of the x-y pair where x-y is either A-B or AB-C.

These results are used to calculate the true anomalies (in radians),  $\theta_{A-B}$  and  $\theta_{AB-C}$ , for the A-B and AB-C systems, respectively

$$\theta_{A-B} = 2 \arctan \left[ \sqrt{\frac{1+e_{A-B}}{1-e_{A-B}}} \tan \frac{\mathcal{E}_{A-B}}{2} \right], \quad (4.3.3.16)$$

$$\theta_{AB-C} = 2 \arctan \left[ \sqrt{\frac{1+e_{AB-C}}{1-e_{AB-C}}} \tan \frac{\mathcal{E}_{AB-C}}{2} \right]. \quad (4.3.3.17)$$

The computation of radial velocities requires the inclusion of geometrical factors, as shown in FIG. 2.2.2. Hence, the radial velocity of the A-B system's center of mass with respect to AB-C's center of mass,  $V_{AB:AB-C}$ , is then given by

$$V_{AB:AB-C} = K_{AB-C} \{e_{AB-C} \cos \omega_{AB-C} + \cos(\theta_{AB-C} + \omega_{A-B})\} \quad (4.3.3.18)$$

The radial velocities of Algol A, B and C with respect to the sun are given respectively by

$$V_{A:\odot} = V_0 + V_{AB:AB-C} + K_A \{e_{A-B} \cos \omega_{A-B} + \cos(\theta_{A-B} + \omega_{A-B})\} \quad (4.3.3.19)$$

$$V_{B:\odot} = V_0 + V_{AB:AB-C} + K_b \{e_{A-B} \cos(\omega_{A-B} + \pi) + \cos(\theta_{A-B} + \omega_{A-B} + \pi)\} \quad (4.3.3.20)$$

and

$$V_{C:\odot} = V_0 + K_C \{e_{AB-C} \cos(\omega_{AB-C} + \pi) + \cos(\theta_{AB-C} + \omega_{AB-C} + \pi)\} \quad (4.3.3.21)$$

The phase of the inner binary, Algol A-B, is calculated using

$$\phi_{A-B} = \left| INT \left[ \frac{(t - t_{pr.min A-B})}{P_{A-B}} \right] - \frac{(t - t_{pr.min A-B})}{P_{A-B}} \right| \quad (4.3.3.22)$$

where  $t_{pr.min A-B}$  is the time of primary minimum for the eclipsing pair.

In a similar manner the phase of the outer binary, the AB-C system, is calculated using

$$\phi_{AB-C} = ABS \left| INT \left[ \frac{(t - t_{AB-C})}{P_{AB-C}} \right] - \frac{(t - T_{AB-C})}{P_{AB-C}} \right| \quad (4.3.3.23)$$

We wrote a program in VBA that iteratively computes the predicted radial velocity of the Algol AB center of mass (Eq. 4.3.3.18) and the predicted radial velocity of Algol A (Eq. 4.3.3.19) as functions of HJD and phase. In order to test the program and refine input parameters, we selected a “best” set of starting parameters, provided in Table 4.3.3.1, and compared our predictions for the radial velocities of Algol A with the results of a study by Hill, et al. (1971). The Hill study used 95 spectroscopic observations of the Algol system, performed over a period of about four years from August 1937 to February 1941, to estimate the radial velocities.

Our calculated Algol A radial velocities as a function of Algol A-B phase are shown in FIG. 4.3.3.2 along with the measured values of Hill. The same results are plotted with respect to the Algol AB-C phase in FIG. 4.3.3.3. The sinusoidal pattern so apparent in both curves on FIG. 4.3.3.2 is due to the nearly circular motion of A about B. The jagged appearance is a consequence of the fact that many points with similar phases actually correspond to times associated with different epochs. Hence, neighboring points may be separated by significant time intervals, where Algol C is imparting a very

different radial velocity. The phase shift between the computed and observed velocity curves seen in both figures is a result of a variation in the period of the A-B system, possibly caused by system activity.

TABLE 4.3.3.1 – INITIAL ALGOL PROPERTIES ADOPTED FOR THIS COMPARISON

Description of Property	Property Symbol	Initial Input Value	Units
Systematic Velocity (km/s) – Should always refer to the entire known system, ie., velocity of Algol AB-C's CM wrt our Sun (Gillet et al. 1989 p.228)	$V_o$	4	km/s
Period of A-B system (days) (Gillet et al. 1989 p.221)	$P_{A-B}$	2.86731077	Days
Eccentricity of A-B system (literature ranges between 0.00 and 0.015)	$e_{A-B}$	0.01	
Angle between line of nodes & periastron of A-B system (degrees) (Gillet et al. 1989 p.228)	$\omega_{A-B}$	163	degrees
Semi-amplitude of A wrt A-B system's CM (km/s) (Tompkin & Lambert 1978)	$K_A$	44	km/s
Semi-amplitude of B wrt A-B system's CM (km/s) (Tompkin & Lambert 1978)	$K_B$	201	km/s
Semi-amplitude of C wrt AB-C's CM (km/s) (Hill et al. 1971 p.450)	$K_C$	31.6	km/s
Time of Periastron passage of A-B system (days) - Time of maximum orbital velocity (Gillet et al. 1989 p.228)	$T_{A-B}$	2,445,639.2146	Days
Period of AB-C system (days) (Pan et al. 1993 p.L131)	$P_{AB-C}$	680.05	Days
Eccentricity of AB-C system (Pan et al. 1993 p.L131)	$e_{AB-C}$	0.225	
Angle between line of nodes & periastron of AB-C system (degrees) (Molnar & Mutel 1998 p.17 note that Pan et al. 1993 lists 310.29)	$\omega_{AB-C}$	130.29	degrees
Semi-amplitude of AB wrt AB-C system's CM (km/s) - Should follow the equality: $M_C/(M_A+M_B+M_C) = K_{ab-c}/K_c \sim .27$ (Hill et al. 1971 p.451)	$K_{AB-C}$	12	km/s
Time of Periastron passage of AB-C system (days) - Time of maximum orbital velocity (Pan et al. 1993 p.L131)	$T_{AB-C}$	2,446,931.4000	Days
Time of primary minimum of Algol A-B (days) (Gillet et al. 1989 p.221)	$t_{PRMIN\_A-B}$	2,445,641.5135	Days



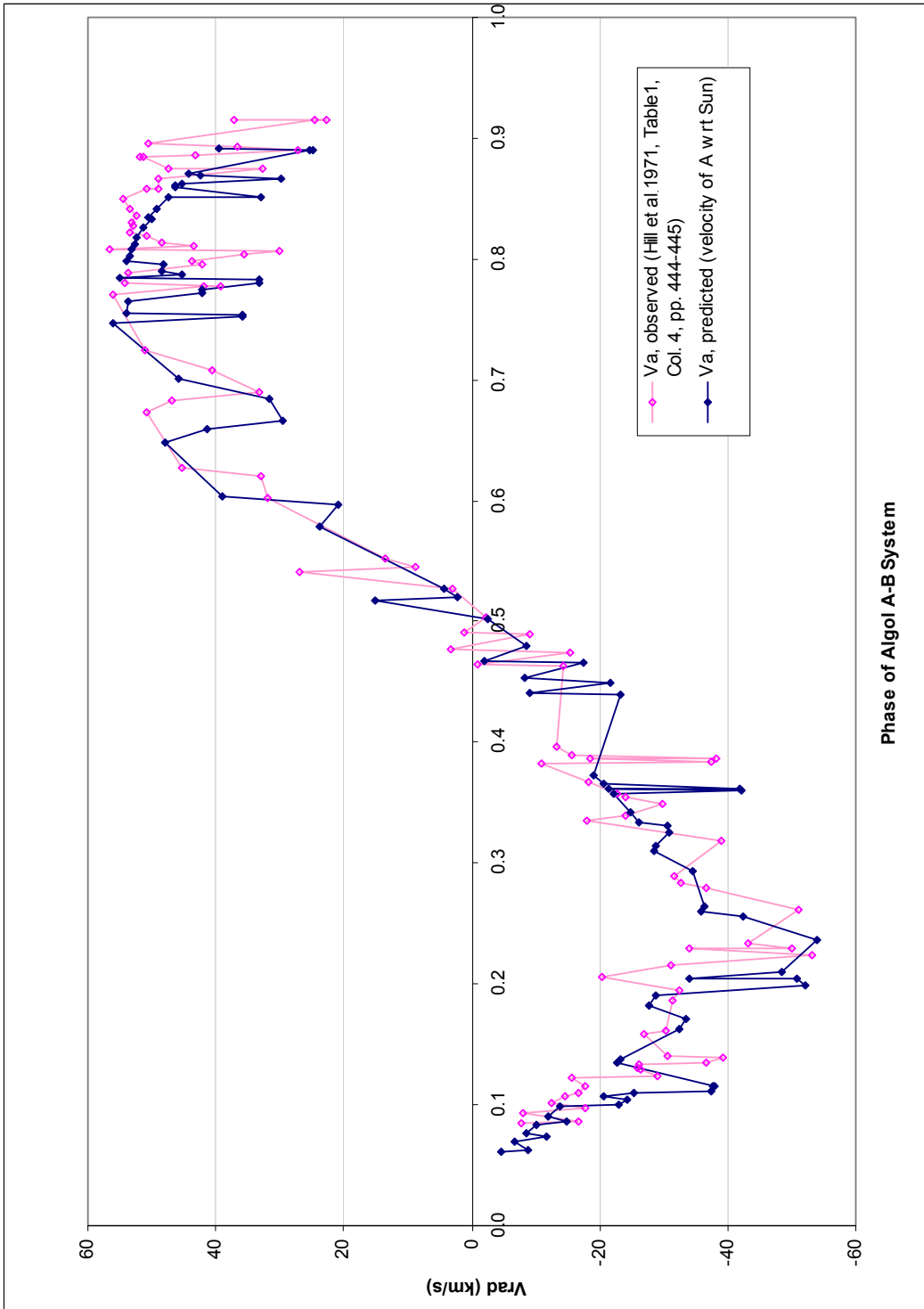


FIG. 4.3.3.2 – RADIAL VELOCITY COMPARISON of ALGOL A wrt the SUN VS. PHASE OF ALGOL A-B

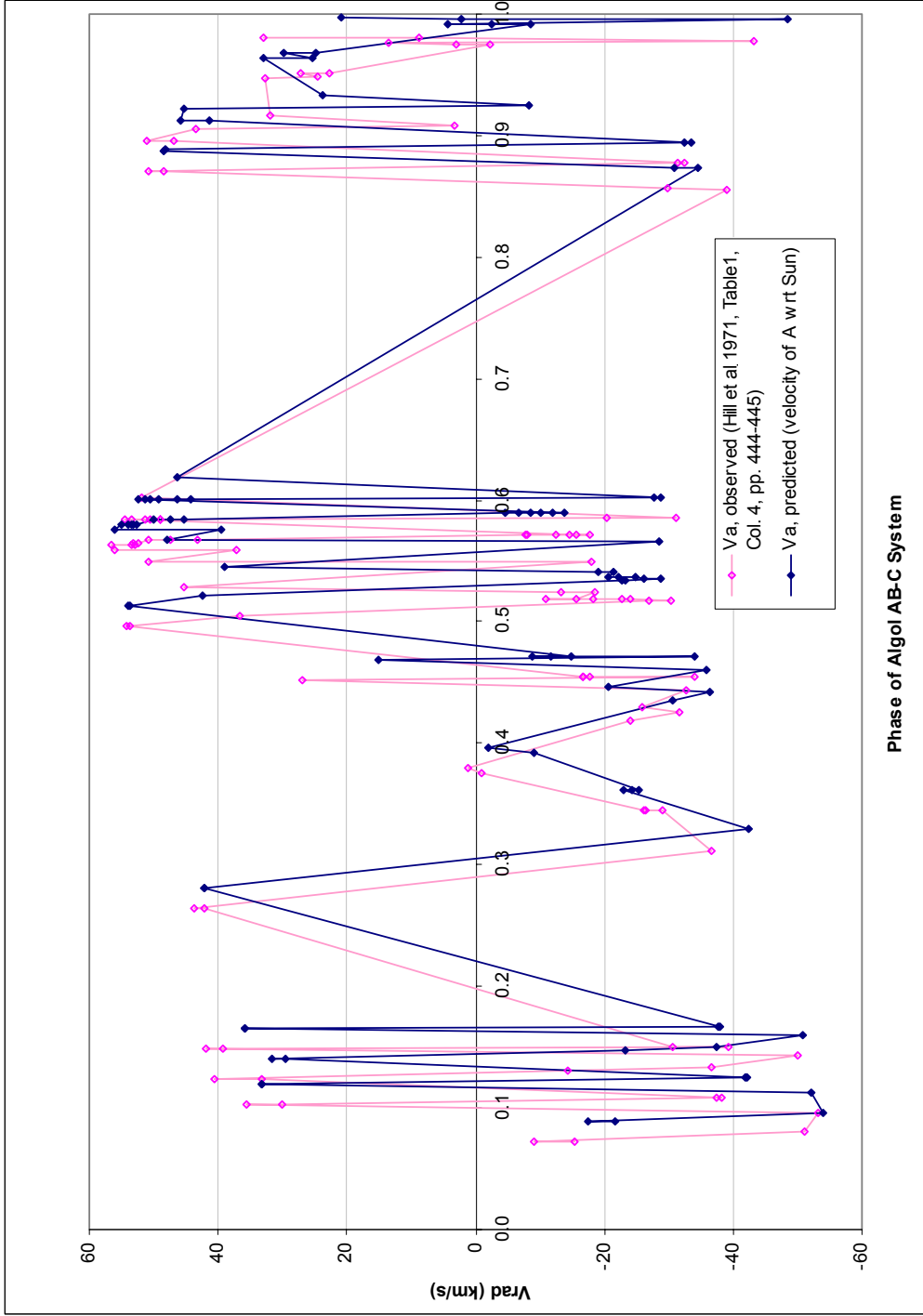


FIG. 4.3.3.3 - RADIAL VELOCITY COMPARISON OF ALGOL A wrt the SUN vs. PHASE of ALGOL AB-C

Ignoring the slight phase differences, the departures from a sinusoidal form for both the computed and observed results shown in FIG. 4.3.3.2 are mostly consequences of the motion of the AB center of mass due to the influence of Algol C. Since the Hill velocities were based upon measurements taken over many periods of the AB system (and we simulate their measurements using the same JDs), a given A-B phase can correspond to different positions of Algol C (different AB-C phases); hence, different AB center of mass contributions to the radial velocity of A. The similarities in the computed and measured velocity curves show clearly that our calculations are capturing the effects of Algol C.

Before applying this approach to the IUE UV data, we make two improvements to our method: a correction for the variation in the A-B line of apsides, and an adjustment of parameters. The line of apsides connects the periastron and apastron points (at opposite sides of the major axis of the ellipse) of the A-B system. The orientation of this line, defined by the longitude of periastron, is found to vary in time, rotating through  $360^\circ$  in about 32 years. (Hill, et al., 1971, Fig. 4, p. 454; also see Hilditch, (2001), Fig. 4.2, p. 134 for an illustration)

In order to incorporate the effect of the time dependence of the longitude of periastron, we follow the approach of Hill, et al. (1971) in assuming a linear dependence on time. Note that this also implies a time dependence for the time of periastron passage. With this adjustment to the computational program, we adjusted parameters to improve the fit to the Hill data. These new parameters are presented in Table 4.3.3.2 and the corresponding radial velocity results in FIG. 4.3.3.4. We estimated best fit parameters for

the linear time dependence of the longitude of periastron of  $a = 0.0308^\circ/\text{d}$  and  $b = 521.392^\circ$ , compared to Hill's parameters of  $a = 0.03079^\circ/\text{d}$  and  $b = 494.327^\circ$ , where

$$\omega(t)_{AB} = at + b$$

and  $t$  represents the heliocentric Julian date.

As a final test, we correct the Hill radial velocity measurements by removing the affect of Algol C. That is, we subtract the radial velocity of the AB center of mass (Eq. 4.3.3.18) from the measured radial velocities. These results, shown in FIG. 4.3.3.5, indicate that many of the non-sinusoidal features have been removed.

This is the process that we use to “correct” our IUE results for the presence of Algol C. However, we need to use a parameter set which is more appropriate to the period of the IUE observations. These parameters are provided in TABLE 4.3.3.3.

TABLE 4.3.3.2 – FINAL ALGOL PROPERTIES ADOPTED FOR THIS COMPARISON

Description of Property	Property Symbol	Final Input Value	Units
Systematic Velocity (km/s) – Should always refer to the entire known system, ie., velocity of Algol AB-C's CM wrt our Sun	$V_o$	4.9	km/s
Period of A-B system (days) (Hill et al. 1971 p.444)	$P_{A-B}$	2.86730807	Days
Eccentricity of A-B system (Hill et al. 1971 p.451)	$e_{A-B}$	0.015	
Angle between line of nodes & periastron of A-B system (degrees) However, the best constant value was $359^\circ$ from trial#3 Research Vol. 10	$\omega_{A-B}$	(function of time)	degrees
Semi-amplitude of A wrt A-B system's CM (km/s) (Hill et al. 1971 p.451)	$K_A$	44	km/s
Semi-amplitude of B wrt A-B system's CM (km/s) (Tompkin & Lambert 1978)	$K_B$	201	km/s
Semi-amplitude of C wrt AB-C's CM (km/s) (Hill et al. 1971 p.450)	$K_C$	31.6	km/s
Time of Periastron passage of A-B system (days) - Time of maximum orbital velocity (Hill et al. 1971 p.451)	$T_{A-B}$	2,428,482.7390	Days
Period of AB-C system (days) (Hill et al. 1971 p.444)	$P_{AB-C}$	680.08	Days
Eccentricity of AB-C system (Hill et al. 1971 p.450)	$e_{AB-C}$	0.23	
Angle between line of nodes & periastron of AB-C system (degrees)	$\omega_{AB-C}$	133	degrees
Semi-amplitude of AB wrt AB-C system's CM (km/s) - Should follow the equality: $M_C/(M_A+M_B+M_C) = K_{AB-C}/K_C \sim .27$ (Hill et al. 1971 p.451)	$K_{AB-C}$	12	km/s
Time of Periastron passage of AB-C system (days) - Time of maximum orbital velocity [calculated from 1952.05 (= 2,434,029.76) listed in Hill et al. 1971 p.451 then adjusted by eye]	$T_{AB-C}$	2,434,022.8500	Days
Time of primary minimum of Algol A-B (days) (Hill et al. 1971 p.444 & 450 which refers to Kopal et al. 1960)	$t_{PRMIN\_A-B}$	2,428,483.4560	Days
Slope of linear equation for $\omega_{A-B}(t)$ (degrees/day) (Hill's slope = .03079 degrees/day calculated from his estimate of $360^\circ$ per 32 years. See Fig. 4 of Hill et al. 1971 p.454)	$m_{PRMIN\_A-B}$	0.03080	degrees/day
y-intercept of linear equation for $\omega_{A-B}(t)$ (degrees) (Hill's y-intercept $\sim -494.327^\circ$ estimated from Fig. 4 of Hill et al. 1971 p.454)	$b_{\omega_{A-B}}$	-521.392	degrees

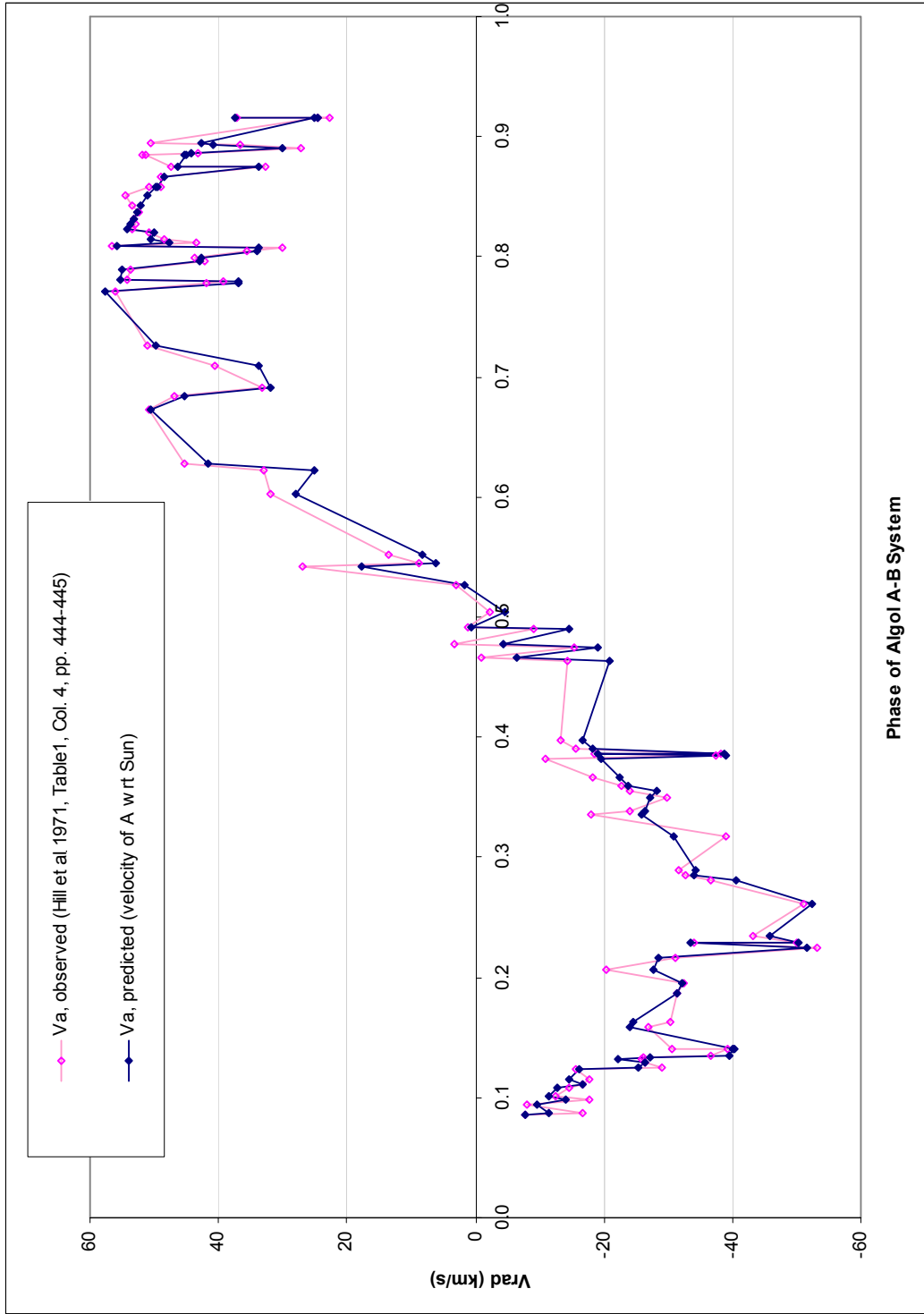


FIG. 4.3.3.4 - RADIAL VELOCITY COMPARISON of ALGOL A wrt the SUN vs. PHASE of ALGOL A-B for  $\omega = \omega(t)$

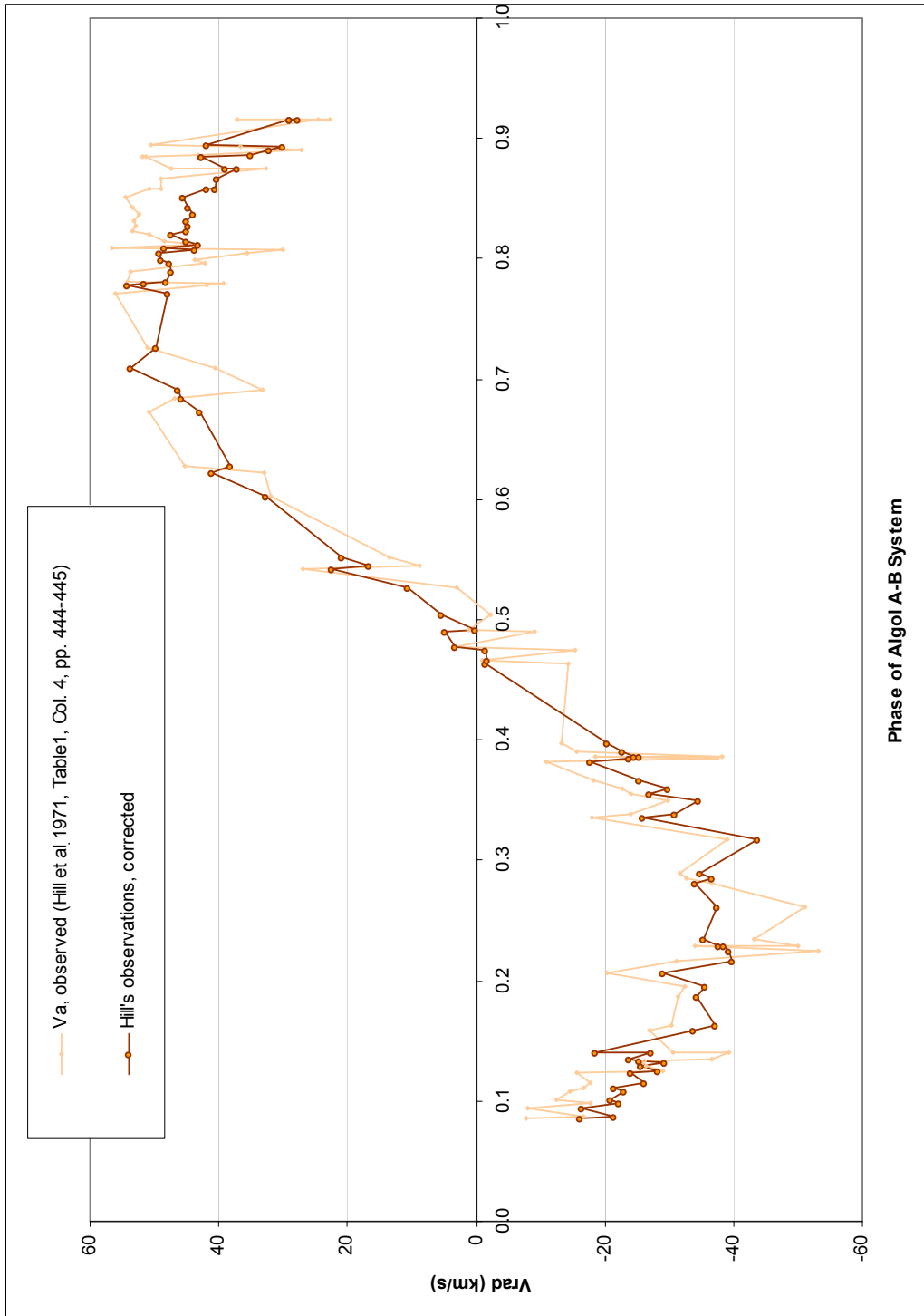


FIG. 4.3.3.5 – Hill's Observed RADIAL VELOCITY COMPARISON of ALGOL A wrt the SUN With Corrections Applied for ALGOL A-B for  $\omega = \omega(t)$

TABLE 4.3.3.3 – FINAL ALGOL PROPERTIES ADOPTED FOR IUE CORRECTIONS

Description of Property	Property Symbol	Final Input Value	Units
Systematic Velocity (km/s) – Should always refer to the entire known system, ie., velocity of Algol AB-C's CM wrt our Sun ( <a href="#">This work</a> )	$V_o$	4.8	km/s
Period of A-B system (days) ( <a href="#">Gillet et al. 1989 p.221</a> )	$P_{A-B}$	2.86731077	Days
Eccentricity of A-B system ( <a href="#">This work</a> )	$e_{A-B}$	0.001	
Semi-amplitude of A wrt A-B system's CM (km/s) ( <a href="#">Hill et al. 1971 p.451</a> )	$K_A$	44	km/s
Semi-amplitude of B wrt A-B system's CM (km/s) ( <a href="#">Tompkin &amp; Lambert 1978</a> )	$K_B$	201	km/s
Semi-amplitude of C wrt AB-C's CM (km/s) ( <a href="#">Hill et al. 1971 p.450</a> )	$K_C$	31.6	km/s
Time of Periastron passage of A-B system (days) - Time of maximum orbital velocity ( <a href="#">Gillet et al. 1989 p.228</a> )	$T_{A-B}$	2,445,639.2146	Days
Period of AB-C system (days) ( <a href="#">Hill et al. 1971 p.444</a> )	$P_{AB-C}$	680.08	Days
Eccentricity of AB-C system ( <a href="#">Pan et al. 1993 p.L131</a> )	$e_{AB-C}$	0.225	
Angle between line of nodes & periastron of AB-C system (degrees) ( <a href="#">Molnar &amp; Mutel 1998 p.17 note that Pan et al. 1993 lists 310.29</a> )	$\omega_{AB-C}$	130.29	degrees
Semi-amplitude of AB wrt AB-C system's CM (km/s) - Should follow the equality: $M_C/(M_A+M_B+M_C) = K_{AB-C}/K_C \sim .27$ ( <a href="#">Hill et al. 1971 p.451</a> )	$K_{AB-C}$	12	km/s
Time of Periastron passage of AB-C system (days) - Time of maximum orbital velocity ( <a href="#">Pan et al. 1993 p.L131</a> )	$T_{AB-C}$	2,446,931.4000	Days
Time of primary minimum of Algol A-B (days) ( <a href="#">Gillet et al. 1989 p.221</a> )	$t_{PRMIN\_A-B}$	2,445,641.5135	Days
Slope of linear equation for $\omega_{A-B}(t)$ (degrees/day) ( <a href="#">Hill's slope = .03079 degrees/day calculated from his estimate of 360° per 32 years. See Fig. 4 of Hill et al. 1971 p.454</a> )	$m_{PRMIN\_A-B}$	0.03080	degrees/day
y-intercept of linear equation for $\omega_{A-B}(t)$ (degrees) ( <a href="#">This work</a> )	$b_{\omega_{A-B}}$	-1,242.734	degrees



## 4.4 Determination of UV Light Curves

### 4.4.1 Method for Determining Continuum Flux

In order to estimate the continuum flux levels we first coplotted the raw and smoothed data in 50 Å intervals as illustrated by FIG. 4.4.1.1. Since the continuum flux is expected to vary only slightly over these intervals, the flux levels were estimated by drawing a “best” horizontal line by eye for each interval. Some degree of subjective

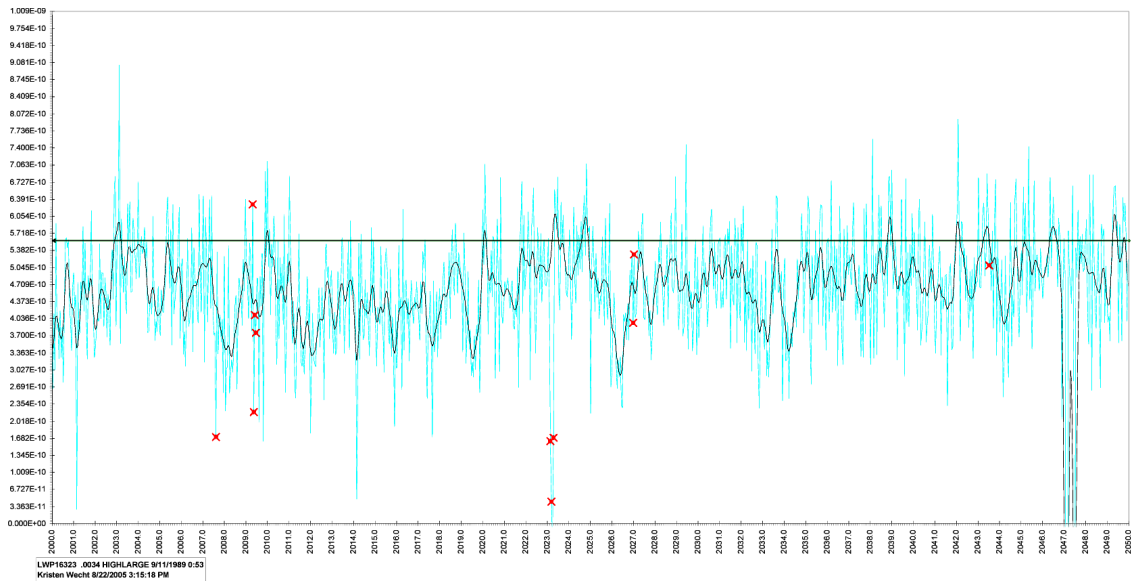


FIG. 4.4.1.1— Flux vs. wavelength in the interval 2000-2050 Å.  
LWP16323  $\phi = 0.003$  9/11/89 large aperture

decisions have to be made due to noise and other instrumental effects. Consistency in the determination of the continuum over all spectra is very important and was one determining factor in the final values obtained in each 50 Å interval. The flux level was then recorded in units of  $1 \times 10^{-10}$  ergs/cm<sup>2</sup>/s/Å. In FIG. 4.4.1.1 the level is

$5.58 \times 10^{-10}$  ergs/cm<sup>2</sup>/s/Å. The SWP and LWP/LWR continuum flux level estimates are reported as described in the following section, and used to determine the UV light curves, showing intensity as function of phase.

#### 4.4.2 *Continuum Flux and Light Curve Results*

FIGs. 4.4.2.1 and 4.4.2.2 show the wavelength dependence of the continuum flux for SWP and LWP/ LWR UV ranges, respectively. In both figures, a range of phases was selected corresponding to the 1989 epoch. Our complete set of continuum flux results are tabulated in Appendix D.2.

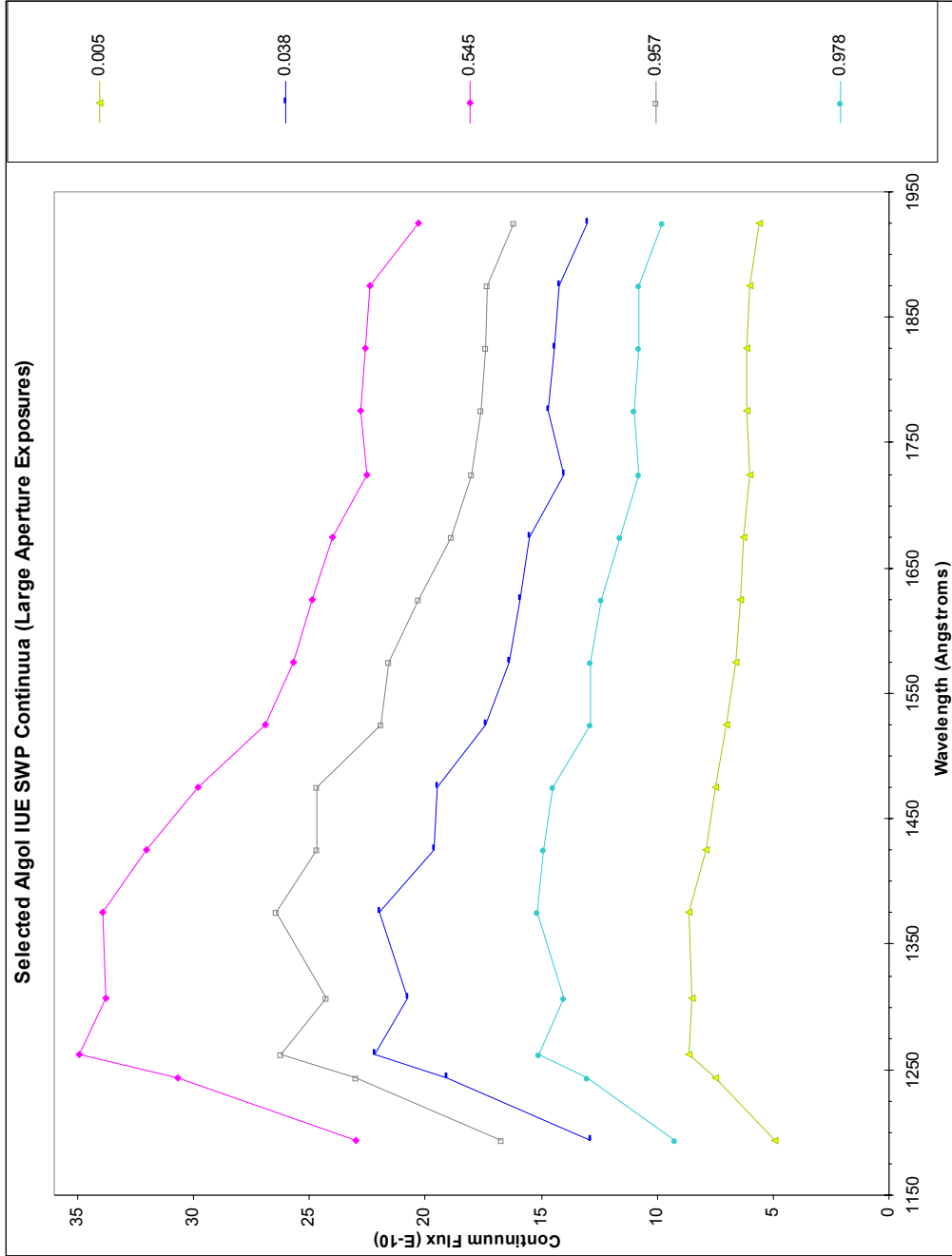


FIG. 4.4.2.1 – Selected Algol IUE SWP Continua (Large Aperture Exposures)

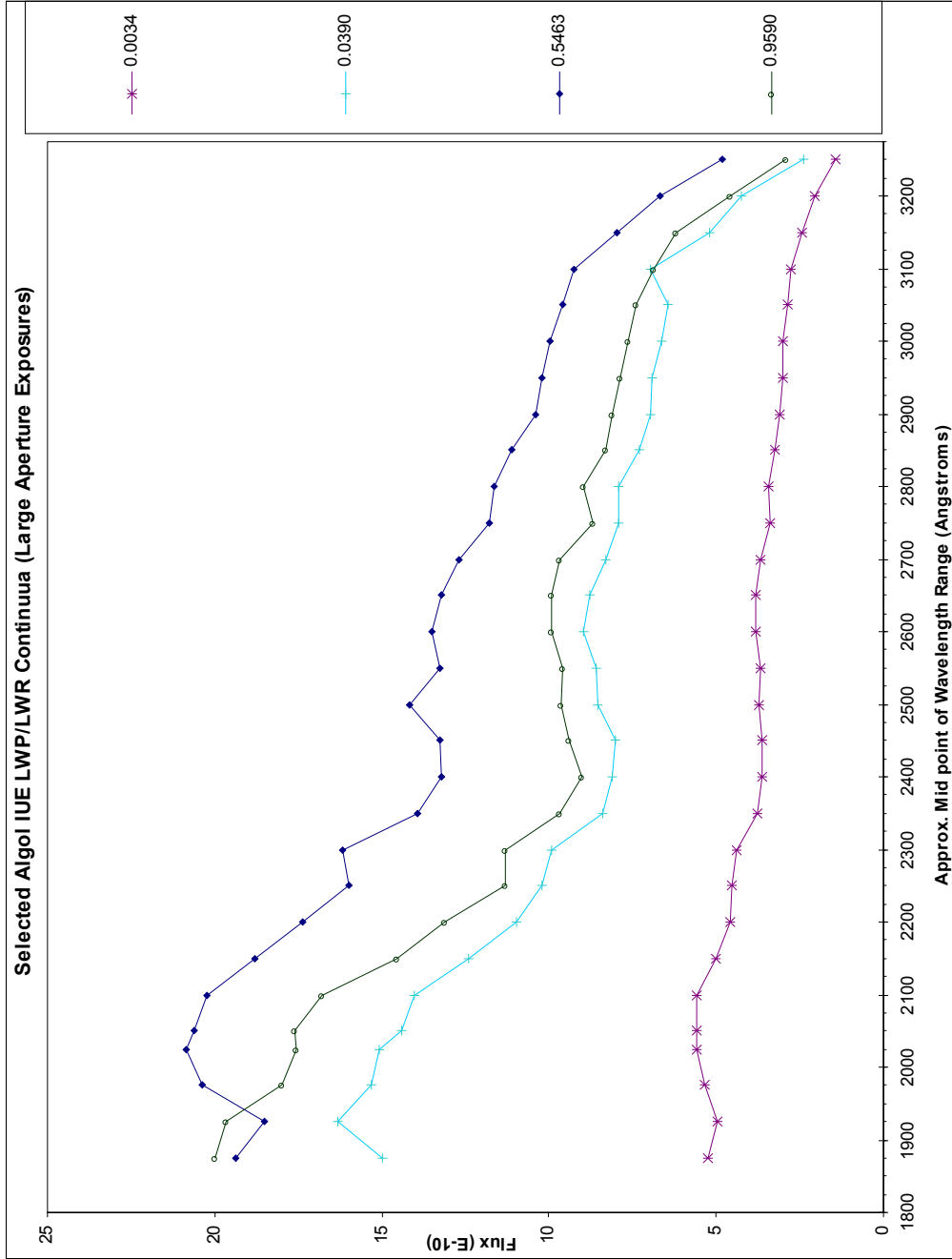


FIG. 4.4.2.2 – Selected Algot IUE LWP/LWR Continua (Large Aperture Exposures)

FIG. 4.4.2.3 compares two SWP continuum flux curves corresponding to about the same phase, but one during an epoch of high activity and the other of moderate activity.

The SWP and LWP/LWR continuum curves of FIGs. 4.4.2.1 and 4.4.2.2 indicate an overall decrease in flux with increasing wavelength beyond approximately 1350 Å. The peak emission for a 12,500 K B8 star should be located at about 2300 Å. Hence, although black-body dependencies contribute to the curves, other factors are more important.

The abrupt flux increase in the 1200 Å region is combination of instrumental effects since this is near the SWP wavelength limit and Lyman alpha absorption. We do not use data near the SWP or LWP/LWR wavelength limits due to such effects. The generally decreasing flux with increasing wavelength is due primarily to the instrumental response.

Most of the LWP/LWR flux curves show a broad absorption feature in the 2100 – 2500 Å spectral image. These broad features might be composed of two overlapping absorptions, in the ranges of 2200 – 2300 Å and 2350 – 2500 Å. The 2100 – 2500 Å range corresponds to 0.21 – 0.25  $\mu\text{m}$  or 4.8 – 4.0  $\mu\text{m}^{-1}$ .

This wavelength range is interesting in the context of interstellar extinction and scattering due to small particles. The average interstellar extinction curve has a significant “bump” centered at  $\sim 4.6 \mu\text{m}^{-1}$ , or 2175 Å, and we speculate that this might be related to our observed features. The origin of the feature is a source of continued study and controversy; however, various models include contributions from particles composed of silicon-carbon composites and graphite along with polycyclic aromatic hydrocarbons

(PAHs). These observations and models are discussed in Whittet (2003; Chapter 3). We will not pursue this interesting topic of interstellar grains further since it is outside the scope of this work.

FIGs. 4.4.2.1 and 4.4.2.2 both show expected phase dependencies. The flux is lowest near primary minima (near phases of 0.0 or 1.0). Among these curves the largest flux occurs at phase 0.55, and they should be slightly higher at a phase of around 0.6, for example, when the system is fully out of the secondary minimum. (See FIGs. 3.3.2.)

FIG. 4.4.2.3 shows a comparison of two epochs, where one shows evidence of greater activity. Notice the overall lower flux during the more active period.

FIGs. 4.4.2.4 and 4.4.2.5 represent SWP and LWP/LWR light curves, showing the phase dependencies of the flux, but presented in a 3-D perspective to cover many wavelength ranges. The curve closest to the “Algol Phase” axis represents the 3225 – 3275 Å continuum flux averages. Primary minimum is clearly seen, and secondary is weak but distinguishable in some curves. After normalization, the light curves in FIGs. 4.4.2.7 and 4.4.2.8 are replotted and stacked in FIGs. 4.4.2.6 and 4.4.2.7.

As expected, the depth of primary minimum decreases as the wavelength increases. The light curve of Algol at 3428 Å (Chen et al. 1977) is coplotted in FIG. 4.4.2.7 for comparison. From this comparison, we see that the light curves we extracted from the IUE data are consistent with the Copernicus satellite data.

A sample normalized SWP light curve, averaged over a 200 Å interval is plotted in FIG. 4.4.2.8, where different epochs are distinguished. Likewise, a sample normalized LWP/LWR light curve averaged over a 400 Å interval is plotted in FIG. 4.4.2.9. FIGs. 4.4.2.10 and 4.4.2.11 are the same, but focused on a narrow range of phases near primary

minimum. The final set of normalized light curves show several interesting features. In particular, the 1984 data is unusual in almost every spectral range, often distinctly different from all other epochs. For example, notice especially in FIG. 4.4.2.10 that the March 1984 feature during ingress at phase 0.9388 is significantly below the light curve appropriate to other epochs (1989 at phase 0.9397 for example). This depression in the continuum can be seen more clearly in the continuum flux comparison of FIG. 4.4.2.3.

Other features are recurring and appear in the same range of phases at a number of epochs; these include dips or bumps in the approach to eclipse. In particular, note the absorption feature at phase 0.89-0.90 in the 1750 – 1950 Å spectral range, shown enlarged in FIG. 4.4.2.10.

Other features will be examined as appropriate in the Discussion and Conclusions chapter.

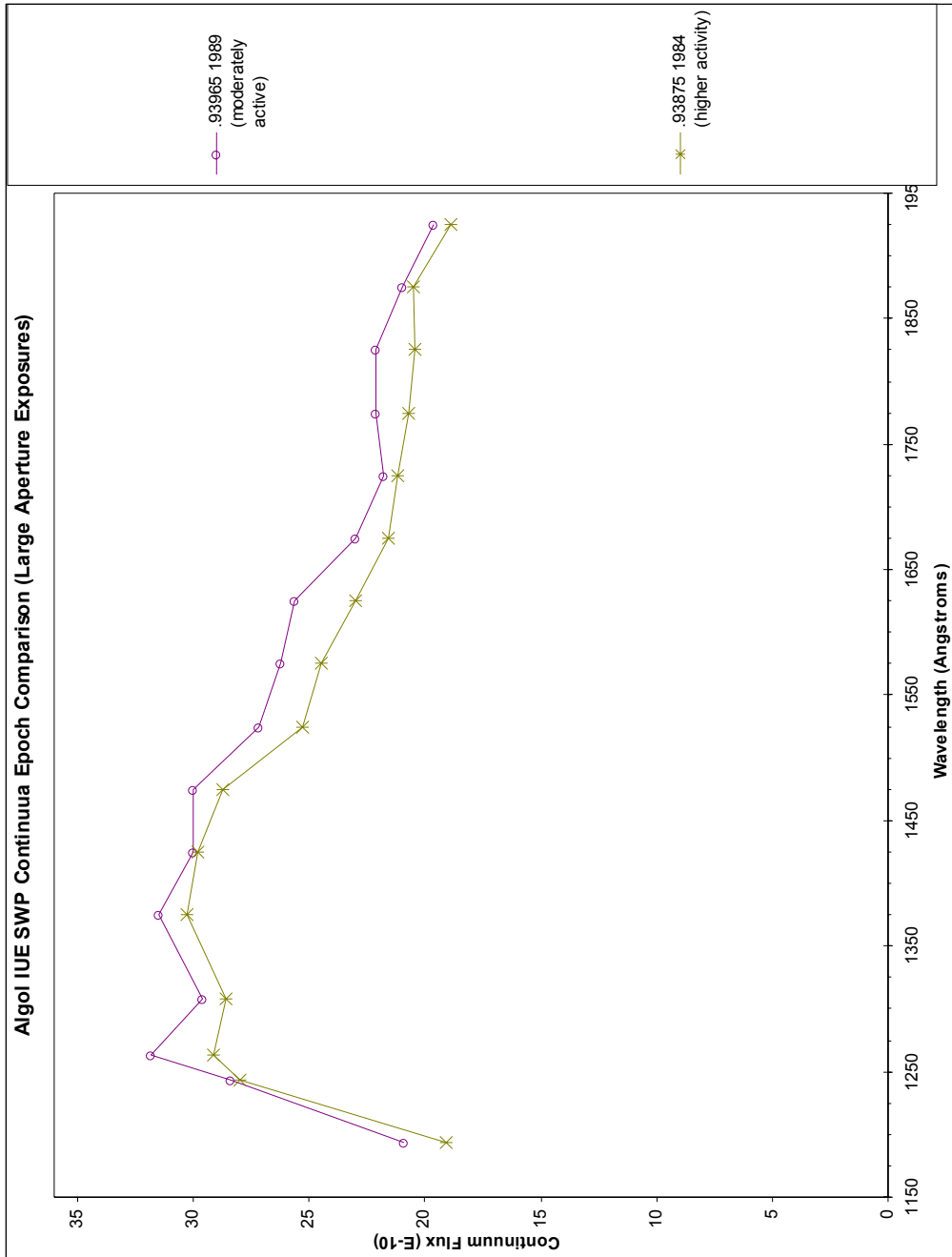


FIG. 4.4.2.3 – Algol IUE SWP Continuum Epoch Comparison (Large Aperture Exposures)



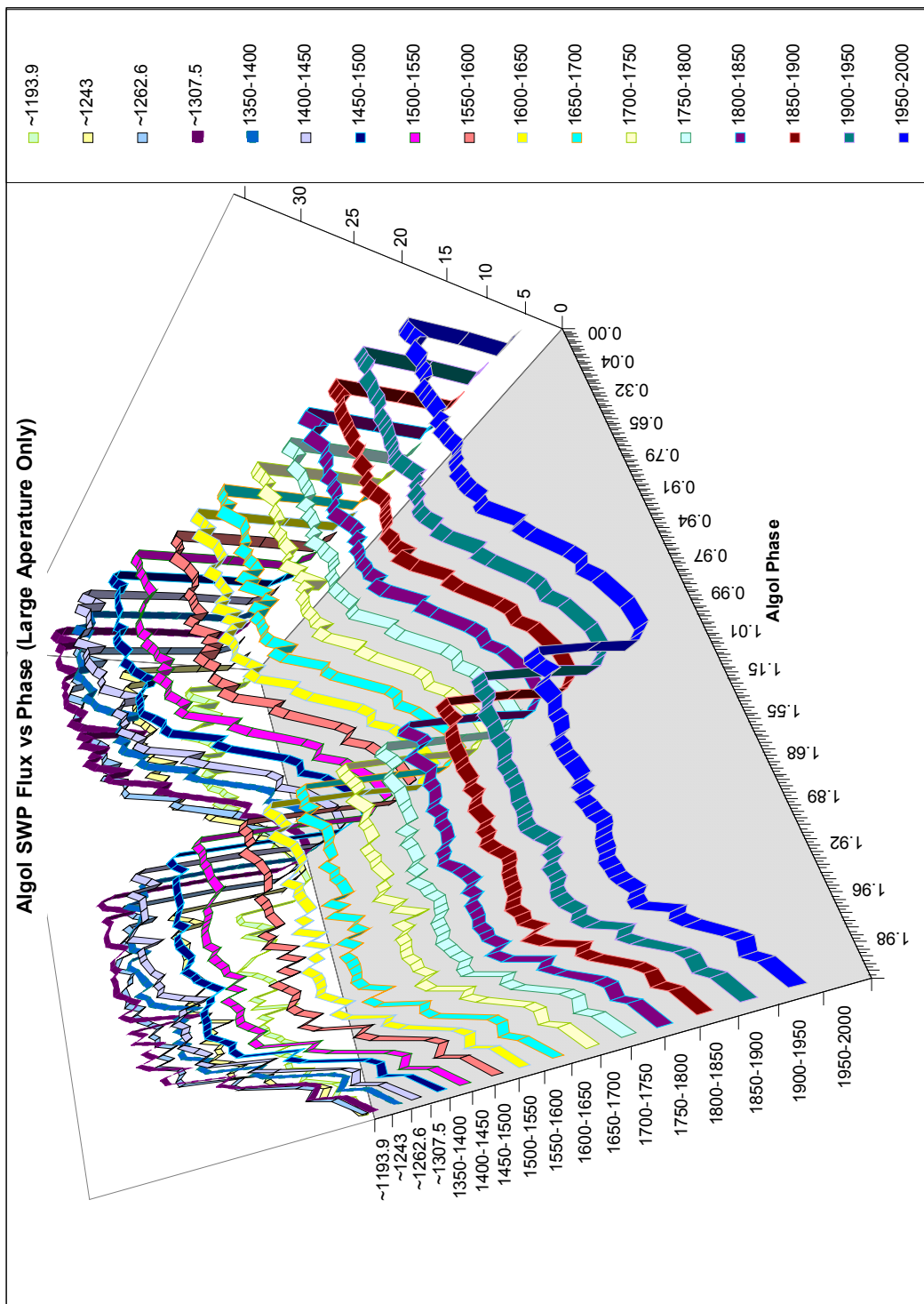


FIG. 4.4.2.4 – Algol SWP vs. Phase (Large Aperture Only)

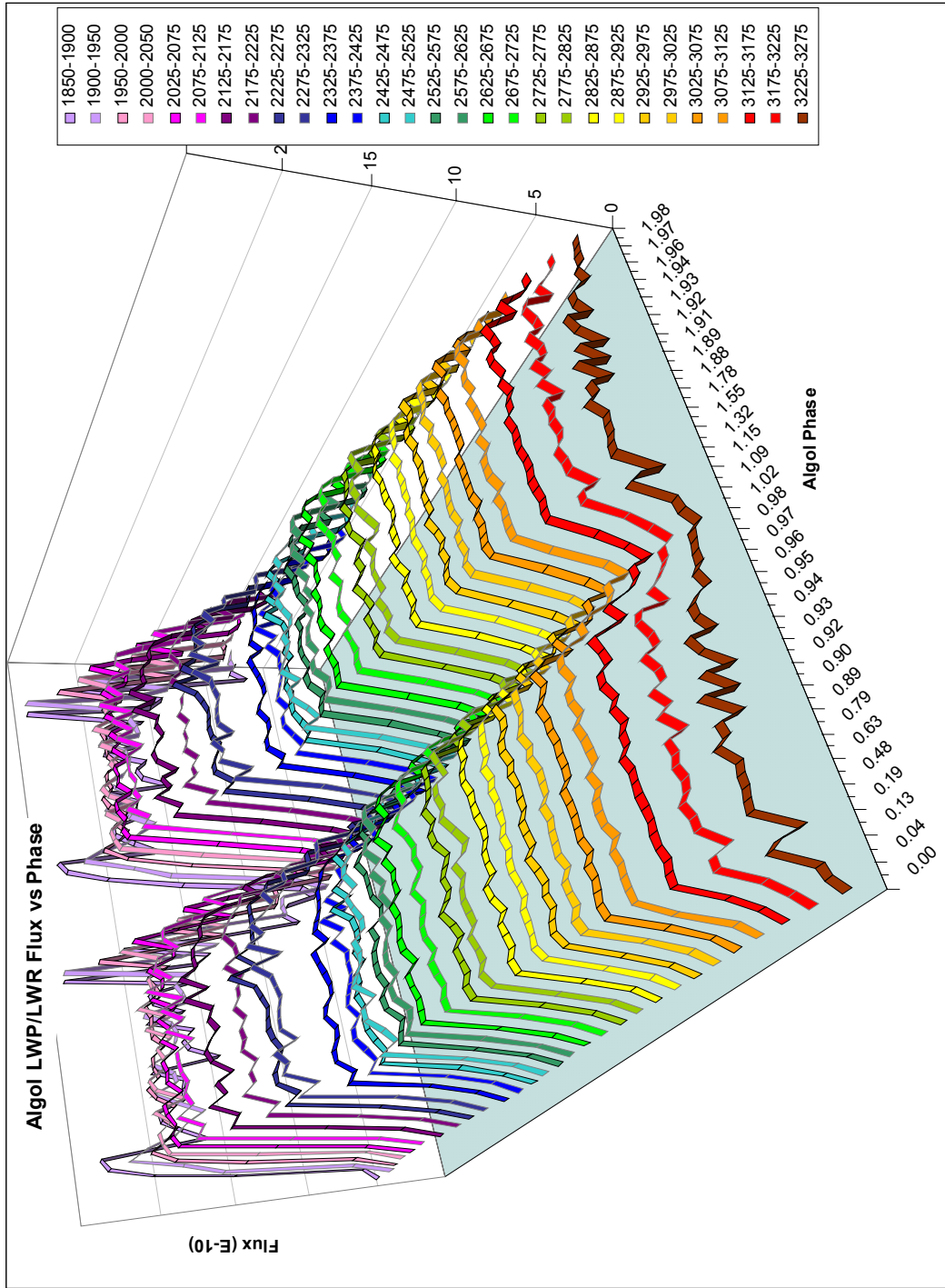


FIG. 4.4.2.5 – Algo LWP/LWR Flux vs. Phase

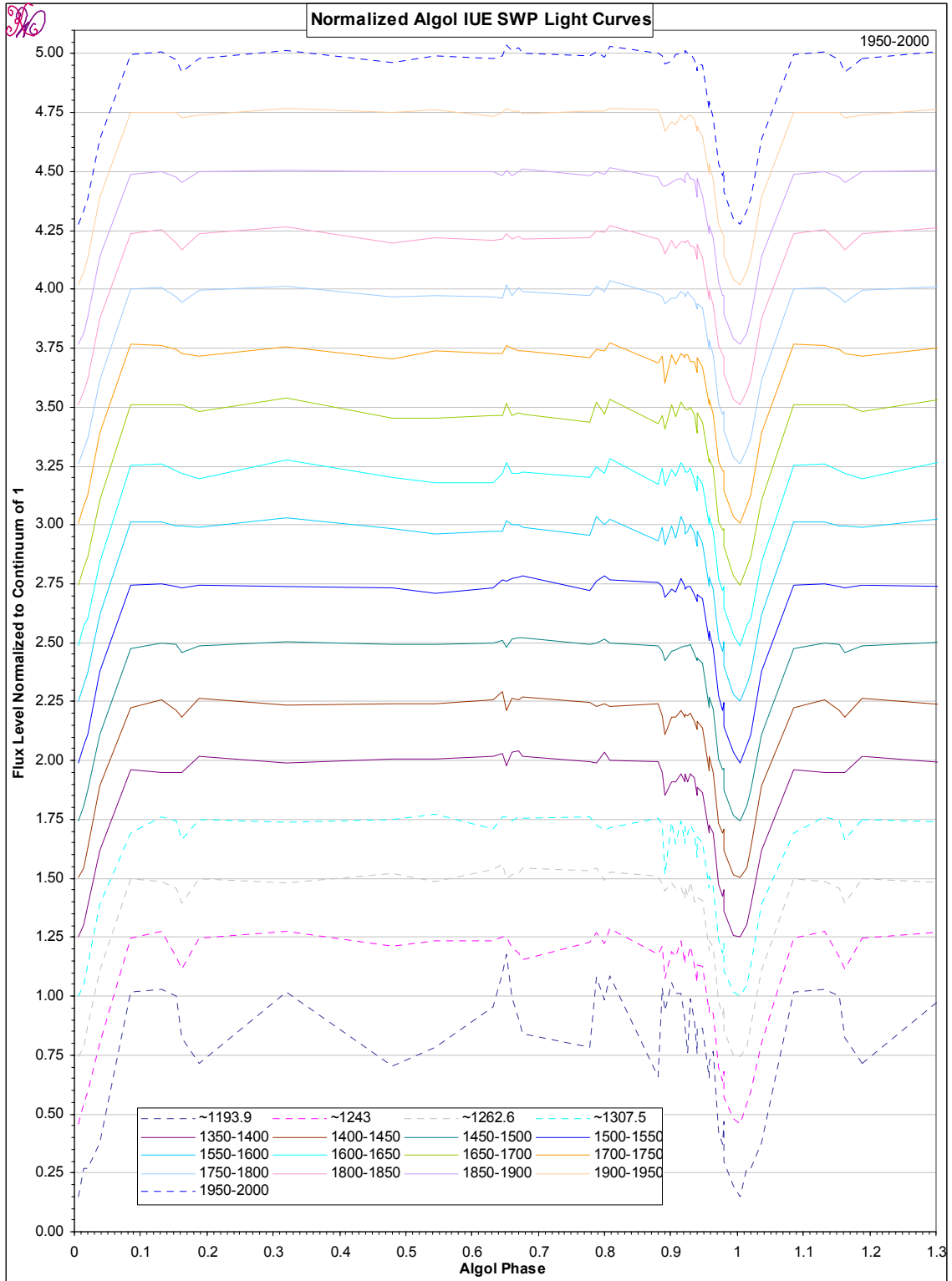


FIG. 4.4.2.6 – *NORMALIZED ALGOL IUE SWP LIGHT CURVES*. The curves are stacked by adding 0.25 to each successively.

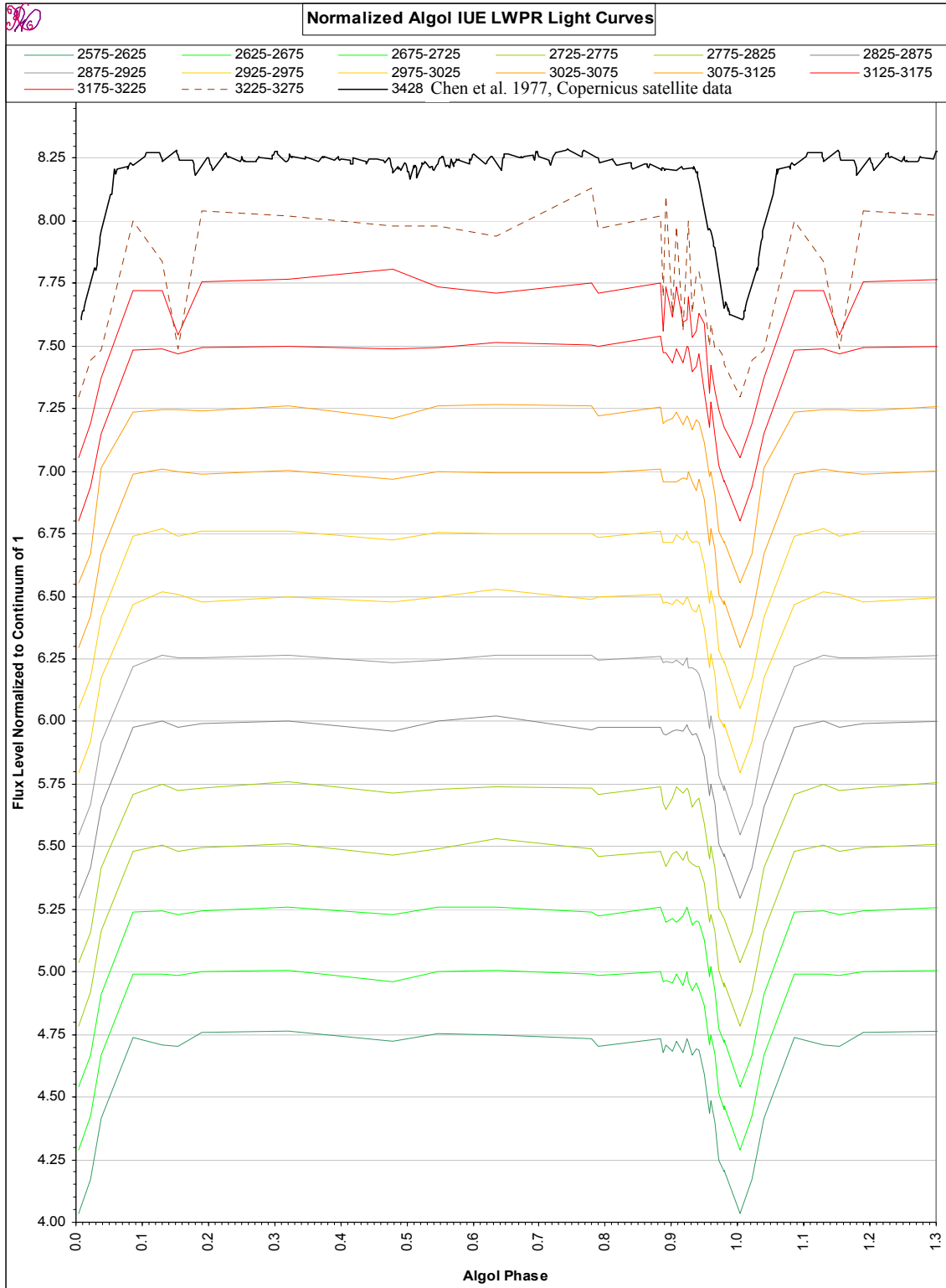


FIG. 4.4.2.7a – *NORMALIZED ALGOL IUE LWP/LWR LIGHT CURVES.* The curves are stacked by adding 0.25 to each successively.

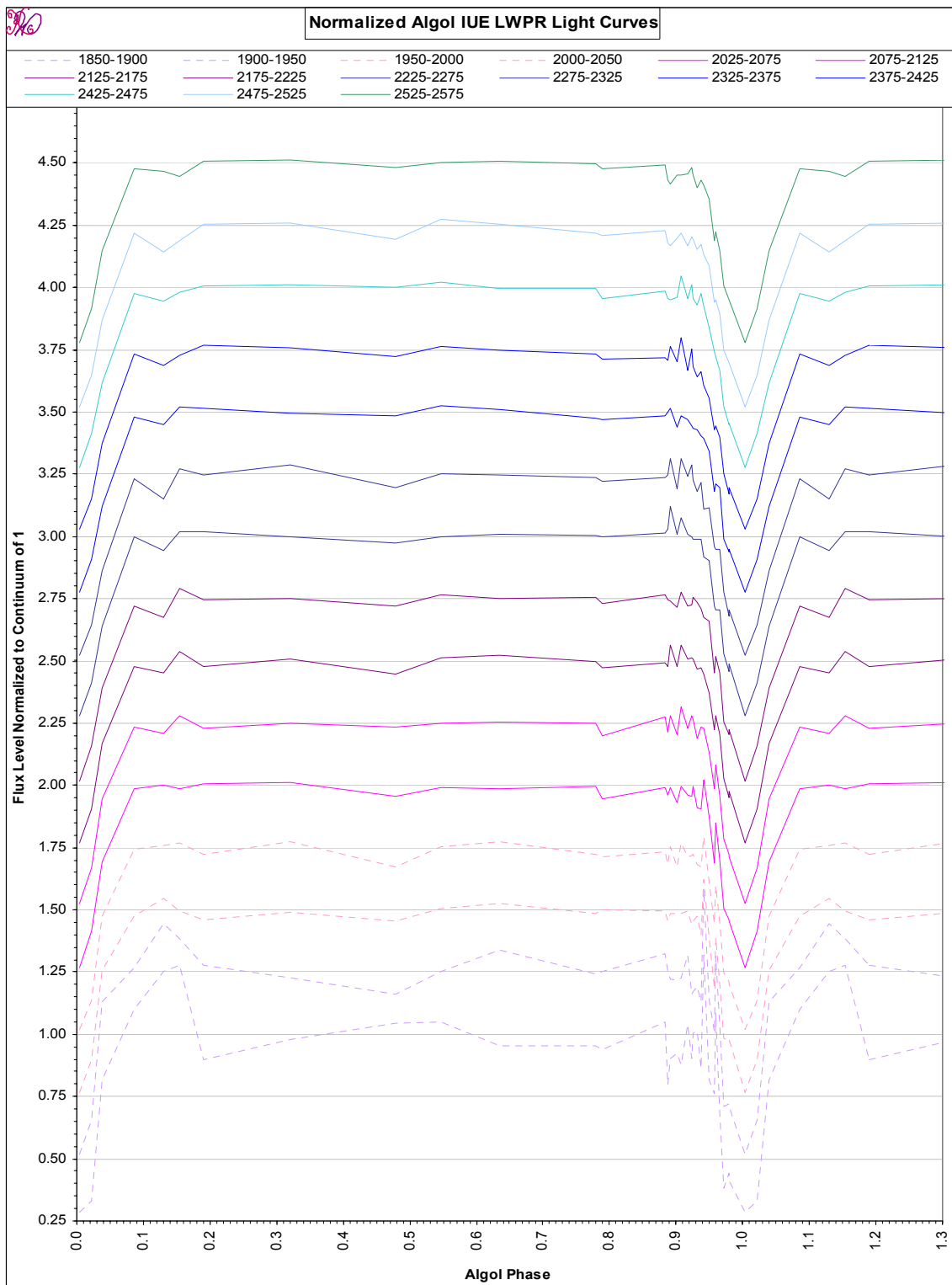


FIG. 4.4.2.7b – *NORMALIZED ALGOL IUE LWP/LWR LIGHT CURVES*

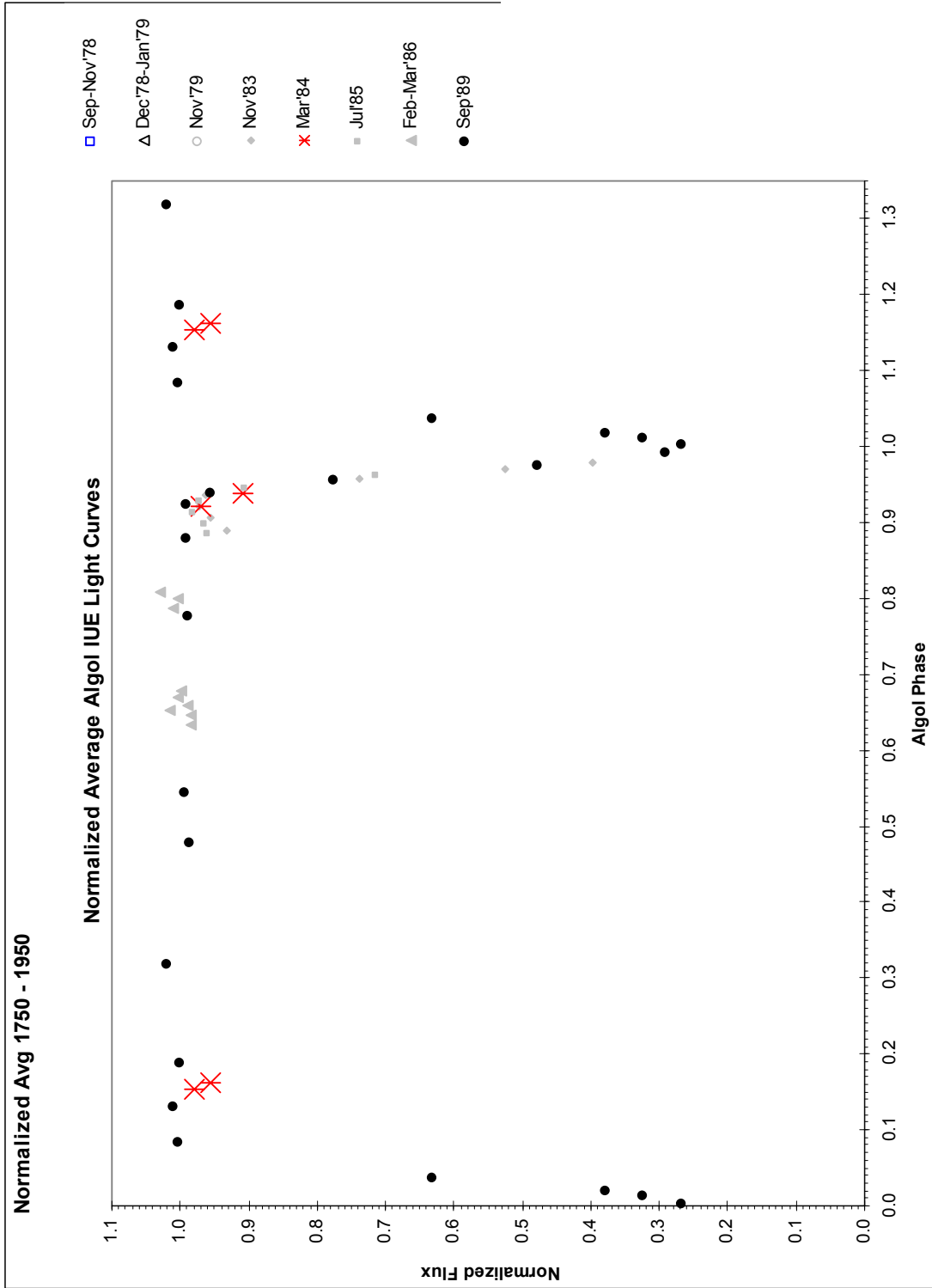


FIG. 4.4.2.8 – SWP Normalized Average Algol IUE Light Curves. 1550 - 1750 Å

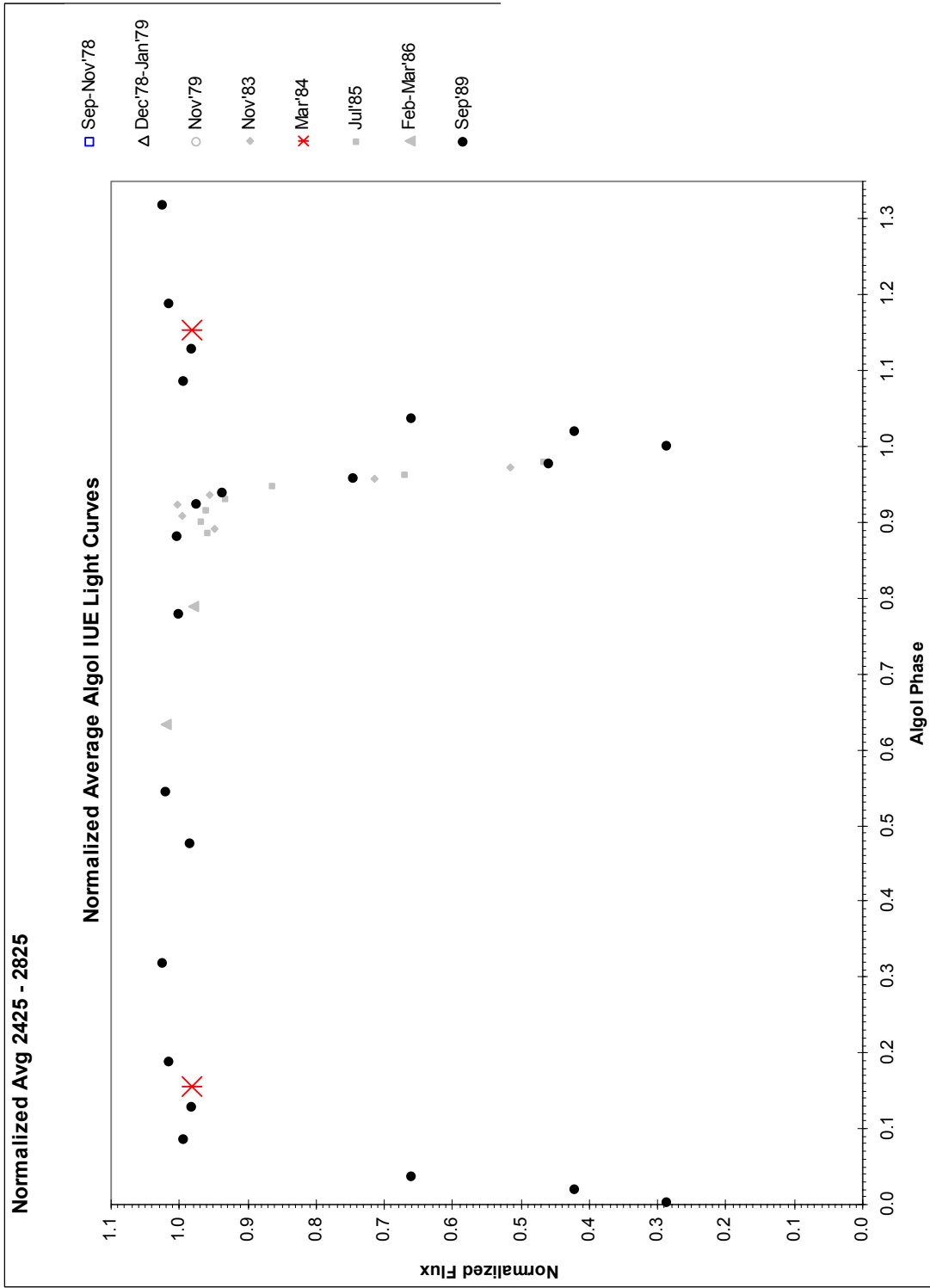


FIG. 4.4.2.9 – LWP/LWR Normalized Average Algol IUE Light Curves. 2425 - 2825 Å

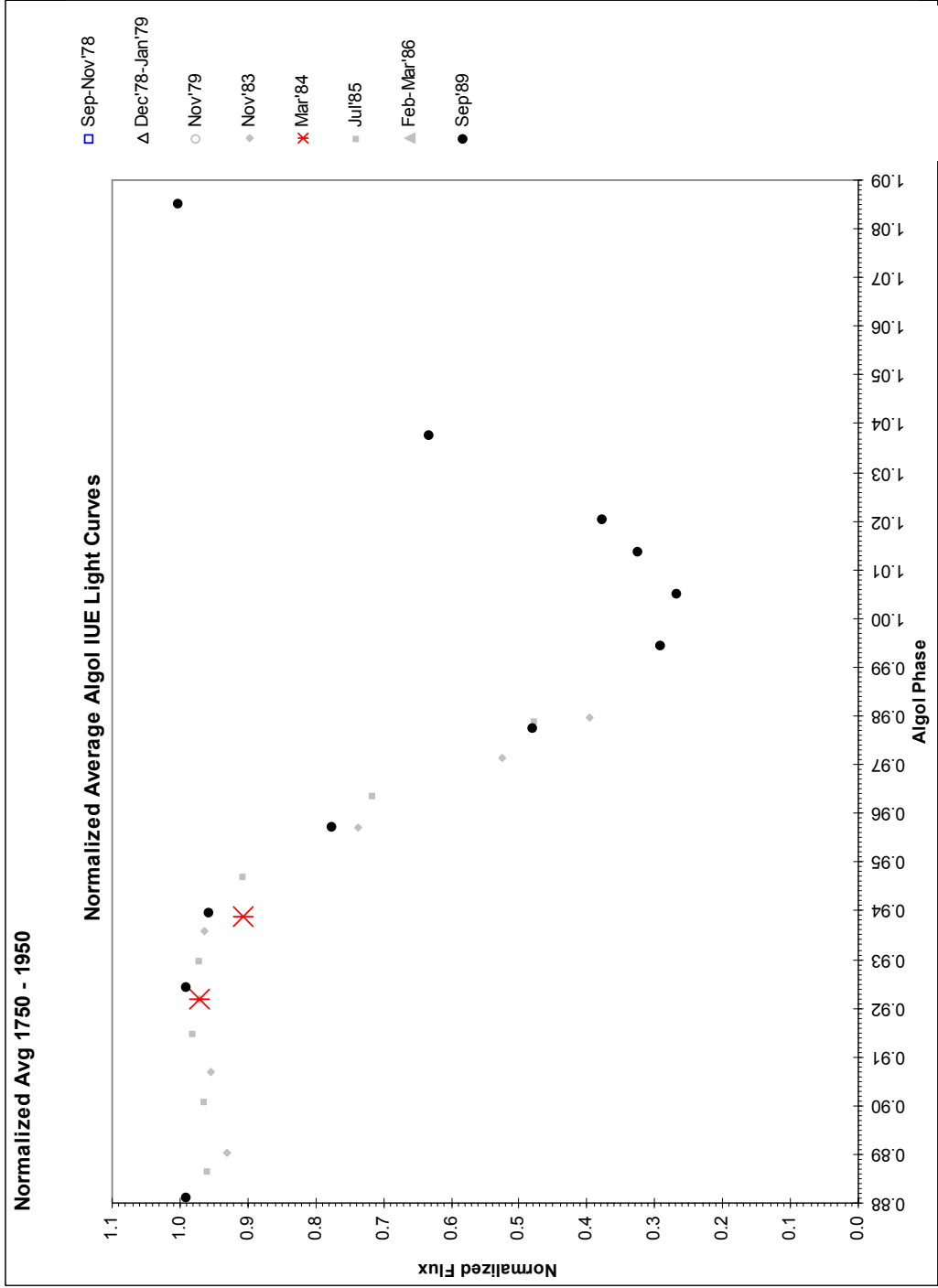


FIG. 4.4.2.10 – SWP Normalized Average Algol IUE Light Curves Near Primary Eclipse. 1550 - 1750 Å



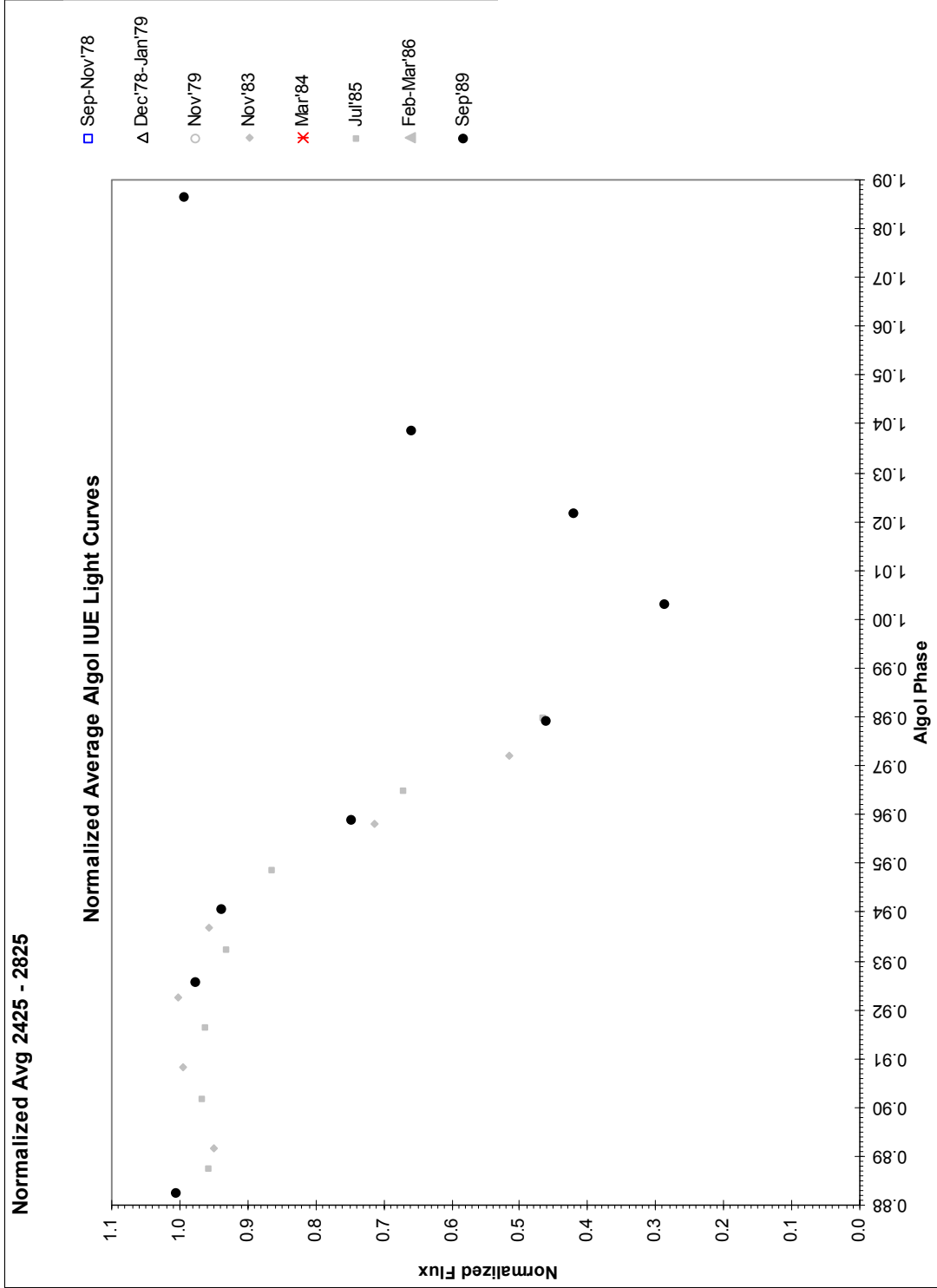


FIG. 4.4.2.11 – LWP/LWR Normalized Average Algol IUE Light Curves Near Primary Eclipse. 2425 - 2825 Å

## 4.5 Determination of Radial Velocities and Absorbing-Gas Characteristics from Spectral Line Analyses

### 4.5.1 Methods of Spectral Line Analyses

After identifying a spectral line, we determined its position, depth, and width for each exposure. Si IV, for instance, appears in the SWP range, where there are 59 SWP exposures; hence, we determined 59 positions, depths, and widths for each of Si IV  $\lambda\lambda 1393, 1402$  lines. Since Mg II appears in the LWP/LWR range, we determine 44 positions, depths, and widths for Mg II  $\lambda\lambda 2796, 2803$  lines and subordinate lines Mg II  $\lambda\lambda 2791, 2798$ .

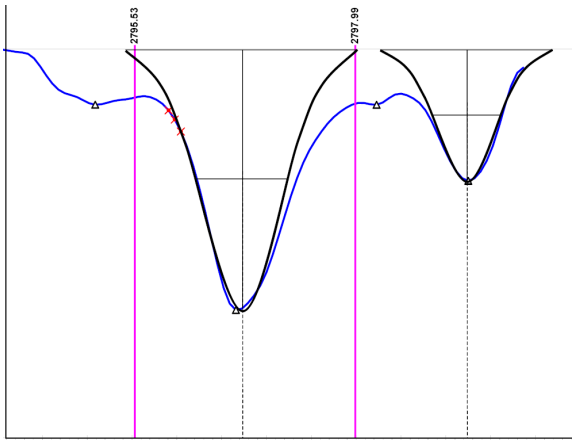


FIG. 4.5.1.1.—Mg II 2796 and Mg II 2798  
 $\phi=0.7798$  9/13/1989 -- *symmetric* -- LWP16347

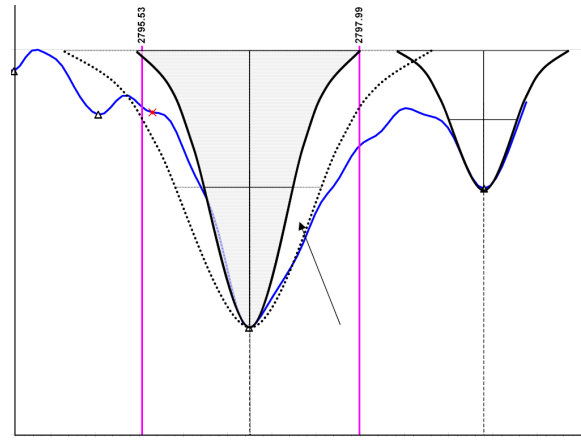


FIG. 4.5.1.2.—Mg II 2796 and Mg II 2798  
 $\phi=0.7884$  3/2/1986 -- *asymmetric* -- LWP07738

The position, depth, and width for each line were determined simultaneously by estimating the best inverted Gaussian shape that fits the line, as shown in FIG. 4.5.1.1. A perpendicular was dropped from the center of the Gaussian shape (narrow dashed line) to the wavelength axis and recorded. The rest wavelength was then subtracted from the recorded value to determine the Doppler shift, and ultimately, the radial velocity. The

depth of the Gaussian shape was measured at its deepest point as a fraction of the continuum level. For the purpose of these calculations, new continuum levels were estimated for each spectral line examined. We used the same method as that described in Section 4.4; however, these were identified using narrower wavelength ranges.

The difference between the continuum flux values and the line depths provided us with measures of residual intensities. These measure the amount of UV flux that is not extinguished along the line of sight.

The width of the Gaussian shape at half of its depth was measured in angstroms and recorded. If the line profile was slightly asymmetric, we captured the essence of the line shape using a symmetrical Gaussian shape as described above, fitting what appeared to be the most unblended half.

If the line profile was noticeably asymmetric, we approximated the line shape with two Gaussian shapes having the same centers and depths, differing only in width. The width of one Gaussian was adjusted to fit the left side of the absorption well, and the width of the other was adjusted to the right side. The position of the line is coincident with the centers of the two overlaid Gaussian shapes. The depth of the line is represented by either Gaussian shape since their depths are also equal. The FWHM was determined by adding the HWHM of the wider Gaussian to the HWHM of the narrower Gaussian.

FIG. 4.5.1.2 is an example of an asymmetric Mg II  $\lambda 2796$  line at phase  $\phi=0.7884$  from March 1986. Its shape was approximated with two Gaussian shapes. The narrower, shaded Gaussian is overlaid and centered on the wider Gaussian shape (dotted curve) that captures the extra red absorption indicated by the arrow.

A measure of the degree of line asymmetry was captured by recording the additional red-shifted or blue-shifted Gaussian half-widths required to fit the line.

#### 4.5.2 Radial Velocity Calculations and Results

We obtained radial velocity curves as functions of phase,  $\phi$ , for each spectral line by using our measured line centers,  $\lambda(\phi)$ , and calculated Doppler shifts from vacuum rest wavelengths,  $\lambda_o$ . The radial velocities, not yet “corrected” to remove the effects of systematic Algol-system motion and the presence of Algol C, are given by Eq. 4.5.2.1, where “uc” indicates “uncorrected.”

$$V_{uc}(\phi) = \frac{c(\lambda(\phi) - \lambda_o)}{\lambda_o} \quad (4.5.2.1)$$

These results are tabulated in Appendix D.3.

The results presented in this section remove the effects due to systematic velocity and the presence of Algol C, as developed in Section 4.3.3. Hence, the “corrected” radial velocities are given by

$$V(\phi) = V_{uc} - V_o - V_{AB:AB-C} \quad (4.5.2.2)$$

FIGS. 4.5.2.1- 4.5.2.11 show radial velocity curves for the following spectral lines: Al II  $\lambda$ 1670, Al III  $\lambda$ 1854, C II  $\lambda$ 1334, Fe II  $\lambda$ 1640, Si III  $\lambda$ 1294, Si IV  $\lambda$  1393, Si IV  $\lambda$ 1402, Fe II  $\lambda$ 2586, Fe II  $\lambda$ 2600, Mg II  $\lambda$ 2796, Mg II  $\lambda$ 2803, respectively.

The solid lines represent our simulation of the radial velocity of the center of mass of Algol A relative to the center of mass of the Algol A-B system. In other words, the systematic velocity and the velocity of the A-B center of mass (i.e., the effect of Algol C) have been removed in producing our solid line, as they have been removed from the data points.

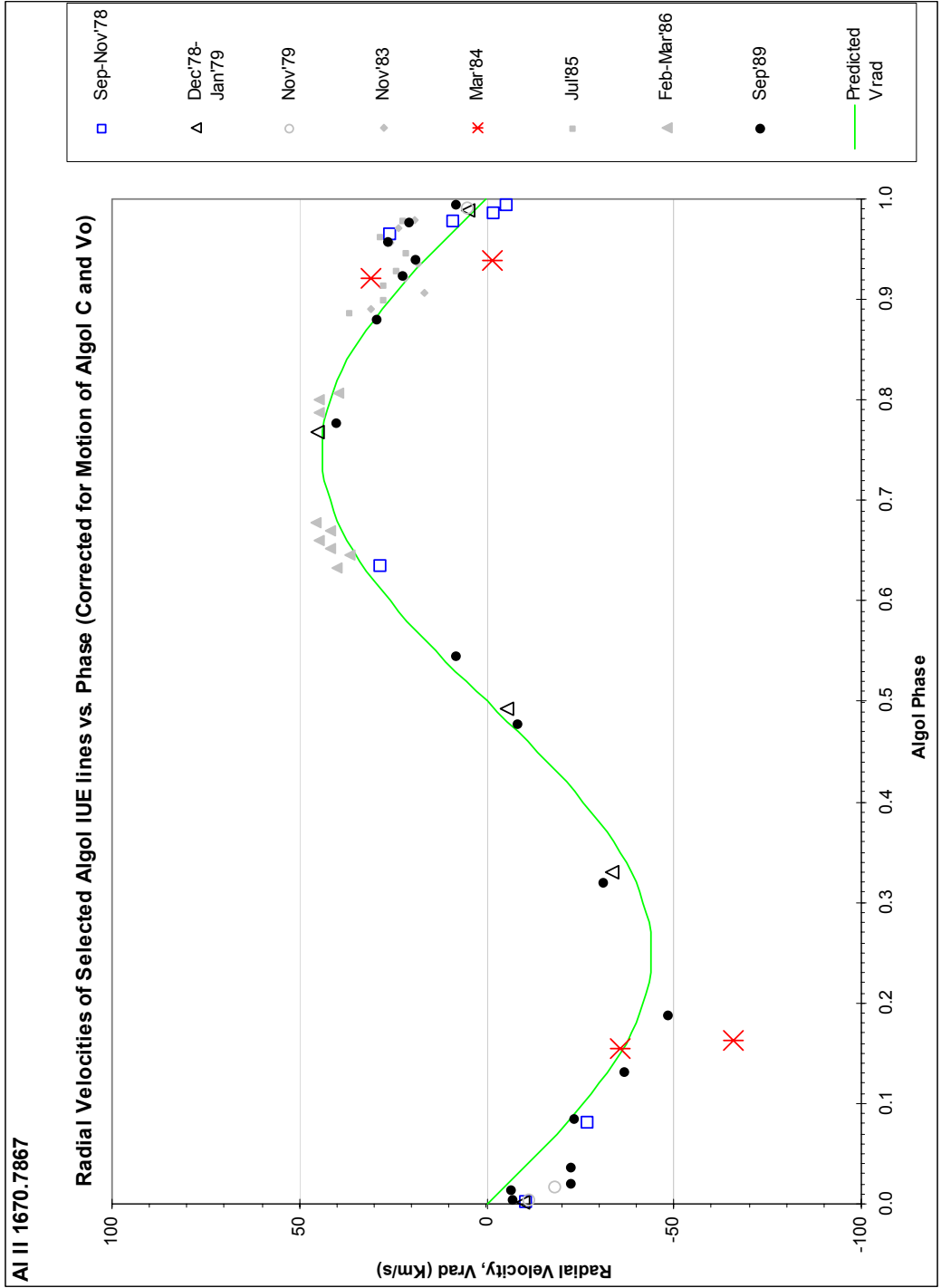


FIG. 4.5.2.1 – Radial Velocity vs Phase AI II 1670

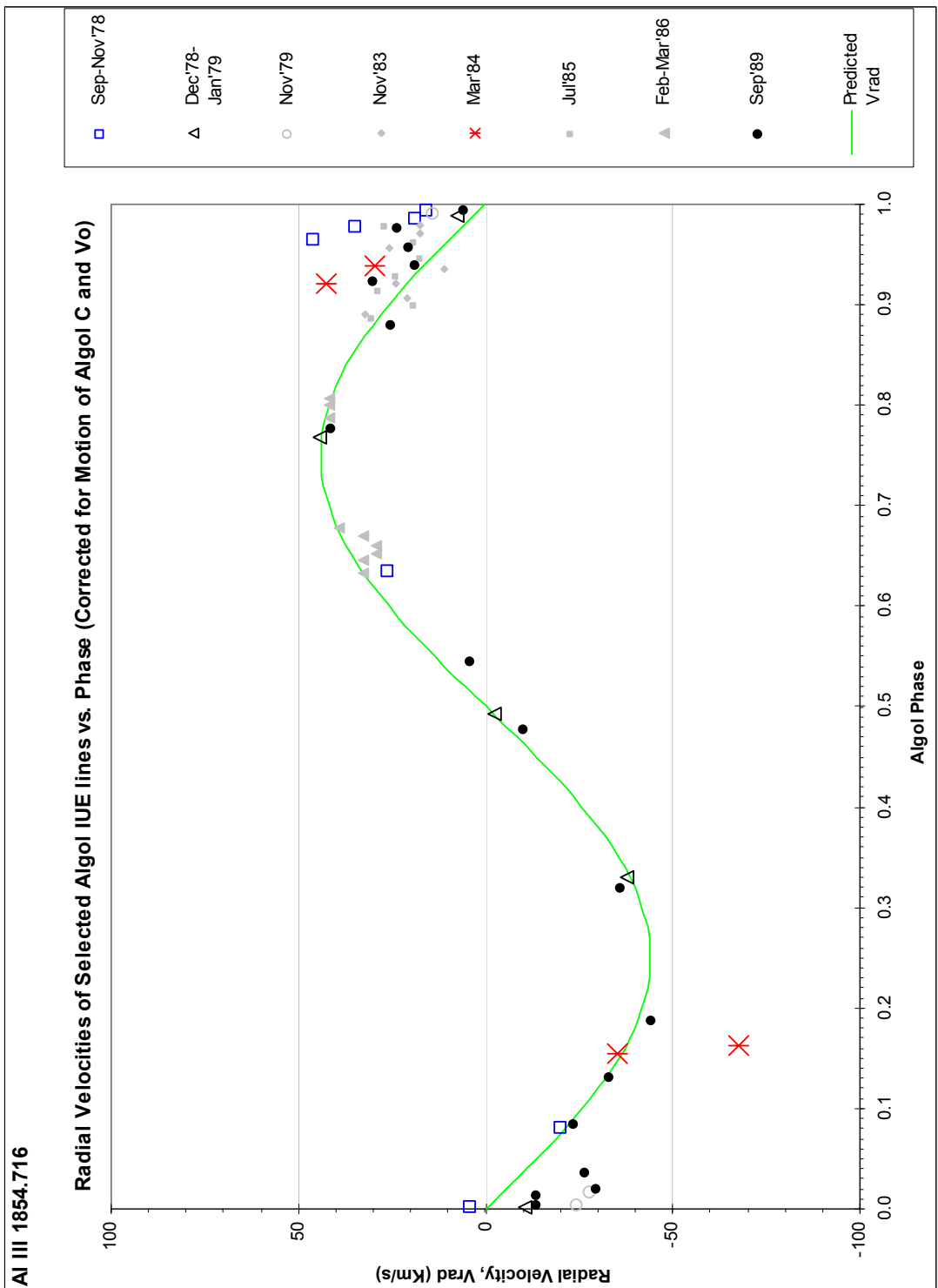


FIG. 4.5.2.2 – Radial Velocity vs Phase Al III 1854

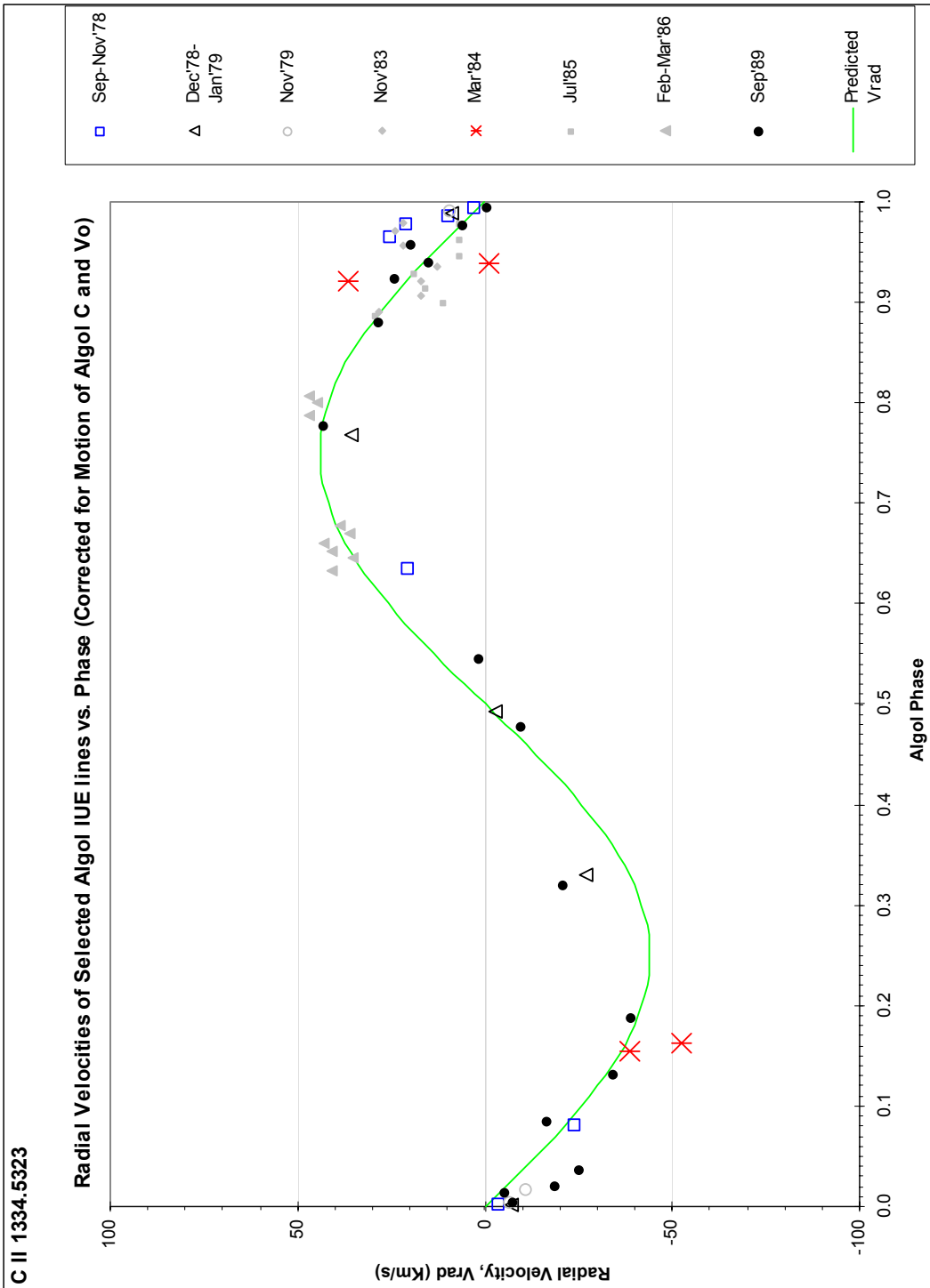


FIG. 4.5.2.3 – Radial Velocity vs Phase C II 1334

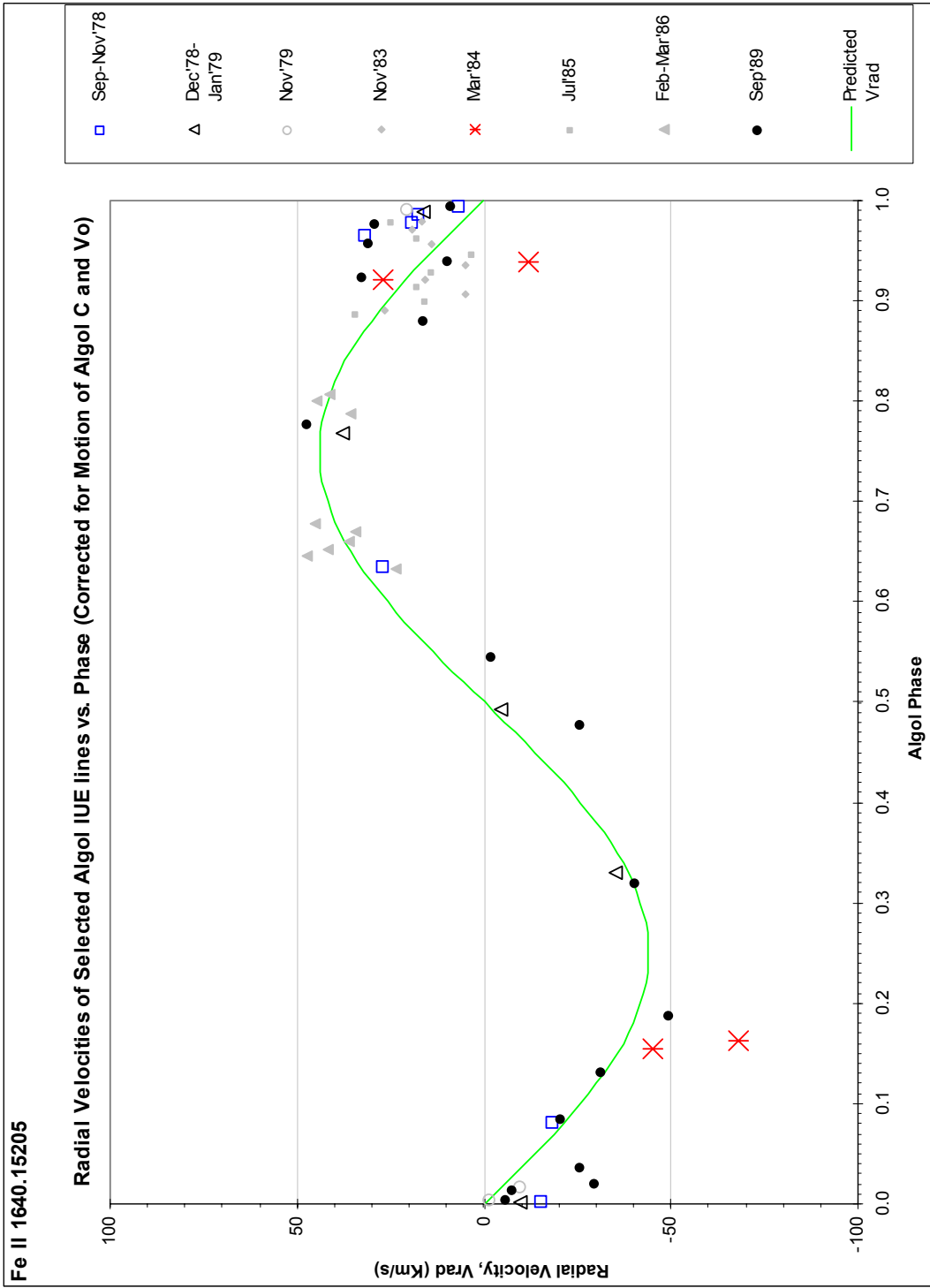


FIG. 4.5.2.4 – Radial Velocity vs Phase Fe II 1640



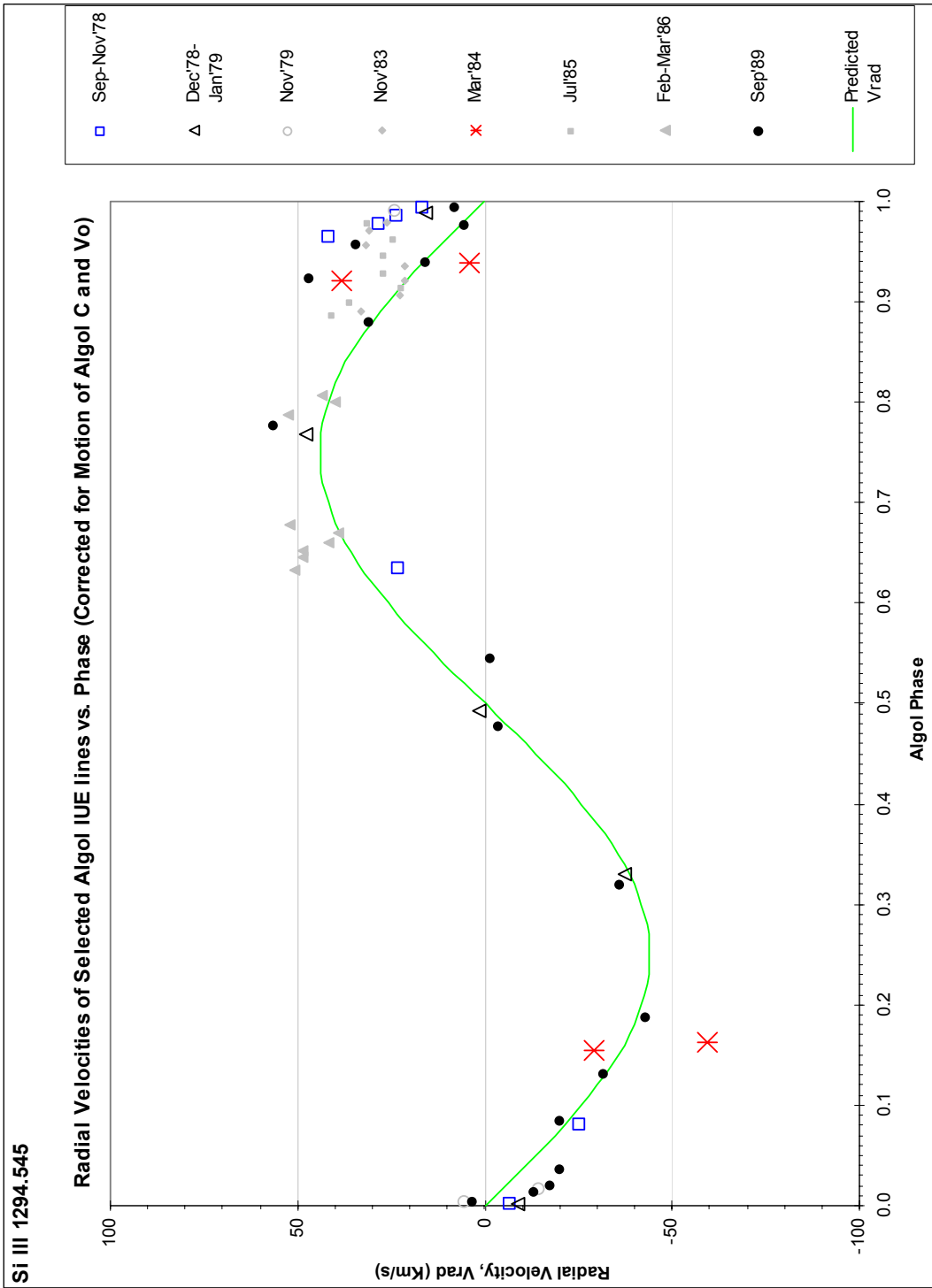


FIG. 4.5.2.5 – Radial Velocity vs Phase Si III 1294

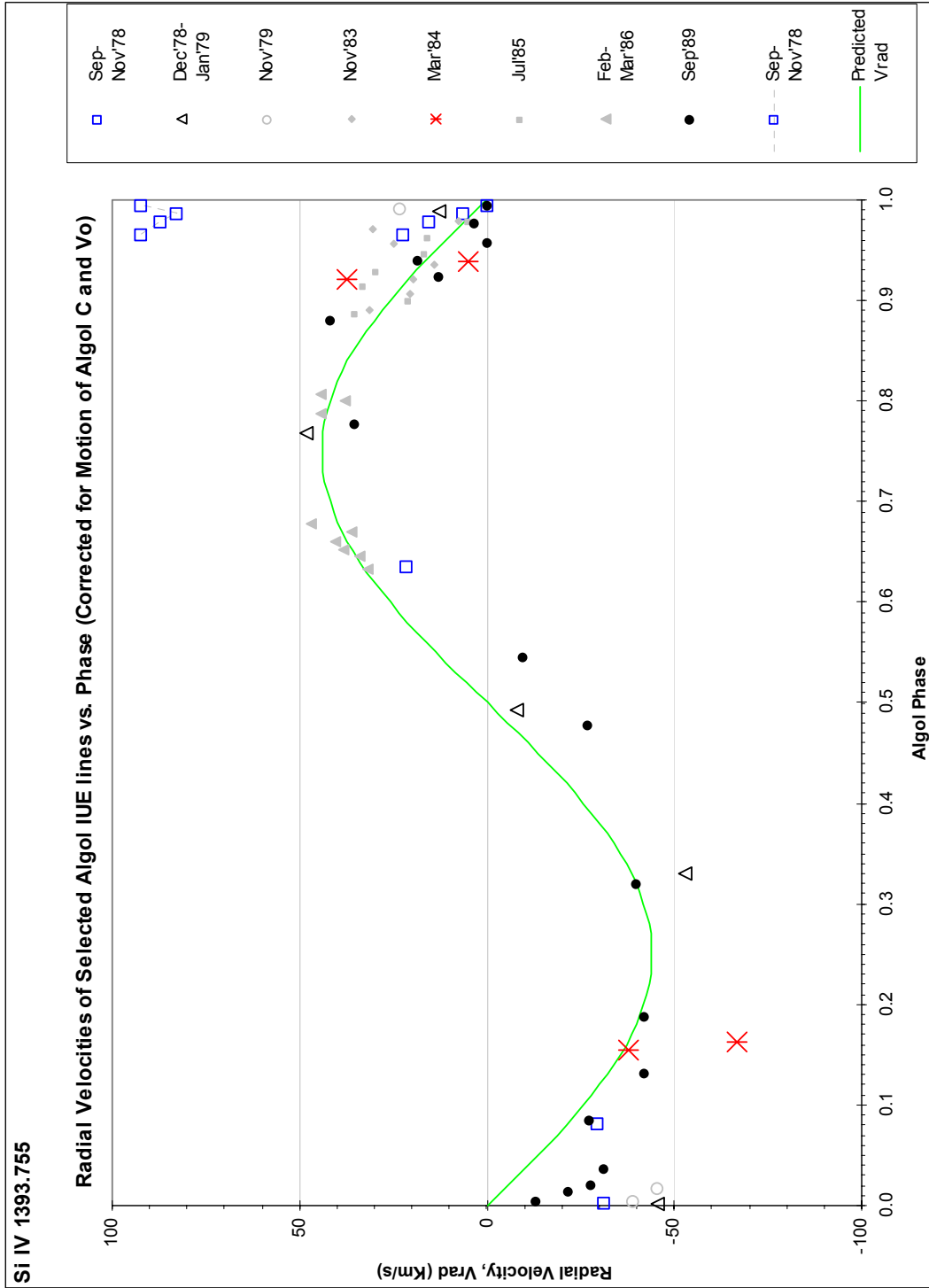


FIG. 4.5.2.6 – Radial Velocity vs Phase Si IV 1393

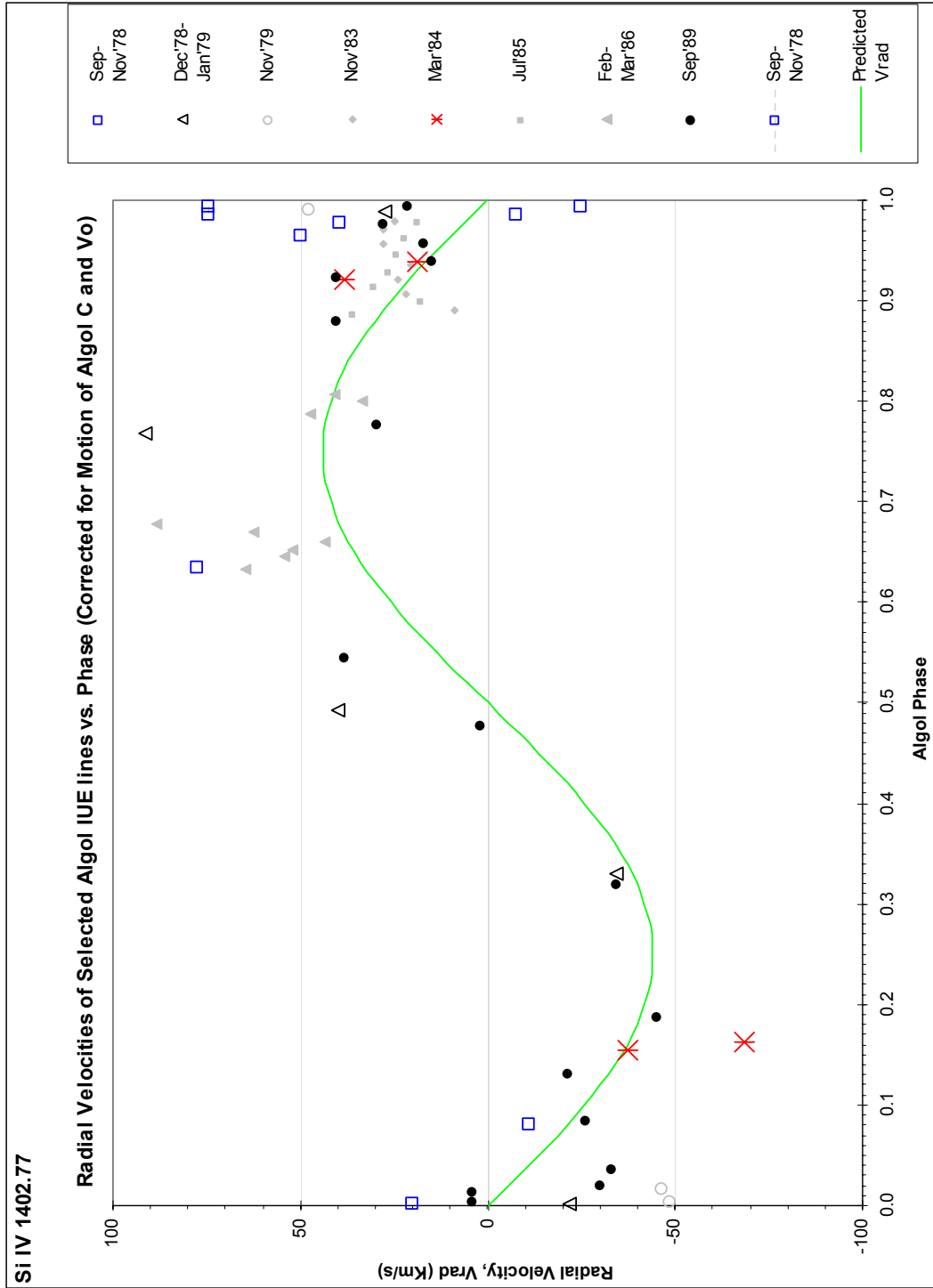


FIG. 4.5.2.7 – Radial Velocity vs Phase Si IV 1402

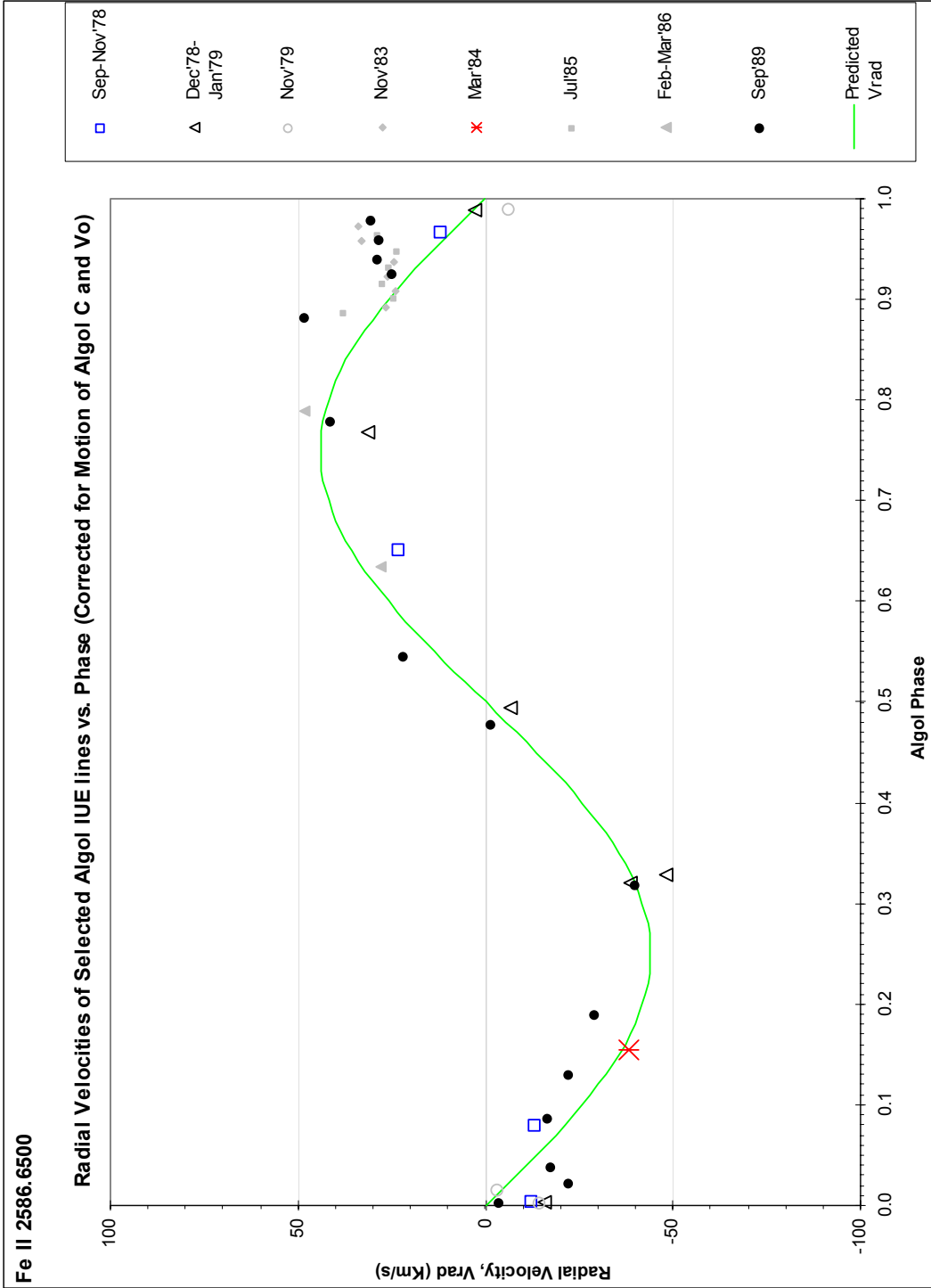


FIG. 4.5.2.8 – Radial Velocity vs Phase Fe 2586

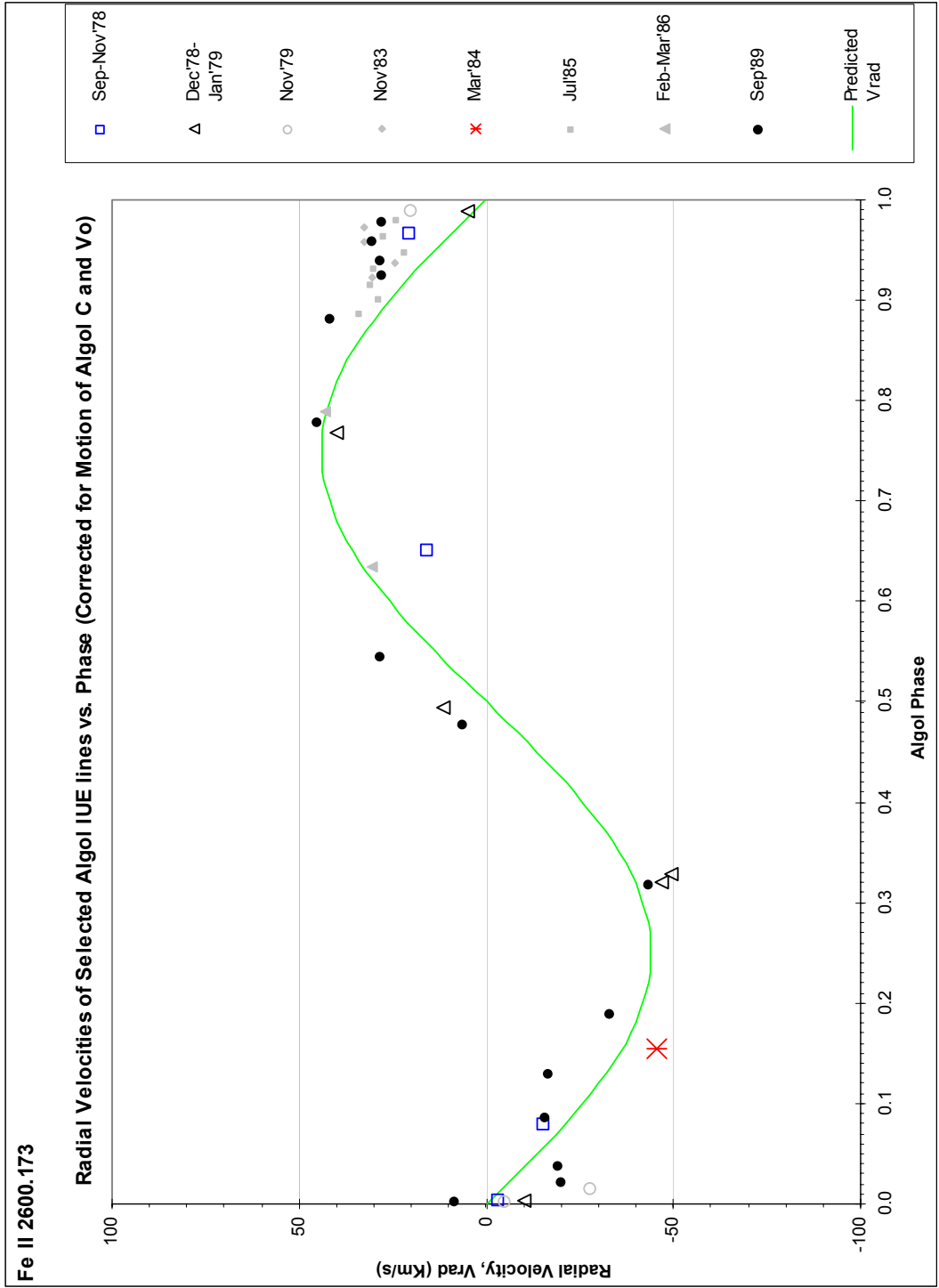


FIG. 4.5.2.9 – Radial Velocity vs Phase Fe II 2600

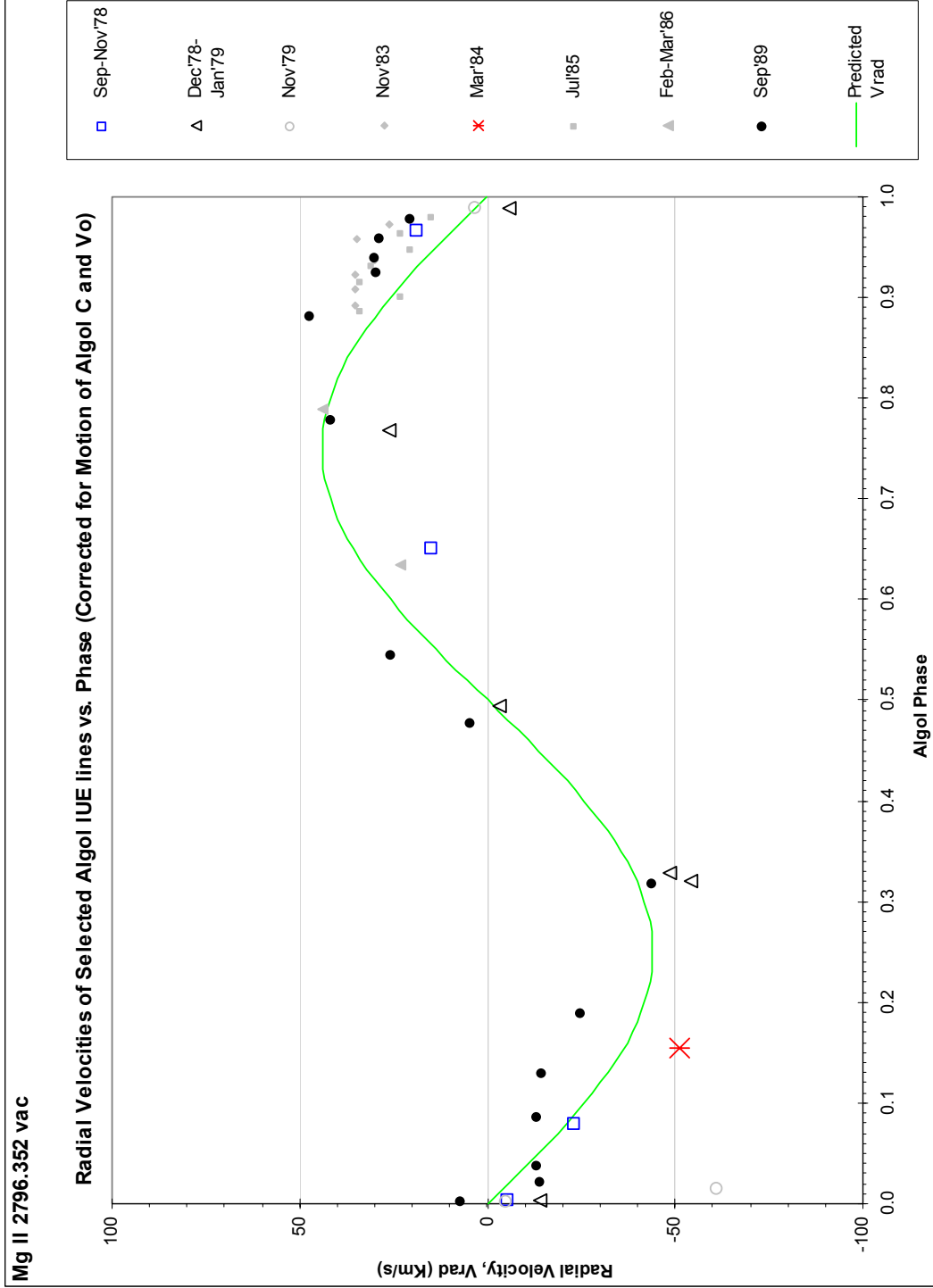


FIG. 4.5.2.10 – Radial Velocity vs Phase Mg II 2796

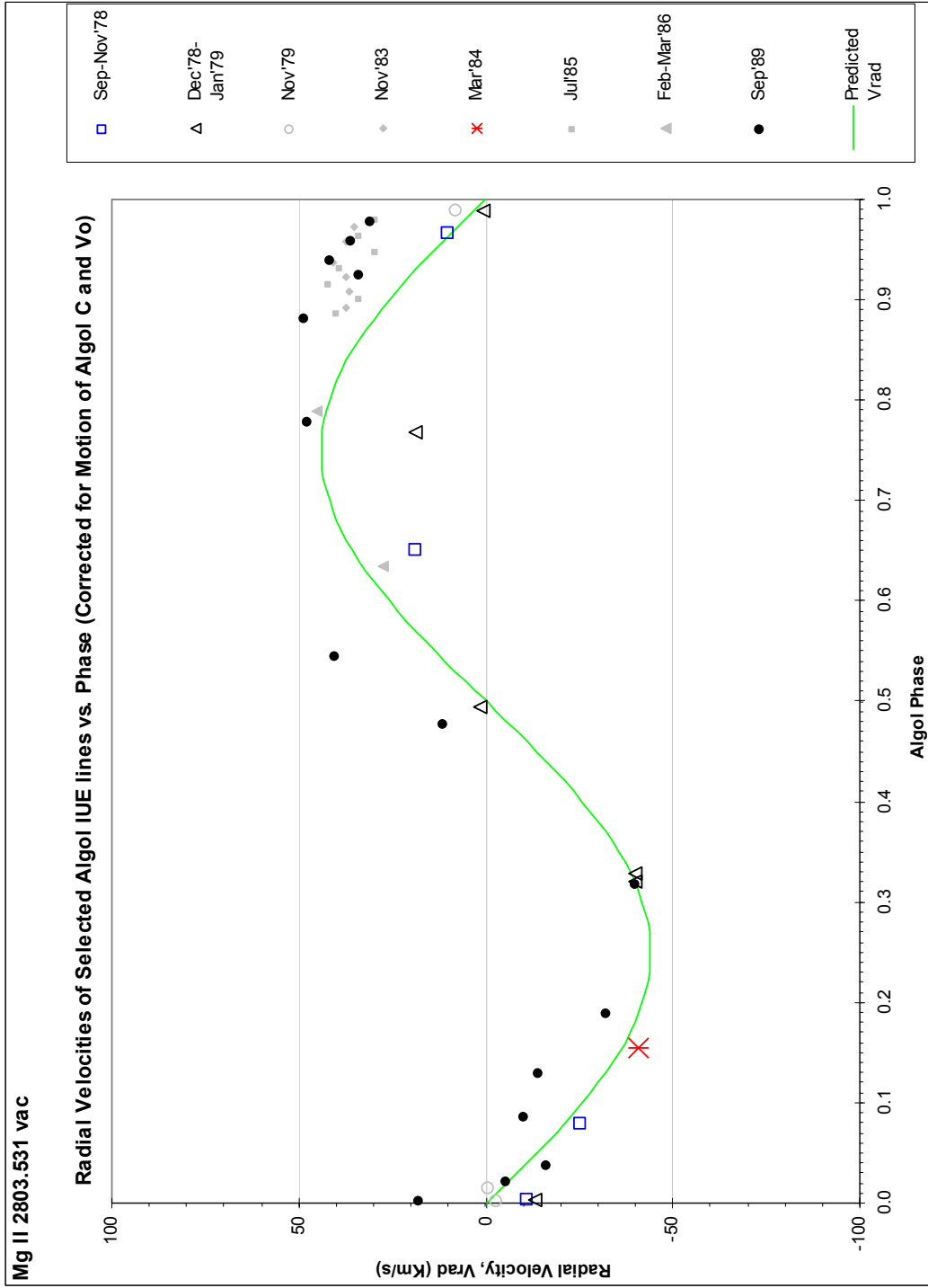


FIG. 4.5.2.11 – Radial Velocity vs Phase Mg II 2803

With the exception of the March '84 epoch, the Al II  $\lambda 1670$  radial velocity data matches closely the phase dependence expected for photospheric gases on Algol A. The data points lie along the predicted curve, except in the phase ranges just before and just after primary minima,  $\phi \approx 0.92 - 0.08$ . This effect is associated with the partial eclipsing of Algol A, revealing the hemisphere with rotational motion directed towards us (egress;  $\phi \approx 0.0 - 0.08$ ) or away from us (ingress;  $\phi \approx 0.92 - 1.0$ ). This is the Rossiter effect, described earlier.

Another feature common to several plots is particularly conspicuous for Al III  $\lambda 1862$ . The observations appear to be uniformly displaced downward to the predicted (photospheric) curve. This occurs when a pair of spectral lines are blended and undistinguishable. In this case, Al III  $\lambda 1862$  is blended with Al II  $\lambda 1862$ . Therefore, these near-uniform downward displacements, or upward displacements in other cases, are not indicative of gas flowing toward us.

We now consider spectral features where red-shifted or blue-shifted data might be indicative of true gas-flow phenomena. Some of these features are associated with certain epochs, indicative of secular changes in the system: outbursts or periods of unusual activity.

One of the most interesting features in the LWP/LWR RV (radial velocity) curves in the 1989 epoch in the phase range of  $\sim 0.1 - 0.3$ . There is a persistent arc-like trajectory with opposite curvature to the photospheric RV trajectory. It is most pronounced in Mg II  $\lambda 2796$  where the peak of the deviation is redshifted almost 20 km/s from the photospheric RV at phase 0.130. This feature also appears in the Fe II  $\lambda 2599$ , Fe II  $\lambda 2600$ , and Fe II  $\lambda 2750$  spectra.



Some spectral lines seem to show blue shifts in the phase range 0.65 - 0.8, such as those shown in FIG. 4.5.2.8 for Fe II  $\lambda$ 2586.

There appears to be a considerable amount of epoch dependence in the 0.9 – 1.0 phase regions, particularly for the '78 and '84 epochs.

Measurements during the '84 epoch were only taken at phases near 0.15 and 0.93, and most of these values depart significantly for the photospheric values. Other features will be considered as appropriate in the Discussion and Conclusions chapter.

### 4.5.3 *Line Widths and Asymmetries*

A plot of the line width as a function of phase gives us an idea of how the velocity gradient of the circumstellar gas varies along different lines of sight and from epoch to epoch. This is illustrated schematically in FIG. 4.5.3.1. The spectral line shown in FIG. 4.5.3.1a is broadened in part by photospheric rotation. This schematic could also represent the motion of circumstellar gases near the photosphere, sometimes referred to as a “pseudo-photosphere.” Since a pseudo-photosphere may have a different temperature than the true photosphere, the two regions may be represented by different ion abundances, hence, different line strengths. In either case, one expects that contributions are mostly symmetrical with line widths relatively constant over phase and epoch changes. On the other hand, UV absorptions due to gas streaming effects could show increased line widths and asymmetries, as suggested by one possible scenario, shown in FIG. 4.5.3.1b. In the case shown, the gas is moving away from the observer and increasing in velocity. Also, in this representation, the line strength is decreasing, as though the line strengths are diminishing as the gas stream approaches Algol A, indicating a temperature gradient along the stream. As seen in the figure, the gas streaming result would clearly depend on viewing angle (phase) and degree of system activity (epoch), as well as velocity and temperature gradients.

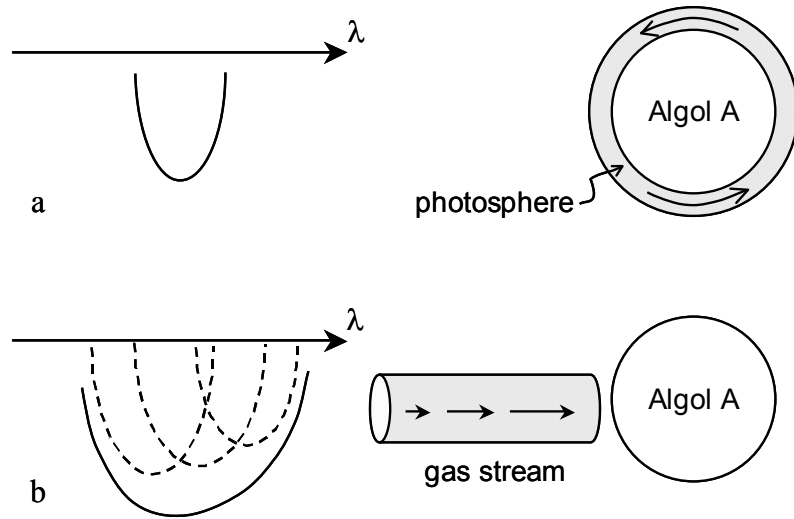


FIG. 4.5.3.1—*Variation in line widths.* Symmetrical (a) and asymmetrical (b) velocity distributions.

In examining FIG. 4.5.3.2 we see that the width of Al II  $\lambda 1670$  is relatively constant across phase and epoch, supporting its photospheric status.

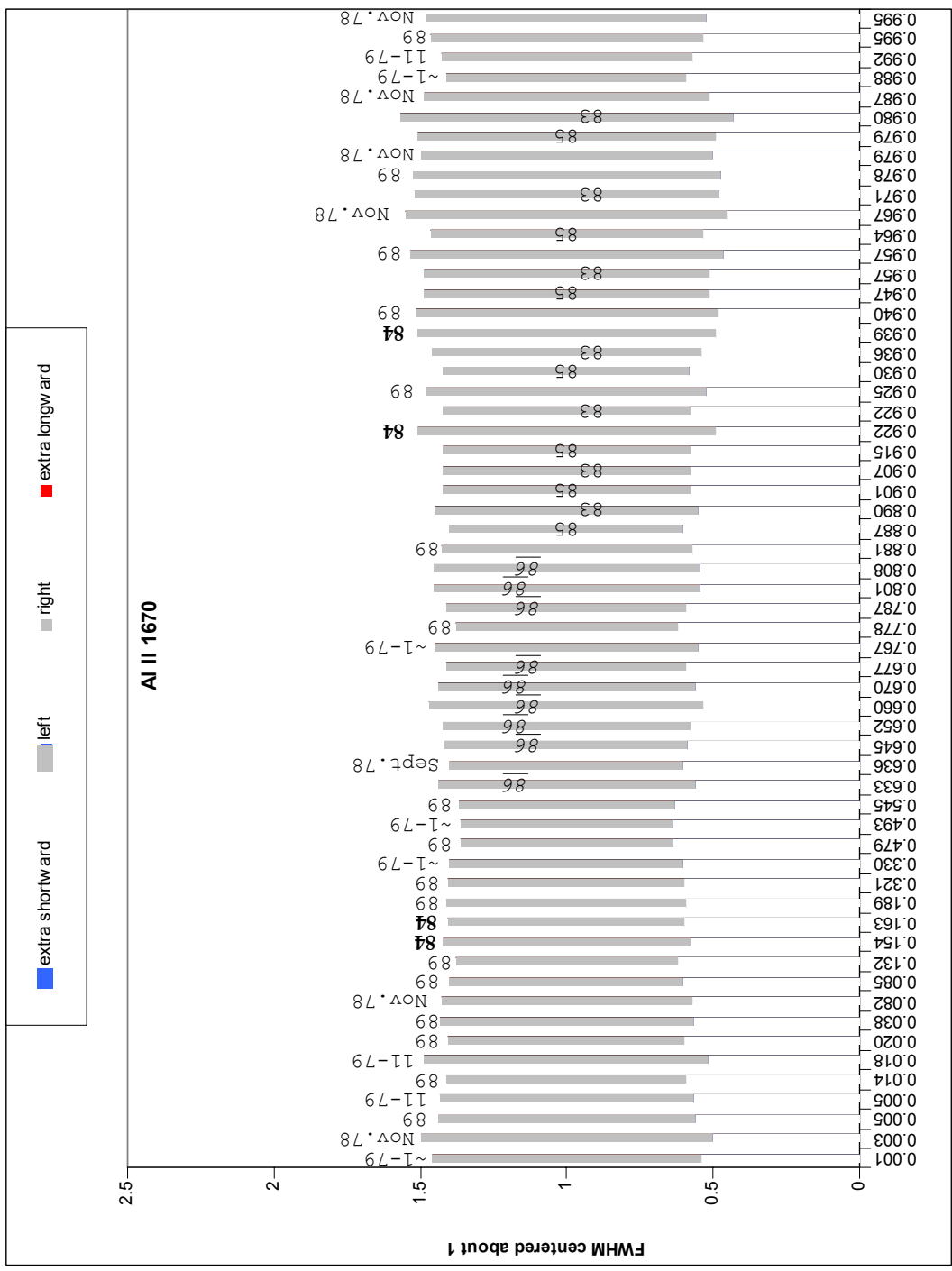


FIG. 4.5.3.2 -- Line width as a function of phase. Al II 1670

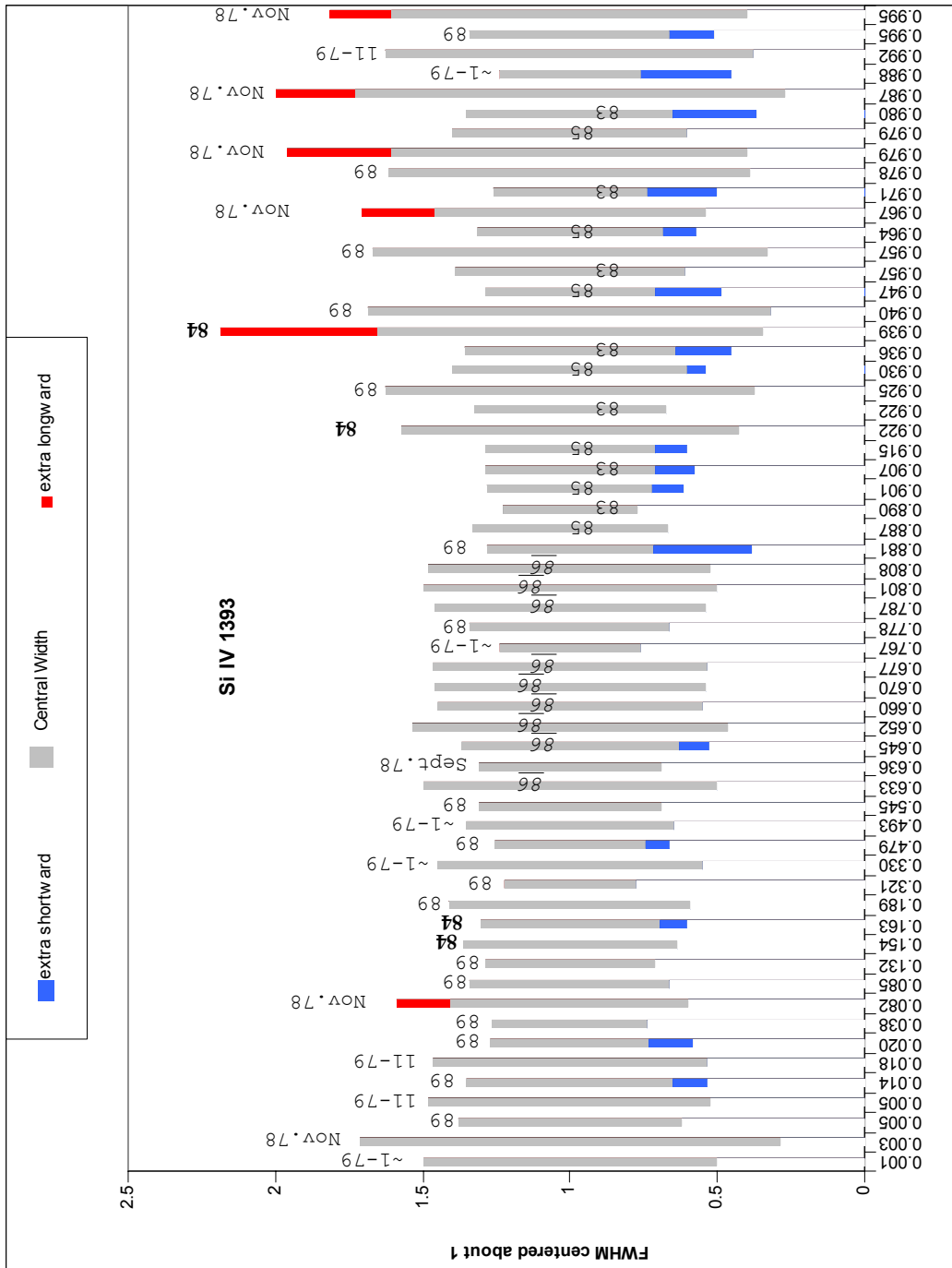


FIG. 4.5.3.3 -- Line width as a function of phase. Si IV 1393

The width of Si IV on the other hand shows dramatic changes over both phase and epoch. The line width increases dramatically on average during primary eclipse ingress near phase 0.922, decreases before primary eclipse, and continues to decrease on average through primary eclipse egress, reaching a minimum near phase 0.5 (secondary minimum). The 1989 results are mostly symmetrical, and show increasing widths as ingress progresses. In the phase range 0.922 – 1.0, there are significant epoch dependences, as evidenced by the larger widths and asymmetries in the 1978 and 1984 data. During these epochs, there is on average more longward (redshifted) width during the first half of primary eclipse, which is indicated by the (darker) top portions of the bars in FIG. 4.5.3.3. This asymmetry is an indicator of gas streaming from the secondary toward the primary, suggesting that these are epochs of increased activity.

A tabulation of all measured line widths are included in Appendix D.3.

#### 4.5.4 *Residual Intensities*

The normalized residual intensities (transmission at line center) of the resonance absorption lines have a clear pattern of variation across the orbital phases especially in the 1989 data shown in FIGs. 4.5.4.1 through 4.5.4.7, where the 1989 data are connected by a smooth line for ease of viewing. The most prominent feature is the distorted asymmetric "W" shape situated about primary eclipse. The first "V" of the "W" has a bump at the base near phase 0.925, especially noticeable in the Al III  $\lambda\lambda$ 1854, 1862 plots (FIGs. 4.5.4.2 and 4.5.4.3). As discussed in section 4.5.1 the residual intensity (RI) is a

measure of the attenuation of the incident intensity after passing through an absorbing region, or the amount of flux that is not extinguished along the line of sight. This bump might be interpreted as an emission region competing with a broader absorbing region.

An outstanding attribute of the "W" shape is its asymmetry, the first "V" being broader, i.e., extending through a larger phase range before primary eclipse than the second "V" does after primary eclipse. This indicates that we are looking through more material before ingress than after egress. In comparison with the 1986 data, which suggests a more extended absorbing region between phases 0.6 and 0.8, 1989 is the less active of the two epochs. It is interesting to note the development of the RIs in the 1986 epoch, which increasingly depart from the 1989 levels across Al II, Al III, and Si IV (FIGs. 4.5.4.1 through 4.5.5). A tabulation of all measured RIs is located in D.4.

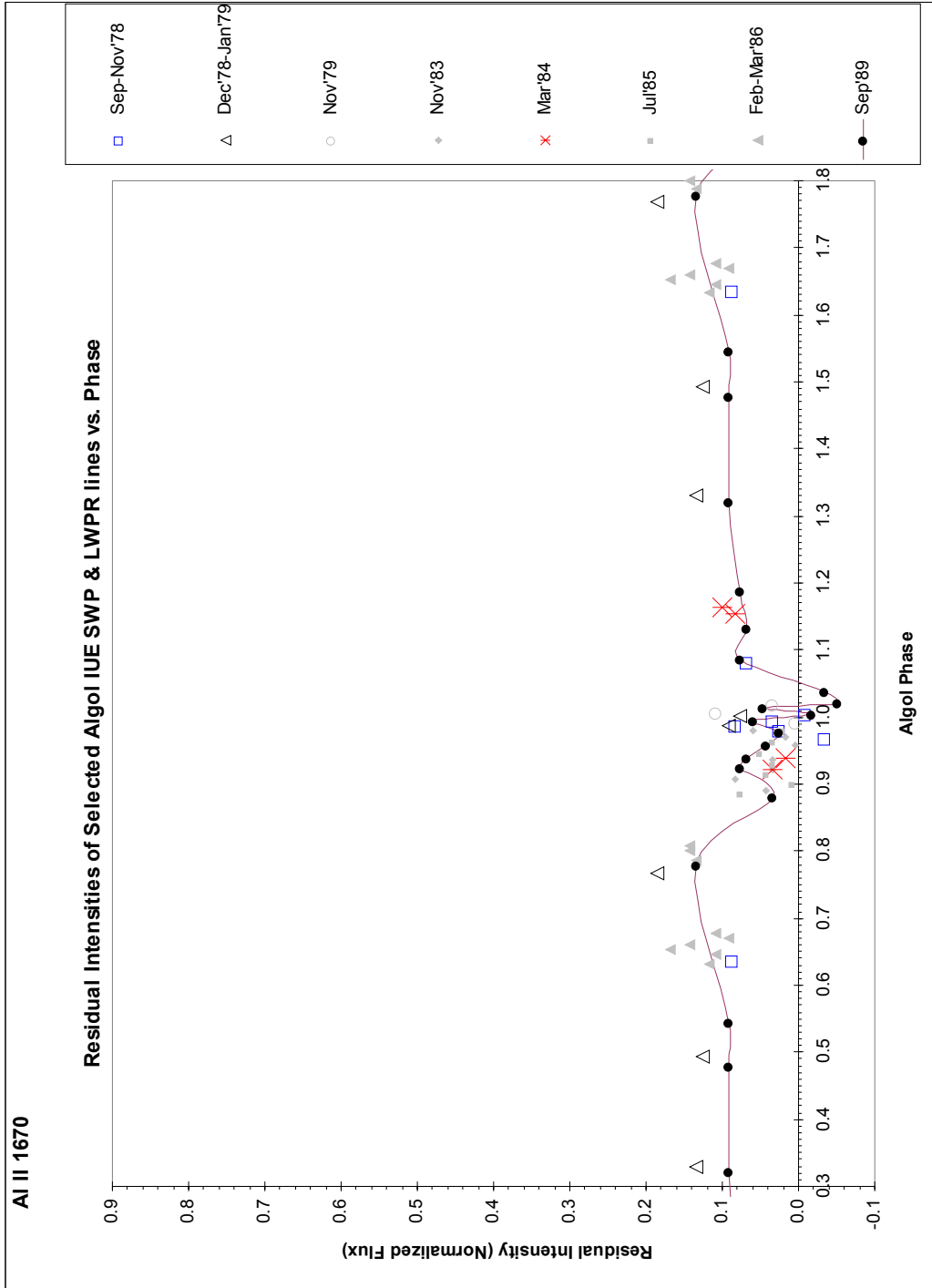


FIG. 4.5.4.1 — Residual Intensities of Selected IUE SWP& LWP/LWR lines vs. Phase AI II 1670



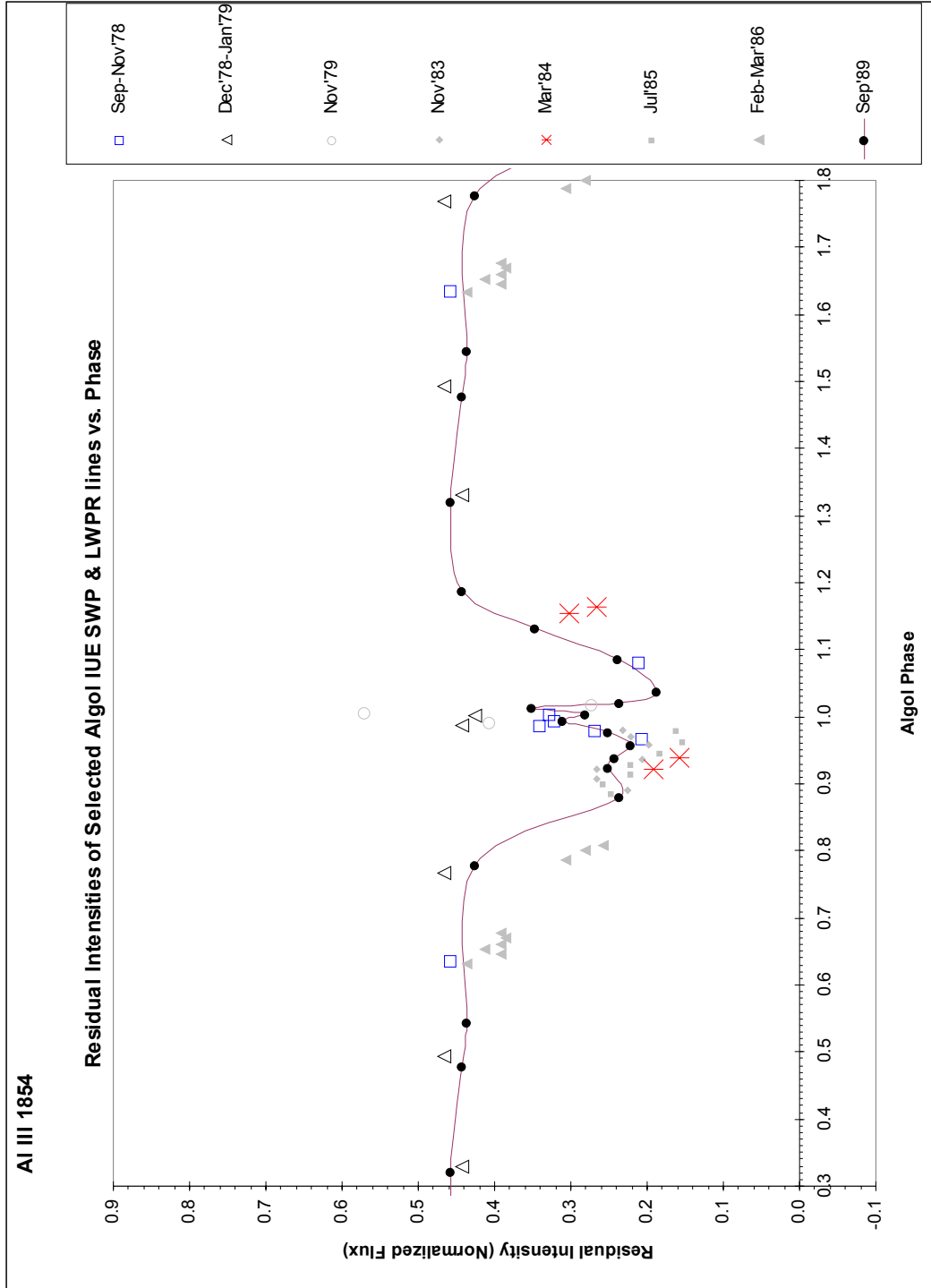


FIG. 4.5.4.2 -- Residual Intensities of Selected IUE SWP & LWP/LWR lines vs. Phase AI III 1854

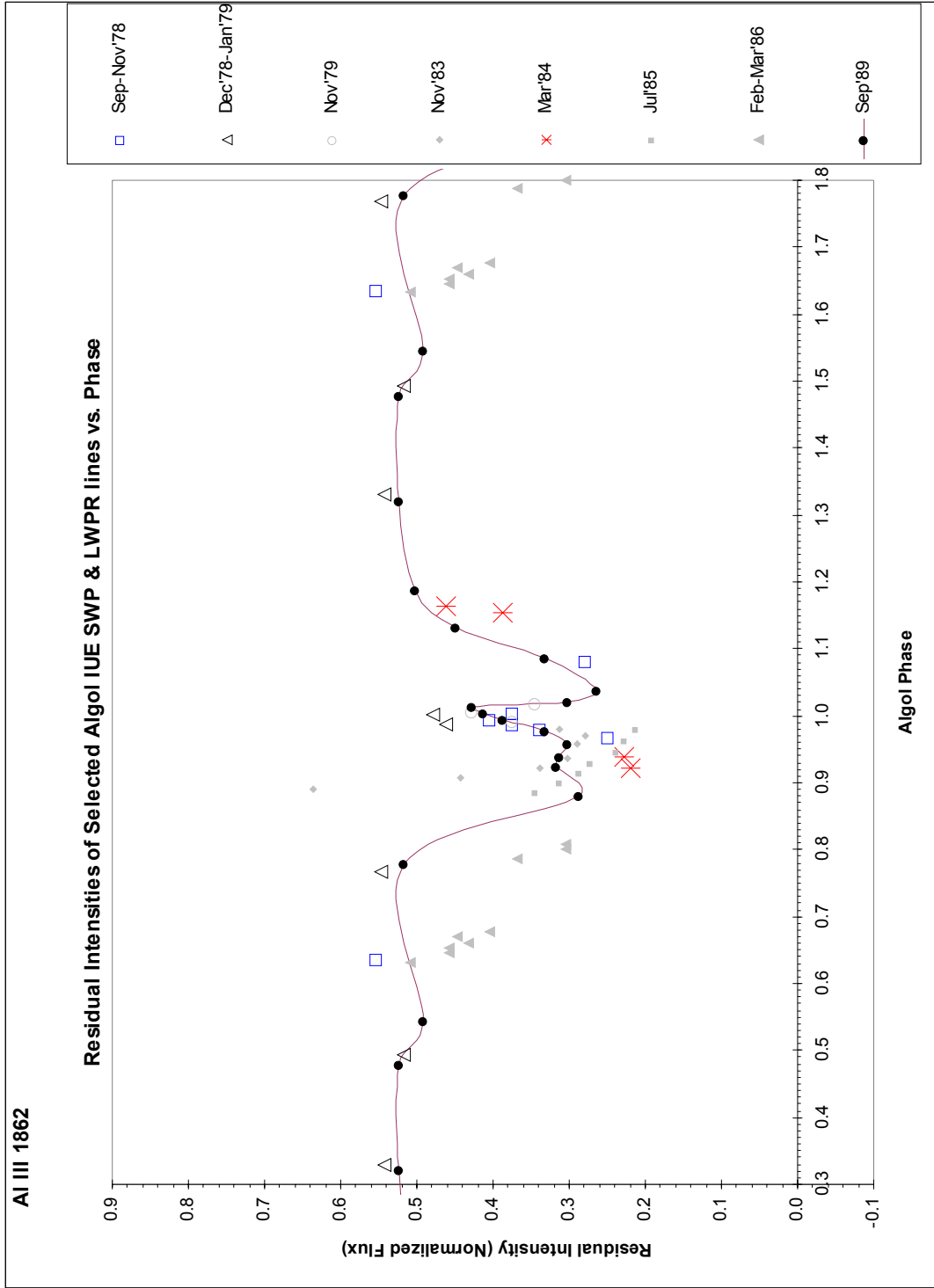


FIG. 4.5.4.3 -- Residual Intensities of Selected IUE SWP & LWPR lines vs. Phase Al III 1862

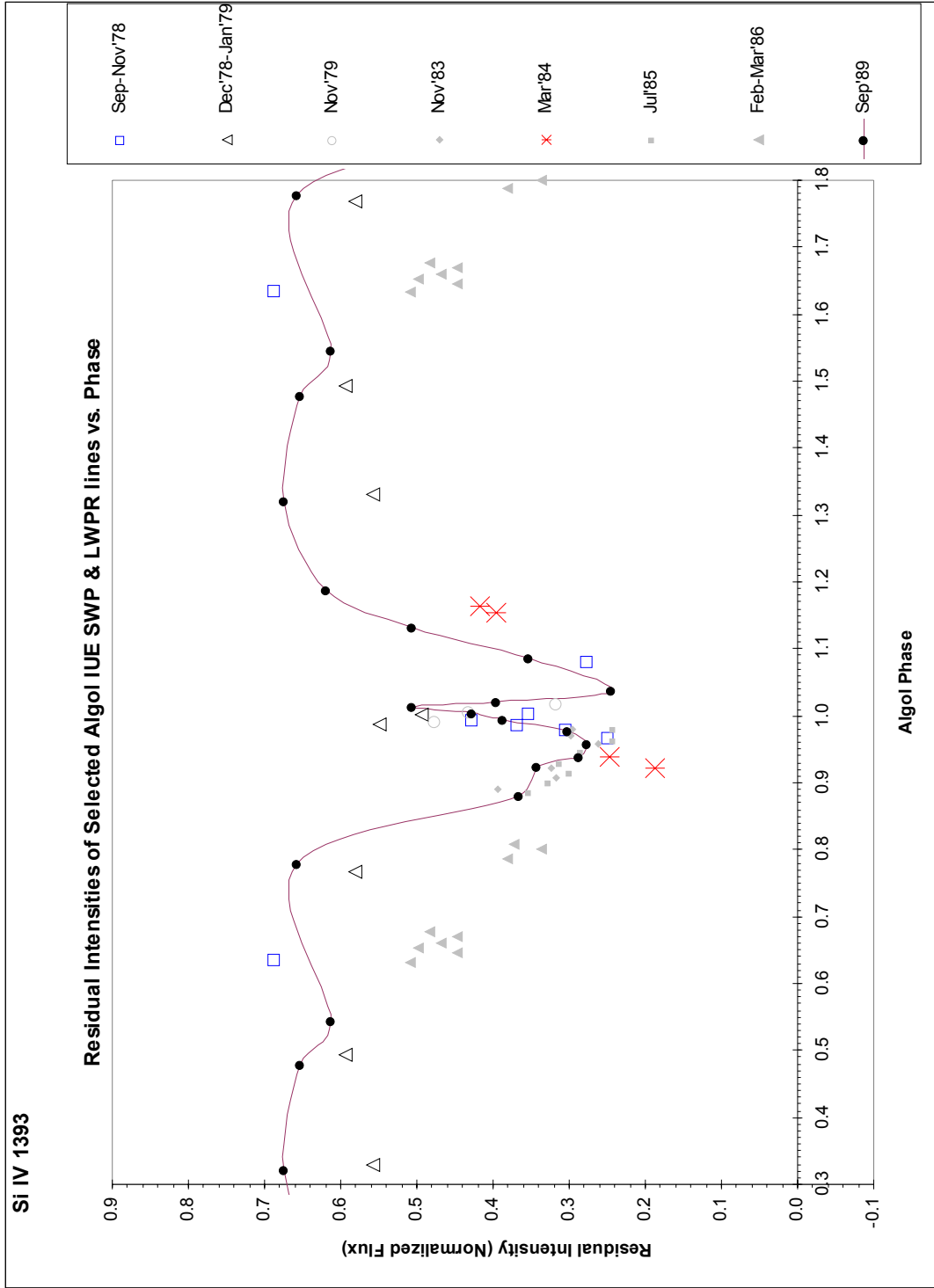


FIG. 4.5.4.4 -- Residual Intensities of Selected IUE SWP & LWP/LWR lines vs. Phase Si IV 1393

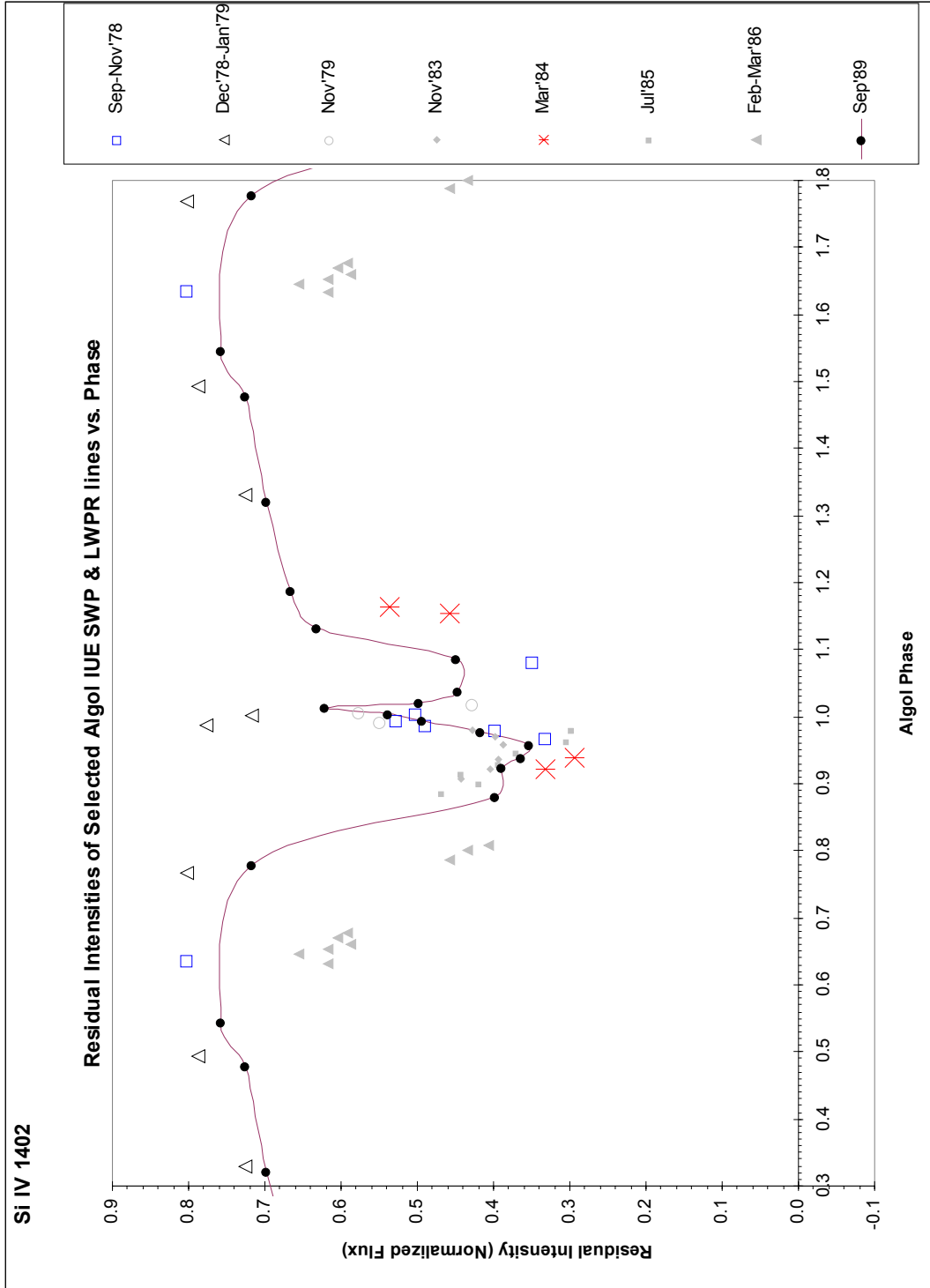


FIG. 4.5.4.5 -- Residual Intensities of Selected IUE SWP & LWPR/LWR lines vs. Phase Si IV 1402

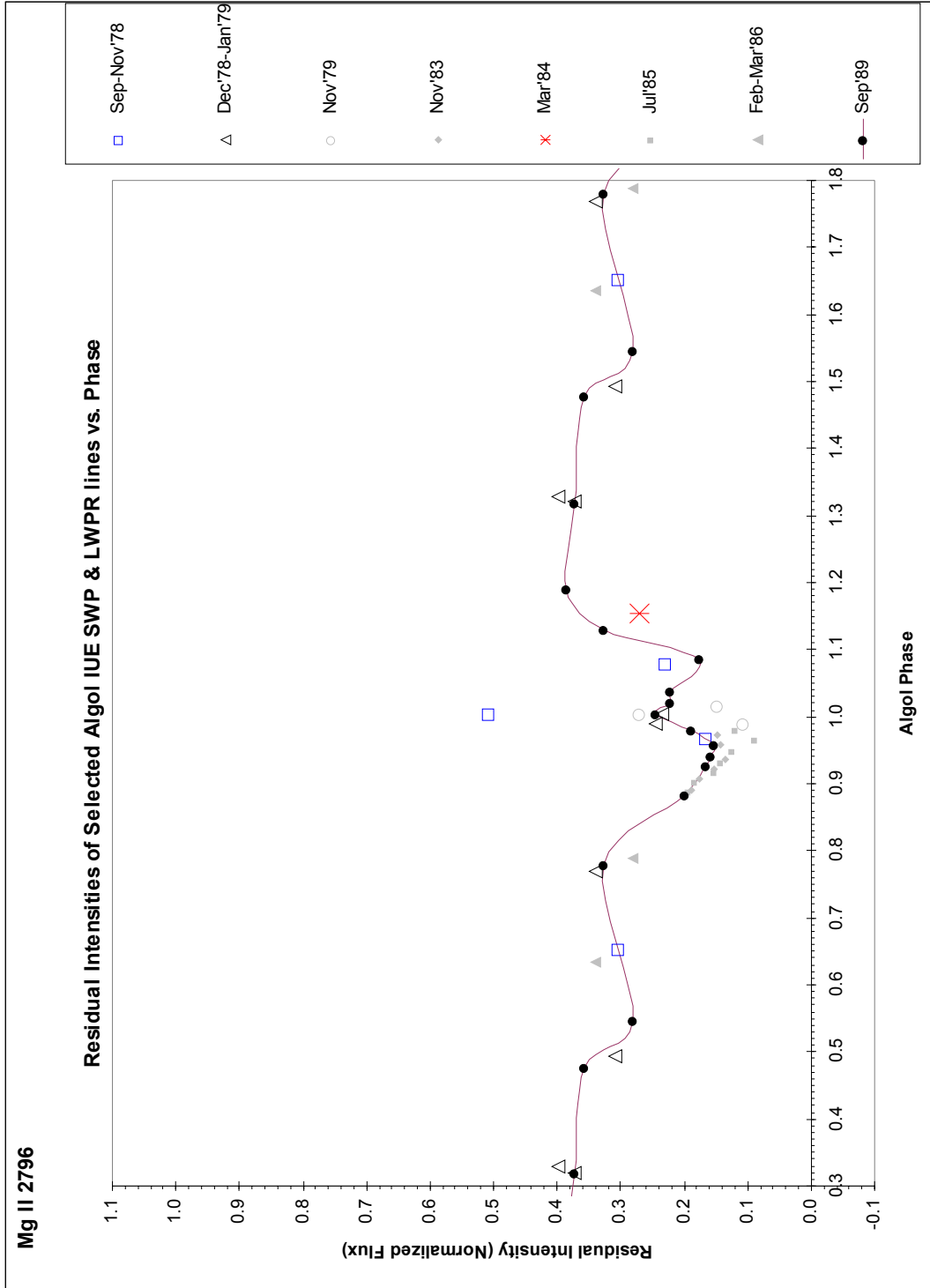


FIG. 4.5.4.6 -- Residual Intensities of Selected IUE SWP & LWP/LWR lines vs. Phase Mg II 2796

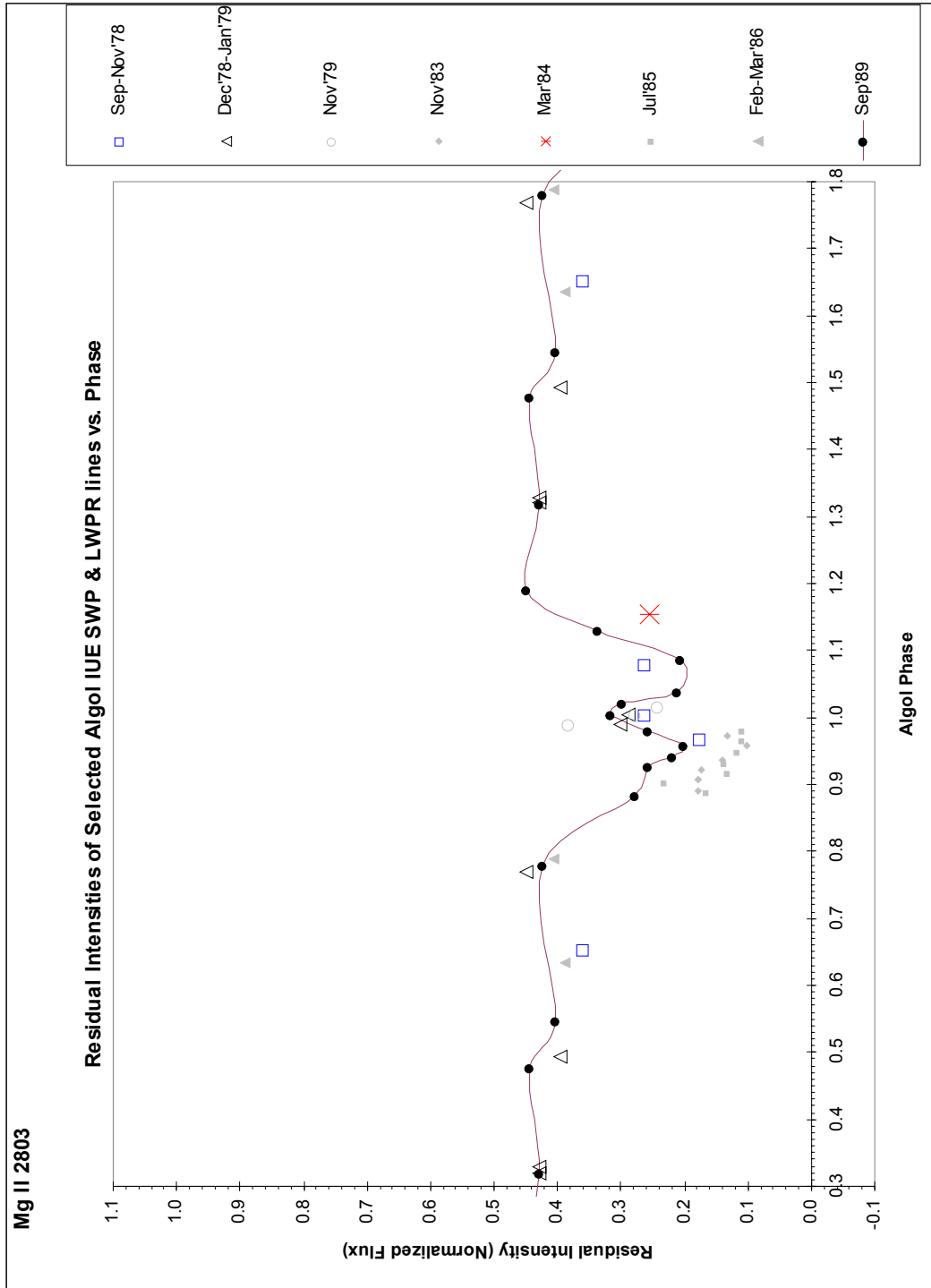


FIG. 4.5.4.7— Residual Intensities of Selected IUE SWP& LWP/LWR lines vs. Phase Mg II 2803

#### 4.5.5 Equivalent Widths and Column Densities

The equivalent width  $W_\lambda$  of a line is an indicator of its strength and is proportional to the number of atoms (“column density”) along our line of sight  $N_A$  if the absorptions are unsaturated. A well behaved photospheric line should vary little with phase since the photosphere is assumed to be uniform in thickness and density. Al II 1670 is the strongest photospheric line in our data, though it indicates an increase in  $N_A$  between phases 0.881 and 0.038. (See FIG. 4.5.5.1.) Si IV ( $\lambda\lambda 1393, 1402$ ), however, shows a dramatic increase in  $W_\lambda$  between phases 0.633 and 0.979 (FIGs. 4.5.5.2 and 4.5.5.3). The equivalent width is a minimum in the phase interval 0.321 to 0.545.

In FIGs. 4.5.5.2 and 4.5.5.3, we see that the region of formation of Si IV is visible to varying degrees in the orbit and across epochs. On average, the number of atoms along the line of sight is the greatest between phases 0.881 and 0.987 ( $\phi \approx .9$ ) and the least between phases 0.321 and 0.545 ( $\phi \approx 0.4$ ). This suggests that the hot structure that forms the Si IV is located in a region between Algol A and Algol B offset from the line connecting the centers of the components by  $\sim 0.1 \times 360^\circ = 36^\circ$ . The complete set of equivalent width measurements is found in Appendix D.2.

If we make an estimate of the gas column volume of the absorbing region we can make an estimate of the gas density, as described in Section 4.5.7.

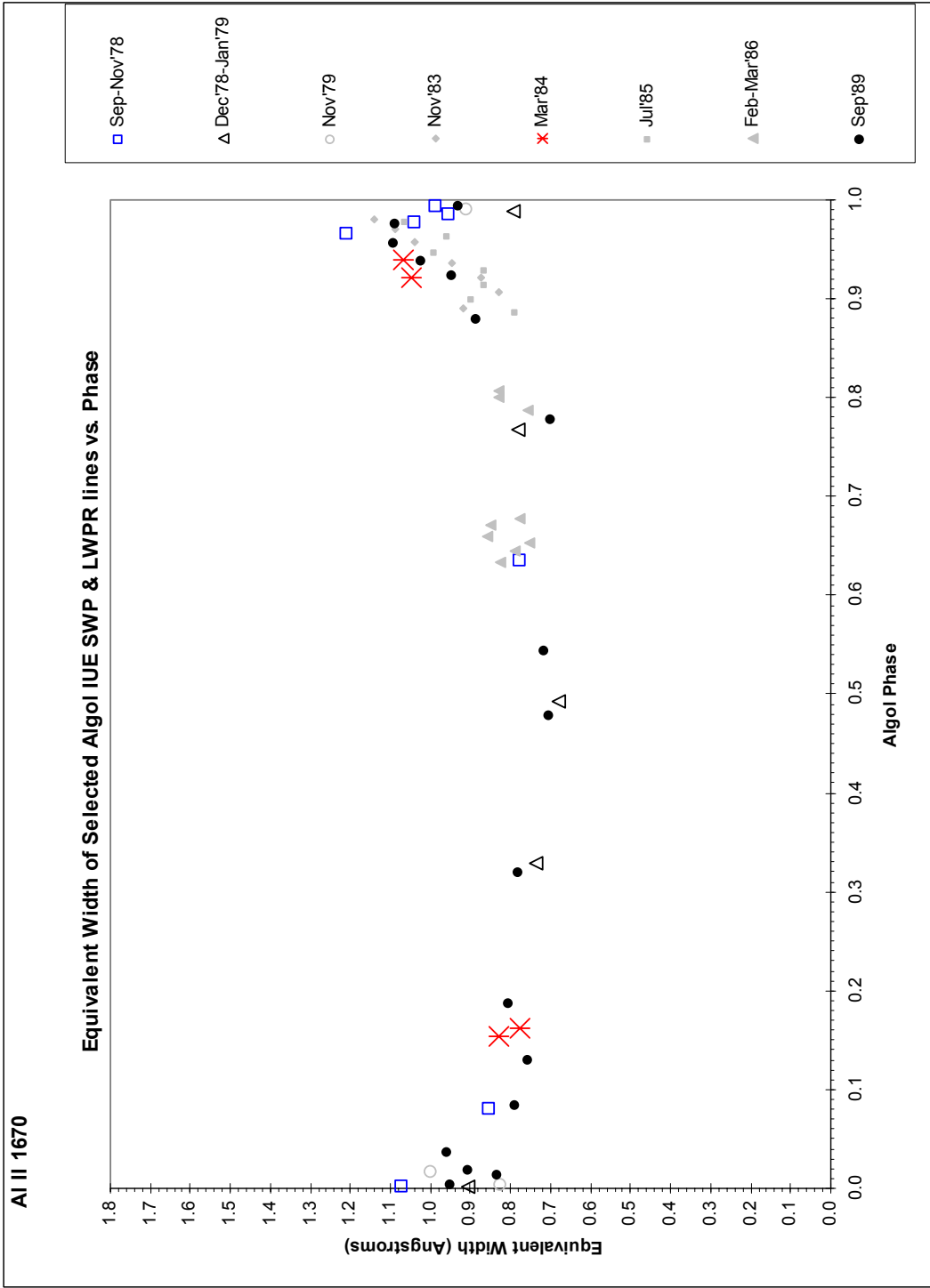


FIG 4.5.5.1 – Equivalent Width AI II 1670 line



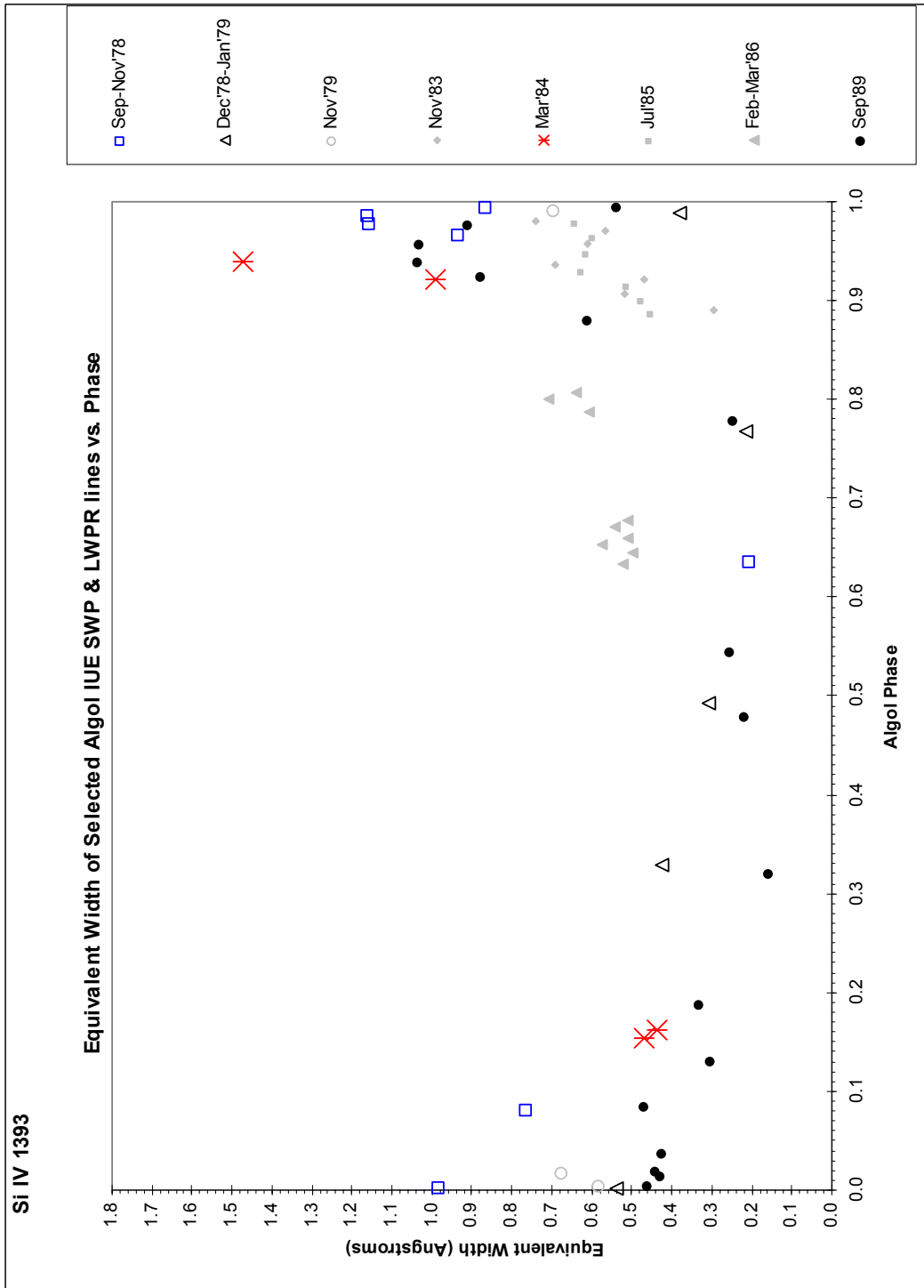


FIG. 4.5.5.2 - Equivalent Width Si IV 1393

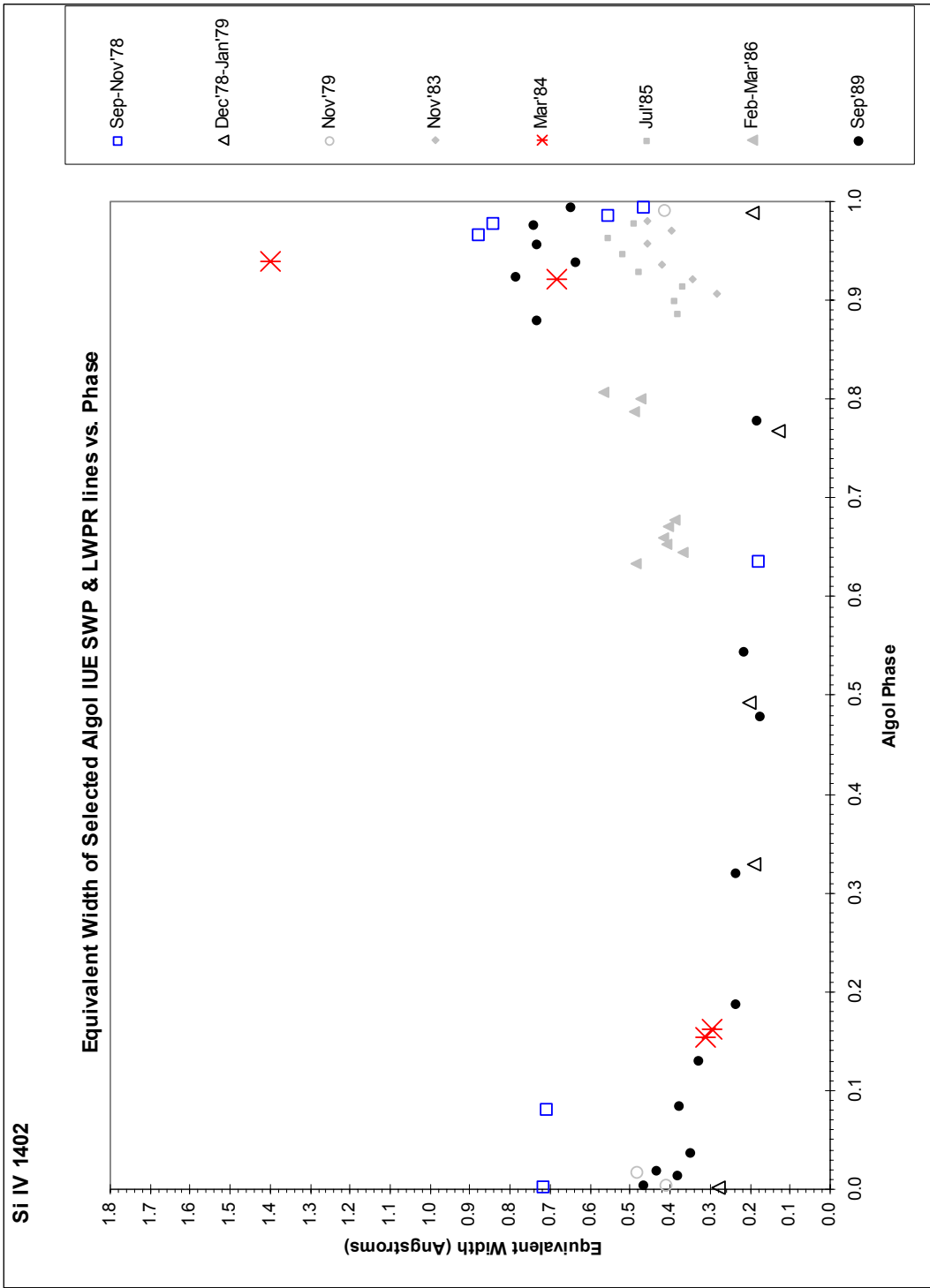


FIG. 4.5.5.3 - Equivalent Width Si IV 1402

#### 4.5.6 *Difference Spectra*

In order to isolate gas flow effects from photospheric and perhaps pseudo-photospheric contributions, we developed an approach that removes the stellar contributions from the spectra. This represents the first time the entire IUE archive for Algol is self-differenced in this manner.

The stellar contribution is assumed to be that of September 1989 exposure at phase 0.3209 since it consistently shows the most well-behaved absorption across the elements. Moreover, as mentioned earlier, the epoch of 1989 has the most complete phase coverage, and based on other work on Algol-type systems, it is reasonable to assume that phases near, first quadrature will show the effects of secular variations the least (Walter 1973, 1980).

To eliminate the assumed photospheric contribution, we subtracted that spectrum from the spectra of all other phases. Kempner and Richards (1999) used the star HD 23432 as a standard B8 V star. Their UV analysis of U Sge was done by subtracting the spectrum of the B8 V standard star HD 23432 from the observed U Sge spectrum. For Algol, this may not be a suitable comparison star because its rotational velocity is 283 km/s (Battrick 1984) where Algol's rotational velocity is 55 km/s. That of U Sge, on the other hand, is estimated to be 100 km/s (Struve, 1949), which is less of a differential. Although extra line broadening is present in HD 23432 as compared with U Sge, they felt that "this extra absorption should be relatively small compared to any emission from the circumstellar gas" (Kempner & Richards 1999, p. 347.) However, since Algol is in a low-activity stage as compared to U Sge (McCluskey et al. 1991, p. 281), it would be

preferable to find a more slowly rotating single B8 V star from the IUE archives taken in high dispersion mode. Unfortunately, no adequate comparison stars appropriate to Algol are included in the IUE data.

Before subtracting the spectra, we normalized them by eye, and then shifted the spectra to the rest frame of the center of mass (CM) of the primary star, since we expect the source of the UV observations to be largely relevant to structures at the surface of, near, and around the primary component. (See Section 4.3.3. Correction for Influence of Algol C).

By using the spectra of Algol itself for differencing, we eliminated the complication of the significant rotational broadening in the spectrum of the standard star, which in Kempner and Richards's words, "prevents us from truly eliminating the primary star's contribution to the spectrum since the standard star has shallower absorption features than desired." However, the choice of using a well-behaved spectrum from Algol itself does not guarantee success in "truly eliminating" the photospheric contribution of Algol A. But we proceeded with this method since it gives us an excellent comparison with Algol itself. The Si IV difference spectra from September 1978 date to September 1989 are presented in FIGs. 4.5.6.1a-c along with the corresponding original spectra.

The observed profiles show variations with orbital phase indicative of mass flow within and from the system.

Starting at phase  $\sim 0.54$  and scanning through to phase  $\sim 0.88$ , we see a double peaked absorption feature developing which we interpret as an asymmetrically distributed disk-like structure. Then from phase  $\sim 0.88$  to phase  $\sim 0.98$ , the redshifted absorption peak

develops as our line of sight from Earth changes from looking across the gas stream to looking along the gas stream. As primary eclipse progresses the gas stream is, for the most part, eclipsed at phase 0.003 where we again see evidence of a disk-like structure with one absorption peak blueshifted and the other redshifted. As the eclipse approaches egress, the gas stream starts to become visible again (phase  $\sim 0.09$ ) as it recedes from us along our line of sight, redshifted. Notice that the absorption after primary is not as strong as the absorption before primary indicative of gas streaming. At phase  $\sim 0.48$ , the gas stream is no longer evident, that is, it is hidden from view as it is occulted during secondary eclipse.

Radial velocities have been recalculated and column ion numbers have been calculated from the spectral features isolated using the difference spectrum method. These results are shown for Mg II  $\lambda 2796$  in FIGs. 4.5.6.6 and 4.5.6.7, respectively. Note that there are two components to the gas stream, moving toward and away from us at about  $\leq$  km/sec, as seen in FIG. 4.5.6.6. FIG. 4.5.6.7 shows the ion numbers appropriate to the two components. These results can be interpreted as representing the two sides of a circumstellar disc located about the primary.

A complete table of these results is provided in Appendix D.6.

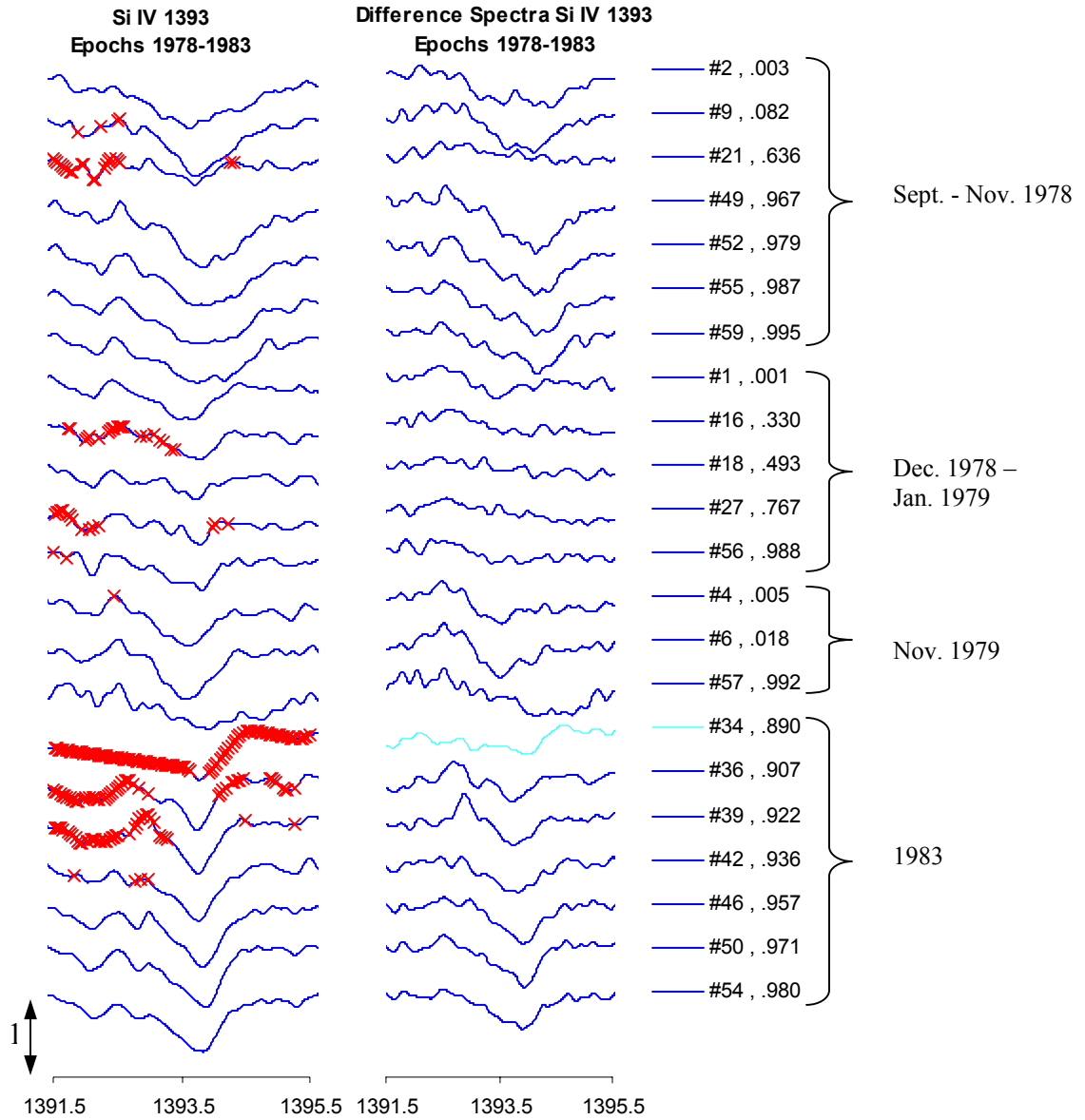


FIG. 4.5.6.1a—ALGOL IUE SWP SPECTRA Si IV 1393. *Left*, smoothed spectra. *Right*, difference spectra.

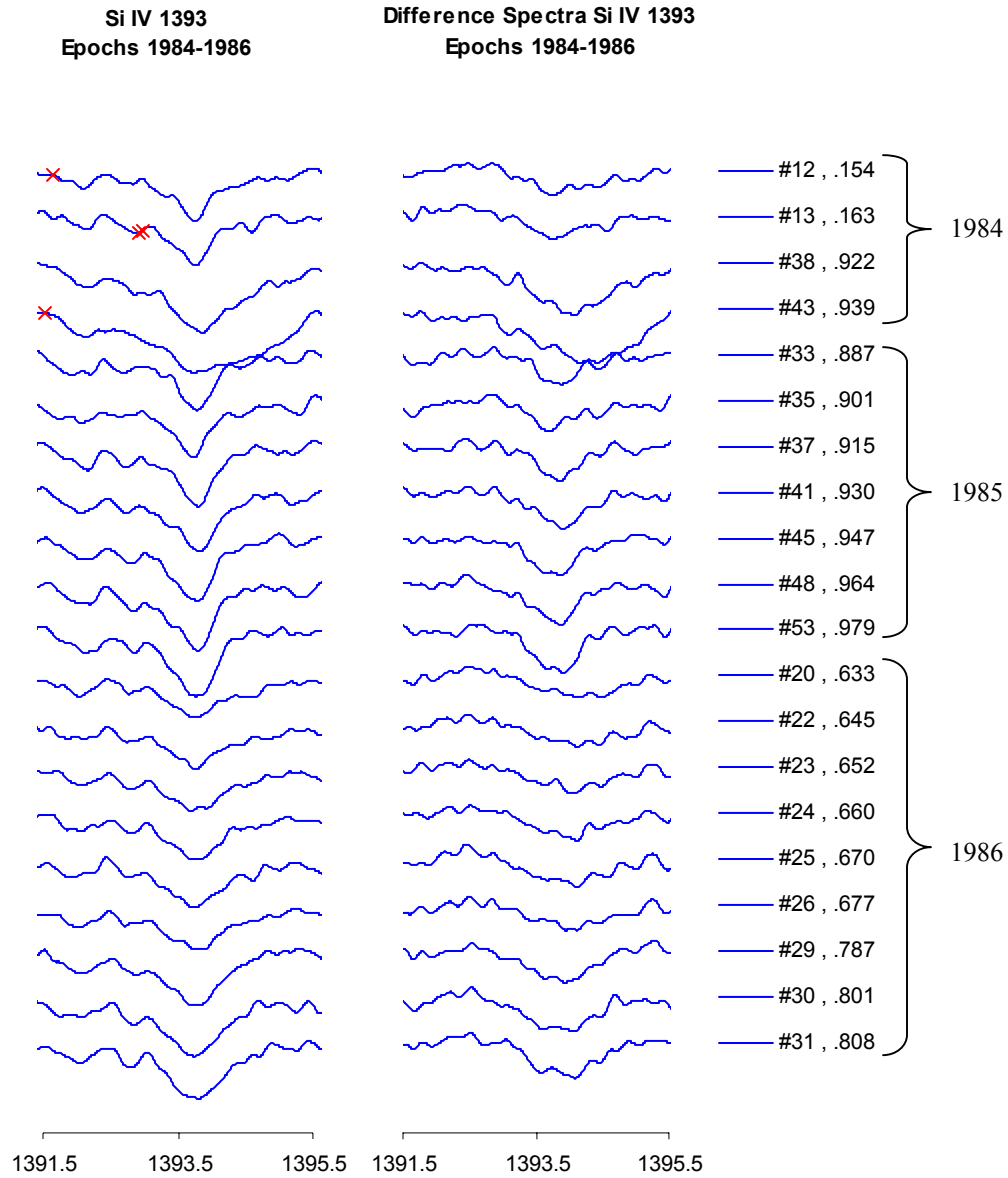


FIG. 4.5.6.1b—ALGOL IUE SWP SPECTRA Si IV 1393. *Left*, smoothed spectra. *Right*, difference spectra.

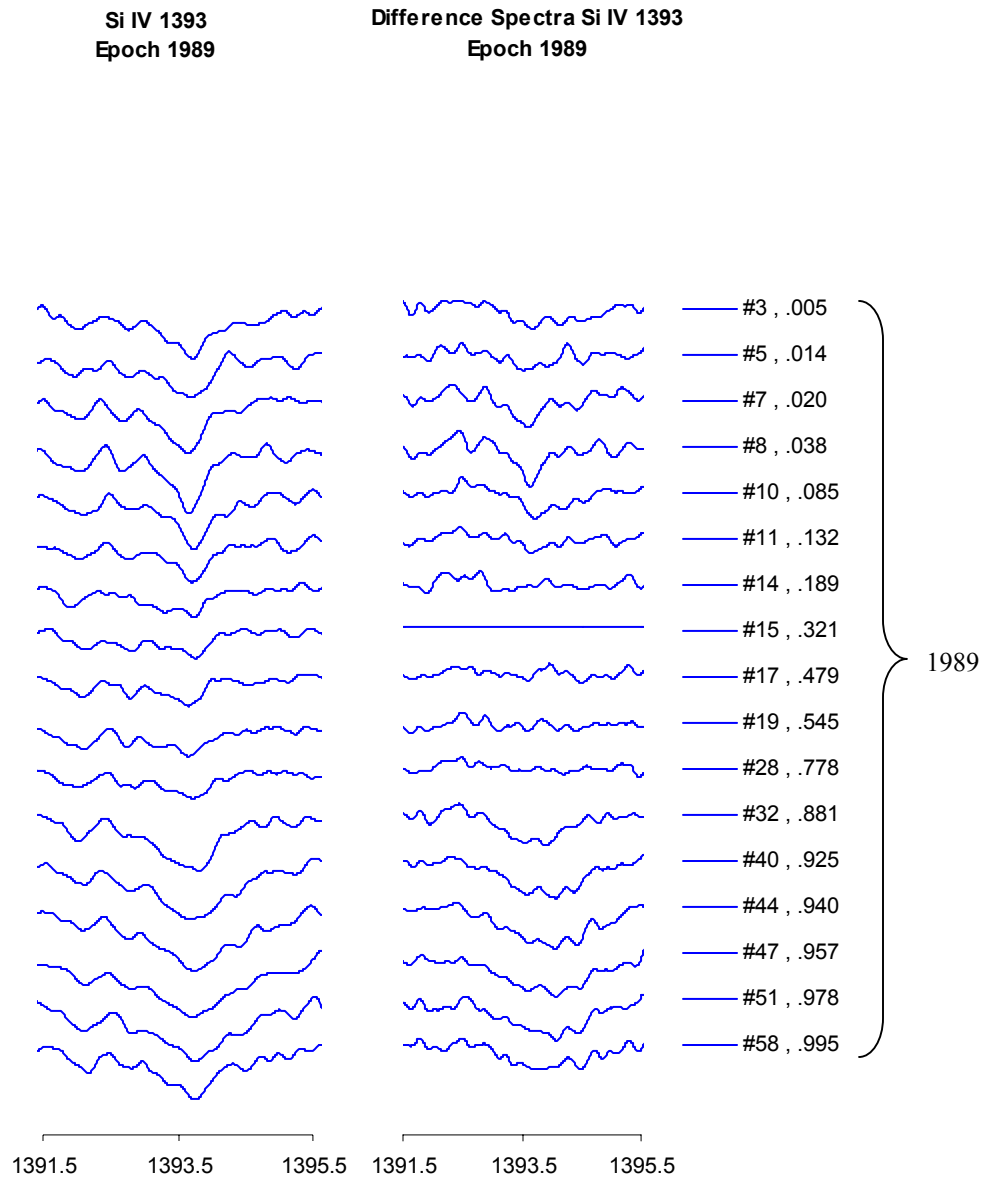


FIG. 4.5.6.1c—ALGOL IUE SWP SPECTRA Si IV 1393. *Left*, smoothed spectra. *Right*, difference spectra.



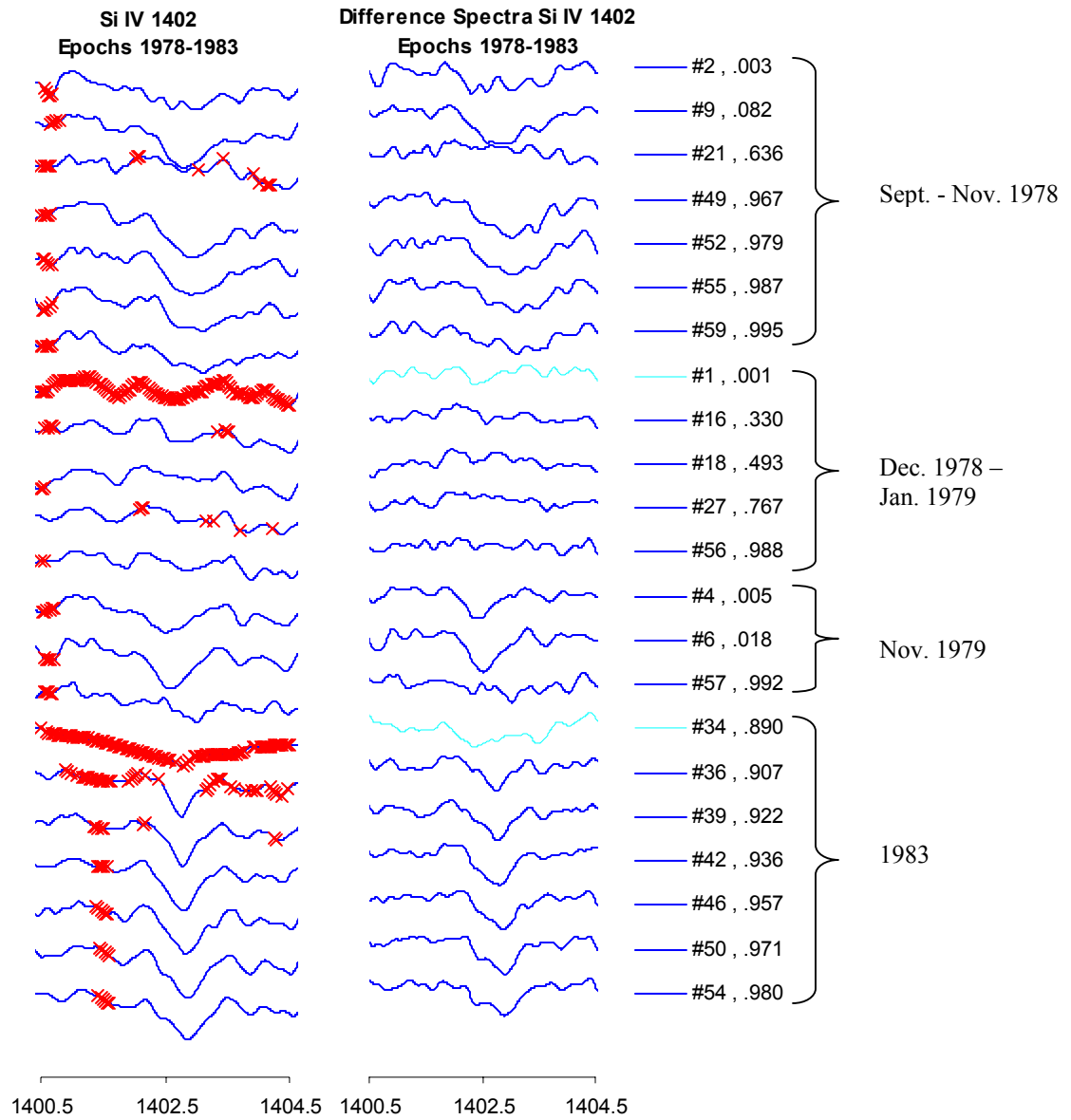


FIG. 4.5.6.2a—ALGOL IUE SWP SPECTRA Si IV 1402. *Left*, smoothed spectra. *Right*, difference spectra.

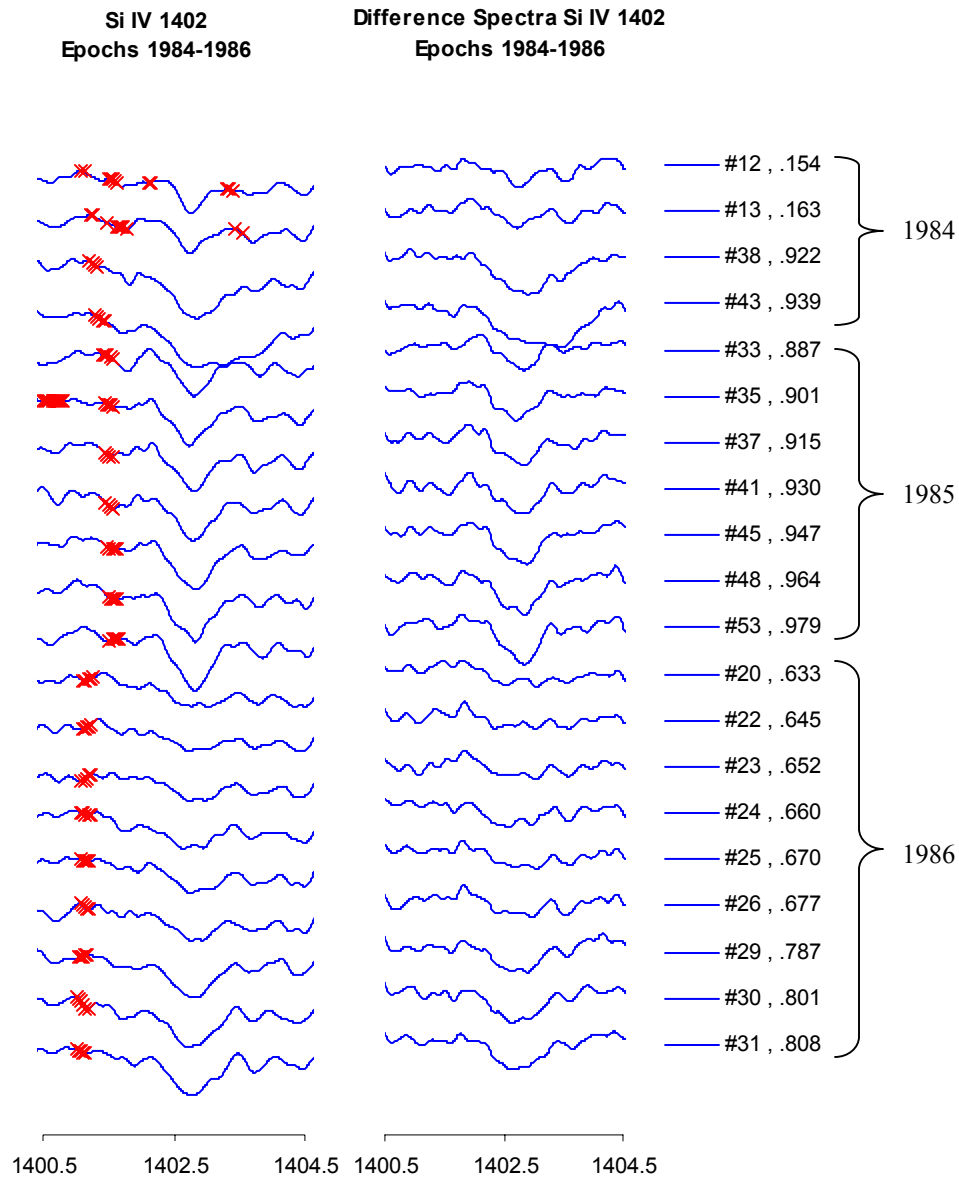


FIG. 4.5.6.2b—ALGOL IUE SWP SPECTRA Si IV 1402. *Left*, smoothed spectra. *Right*, difference spectra.

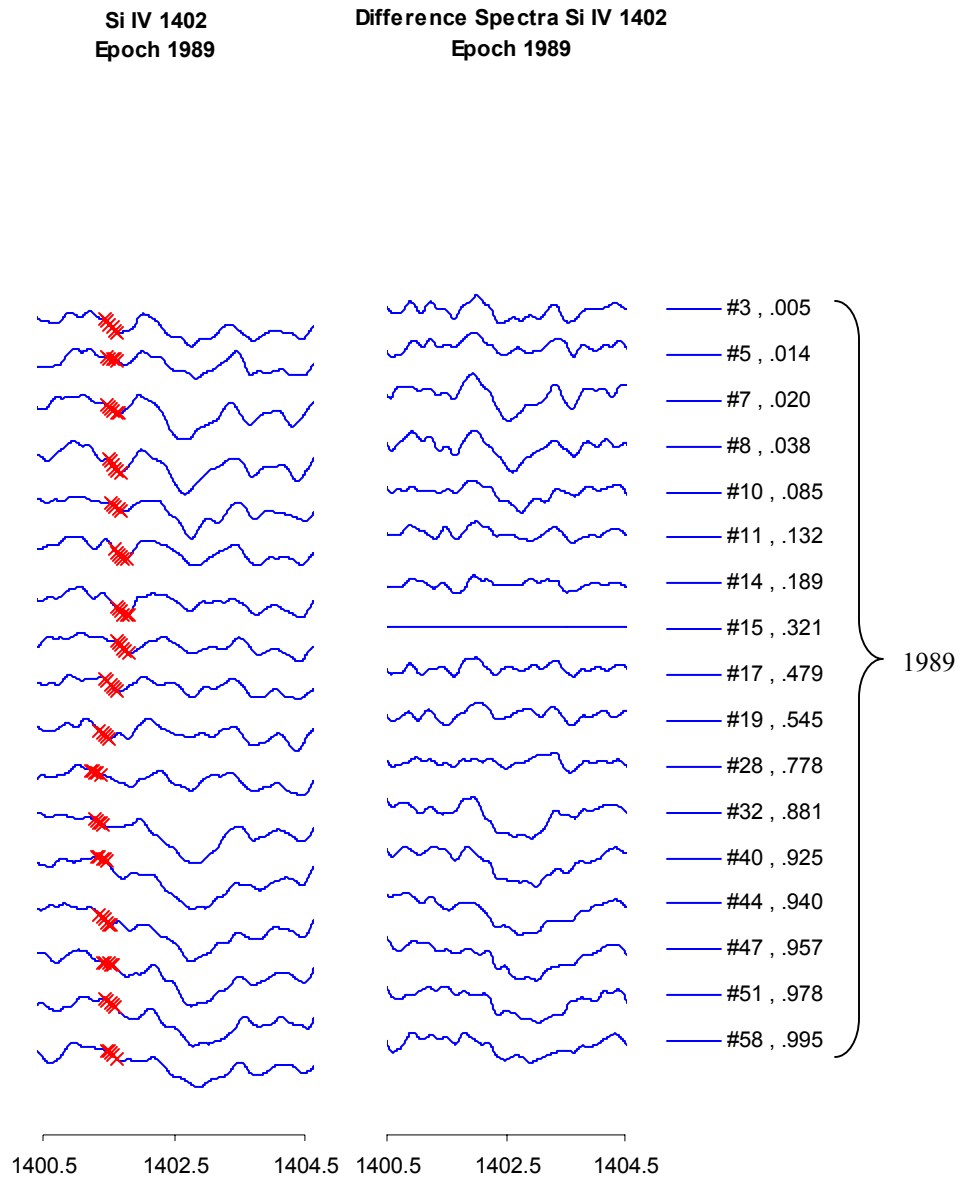


FIG 4.5.6.2c—ALGOL IUE SWP SPECTRA Si IV 1402. *Left*, smoothed spectra. *Right*, difference spectra.

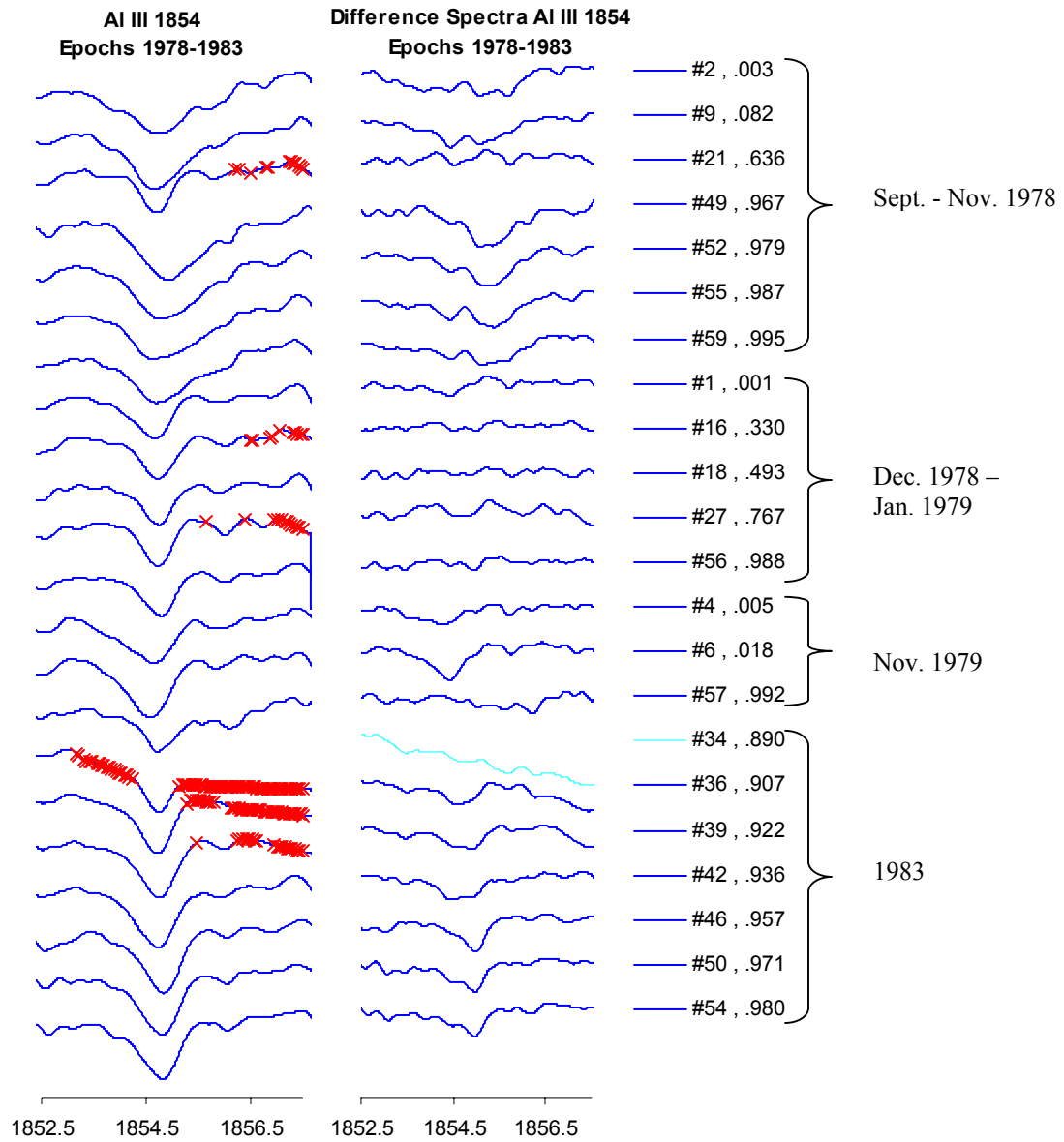


FIG. 4.5.6.3a—ALGOL IUE SWP SPECTRA Al III 1854. *Left*, smoothed spectra. *Right*, difference spectra.

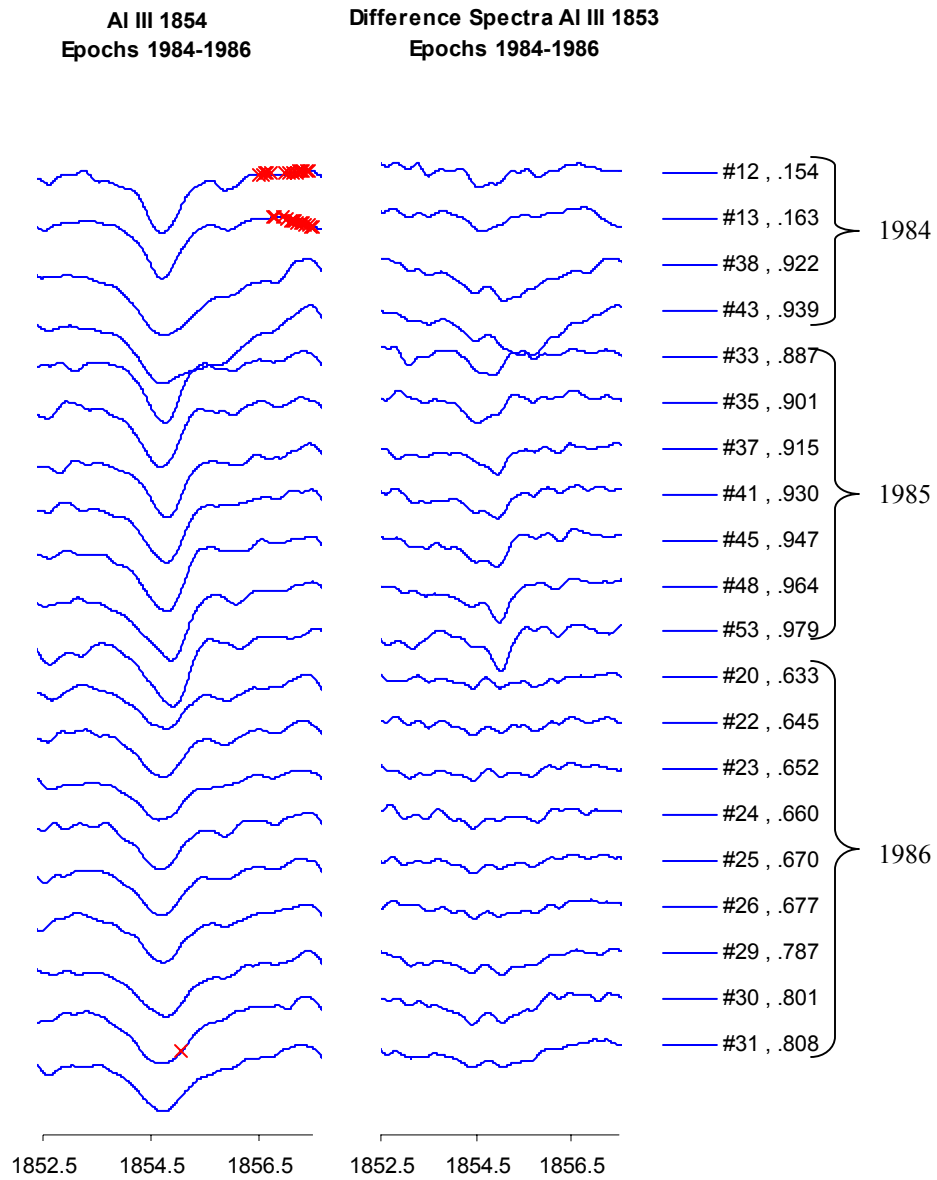


FIG. 4.5.6.3b—ALGOL IUE SWP SPECTRA Al III 1854. *Left*, smoothed spectra. *Right*, difference spectra.

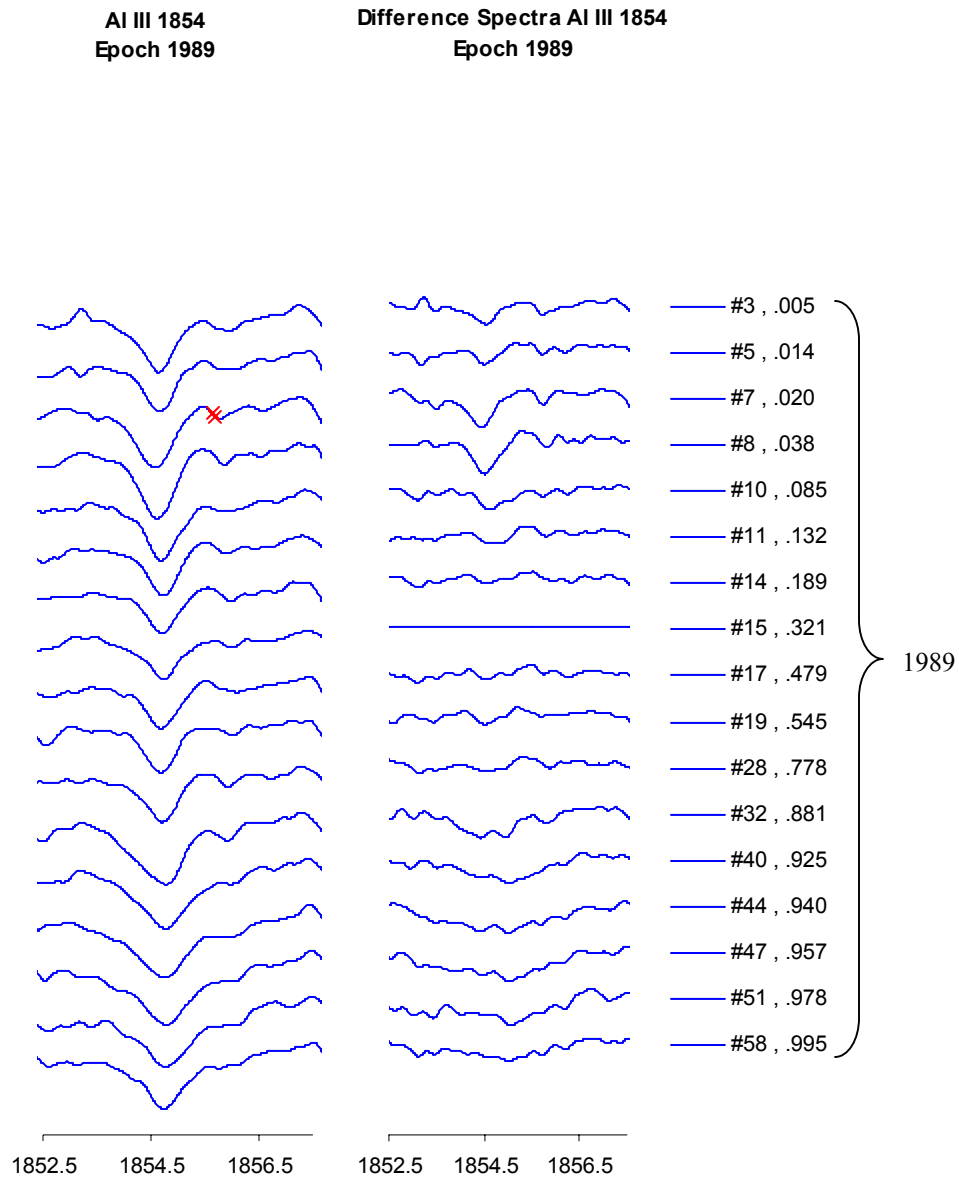


FIG. 4.5.6.3c—ALGOL IUE SWP SPECTRA Al III 1854. *Left*, smoothed spectra. *Right*, difference spectra.

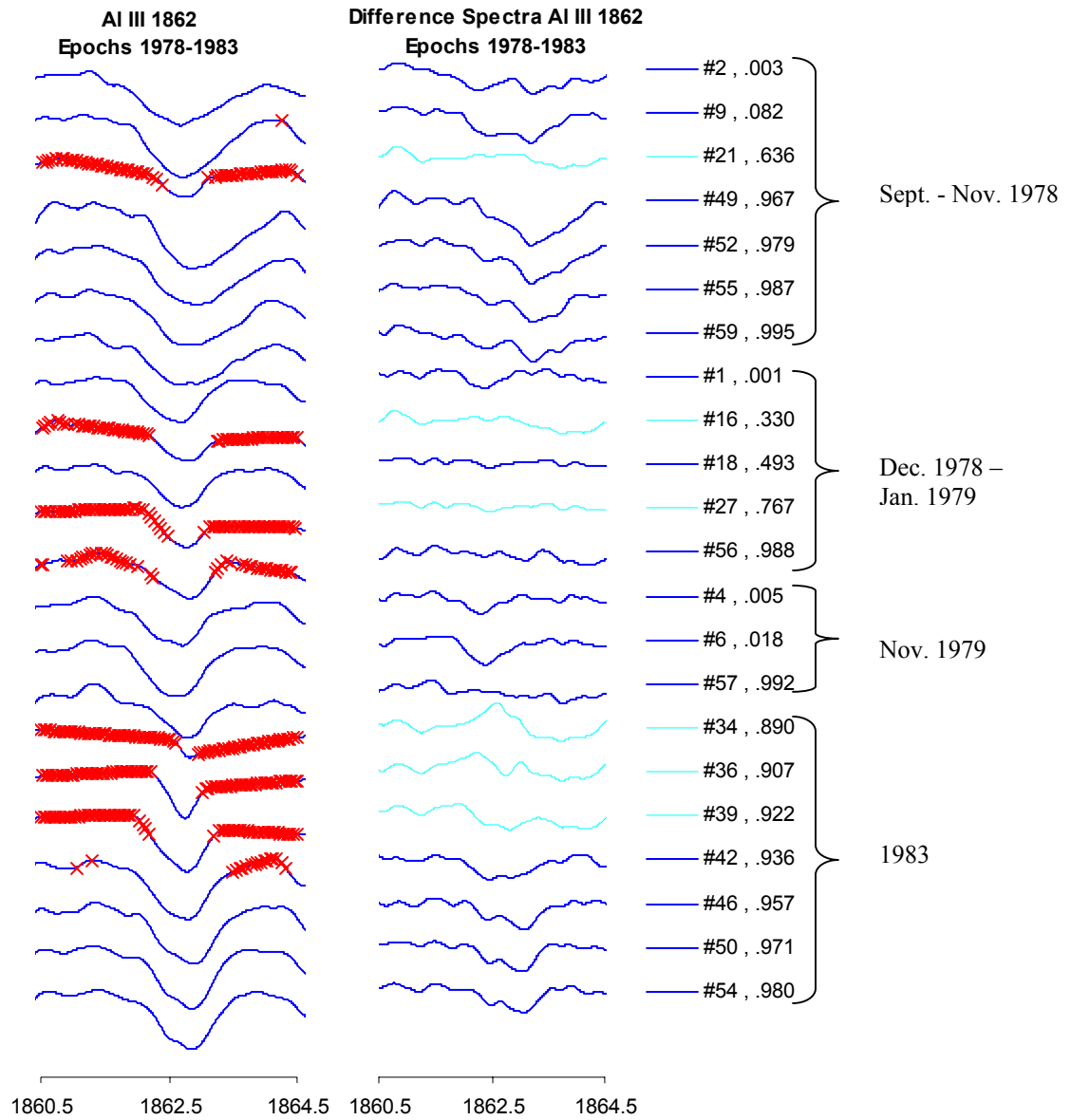


FIG 4.5.6.1.4a—ALGOL IUE SWP SPECTRA Al III 1862. *Left*, smoothed spectra. *Right*, difference spectra.

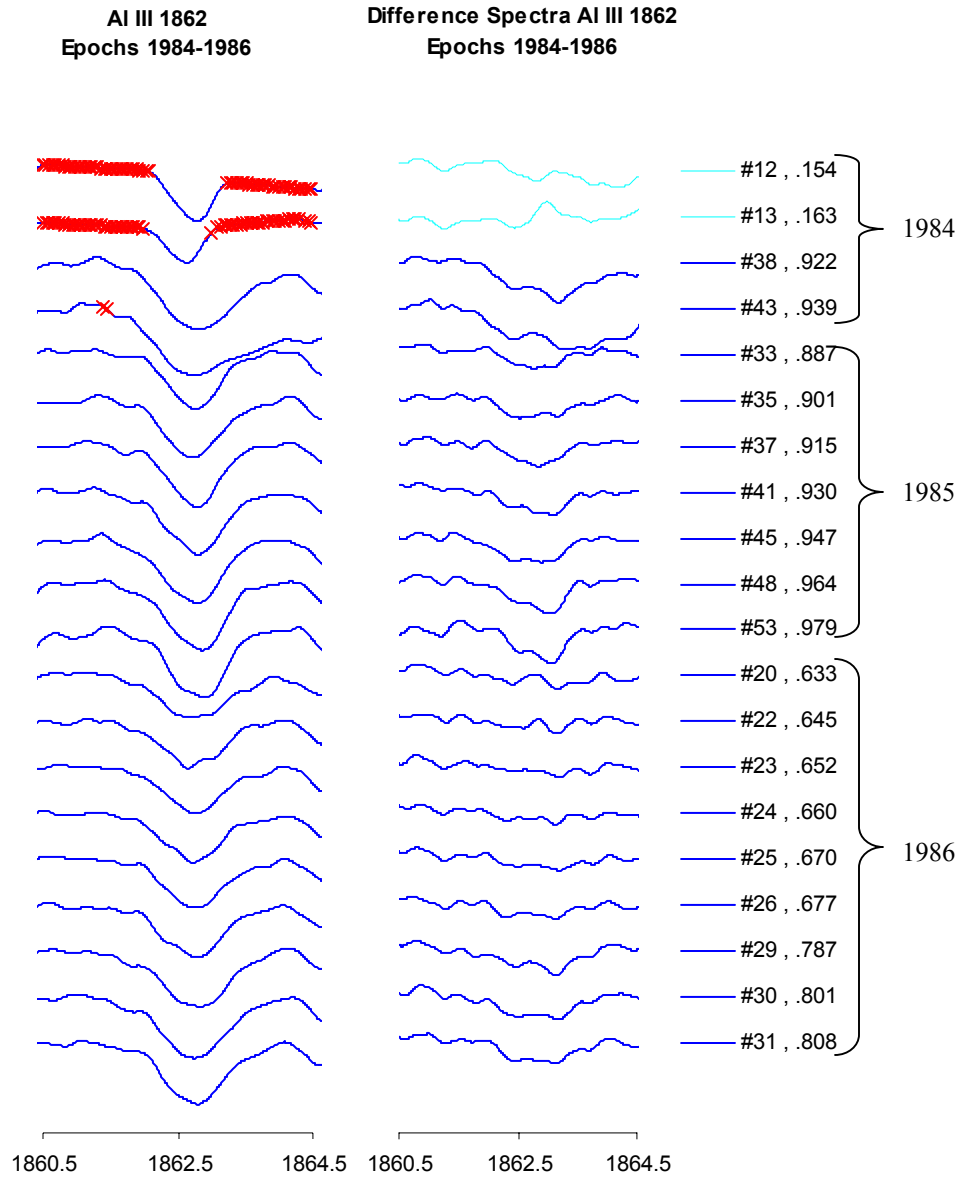


FIG. 4.5.6.4b—ALGOL IUE SWP SPECTRA Al III 1862. *Left*, smoothed spectra. *Right*, difference spectra.



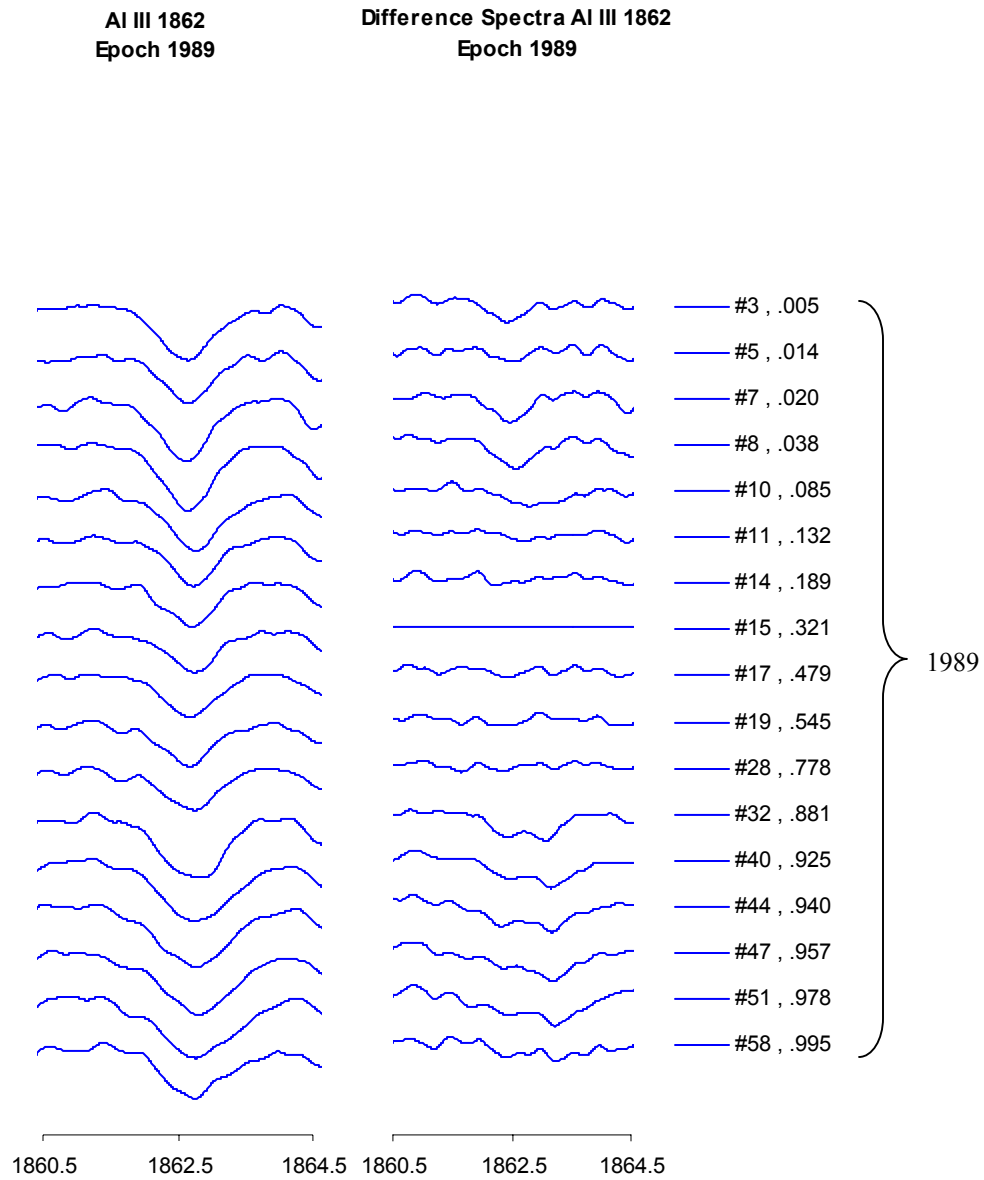


FIG. 4.5.6.4c—ALGOL IUE SWP SPECTRA Al III 1862. *Left*, smoothed spectra. *Right*, difference spectra.

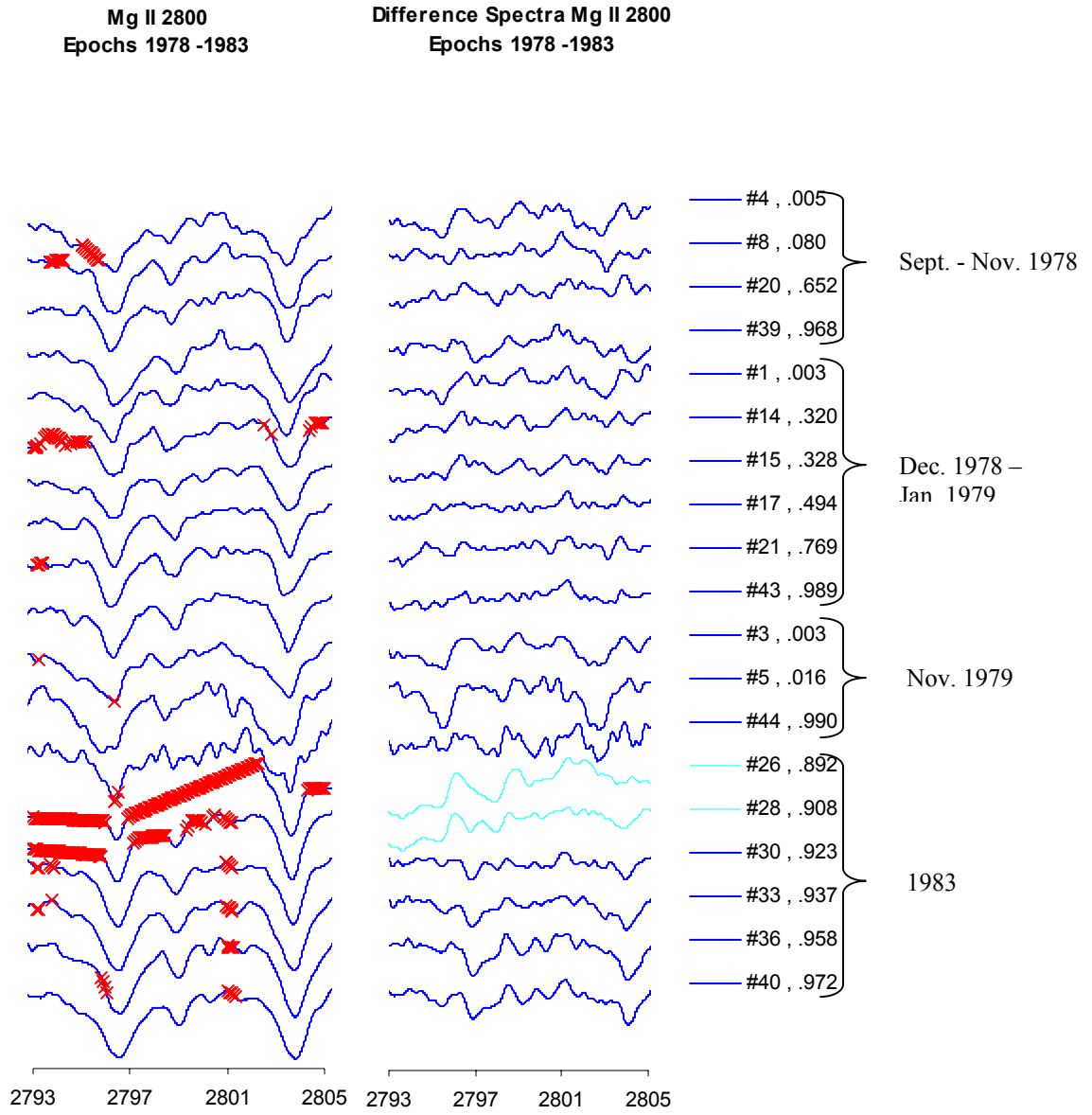


FIG. 4.5.6.5a—ALGOL IUE LWP/LWR SPECTRA Mg II near 2800. *Left*, smoothed spectra. *Right*, difference spectra.

Mg II 2800  
Epochs 1984 - 1986

Difference Spectra Mg II 2800  
Epochs 1984 - 1986

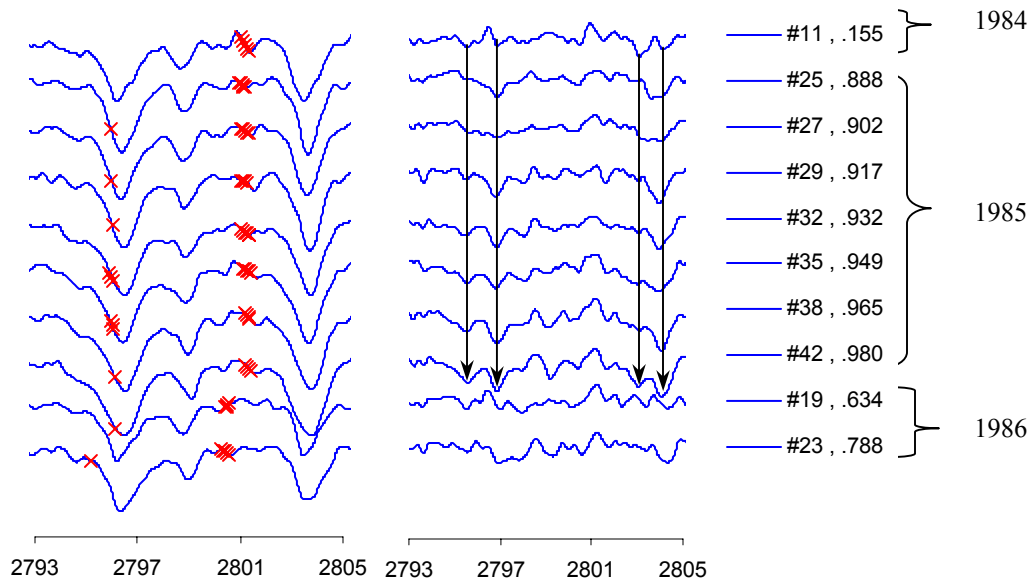


FIG. 4.5.6.5b—ALGOL IUE LWP/LWR SPECTRA Mg II near 2800. *Left*, smoothed spectra. *Right*, difference spectra. Arrows indicate sets of double peaked absorption features.

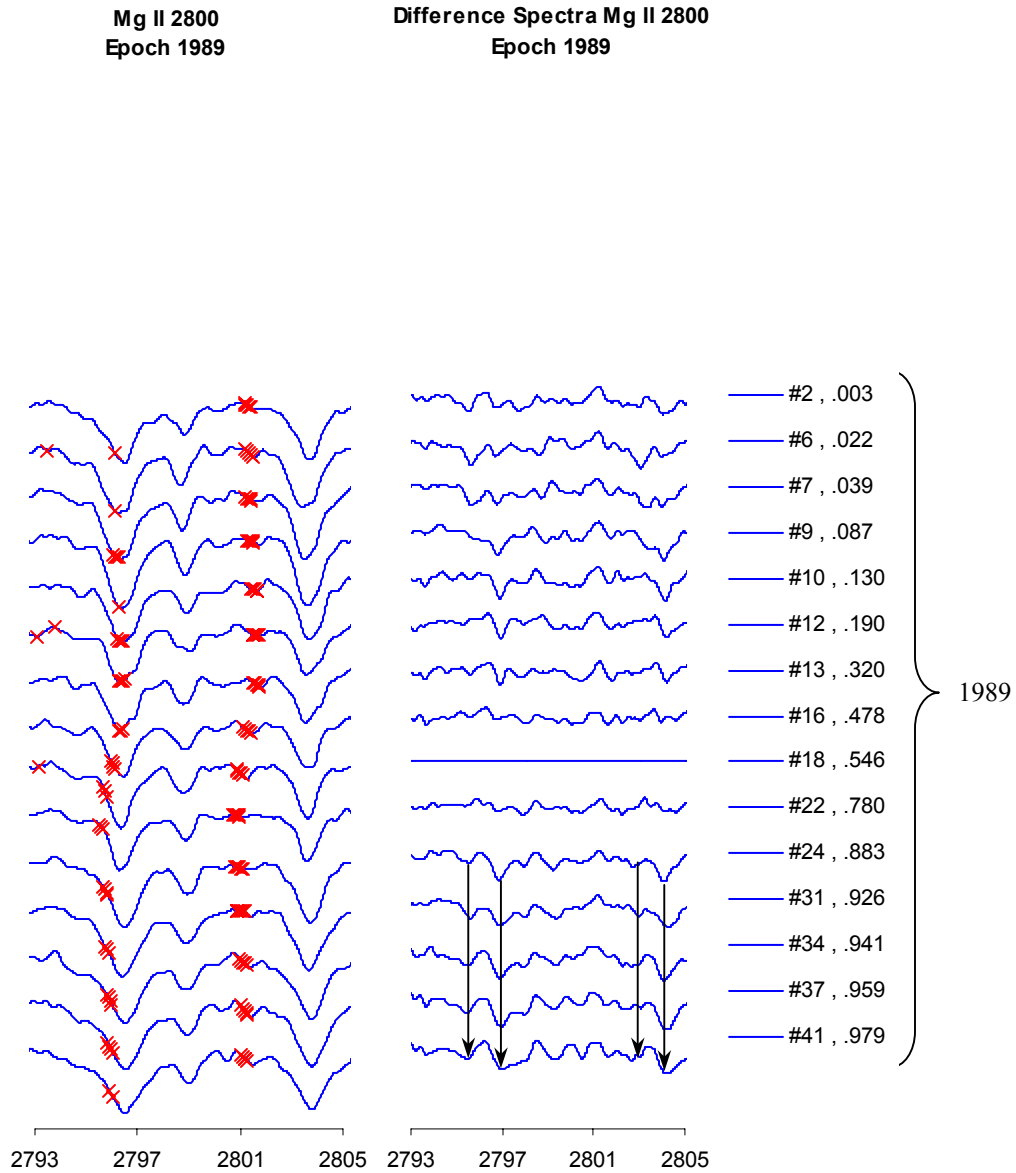


FIG. 4.5.6.5c—ALGOL IUE LWP/LWR SPECTRA Mg II near 2800. Left, smoothed spectra. Right, difference spectra. Arrows indicate sets of double peaked absorption features.

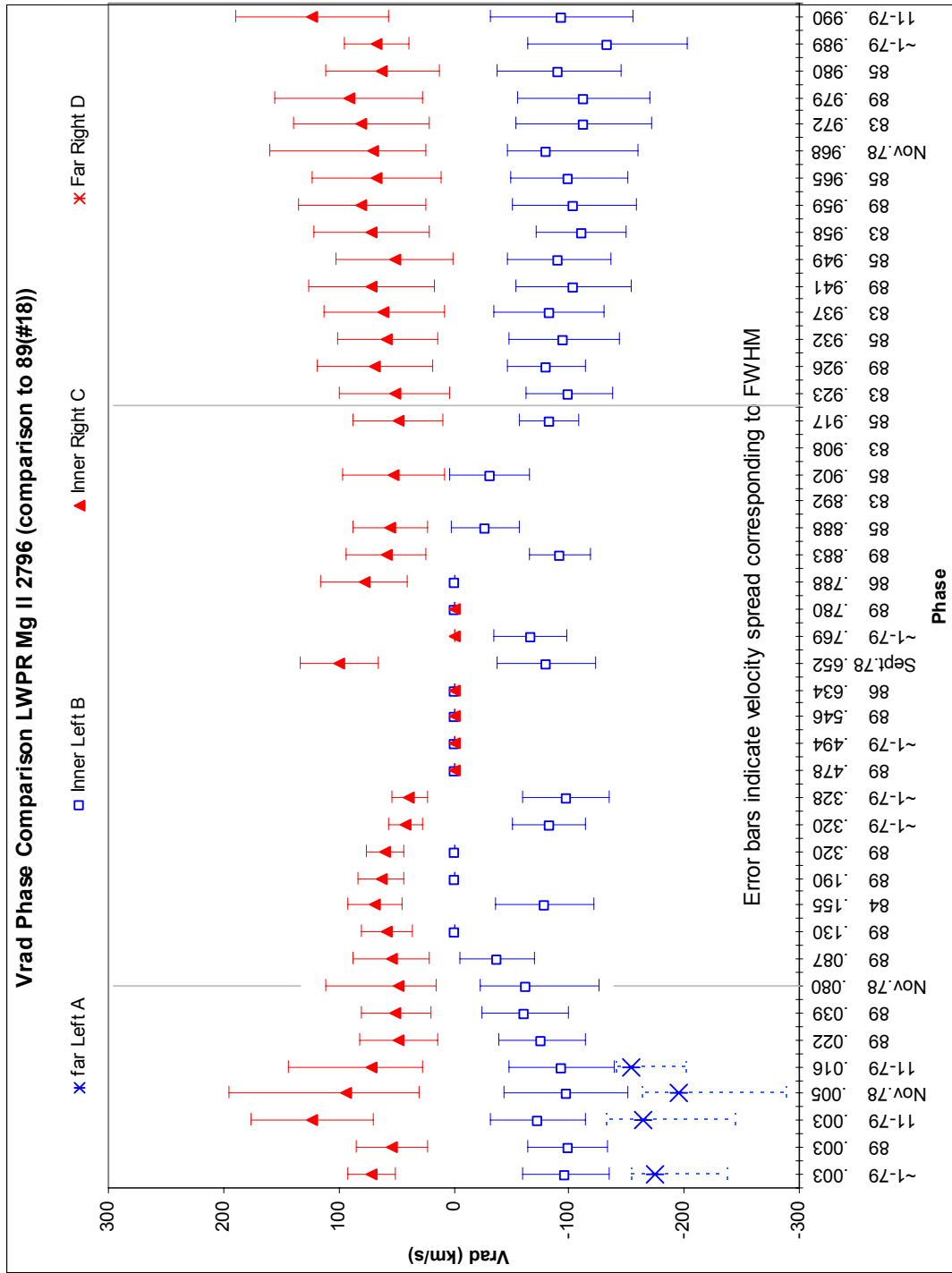


FIG. 4.5.6.6—Vrad Phase Comparison LWP/LWR Mg II 2796

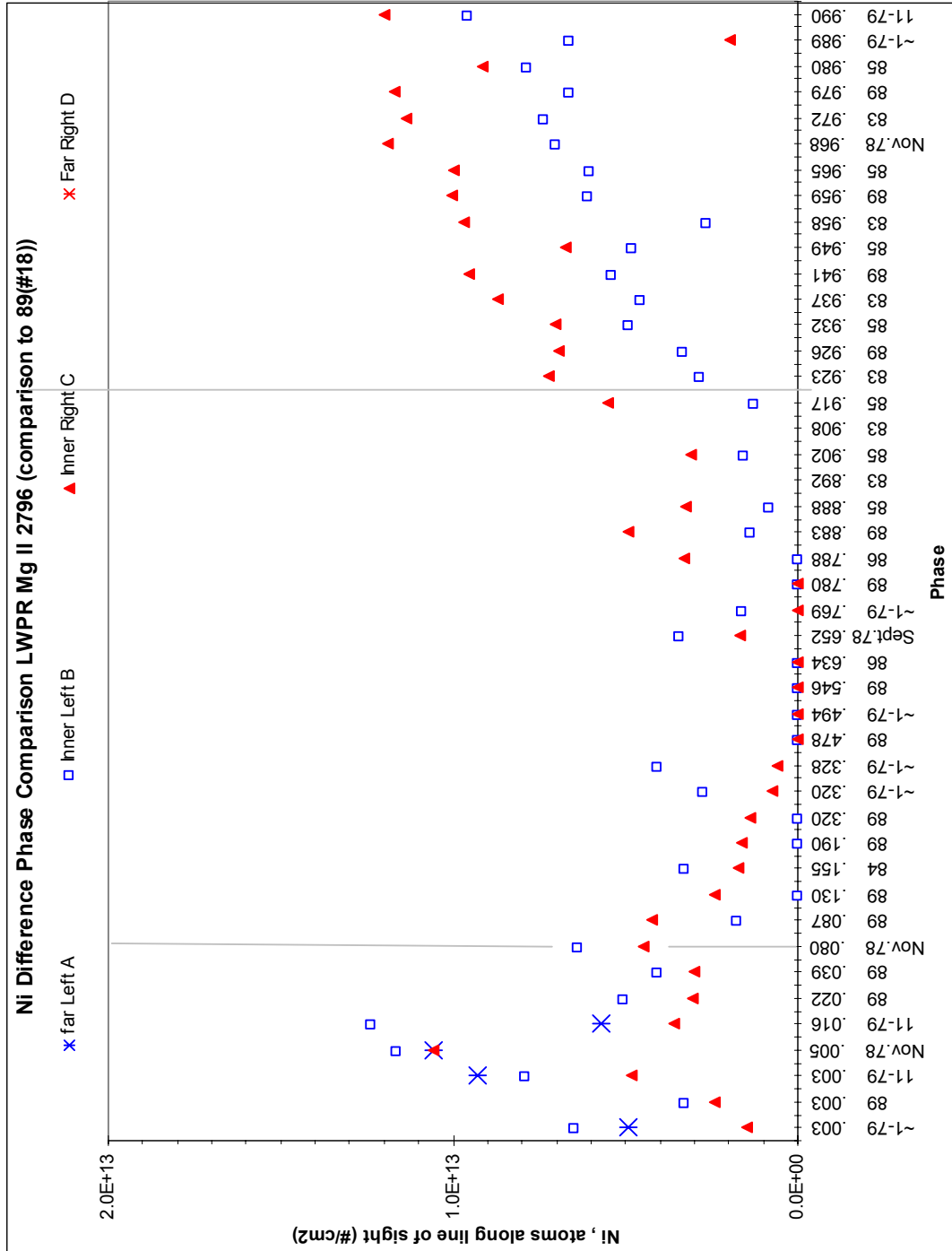


FIG. 4.5.6.7—Ni Difference Phase Comparison LWP/LWR Mg II 2796

In anticipation of our mass flow calculation in the following sections, we must consider complications due to the Rossiter effect as they contribute to our difference spectra. Therefore, we follow the method of Cugier and Chen (1977) where they differenced in-eclipse exposures of Algol (taken with the Copernicus satellite 1974 January 4) situated approximately symmetrically about the time of mid-primary eclipse. FIG. 4.5.6.8 is a coplot of such a pair from their data at phases  $\sim 0.928$  (solid line) and  $\sim 0.074$  (broken line).

If primary eclipse is symmetric the difference between these two symmetrically placed exposures about primary eclipse should be zero. However, Cugier and Chen demonstrated that there is an additional absorption component evident in the difference spectrum, shown in FIG. 4.5.6.9, which indicates gas flowing from the secondary star. Our difference spectra (next section) are also consistent with a gas flow model.

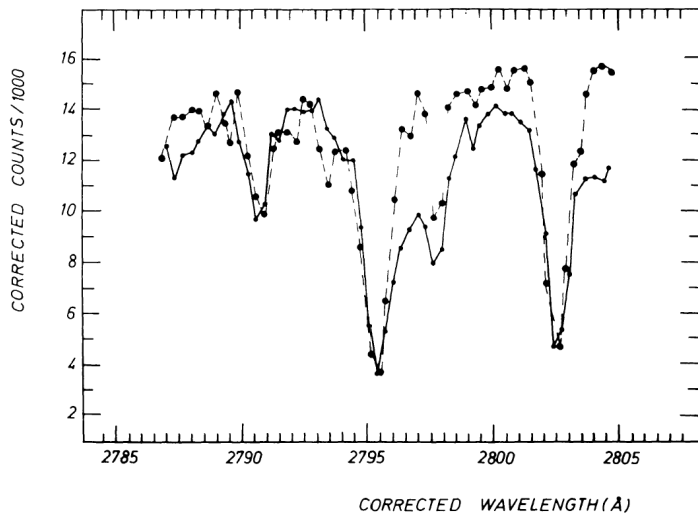


FIG 4.5.6.8—Mg II  $\lambda\lambda 2796, 2803$ . (Source Fig. 1, p. 170, Cugier and Chen 1977)

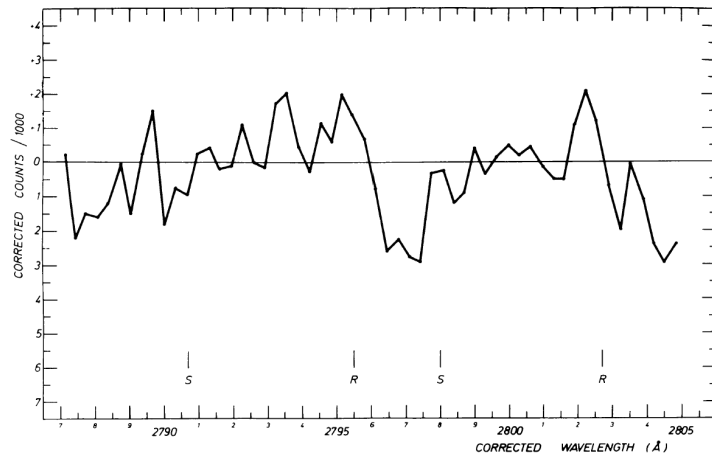


FIG 4.5.6.9—Mg II  $\lambda\lambda$ 2796, 2803 Difference Spectrum. (Source Fig. 2, p. 171, Cugier and Chen 1977)



#### 4.5.7 Mass Loss Rates

Using the method of Cugier and Chen (1977), we estimate the mass loss rate from the secondary star. The first step is to identify pairs of spectra situated symmetrically with respect to the time of primary minimum ( $\phi = 0.0$ ), where one of the pair contains extra absorption presumed to be the gas stream. Selected phase pairs in epoch 1989 are:  $\phi = 0.022$  and  $0.9794$ ,  $0.959$  and  $0.039$ , and  $0.9259$  and  $0.0867$ . See Table 4.5.7.1.

TABLE 4.5.7.1  
PHASES USED FOR MIRROR COMPARISON OF Mg II

LWP/LWR Group I.D.	Phase	Epoch	Lines Used
41 6	0.9794 0.022	1989	Mg II 2796 and 2803
37 7	0.959 0.039	1989	Mg II 2796 and 2803
31 9	0.9259 0.0867	1989	Mg II 2796 and 2803

The difference spectrum is then calculated between each mirror pair, i.e., 41 minus 6, 37 minus 7, and 31 minus 9. FIG. 4.5.7.1. shows the 41-6 pair which corresponds to exposure LWP16322 ( $\phi = 0.9794$ , LWP/LWR ID: 41) minus exposure LWP16324 ( $\phi = 0.022$ , LWP/LWR ID: 6). See TABLE 3.2.3 for the index of LWP/LWR IDs. The two upper curves are the spectra before differencing. The lower curve is the difference spectrum.

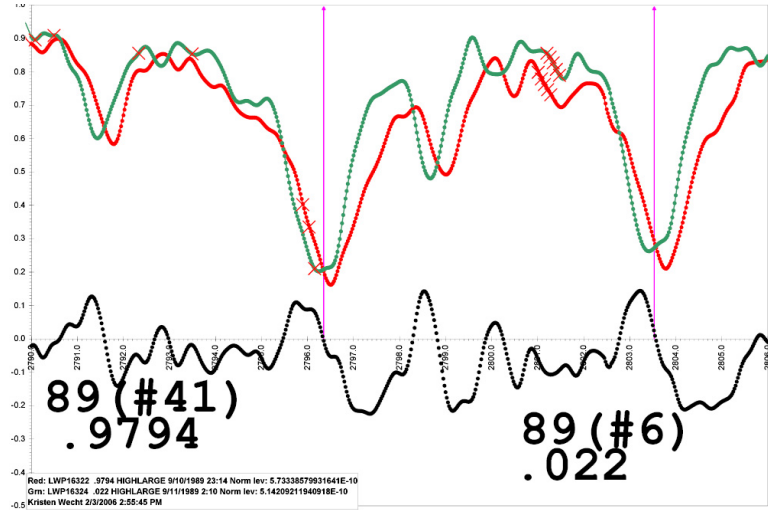


FIG. 4.5.7.1– *Difference Spectrum Corresponding Phases Symmetrically Situated About Primary Eclipse*

Equivalent widths and radial velocities of the extra absorption components are measured and the number of atoms along the line of sight is calculated using (in SI units)

$$N = \frac{4\epsilon_0 c^2 m_e}{e^2 \lambda^2 f_{ik}} W_\lambda \quad (4.5.7.1)$$

where  $f_{ik}$  is the oscillator strength (NIST online archive)

The mass loss rate may now be calculated using Equations (1), (2), and (3), Cugier and Chen (1977), page 173.

Their Equation (1) states that the equivalent width  $W_\lambda$  is proportional to the product of the mean density of the gas stream  $\rho$ , the geometrical depth along the line of sight  $\Delta Z$ , and the ratio of the number of Mg II atoms to the total number of Mg atoms  $N$  (Mg II)/ $N$ (Mg).

$$W_\lambda \propto \rho \times \Delta Z \times \frac{N(\text{Mg II})}{N(\text{Mg})} \quad (4.5.7.2)$$

For a rough estimate, we assume that most of the Mg is singly ionized, i.e.,

$$\frac{N(\text{Mg II})}{N(\text{Mg})} \approx 1 \quad (4.5.7.3)$$

And since

$$N_i \propto W_\lambda, \quad (4.5.7.4)$$

we have

$$N_i \propto \rho \times \Delta Z \quad (4.5.7.5)$$

But  $N_i$  is in units of atoms/area and  $\rho \times \Delta Z$  is in units of mass/ area. Therefore, we multiply  $N_i$  by mass/atom, which for Mg is (24.305 amu)  $\times$  (1.6606  $\times 10^{-24}$  g/amu)

$$= 4.036 \times 10^{-23} \text{ g/ Mg atom}$$

Therefore,

$$\rho = \frac{N_i (4.036 \times 10^{-23} \text{ g/ Mg atom})}{\Delta Z} \quad (4.5.7.6)$$

Cugier and Chen (1977) estimate  $\Delta Z \approx 1 R_A$  and the cross section of the stream  $\sigma \sim (R_A)^2$ . We then let the velocity of the stream  $v \approx V_{\text{rad}}$ . The mass is then calculated using the relation

$$\begin{aligned} \frac{dM}{dt} &= \rho \times \sigma \times v \\ &\approx \left( 4.036 \times 10^{-23} \frac{\text{g}}{\text{Mg atom}} \right) N_i R_A V_{\text{rad}} \left( \frac{M_\odot}{M_{\text{mg}}} \right) \end{aligned} \quad (4.5.7.7)$$

where  $R_A = 2.01837 \times 10^{11}$  cm (See Appendix A, Table 27.)

$$M_{\text{Mg}} = .00076 M_\odot \text{ (assuming solar abundances)} \quad (4.5.7.8)$$

The final convenient equation we used to calculate the mass loss rate is

$$\frac{dM}{dt} = (1.295 \times 10^{-32}) N_i V_{rad} \quad (4.5.7.9)$$

which gives the results in units of  $M_{\odot}/\text{yr}$  when  $N_i$  is expressed as the number of Mg atoms per  $\text{cm}^2$  and  $V_{rad}$  is expressed in km/s. The results are listed in TABLE 4.5.7.2. The mirror difference pair 41 ( $\phi = 0.9794$ ) minus 6 ( $\phi = 0.022$ ) gives the highest mass loss rate  $\frac{dM}{dt} = (1.9 \times 10^{-14}) M_{\odot}/\text{yr}$  in the 1989 epoch. The mass loss rate estimated by Cugier and Chen (1977) from the Copernicus satellite data is  $10^{-13} M_{\odot}/\text{yr}$ . This would indicate that January 1974 is an epoch of higher activity than September 1989.

There are several sources of error to consider. The spectra are noisy and although the smoothing process is helpful in distinguishing noise from real features it slightly changes the line width and depth. We are estimating the line profile assuming a Gaussian shape which is not necessarily the shape of the line if the instrumental broadening is significant. This does not affect the equivalent width measurements, however it may affect the estimate of the velocity gradients and thus the difference spectra. The eclipse spectra have a lower continuum and therefore the signal to noise ratio is less as well.

To obtain an estimate of the error the mass loss rate can be calculated using the difference spectra of other spectral lines.

TABLE 4.5.7.2  
 PROPERTIES OF LONGWARD MIRROR – DIFFERENCE COMPONENT

MIRROR DIFFERENCE PAIR	$W_\lambda$ $\lambda_{2796}$ $\lambda_{2803}$	$W_\lambda$ AVG ( $\text{\AA}$ )	$N_i$	$N_i$ Avg ( $\#/\text{cm}^2$ )	$V^{\text{rad}}$	$V^{\text{rad}}$ Avg (km/s)	HWHM	HWHM <sub>Avg</sub> (km/s)	$\frac{dM}{dt}$ ( $M_\odot/\text{yr}$ )
41 - 6	.23 .33	.28	$5.58 \times 10^{12}$ $1.55 \times 10^{13}$	$1.054 \times 10^{13}$	100.6 115.4	108	52.5 77.5	65	$1.94 \times 10^{-14} \pm 1.17 \times 10^{-14}$
37 - 7	.15 .15	.15	$3.48 \times 10^{12}$ $6.99 \times 10^{12}$	$5.235 \times 10^{12}$	73.8 80.1	77.45	32.1 30.5	31.3	$6.9 \times 10^{-15} \pm 2.79 \times 10^{-15}$
31 - 9	.08 .09	.085	$1.99 \times 10^{12}$ $4.08 \times 10^{12}$	$3.035 \times 10^{12}$	99.5 123.9	111.7	34.8 41.2	38	$5.8 \times 10^{-15} \pm 1.965 \times 10^{-15}$

## 5. DISCUSSION AND CONCLUSIONS

In the previous chapter, we presented several analyses of the IUE data resulting in various measures of Algol system properties. These measures pertain to the ionized gases flowing into and about Algol A and those constituting the photospheric region. And, they tell a story that is difficult to unravel. Although a degree of interpretation was provided with each analysis, it is the intention of this final chapter to expand on these interpretations, with the particular goal of integrating these measures into a coherent picture. Furthermore, we suggest steps that can be taken in subsequent studies to further expand our understanding.

Most of the results presented in the previous chapter (Sections 4.5.1 - 4.5.5 ) do not directly distinguish photospheric or photospheric-like regions from other ionized-gas contributions. It was our goal in the last two sections (4.5.6 and 4.5.7) to isolate and distinguish photosphere-related effects from other gas-flow contributions. This “Difference” approach has the advantage over the “Direct” approach of potentially unraveling several distinct contributions to the IUE data, particularly isolating those associated with the gas flow and circumstellar characteristics that define Algol-type systems. However, it also has several disadvantages: it can only be used where spectra are available that do not contain the gas-flow effects being isolated; and such difference spectra always contain the possibility of spurious features.

We begin this chapter with a discussion of the “Direct” (non-difference) approach, with particular attention to phase dependences of the system during the 1989 epoch.

### 5.1. *Direct Approach*

An examination of the 1989 phase dependences of the equivalent widths reveals common features among the different ion species. We focus on the absorption lines, Al II  $\lambda$ 1670, Al III  $\lambda$ 1854, Mg II  $\lambda\lambda$ 2796, 2803, and Si IV  $\lambda\lambda$ 1393, 1402. The Al II, Al III, and Mg II observations reveal equivalent width curves that are relatively flat and featureless at phases in the approximate range of 0.2 – 0.8, though Al II and Mg II are slightly elevated within the 0.2 – 0.4 range. The equivalent widths for all of these ions are elevated in the 0.0 – 0.1 (egress) and 0.8 – 1.0 (ingress) phase ranges, but higher during ingress.

The Si IV equivalent widths show a gradual but uneven decrease in the 0.0 – 0.8 range, then increasing sharply in the 0.8 – 1.0 range. Incidentally, equivalent widths for Si II and C II are uneven, but relatively level.

Al II and Al III show very photospheric radial velocities as functions of phase, indicating photospheric motions, or motions with symmetry or apparent symmetry about the photospheric values.

Mg II and Si IV show radial velocity features distinctly different from Al II and Al III, though both contain the rough, overall features of photospheric motion. Mg II is slightly red shifted during egress, and then shows a characteristic rise and reverse curvature in the 0.1 – 0.3 phase range. It is mostly red shifted in the remaining phase range as well, except for reductions to about photospheric velocities at phases of  $\sim$ 0.33 and  $\sim$ 0.8. Interestingly, Si IV  $\lambda$ 1402 exhibits features qualitatively similar to those of Mg II. However, Si IV  $\lambda$ 1393 shows blue shifts in the 0.0 – 0.2 and 0.5 – 0.8 ranges.

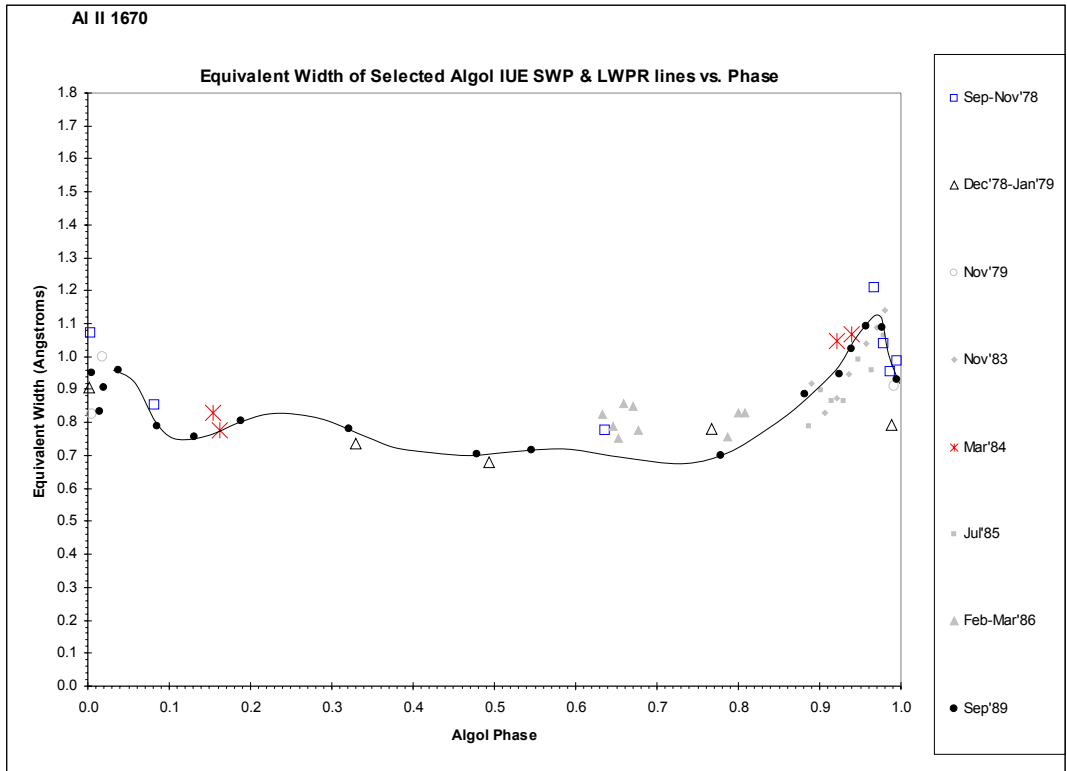


FIG. 5.1.1a—Al II 1670 Equivalent Width vs. Phase

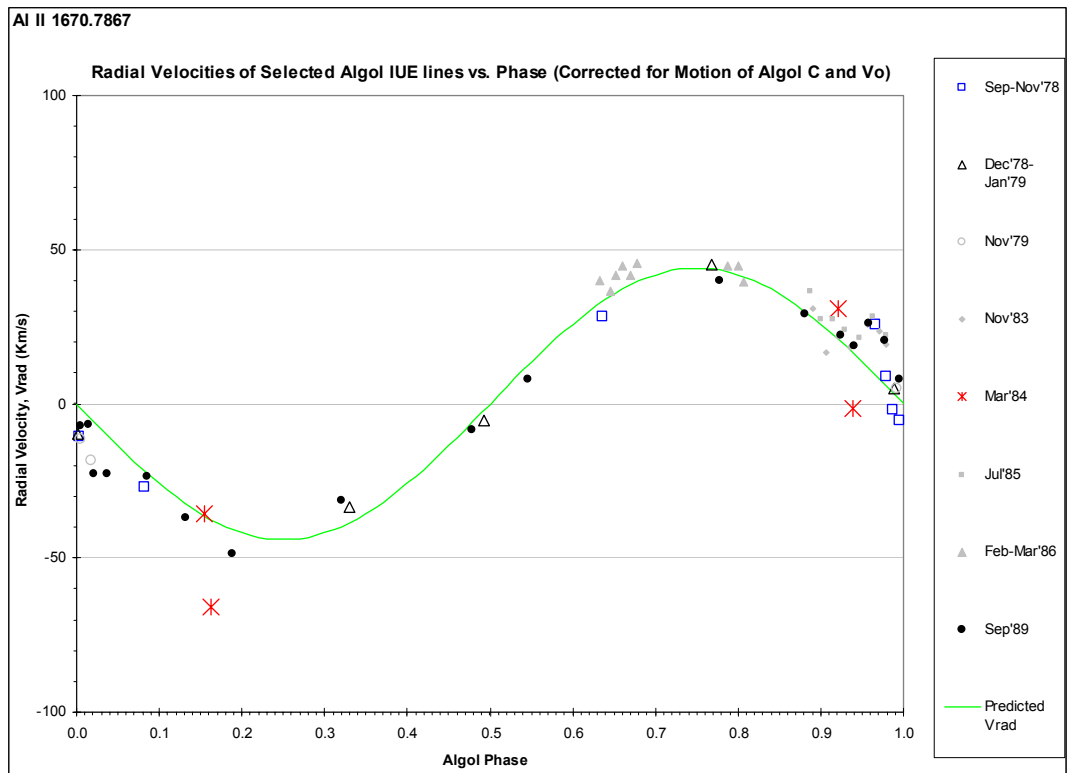


FIG. 5.1.1b—Al II 1670 Radial Velocity Curve



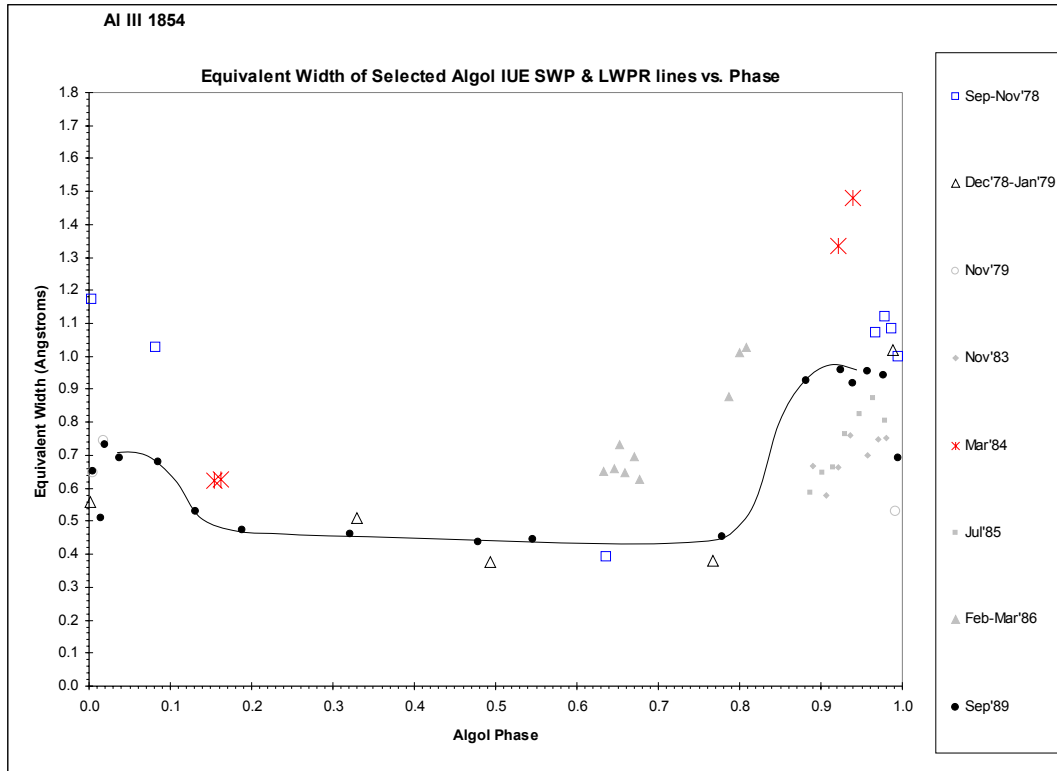


FIG. 5.1.2a—Al III 1854 Equivalent Width vs. Phase

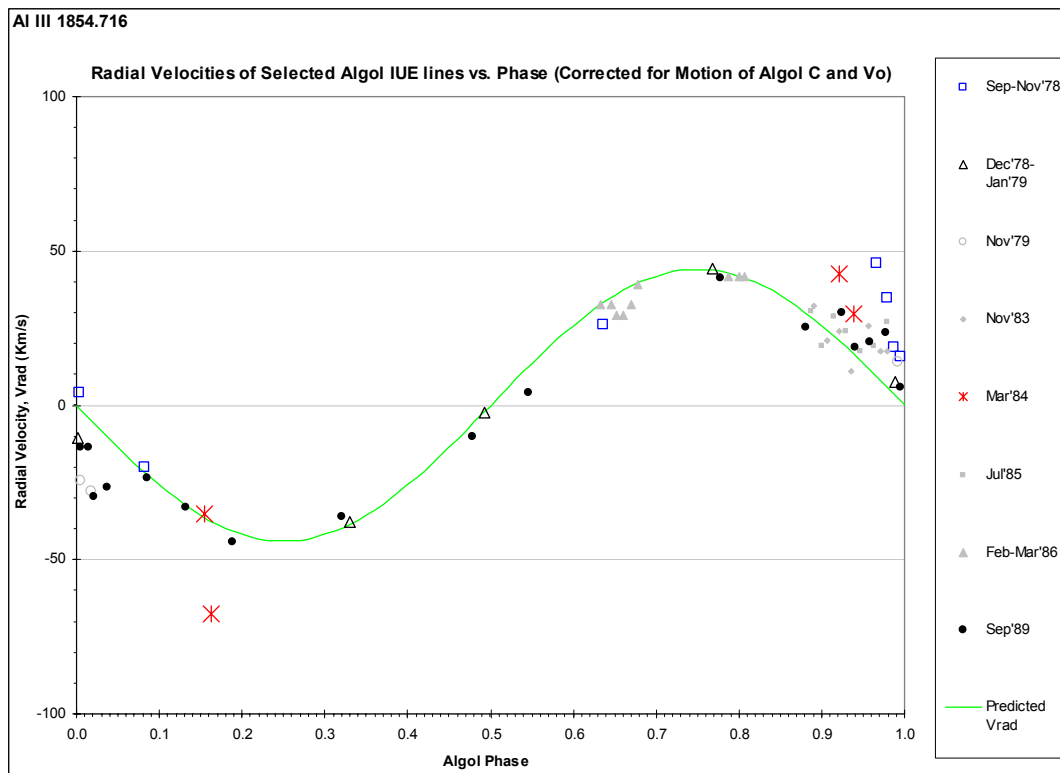


FIG. 5.1.2b—Al III 1854 Radial Velocity Curve

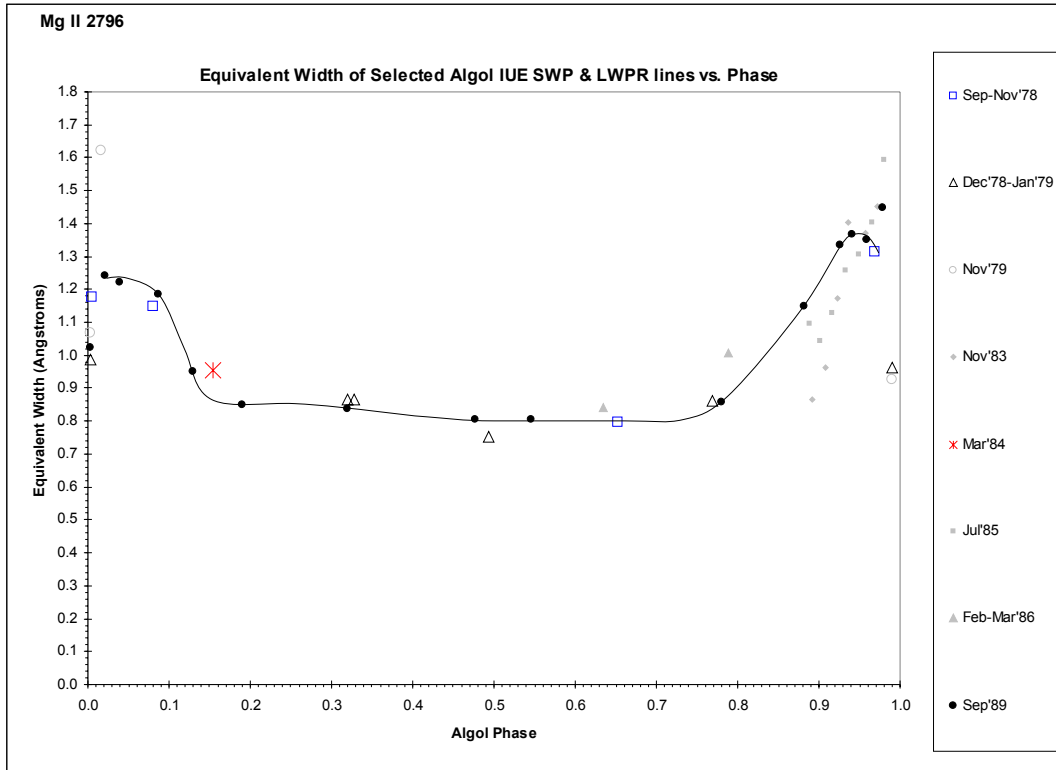


FIG. 5.1.3a—Mg II 2796 Equivalent Width vs. Phase

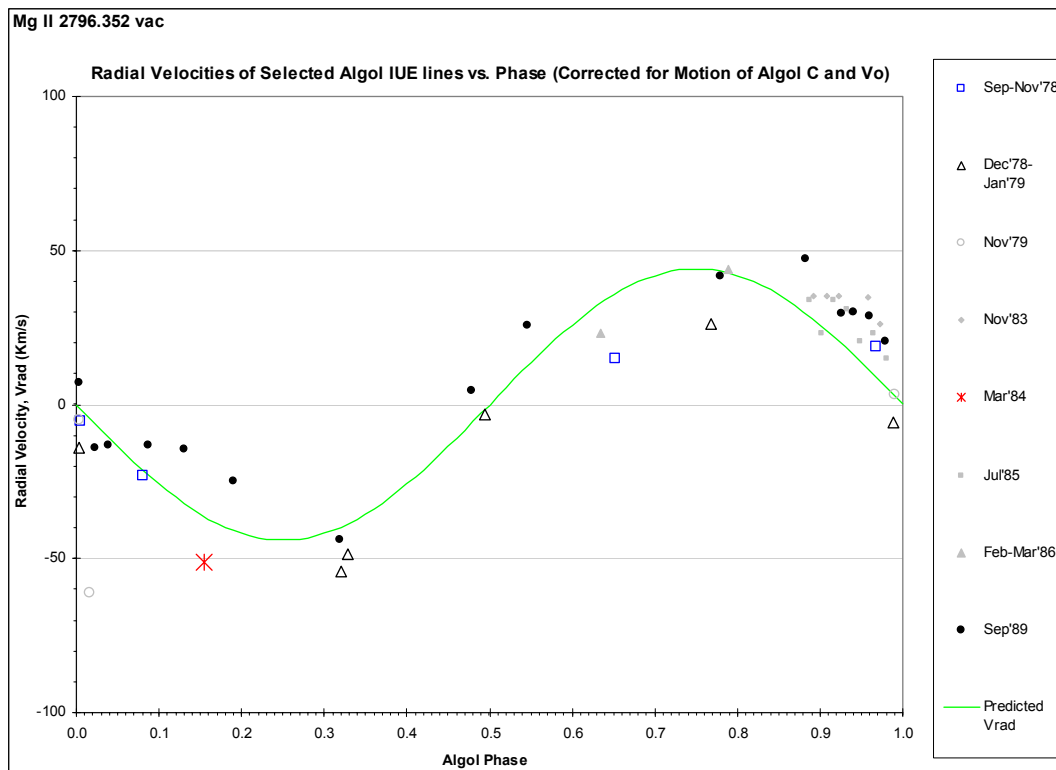


FIG. 5.1.3b—Mg II 2796 Radial Velocity Curve

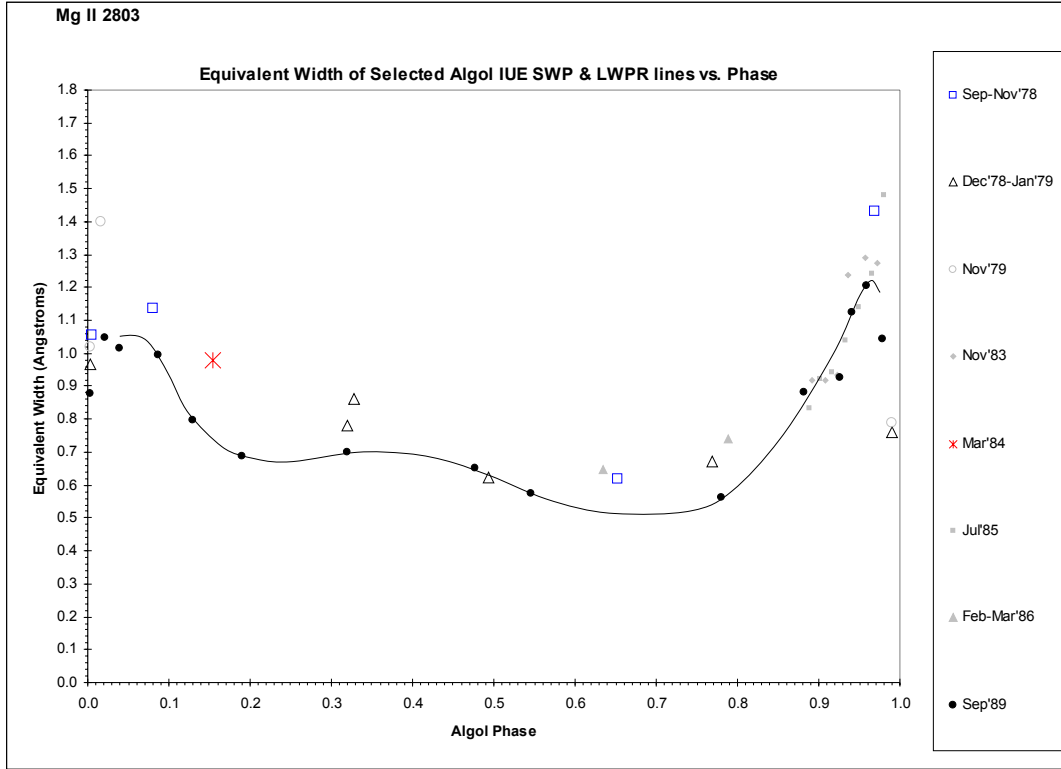


FIG. 5.1.4a—Mg II 2803 Equivalent Width vs. Phase

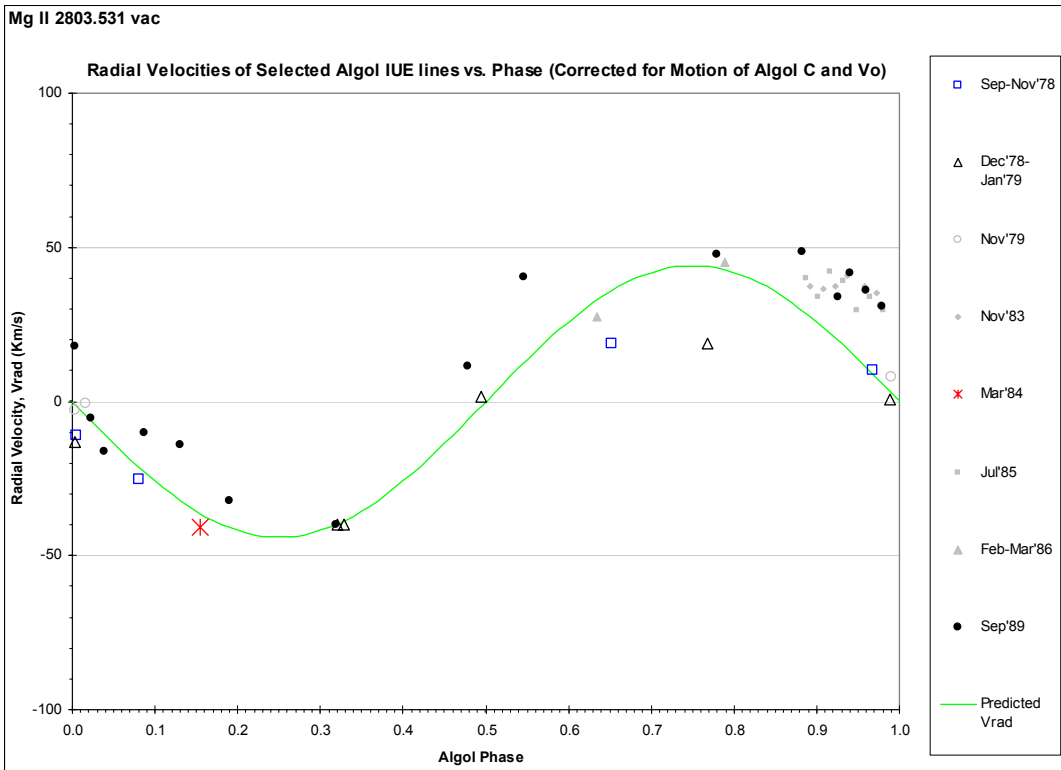


FIG. 5.1.4b—Mg II 2803 Radial Velocity Curve

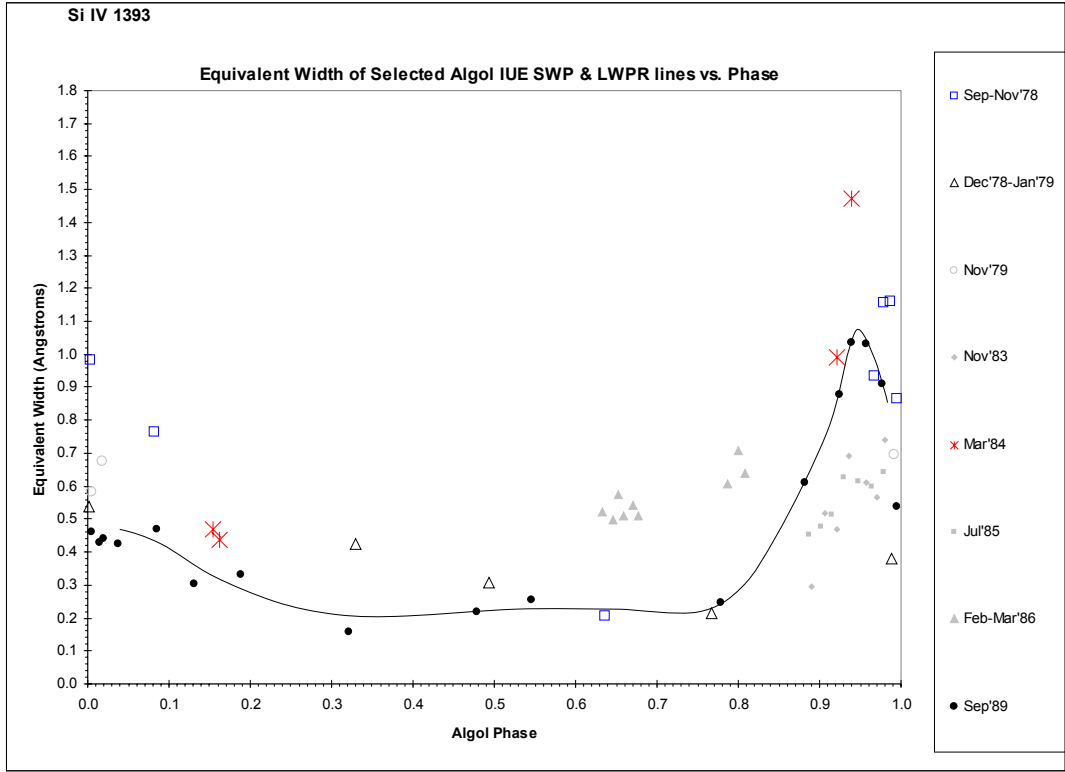


FIG. 5.1.5a—Si IV 1393 Equivalent Width vs. Phase

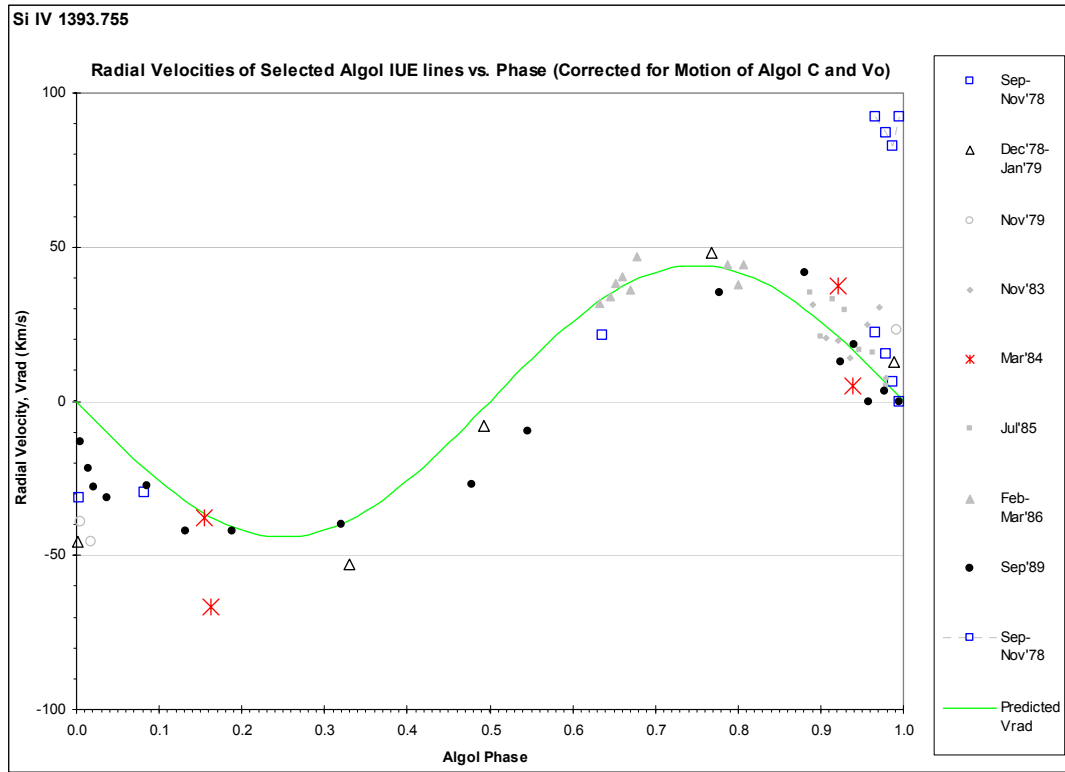


FIG. 5.1.5b—Si IV 1393 Radial Velocity Curve

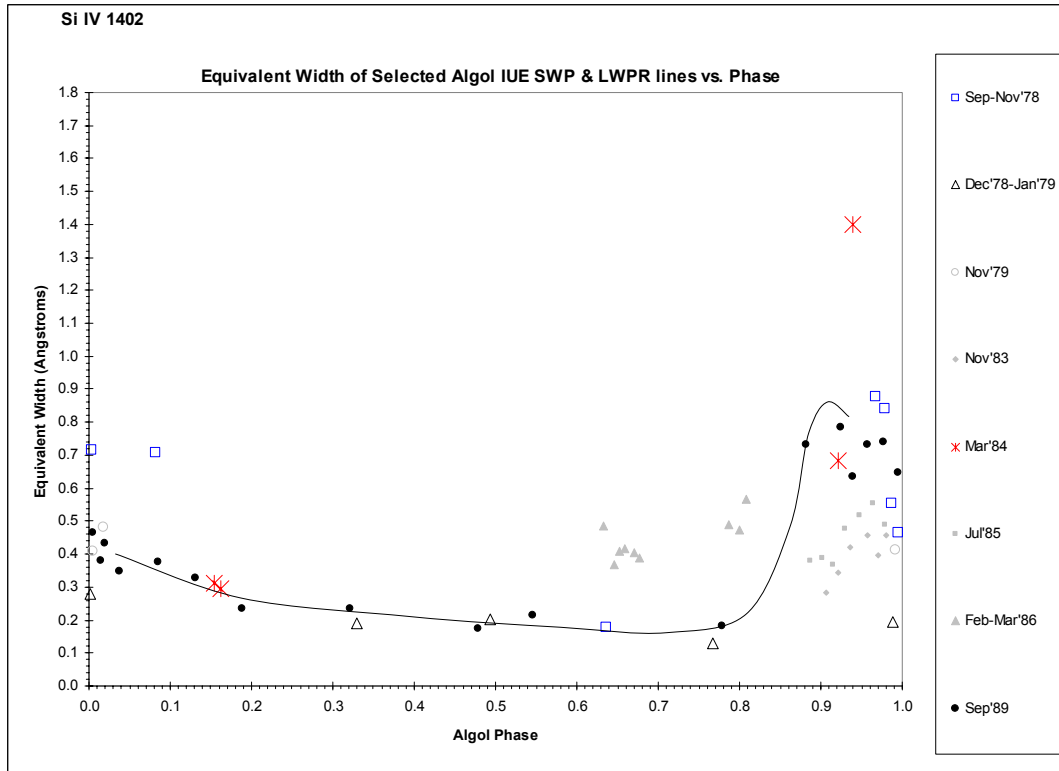


FIG. 5.1.6a—Si IV 1402 Equivalent Width vs. Phase

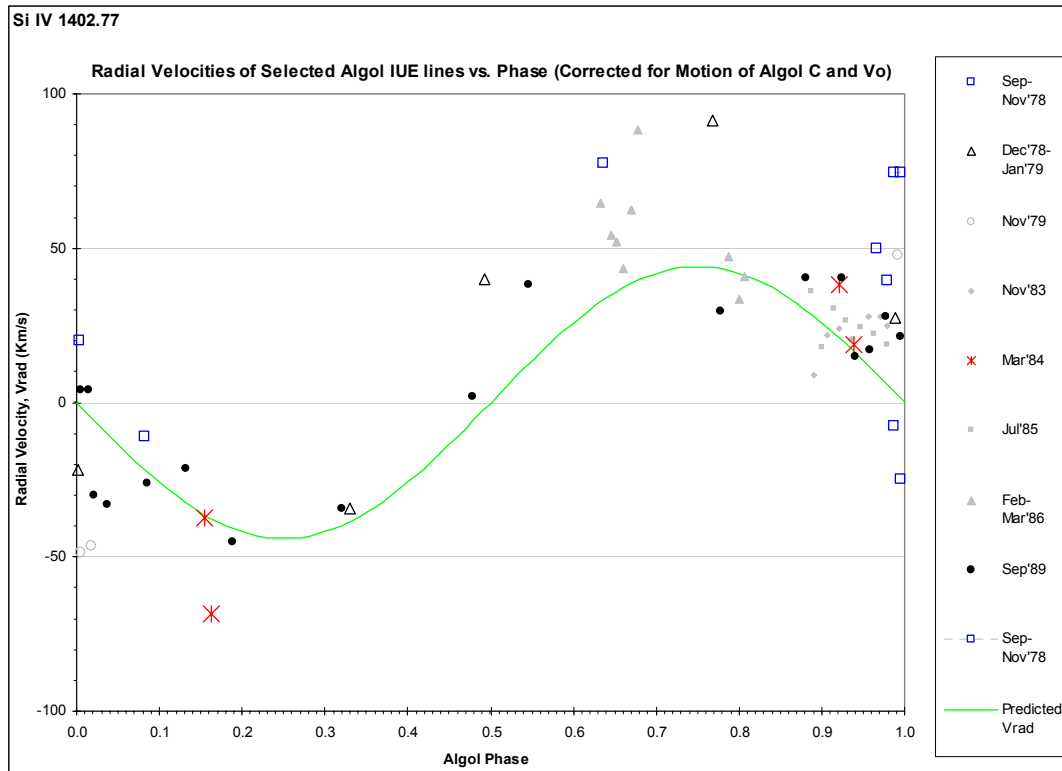


FIG. 5.1.6b—Si IV 1402 Radial Velocity Curve

These differences between the Si IV  $\lambda\lambda 1393, 1402$  lines then must be associated with blending and significant velocity or density differences or gradients; this blending is probably most significant for Si IV  $\lambda 1402$ .

The predominance of Al II and Al III photospheric characteristics can be understood by an examination of the ionization fractions. Ionization fractions appropriate to selected ions, temperatures, and electron pressures have been identified from the ionization fraction plots. The only candidates for normal photospheric features for Algol A (temperature 12,300 K; log of electron pressure 2.5) from among those examined in this work are singly ionized Al, Si, and Fe (Al II, Si II, and Fe II), doubly ionized Al, Mg, Si, and Fe (Al III, Mg III, Si III, and Fe III), and possibly Mg II. As seen in FIG. 4.2.2.2, Al II and Al III appear in equal concentrations under the photospheric conditions of Algol A.

The substantial presence of Mg II and Si IV, whose appearances respectively require lower and higher temperatures than the Algol A photosphere, indicate that competition with photospheric features is likely.

In order to explain these observations and those involving the Difference Approach to be described shortly, we propose the model shown in FIG. 5.1.7. Al II, Al III, Mg II, and Si IV all show high equivalent widths in the vicinity of ingress (phase range 0.8 – 0.92). This can be ascribed to the gas flow from Algol B to Algol A which, in this phase range, intervenes between Earth and Algol A and is moving away from us. The aluminum radial velocities are dominated by the photospheric contributions. However, Mg II is moving away in this region. This is consistent with the cool flow from the Lagrange point vicinity toward Algol A. The Si IV results indicate movement

away from us in the 0.8 phase range; however, the results are very uneven in the 0.5 – 1.0 range, suggestive of competing effects. This is not surprising since the Si IV would only exist in a higher temperature region, where gas flow would be interacting strongly with the photospheric region of Algol A.

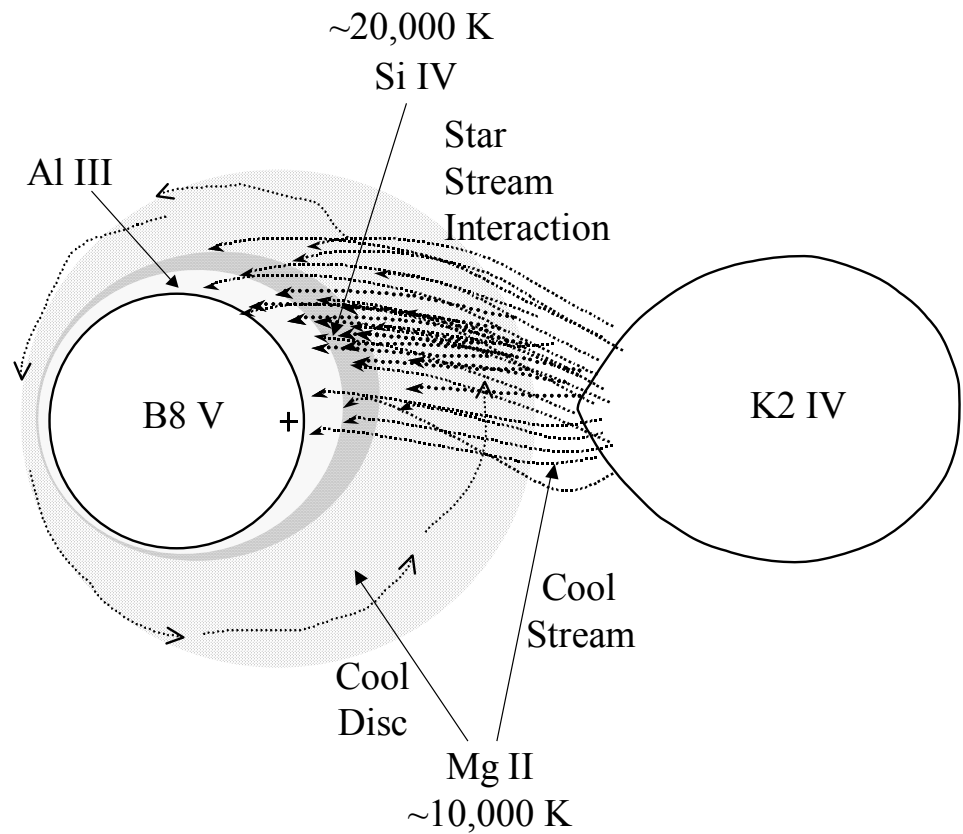


FIG 5.1.7—Algol Model

The Mg II results show high equivalent widths and receding gas motion also around egress. The motion of receding cool gas flow is consistent with the model. This effect is less pronounced for Al II and Al III, again due to the strong competition from

photospheric contributions, and the fact that the abundance of aluminum is about an order of magnitude less than that of magnesium. The asymmetry between egress and ingress can be understood as a consequence of coriolis force deflection, which produces a greater density on the ingress side.

Si IV, however, shows a clear photospheric radial velocity curve at egress, including a very pronounced Rossiter effect. In fact, the Rossiter effect during egress is also exhibited by the Mg II. This suggests that there is gas flow that moves around Algol A in some form of circumstellar disk. However, its velocity is too low to constitute Keplerian orbital motion since that would require a velocity in the range of hundreds of kilometers per second.

This implies the presence of a disk about Algol A that rotates roughly with the star, and relatively close to its surface. The presence of both Mg II and Si IV is indicative of regions of different temperature, and presumably different densities (lower than the photospheric values).

The variations in the residual intensities, in particular the distorted "W" shape (FIGs. 4.5.4.1 - 4.5.4.7) situated about primary eclipse, are consistent with this model. The changes in residual intensities are due to the varying column densities projected onto the visible part of the disk as it is being eclipsed. The photosphere is a continuous source of absorption which is approximately uniform over the disk. The gas stream is projected against the disk during the later half of the orbit and does not cover the entire disk, however it is more extensive than the hot spot which is localized. The distorted "W" shape is the effect of the progressive occultation of these combined features that have different extents, densities, and temperatures.



## 5.2 *Difference Approach*

In order to examine these effects more thoroughly, we attempt to isolate the multiple contributions to the gas flow that make the previous plots difficult to interpret. We accomplish this by the Difference Approach. These calculations support the model presented in FIG. 5.1.7. However, we choose instead to focus here on a comparison across epochs. Since 1989 has the best phase coverage, we will use this epoch as the baseline to compare the other epochs.

In 1989 there is evidence of irregularly distributed circumstellar material around the B8 V star (primary) and gas streaming from the K2 IV star (secondary) toward the primary. We infer circumstellar gas (disk-like) absorption from the difference spectrum 32 – 15 ( $\phi = 0.881$ ) where there is a double peaked absorption feature in Al III  $\lambda\lambda 1854, 1862$  and Si IV  $\lambda 1393$ . In Si IV  $\lambda 1402$ , the absorption feature has a rectangular shape. The difference spectra of Mg II  $\lambda\lambda 2796, 2803$  show double peaked absorption from phase 0.883 through phase 0.0867.

There is evidence for a gas stream in the difference spectra in that the longward component of the double peaked absorption increases in strength and radial velocity as the line of sight changes from looking across the stream (near phase 0.75) to looking along the stream (near phase 0.95).

The 1983 difference spectra show a similar development of the gas stream from phase 0.9082 through phase 0.972, though the disk-like feature is not apparent (due to limited phase coverage) and the stream feature is not as strong, suggesting a period of

lesser activity. Epoch 1985 also shows the development of a gas stream, from phase 0.8866 to 0.979. The stream is marginally stronger in 1985 than 1983 and there is evidence of a disk-like structure.

Epoch 1986 has evidence of a disk-like structure that is more extensive than 1989, with distinct double peaked absorption features across Al III and Si IV. Though the 1986 phase coverage does not extend beyond phase 0.808, the strength of the development of the gas stream component indicates that 1986 is more active than 1989. The phase coverage of 1984 is limited, however the spectra show direct evidence that 1984 is the epoch of greatest mass flow from the secondary toward the primary. In particular, exposure SWP ID: 43 (SWP22439,  $\phi = 0.939$ ) has the strongest and most asymmetric longward absorption features. The 1984 anomaly is substantial enough to depress continuum, evident in the light curve at primary eclipse ingress.

The November 1978 exposures (0.970 – 0.082) also show evidence of increase of mass flow compared to 1989. However direct comparison between 1984 and November 1978 is not available due to limited phase coverage. We will leave open the possibility that November 1978 is more active than 1984.

The lone September 1978 spectrum at phase 0.636 appears to be normal. This indicates that Algol can undergo abrupt changes within a month.

The December 1978 – January 1979 epoch is the least active epoch. Evidence of gas streaming at phase 0.0015 is weak compared to 1989.

November 1979 appears to be more active than December 1978 – January 1979, less active than November 1978, and comparable to 1989.

TABLE 5.2.1- EPOCH ACTIVITY LEVEL COMPARISON

	Epoch
Least Active	Dec. 1978 – Jan. 1979 1983 1985 1989, Nov. 1979 1986 1978
Most Active	1984

Overall the radial velocity deviations from the orbital motion of Algol A extracted from the difference spectra range from  $\sim \pm 100$  km/s for Mg II, Al III, and Si IV. These low velocities along with the low mass loss rate of  $\sim 10^{-14} M_{\odot}/\text{yr}$  indicate that the Algol system is currently undergoing an epoch of conservative mass transfer.

### 5.3. Concluding Remarks

Beta Persei (Algol), from our analysis, behaves as expected like other Algol-type binary systems. We have detected gas streaming effects with short term increases in activity. The light curves follow the expected pattern of increasing depth of primary minimum with decreasing wavelength. These results confirm previous results that at present, Algol is in a variable but relatively low activity state with respect to Algol-type binaries in general.

In the future the secondary star will become a white dwarf and a period of quiescence will follow until the B8 star begins to evolve. It will overflow its critical Roche lobe and accretion of H-He rich material by the white dwarf together with a

decrease in orbital period due to systemic mass loss and viscous forces may lead to super-soft x-ray source activity on the white dwarf. Eventually, a pair of inactive, cooling white dwarfs will result. It is possible that the older white dwarf will accrete and retain sufficient mass to reach the Chandrasekhar limit and undergo a Type Ia supernova explosion. Detailed evolutionary calculations would have to be carried out to determine the likelihood of such an ending to the prototype of the Algol-binary systems.

## BIBLIOGRAPHY

- Abt, H. A., Levato, H., & Grosso, M. 2002, *Astrophysical Journal*, 573, 359
- Ahmad, I. A. 1981, *IUE ESA Newsletter*, 14, 129
- Aitken, R. G. 1935, *The binary stars*, Vol. 3. (2d ed. ed.; New York and London: McGraw-Hill book company, inc.)
- Allan, A. 2005, *Modern Observations, Algol*, [Online document] Cited 5/18/05, <http://homepage.mac.com/antallan/algol2.html>, Last updated Friday 15 July 2005
- Aller, L. H. 1963, *Astrophysics; the atmospheres of the sun and stars* (2d ed.; New York,: Ronald Press Co.)
- Al-Naimiy, H. M. K., Mutter, A. A. A., Flaih, H. A., & Al-Roubaie, A. H. A. 1984, *Informational Bulletin on Variable Stars*, 2520, 1
- Al-Naimiy, H. M. K., Mutter, A. A. A., Flaih, H. A., & Al-Roubaie, A. H. A. 1984, *Informational Bulletin on Variable Stars*, 2520, 1
- Ambartsumyan, V. A. 1958, *Theoretical astrophysics* (New York: Pergamon Press)
- Bachmann, P. J., & Hershey, J. L. 1975, *Astronomical Journal*, 80, 836
- Baldwin, M. E., & Samolyk, G. 1995, OBSERVED MINIMA TIMINGS OF ECLIPSING BINARIES, Number 2, The American Association of Variable Star Observers, [Online document] Cited Oct 20, 2005, <http://www.aavso.org/observing/programs/eb/number2.asc>, Cited Oct 20, 2005
- Baldwin, M. E., & Samolyk, G. 1999, OBSERVED MINIMA TIMINGS OF ECLIPSING BINARIES, Number 5, The American Association of Variable Star Observers, [Online document] Cited Oct 20, 2005,

- <http://www.aavso.org/observing/programs/eb/number5.asc>, Cited Oct 20, 2005
- Baldwin, M. E., & Samolyk, G. 2002, OBSERVED MINIMA TIMINGS OF ECLIPSING BINARIES, Number 7, The American Association of Variable Star Observers, [Online document] Cited Oct 20, 2005, <http://www.aavso.org/observing/programs/eb/number7.asc>, October 2002
- Barker, P. K. 1984, *Astronomical Journal*, 89, 899
- Barney, I. 1923, *Astronomical Journal*, 35, 95
- Benvenuto, O. G., Serenelli, A. M., Althaus, L. G., Barbá, R. H., & Morrell, N. I. 2002, *Monthly Notices of the Royal Astronomical Society*, 330, 435
- Bevington, P. R. 1969, *Data reduction and error analysis for the physical sciences* (New York: McGraw-Hill)
- Binnendijk, L. 1960, *Properties of double stars; a survey of parallaxes and orbits* (Philadelphia: University of Pennsylvania Press)
- Bogges, A., Carr, F. A., Evans, D. C., Fischel, D., Freeman, H. R., Fuechsel, C. F., Klinglesmith, D. A., Krueger, V. L., Longanecker, G. W., Moore, J. V., Pyle, E. J., Rebar, F., Sizemore, K. O., Sparks, W., Underhill, A. B., Vitagliano, H. D., West, D. K., Macchetto, F., Fitton, B., Barker, P. J., Dunford, E., Gondhalekar, P. M., Hall, J. E., Harrison, V. A. W., Oliver, M. B., Sandford, M. C. W., Vaughan, P. A., Ward, A. K., Anderson, B. E., Boksenberg, A., Coleman, C. I., Snijders, M. A. J., & Wilson, R. 1978, *Nature*, 275, 372
- Bolton, C. T. 1989, *Space Science Reviews*, 50, 311
- Bonneau, D. 1979, *Astronomy and Astrophysics*, 80, L11
- Borkovits, T., Érdi, B., Forgács-Dajka, E., & Kovács, T. 2003, *Astronomy and*

- Astrophysics, 398, 1091
- Bower, G. A. 1982, Informational Bulletin on Variable Stars, 2127, 1
- Bowers, R. L., & Deeming, T. 1984, *Astrophysics I Stars* (Boston: Jones and Bartlett Publishers)
- Boyarchuk, A. A. 2002, *Mass transfer in close binary stars* (London ; New York: Taylor & Francis)
- Brandi, E., Garcia, L. G., Kondo, Y., & Sahade, J. 1989, *Astronomy and Astrophysics*, 215, 331
- Bruhweiler, F. C., Grady, C. A., & Chiu, W. A. 1989, *Astrophysical Journal*, 340, 1038
- Budding, E. 1986, *Astrophysics and Space Science*, 118, 241
- Carroll, B. W., & Ostlie, D. A. 1996, *An introduction to modern astrophysics* (Reading, Mass.: Addison-Wesley Pub.)
- Cassatella, A., Altamore, A., González-Riestra, R., Ponz, J. D., Barbero, J., Talavera, A., & Wamsteker, W. 2000, *Astronomy and Astrophysics Supplement Series*, 141, 331
- Cassatella, A., Selvelli, P. L., Ponz, J. D., Gonzalez-Riestra, R., & Vogel, M. 1994, *Astronomy and Astrophysics*, 281, 594
- Chaubey, U. S. 1984, *Astrophysics and Space Science*, 103, 55
- Chen, K.-Y., Barker, E. S., & Wood, F. B. 1981, *Astronomical Journal*, 86, 258
- Chen, K.-Y., Merrill, J. E., & Richardson, W. W. 1977, *Astronomical Journal*, 82, 67
- Chen, K.-Y., & Rhein, W. J. 1969, *Publications of the Astronomical Society of the Pacific*, 81, 387
- Chen, K.-Y., & Rhein, W. J. 1971, *Publications of the Astronomical Society of the*

- Pacific, 83, 449
- Chen, K.-Y., & Rhein, W. J. 1973, *Acta Astronomica*, 23, 247
- Chen, K.-Y., & Wood, F. B. 1976, *Monthly Notices of the Royal Astronomical Society*, 176, 5P
- Chung, S. M., Drake, J. J., Kashyap, V. L., Lin, L. W., & Ratzlaff, P. W. 2004, *Astrophysical Journal*, 606, 1184
- Cowley, A. 1972, *Astronomical Journal*, 77, 750
- Crawford, J. A. 1955, *Astrophysical Journal*, 121, 71
- Crenshaw, D. M., Bruegman, O. W., Johnson, R., & Fitzurka, M. 1996, *Publications of the Astronomical Society of the Pacific*, 108, 925
- Cugier, H. 1979, *Acta Astronomica*, 29, 549
- Cugier, H. 1982, *Acta Astronomica*, 32, 379
- Cugier, H., & Chen, K.-Y. 1977, *Astrophysics and Space Science*, 52, 169
- Cugier, H., & Molaro, P. 1983, *Astronomy and Astrophysics*, 128, 429
- Cugier, H., & Molaro, P. 1984, *Astronomy and Astrophysics*, 140, 105
- de Mello, D. F., Leitherer, C., & Heckman, T. M. 2000, *Astrophysical Journal*, 530, 251
- Diaz-Cordoves, J., Claret, A., & Gimenez, A. 1995, in *Astronomy and Astrophysics Supplement Series*, 329
- Dickinson, T. 1999, *The Universe and Beyond* (3rd ed. ed.: Firefly)
- Drake, J. J. 2003, *Astrophysical Journal*, 594, 496
- Drakos, N. 1996, Introduction, [Online Document]: cited December 6, 2002, <http://www.astroscu.unam.mx/Publicaciones/RevistaMexAstron/SAHADE/gimenez/node1.html>,



- Dugan, R. S. 1924, Contributions from the Princeton University Observatory, 6, 1
- Ebbighausen, E. G. 1958, Astrophysical Journal, 128, 598
- Eggen, O. J. 1948, Astrophysical Journal, 108, 1
- Fitzpatrick, E. L., Ribas, I., Guinan, E. F., DeWarf, L. E., Maloney, F. P., & Massa, D. 2002, ApJ, 564, 260
- Frieboes-Conde, H., Herczeg, T., & Hog, E. 1970, Astronomy and Astrophysics, 4, 78
- Gillet, D., Mouchet, M., & North, P. 1989, Astronomy and Astrophysics, 219, 219
- Gimenez, A. 1996. in Revista Mexicana de Astronomia y Astrofisica Conference Series, UV Observations of Mass Transfer in ALGOLS (Invited Paper), 21
- Gimenez, A., & Garcia-Pelayo, J. M. 1983, Astrophysics and Space Science, 92, 203
- Goodricke, J. 1783, Philosophical Transactions of the Royal Society of London, 73, 474
- Goodricke, J. 1783, Philosophical Transactions of the Royal Society of London, 74, 287
- Guinan, E. F. 1989, Space Science Reviews, 50, 35
- Halenka, J., & Grabowski, B. 1977, Astronomy and Astrophysics, 54, 757
- Hall, D. S. 1989, Space Science Reviews, 50, 219
- Hall, D. S., & Neff, S. G. 1976. in IAU Symp. 73: Structure and Evolution of Close Binary Systems, Mass Transfer Rates in Algol Binaries Deduced from Their Period Changes, 283
- Harnden, F. R., Jr., Fabricant, D., Topka, K., Flannery, B. P., Tucker, W. H., & Gorenstein, P. 1977, Astrophysical Journal, 214, 418
- Harrington, R. S. 1984, Astrophysical Journal, 277, L69
- Hellier, C. 2001, *Cataclysmic variable stars: How and why they vary* (London; New York; Chichester, UK: Springer; Published in association with Praxis Pub)

- Herczeg, T. 1959, *Zeitschrift fur Astrophysik*, 48, 298
- Herschel, W. 1783, *Philosophical Transactions of the Royal Society of London*, 73, 247
- Herzberg, G., & Spinks, J. W. T. 1944, *Atomic spectra and atomic structure* (2d ed.; New York: Dover)
- Hilditch, R. W. 2001, *An introduction to close binary stars* (Cambridge ; New York: Cambridge University Press)
- Hill, G., Barnes, J. V., Hutchings, J. B., & Pearce, J. A. 1971, *Astrophysical Journal*, 168, 443
- Hill, G., Perry, C. L., & Khalessheh, B. 1993, *Astronomy and Astrophysics Supplement Series*, 101, 579
- Huang, R. Q., & Yu, K. N. 1998, *Stellar astrophysics* (Singapore; New York: Springer)
- Irwin, A. W. 1981, *Astrophysical Journal Supplement Series*, 45, 621
- Irwin, J. B. 1952, *Astrophysical Journal*, 116, 211
- Irwin, J. B. 1959, *Astronomical Journal*, 64, 149
- IUE, a [online document: cited 05/08/06], <http://sci.esa.int/science-e/www/area/index.cfm?fobjectid=31284>
- IUE, b [online document: cited 05/08/06], <http://sci.esa.int/science-e/www/area/index.cfm?fobjectid=31315>
- IUE, c [online document: cited 05/08/06], [http://sci.esa.int/esaCP/Pr\\_36\\_1997\\_i\\_EN.html](http://sci.esa.int/esaCP/Pr_36_1997_i_EN.html)
- IUE, d [online document: cited 05/08/06], <http://ines.laeff.esa.es/ines/docs/report.pdf>  
also, esa report 1215, Sept 1997
- IUE, e [online document: cited 05/08/06], <http://sci.esa.int/science-e/www/area/index.cfm?fobjectid=31290>

- IUE, f [online document: cited 05/08/06], <http://sci.esa.int/science-e/www/area/index.cfm?fobjectid=31297>
- IUE, g [online document: cited 05/08/06], <http://sci.esa.int/science-e/www/area/index.cfm?fobjectid=31285>
- IUE, h [online document: cited 05/08/06], <http://esapub.esrin.esa.it/br/br200/Iue.pdf>
- IUE, i [online document: cited 05/08/06], <http://sci.esa.int/science-e/www/area/index.cfm?fobjectid=31311>
- Johnson, J. 2004, Software, Unpublished,
- Kallrath, J., & Milone, E. F. 1999, *Eclipsing Binary Stars: Modeling and Analysis* (New York: Springer)
- Kamp, L. W. 1982, *Astrophysical Journal Supplement Series*, 48, 415
- Kempner, J. C., & Richards, M. T. 1999, *Astrophysical Journal*, 512, 345
- Keskin, V., & Pohl, E. 1989, *Informational Bulletin on Variable Stars*, 3355, 1
- Kim, H.-I. 1989, *Astrophysical Journal*, 342, 1061
- Kitchin, C. R. 1995, *Optical astronomical spectroscopy* (Bristol; Philadelphia: Institute of Physics Pub.)
- Kitchin, C. R. 1998, *Astrophysical techniques* (3rd ed.; Philadelphia, Pa.: Institute of Physics Publishing)
- Kizilirmak, A., & Pohl, E. 1971, *Informational Bulletin on Variable Stars*, 530, 1
- Kizilirmak, A., & Pohl, E. 1974, *Informational Bulletin on Variable Stars*, 937, 1
- Kondo, Y., McCluskey, G. E., Jr. , & Parsons, S. B. 1985, *Astrophysical Journal*, 295, 580
- Kondo, Y., Modisette, J. L., & Morgan, T. H. 1977, *Informational Bulletin on Variable*

Stars, 1312, 1

Kondo, Y., Morgan, T. H., & Modisette, J. L. 1977, *Publications of the Astronomical Society of the Pacific*, 89, 675

Kopal, Z. e. 1959, *Close Binary Systems* (New York: Wiley)

Kopal, Z. e. 1978, *Dynamics of Close Binary Systems* (Dordrecht; Boston: D. Reidel)

Kurucz, R. L. 1995. in ASP Conf. Ser. 81: *Laboratory and Astronomical High Resolution Spectra, An Atomic and Molecular Data Bank for Stellar Spectroscopy*, 583

Lázaro, F. C., & Arévalo, M. J. 2001, *Binary Stars: Selected Topics on Observations and Physical Processes: Lectures held at the Astrophysics School XII, organized by the European Astrophysics Doctoral Network (EADN) in La Laguna, Tenerife, Spain, 6-17 September 1999* (Berlin; New York: Springer)

Lestrade, J.-F., Phillips, R. B., Hodges, M. W., & Preston, R. A. 1993, *Astrophysical Journal*, 410, 808

Loiseau, N. 2005, INES Data Description, [Online document] Cited 9/8/05,  
<http://ines.laeff.esa.es/ines/docs/inesdata.pdf>, Cited 9/8/05

Lubow, S. H., & Shu, F. H. 1975, *Astrophysical Journal*, 198, 383

Lubow, S. H., & Shu, F. H. 1976, *Astrophysical Journal*, 207, L53

M.P. Garhart, M. A. S., B.E. Turnrose, K.L. Levay, and R.W. Thompson 1997,  
*International Ultraviolet Explorer New Spectral Image Processing System Information Manual Version 2.0*, [online document] Cited 9/2/03,  
<http://archive.stsci.edu/iue/manual/newsips/> , &  
<http://archive.stsci.edu/pub/iue/manuals/newsips.pdf>,

- Mallama, A. D. 1978, *Publications of the Astronomical Society of the Pacific*, 90, 706
- Mallama, A. D., Skillman, D. R., Pinto, P. A., & Krobusek, B. A. 1977, *Informational Bulletin on Variable Stars*, 1249, 1
- MAST 2003, Multimission Archive at Space Telescope, IUE Search, [Online Document]:  
cited on March 3, 2003, <http://archive.stsci.edu/iue/search.php>,
- Mayer, P. 1990, *Bulletin of the Astronomical Institutes of Czechoslovakia*, 41, 231
- McCluskey, G. E., Jr. , & Kondo, Y. 1984, in *Future of Ultraviolet Astronomy Based on Six Years of IUE Research*, 382
- McCluskey, G. E., Jr. , Kondo, Y., & Olson, E. C. 1988, *Astrophysical Journal*, 332, 1019
- McCluskey, G. E., Jr. , McCluskey, C. P. S., & Kondo, Y. 1991, *Astrophysical Journal*, 378, 281
- Mihalas, D. 1978, *Stellar Atmospheres* (2d ed.; San Francisco: W. H. Freeman)
- Molnar, L. A. 1998, in, ed. R. L. Mutel (Online document), 27 pages
- Molnar, L. A., & Mutel, R. L. 1996, *Bulletin of the American Astronomical Society*, 188, 921
- Molnar, L. A., & Mutel, R. L. 1996, *Bulletin of the American Astronomical Society*, 188, 921
- Molnar, L. A., & Mutel, R. L. 1996, *Dynamical Evolution of the Algol Triple System*  
Presented as a poster 12 June 1996 at the AAS meeting in Madison, <http://www-astro.physics.uiowa.edu/~lam/research/algol/>, Cited Oct 20, 2005
- Morgan, W. W. 1935, *Astrophysical Journal*, 81, 348
- Mukherjee, J., Peters, G. J., & Wilson, R. E. 1996, *Monthly Notices of the Royal*

- Astronomical Society, 283, 613
- Mutel, R., Molnar, L., & Sharringhausen, B. 1996, Bulletin of the American  
Astronomical Society, 188, 921
- Mutel, R. L., Molnar, L. A., Waltman, E. B., & Ghigo, F. D. 1998, Astrophysical Journal,  
507, 371
- Napier, W. M. 1981, Monthly Notices of the Royal Astronomical Society, 194, 149
- Nelemans, G., Steeghs, D., & Groot, P. J. 2001, Monthly Notices of the Royal  
Astronomical Society, 326, 621
- Ness, J.-U., Schmitt, J. H. M. M., Burwitz, V., Mewe, R., & Predehl, P. 2002, Astronomy  
and Astrophysics, 387, 1032
- Ness, J.-U., Schmitt, J. H. M. M., Burwitz, V., Mewe, R., Raassen, A. J. J., van der Meer,  
R. L. J., Predehl, P., & Brinkman, A. C. 2002, Astronomy and Astrophysics, 394,  
911
- Nha, I. S., & Jeong, J. H. 1979, Informational Bulletin on Variable Stars, 1712, 1
- Nichols, J. S., & Linsky, J. L. 1996, Astronomical Journal, 111, 517
- Ogoza, W. 1995, Informational Bulletin on Variable Stars, 4263, 1
- Olson, E. C. 1980, Astrophysical Journal, 241, 257
- Pan, X., Shao, M., & Colavita, M. M. 1993, Astrophysical Journal, 413, L129
- Pavel, F. 1949, Astronomische Nachrichten, 278, 57
- Peters, G. J., & Polidan, R. S. 1984, Astrophysical Journal, 283, 745
- Pohl, E., & Kizilirmak, A. 1976, Informational Bulletin on Variable Stars, 1163, 1
- Pohl, E., & Kizilirmak, A. 1976, Informational Bulletin on Variable Stars, 1203, 2
- Polubek, G. 1998. in ASP Conf. Ser. 145: Astronomical Data Analysis Software and

Systems VII, Modelling Spectro-photometric Characteristics of Eclipsing  
Binaries, 19

- Polubek, G. 2003, *Advances in Space Research*, 31, 393
- Prendergast, K. H., & Taam, R. E. 1974, *Astrophysical Journal*, 189, 125
- Press, W. H. 1992, *Numerical Recipes in FORTRAN: The Art of Scientific Computing*  
(2nd ed.; Cambridge, England; New York, NY: Cambridge University Press)
- Pringle, J. E., & Wade, R. A. 1985, *Interacting Binary Stars* (Cambridge University  
Press)
- R.L. Kurucz, B. B. 1995, Atomic Line Data (R.L. Kurucz and B. Bell) Kurucz CD-ROM  
No. 23. Cambridge, Mass.: Smithsonian Astrophysical Observatory., online  
database, <http://www.cfa.harvard.edu/amdata/ampdata/kurucz23/sekur.html>,
- Retter, A., Richards, M. T., & Wu, K. 2005, *Astrophysical Journal*, 621, 417
- Riazi, N. 1992, *Astronomical Journal*, 104, 228
- Ribas, I., Arenou, F., & Guinan, E. F. 2002, *Astronomical Journal*, 123, 2033
- Richards, M. 2002, *The Journey* (Adapted from Richards, M. 2000, *The Journal to Algol*,  
*Mercury*, Vol. 29, No. 4, p. 34.), [Online Document]: cited on December 6, 2002,  
<http://www.astro.psu.edu/users/mrichards/research/journey.html>,
- Richards, M. T. 1993, *Astrophysical Journal Supplement Series*, 86, 255
- Richards, M. T. 2001, *LNP Vol. 573: Astrotomography, Indirect Imaging Methods in  
Observational Astronomy*, 573, 276
- Richards, M. T., Jones, R. D., & Swain, M. A. 1996, *Astrophysical Journal*, 459, 249
- Richards, M. T., Mochnacki, S. W., & Bolton, C. T. 1988, *Astronomical Journal*, 96, 326
- Richards, M. T., Waltman, E. B., Ghigo, F. D., & Richards, D. S. P. 2003, *Astrophysical*

- Journal Supplement Series, 147, 337
- Rodríguez-Merino, L. H., Chavez, M., Bertone, E., & Buzzoni, A. 2005, *Astrophysical Journal*, 626, 411
- Sahade, J., & Hernandez, C. A. 1985, *Revista Mexicana de Astronomia y Astrofisica*, vol. 10, 10, 257
- Sahade, J., McCluskey, G. E., & Kondo, Y. 1993, *The Realm of Interacting Binary Stars* (Dordrecht ; Boston: Kluwer Academic)
- Sahade, J., & Wood, F. B. 1978, *Interacting Binary Stars* (Oxford; New York: Pergamon Press)
- Sarna, M. J. 1993, *Monthly Notices of the Royal Astronomical Society*, 262, 534
- Schmitt, J. H. M. M., & Ness, J.-U. 2002, *Astronomy and Astrophysics*, 388, L13
- Schroeder, D. J. 2000, *Astronomical Optics* (San Diego: Academic Press)
- Sears, F. W., & Salinger, G. L. 1986, *Thermodynamics, Kinetic Theory and Statistical Thermodynamics* (3rd ed.; Reading, Mass.: Addison-Wesley Pub. Co.)
- Shajn, G., & Struve, O. 1929, *Monthly Notices of the Royal Astronomical Society*, 89, 222
- Shore, S. N., & King, A. R. 1986, *Astronomy and Astrophysics*, 154, 263
- Simon, V. 1998. in 29th Conference on Variable Star Research, Relation of the Period Changes with other Kinds of Activity in Algol-type Binaries, 193
- Smeyers, P., & Willems, B. 2001, *Astronomy and Astrophysics*, 373, 173
- Snijders, M. A. J., & Lamers, H. J. G. L. M. 1975, *Astronomy and Astrophysics*, 41, 245
- Soderhjelm, S. 1975, *Astronomy and Astrophysics*, 42, 229
- Soderhjelm, S. 1980, *Astronomy and Astrophysics*, 89, 100



- Star Gaze 1998, Hubble's View of The Universe. DVD. Real Magic Publishing
- Stern, R. A., Lemen, J. R., Antunes, S., Drake, S. A., Nagase, F., Schmitt, J. H. M. M., Singh, K., & White, N. E. 1998. in ASP Conf. Ser. 154: Cool Stars, Stellar Systems, and the Sun, Multiwavelength EUVE/ASCA/RXTE Observations of Algol and the [Fe/H] Abundance, 1166
- Stern, R. A., Lemen, J. R., Schmitt, J. H. M. M., & Pye, J. P. 1995, *Astrophysical Journal*, 444, L45
- Sterne, T. E. 1939, *Monthly Notices of the Royal Astronomical Society*, 99, 451
- Sterne, T. E. 1939, *Monthly Notices of the Royal Astronomical Society*, 99, 670
- Sterne, T. E. 1939, *Monthly Notices of the Royal Astronomical Society*, 99, 662
- Sterne, T. E. 1941, *Proceedings of the National Academy of Science*, 27, 93
- Sterne, T. E. 1941, *Proceedings of the National Academy of Science*, 27, 99
- Sterne, T. E. 1941, *Proceedings of the National Academy of Science*, 27, 106
- Struve, O. 1941, *Astrophysical Journal*, 93, 104
- Struve, O. 1956, *Vistas in Astronomy*, 2, 1371
- Struve, O., & Elvey, C. T. 1931, *Monthly Notices of the Royal Astronomical Society*, 91, 663
- Struve, O., & Sahade, J. 1957, *Publications of the Astronomical Society of the Pacific*, 69, 41
- The Planets 1999, Vol. 3 Stars and Atmosphere, DVD. BBC/A&E Network coproduction
- Tomkin, J., & Lambert, D. L. 1978, *Astrophysical Journal*, 222, L119
- United States Naval Observatory. Nautical Almanac Office., Great Britain. Nautical Almanac Office., Science and Engineering Research Council (Great Britain),

Science Research Council (Great Britain), Rutherford Appleton Laboratory.,  
Council for the Central Laboratory of the Research Councils (Great Britain), &  
United States. Dept. of the Navy. 2002, in (Washington; London: U.S. G.P.O. ;  
H.M.S.O.), v.

Unknown. 1895, *The Observatory*, 18, 229

van Hamme, W. 1993, *Astronomical Journal*, 106, 2096

Verricatt, W. P., Ashok, N. M. 1999, *Astronomical Journal*, 117, 2980

Walter, K. 1973, *Astrophysics and Space Science*, 21, 289

Walter, K. 1980, *Astronomy and Astrophysics*, 92, 86

Walter, K. 1980. in *IAU Symp. 88: Close Binary Stars: Observations and Interpretation*,  
*On the Location of Gas Streams in Algol Systems*, 305

Website: 1994, "The Astronomical Society of the Pacific '106th Annual Meeting"  
History Sessions, <http://www.phys-astro.Sonoma.edu/people/faculty/tenn/asphistory/1994.html>,

Website: 2003, URL:[http://spdex.t.estec.esa.nl/content/doc/ac/2476\\_.htm](http://spdex.t.estec.esa.nl/content/doc/ac/2476_.htm),

Website: 2003, URL:[http://spdex.t.estec.esa.nl/content/doc/b1/2481\\_.htm#top](http://spdex.t.estec.esa.nl/content/doc/b1/2481_.htm#top),

Website: 2003, URL:[http://spdex.t.estec.esa.nl/content/doc/bb/2491\\_print.htm](http://spdex.t.estec.esa.nl/content/doc/bb/2491_print.htm),

Website: 2003, URL:[http://iuearc.vilspa.esa.es/Ines\\_PC/iue.shtml](http://iuearc.vilspa.esa.es/Ines_PC/iue.shtml),

Website: 2003, URL:<http://iueacr.vilspa.esa.es/>,

Website: 2003, URL:[http://spdex.t.estec.esa.nl/content/doc/ad/2477\\_.htm](http://spdex.t.estec.esa.nl/content/doc/ad/2477_.htm),

Website: 2003, URL:<http://godot.u-strasbg.fr/ines/docs/p13.pdf>,

Website: 2003, URL:<http://achive.stsci.edu/iue/instrument.html>,

Website: 2006, "What is a Star?" *Stellar Evolution*

- <http://nmm.ac.uk/server/show/conMediafile.6644>,
- Website: 2006, URL:[http://en.wikipedia.org/wiki/International\\_ultraviolet\\_Explorer](http://en.wikipedia.org/wiki/International_ultraviolet_Explorer),
- Website: 2006, NIST Atomic Spectra Database Lines Form, online Database,  
[http://physics.nist.gov/PhysRefData/ASD/lines\\_form.html](http://physics.nist.gov/PhysRefData/ASD/lines_form.html),
- Whittet, D. C. B. 2003, *Dust in the galactic environment* (2nd ed. ed.: Institute of Physics  
(IOP) Publishing)
- Willems, B., & Claret, A. 2003, *Astronomy and Astrophysics*, 398, 1111
- Wilson, R. E. 1979, *Astrophysical Journal*, 234, 1054
- Wilson, R. E., & Devinney, E. J. 1971, *Astrophysical Journal*, 166, 605
- Wolf, M., Diethelm, R., & Sarounová, L. 1999, *Astronomy and Astrophysics*, 345, 553
- Wolf, M., Harmanec, P., Diethelm, R., Hornoch, K., & Eenens, P. 2002, *Astronomy and  
Astrophysics*, 383, 533
- Wolf, M., & Sarounova, L. 1995, *Astronomy and Astrophysics Supplement Series*, 114,  
143
- Wyithe, J. S. B., & Wilson, R. E. 2002, Photometric Solutions for Semi-Detached  
Eclipsing Binaries: Selection of Distance Indicators in the Small Magellanic  
Cloud, [Online Document]: cited January 2003, <http://arxiv.org/abs/astro-ph/0201255v1>,
- Wyithe, J. S. B., & Wilson, R. E. 2002, *Astrophysical Journal*, 571, 293
- Yamasaki, A. 1986, *Publications of the Astronomical Society of Japan*, 38, 449
- Zavala, R. T., McNamara, B. J., Harrison, T. E., Galvan, E., Galvan, J., Jarvis, T.,  
Killgore, G., Mireles, O. R., Olivares, D., Rodriguez, B. A., Sanchez, M., Silva,  
A. L., Silva, A. L., & Silva-Velarde, E. 2002, *Astronomical Journal*, 123, 450

Zeilik, M., & Gregory, S. A. 1998, *Introductory Astronomy & Astrophysics* (4th ed.; Fort Worth: Saunders College Pub.)

# APPENDIX A

## Published Estimates of Algol Parameters

### TABLE OF CONTENTS

ALGOL Identifying Terms .....	211
Table	
1 Systemic Velocity a.k.a. Gamma Velocity .....	211
2 Period of A-B System in Days.....	212
3 Period of AB-C System in Days .....	213
4 Eccentricity of A-B System .....	214
5 Eccentricity of AB-C System in Days .....	214
6 Longitude of periastron.....	215
7 Angle between line of nodes & periastron of AB-C system .....	215
8 Rate in Change of $\omega_{AB}$ with time .....	216
9 Semi-amplitude of A with respect to A-B system CM, $K_A$ (km/s).....	216
10 Semi-amplitude of B with respect to A-B system CM, $K_B$ (km/s).....	216
11 Semi-amplitude of C with respect to AB-C system CM, $K_C$ (km/s) .....	217
12 Semi-amplitude of AB with respect to AB-C ( $K_{AB-C}$ ) system CM (km/s).....	217
13 Time of Periastron passage of A-B System .....	217

# APPENDIX A

## TABLE OF CONTENTS - continued

14	Periastron passage of AB-C System .....	218
16	Light elements (a.k.a. ephemeris, or epoch of primary minimum) .....	218
16A	Rate of mass loss $dm/dT$ solar mass per year .....	219
18	Full Width at Half Maximum (FWHM) Å. ....	219
19	Radial velocity, $V_{rad}$ .....	220
20	The orbital inclination $i_{A-B}$ .....	220
21	The orbital inclination of the AB-C ( $i_{AB-C}$ ) .....	221
22	$V_{rot} \sin i$ (Rotational Velocity) .....	221
23	$a \sin i$ (km/s) .....	222
24	Mass of Algol A .....	222
25	Mass of Algol B .....	223
26	Mass of Algol C .....	224
27	Radius ( $R_{\odot}$ ) A .....	225
28	Radius ( $R_{\odot}$ ) B .....	226
29	Radius ( $R_{\odot}$ ) C .....	227
30	Temp $T_A$ .....	228
31	Temp $T_B$ .....	229
32	Temp $T_C$ .....	230
33	Log of surface gravity $\log g$ of Algol A .....	230

# APPENDIX A

## TABLE OF CONTENTS – continued

34	Log of surface gravity, log g Algol B.....	231
35	Log of surface gravity, log g of Algol C.....	231
36	Distance to Algol AB-C system (parasecs) .....	232
37	Spectral Type Algol A .....	233
38	Spectral Type Algol B .....	234
39	Spectral Type Algol C .....	235
40	Mass ratio of Algol A-B system $q = m_b/m_a$ .....	236
40a	Mass ratio of AB-C system $q = M_{AB}/M_C$ .....	236
41	Separation ( $R_\odot$ ) of center of A to center of B Sep. ab ( $R_\odot$ ).....	237
42	Separation of center of AB system to center of C (astronomical units AU).....	237
43	$\Omega$ omega A-B system.....	237
43a	$\Omega$ omega of AB-C system .....	238
44	Mass function of AB system $f(m)$ AB .....	238
45	Rotational velocity ( $V_{rot}$ ) (km/s).....	238
46	Roche Lobe (fill out factor) $F_A$ or ratio of Algol A .....	239

# APPENDIX A

## TABLE OF CONTENTS – continued

47	Roche Lobe (fill out factor) $F_B$ or ratio of Algol B.....	239
48	$\beta_A$ , Beta gravity darkening exponent or coefficient for Algol A .....	239
49	$\beta_B$ , Beta gravity darkening exponent or coefficient for Algol B.....	239
50	Bolometric Albedo (or reflection coefficient) for Algol A.....	240
51	Bolometric Albedo (or reflection coefficient) for Algol B.....	240
52	Luminosity of A.....	241
53	Luminosity of B .....	242
54	Luminosity C .....	242
55	Limb darkening coefficient (1 <sup>st</sup> order) for Algol A .....	243
56	Limb darkening coefficient (2 <sup>nd</sup> order) for Algol A .....	243
57	Limb darkening coefficient (1 <sup>st</sup> order) for Algol B .....	243
58	Limb darkening coefficient (2 <sup>nd</sup> order) of Algol B.....	244
59	Position angle of the nodal point between 0° and 180° Also the position angle of the line of nodes .....	244



Previously published ALGOL Identifying Terms

$\beta$ Persei	Sahade, J. & Hernandez, C. A. (1985), p. 257 (Introduction)	
$\beta$ Per		
26 Persei		
Algol		
HR 936		
HD 19356		
SAO 38592		
BD + 40°0673		
ADS 2362		
$\alpha = 3^{\text{h}} 04^{\text{m}} 54^{\text{s}}$		
$\delta = +40^{\circ}46'0 (1950.0)$		
B = 2.0 – 3.3 mag.		
The first eclipsing variable to be discovered (actually a Triple System).		

TABLE 1

Previously published estimates of Systemic Velocity  
a.k.a. Gamma Velocity =  $V_{\gamma}$  =  $V_{\text{gamma}}$  (km/s should always refer to whole system, ie.,  
velocity of Algol AB-C's) CM with respect to our Sun

$V_o$	Source	Notes/Comments
$V_{\gamma}$ (km/sec) = -9.0 (3.9)	Mukherjee et al (1996) p. 620	
$V_o$ (kms <sup>-1</sup> ) = $3.8 \pm 1.7$	Hill et al. (1971) Eaton (1975) Ebbighausen & Gange (1963) Stein & Beardsley (1977)	Richards, M. T. (1993) p. 257, Table 1A
$V_o = 4.9 \pm 1.6$ km/sec	Hill et al. (1971)	Richards et al. (1993) p. 262
4 km/s	Gillet et al. (1989), p. 221	
4.8 km/s	This work	

TABLE 2

Previously published estimates of Period of A-B System in Days

$P_{A-B}$	Source	Notes/Comments
Pa-b 2.867315	S&T (1993), 86, 79	Richards et al. (2003), p. 338
Period in Days 2.87	Soderhjelm (1980)	Drake (2003), p. 497, Table I
2.8673	Soderhjelm (1980) Lestrade (1993)	Borkovits et al. (2003) p.1096, Table 1
2.8673	Zavala et al. (2002)	p. 456 ( $\beta$ per), Column 8
Days $P = 2.87^d$	Richards (2002)	p. 7
$\beta$ per – Period in Days 2.8673	Mukherjee et al. (1996), p. 620, Table 2	& Richards, M. T. (1993) p. 257 Hill et al. (1971)
Period Days 2.87	Gimenez, A. (1996) p. 23 #2 The Case of Algol	
2.8673d	Soderhjelm (1980)	Sarna MJ (1993) p. 1 (Intro.)
$\beta$ per $P = 2.87$ days	Stern et al. (1998) p. 1166 (Intro.)	
$P = 2.86$ days	Mutel et al. (1998), p. 371	
$\beta$ per $2.7 < P < 4.5$ $P = \text{days}$ $P = 2.87$ days	Richards, M. T. (2001), pp. 284, 295	See chart: p. 284, (Table 1) Single Peaked Emissions
$2^d.8673$	Pan, X. et al. (1993) p. L129	
2.9 days	Lestrade et al. (1993), p. 808	
2.8673	Lestrade et al. (1993), p. 809 Table 1B	
2.87 days	Guinan, E. F. (1989) p. 37	
2.87 days	Sahade, J. & Hernandez, C.A. (1985), p. 257	
2.867 days	Cugier, H. & Molaro, P. (1984) p. 105	
Binary Computed $\beta$ Per $\frac{Po/P}{0.87}$ Trend Increase	(observed trend of period Variation) <u>Year of Observation</u> 1783-1967	(Kriner) 1971 Chaubey, U.S. (1984) p. 56, Table 1
$2^d.87$ & 2.8673 p. 110	Soderhjelm, S. (1980)	Original
$2^d.8674$ days	Bachmann & Hershey (1975)	Cugier, H. (1979), p. 449
2.8673 days	Tomkin & Lambert (1978), PL 119	Concluded the $2^{nd}$ filled its Roche Lobe
$2^d.867$	Cugier & Chen (1977) p. 169	
2.86730807	Hill et al. (1971) p.444	
$2^d.8673$	Frieboes-Conde, H et al. (1970), p.78	
2.87 days	Ida Barry (1923)	Ebbighausen, E.G. (1958)
2.87 days	Struve, O. & Sahade, J. (1957) p. 41	
2.867 day	Eggen, O.J. (1948) p. 1	
2.86731077	Gillet et al. 1989, p. 221	

TABLE 3

Previously published estimates of Period of AB-C System in Days

$P_{AB-C}$	Source	Notes/Comments
P 679.9 days	Borkovits et al. (2003) p. 1096, Table 2	
(P =1.87 yr.) AB & C distant A star in a long period Orbital period 1.87 yr.	Mutel et al. (1998), p. 371	
1.862 yr. orbit	Gimenez, A. (1996) p. 23, #2 The case of Algol	
679.9 ± 02 days	Sarna, M. J. (1993) p. 1 (Intro.)	Sarna, M. J. (1993) p. 535, Table 1
P = days 680.08	Hill et al. (1971) Ebbighausen (1958) Frieboes-Conde et al. (1970)	Richards, M. T. (1993) p. 257, Table 1-A
P = 680 <sup>d</sup> .05 ± 0 <sup>d</sup> .06 (AB-C) 1.86 yr.	Pan, X. et al. (1993), p. L129	
1.86 yr.	Pan, X. et al. (1993), p. L129	
679.9 days	Lestrade et al. (1993) p. 808	
1.87 yrs.	Lestrade et al. (1993) p. 809, Table 1-B	
680 days	Guinan, E. F. (1989), p. 37	
1.862 yrs.	Gillet, D. et al. (1989), p. 219	P. 110 6.79.9 ±0.2
1.862 yrs.	Sahade, J. & Hernandez, C.A. (1985), p. 257	
680 days	Cugier, H. & Molaro, P. (1984) p. 105	
1.862	Soderhjelm, S. (1980) original	
1.862 yrs.	Cugier, H. (1979) p. 550	
1.862 yrs.	Tomkins & Lambert (1978) p L 119	
1.862 yrs.	Bachmann & Hershey (1975) original	With an astrometric half amplitude of 0 <sup>''</sup> . <sup>01</sup>
1.862 yrs.	Hill et al. (1971) p. 443	
1.862 yrs. 1.873 (an earlier quote)	Ebbinghausen (1958)	Frieboes-Conde, H. et al. (1970)
1.733	Blopolsky (1906) (1908) (1909) (1911)	Ebbighausen, E. G. (1958), p. 598, Paragraph 1
1.899	Curis's (1908)	
1.874	Schlesinger (1912)	
1.873	McLaughlin (1937)	
1.873	Eggen (1948)	
1.873	Pavel (1950)	
1.87 yrs.	Struve, O. & Sahade, J. (1957) p. 41	
1.873 yrs,	Eggen, O. J. (1948), p. 1	A fourth component star with a period of 188.4 years is suggested by Eggen

TABLE 4

Previously published estimates of Eccentricity of A-B System

$e_{A-B}$	Source	Notes/Comments
$e_{a-b} = 0.0$	Borkovits et al. (2003), p. 1096, Table 1	
$e_{a-b} = 0$	Soderhjelm (1980)	Sarna, M.J. (1993) p. 535, Table 1
$e_{ab} = 0.0$	Richards, M. T. (1993) p. 257, Table 1-A	
$e_{ab} = 0.000$	Lestrade et al. (1993)	p. 809, Table 1-B
$e_{ab} = 0.000$	Soderhjelm, S. (1980)	p. 110
$e_{ab} = 0.26$	McLaughlin (1937)	Ebbighausen, E.G. (1958) p. 600, Table 2
$e_{ab} = 0.47$	Eggen (1949)	Ebbighausen, E.G. (1958) p. 600, Table 2
$0.015 \pm .008$	Hill et al. (1971), p. 451	

TABLE 5

Previously published estimates of Eccentricity of AB-C System in (Days)

$e_{AB-C}$	Source	Notes/Comments
$e = 0.23$	Borkovits et al. (2003), p. 1096, Table 1	
$e_{AB-C} = 0.22 \pm 0.02$	Soderhjelm (1980)	Sarna, M. J. (1993) p. 535, Table 1
$e_{AB-C} = 0.23 \pm 0.04$	Richards et al. (1988) Ebbighausen (1958) Bachmann & Hershey (1975)	Richards, M. T. (1993), p. 257, Table 1-A
$e_{ab-c} = 0.225 \pm 0.005$	Pan, X. et al. (1993), p. L129	
$e_{ab-c} = 0.22$ days	Lestrade et al. (1993) p. 809, Table 1-B	
$e_{ab-c} = 0.22 \pm 0.02$	Soderhjelm, S. (1980), p. 110	
$e_c = 0.211 \pm 0.005$	Ebbighausen, E. G. (1958) p. 600, Table 2	
$e = 0.2557 \pm 66.10^{-4}$	Pavel, F. (1949), p. 59	
$e = 0.25$	Eggen, O. J. (1948), p. 1	
$e = 0.23$	Hill et al. (1971), p. 450	

TABLE 6

Previously published estimates of longitude of periastron, ie. Angle between the line of nodes and periastron of A-B System (degrees)

$\omega_{A-B}$	Source	Notes/Comments
$\omega_{\text{Algol AB}} = 133^\circ$	Hill et al. (1971)	Richards, M. T. (1993) p. 257, Table 1-A
$163^\circ$	Gillet et al. (1989), p. 228	
$\omega_{A-B} = 359^\circ$ , if $\dot{\omega}_{A-B} = 0$ , for epoch of Hill et al. (1971) data	This work	
$\omega(t) = (.0308^\circ/\text{day})t - 521.392$ if $\dot{\omega}_{A-B} \approx \frac{360^\circ}{32 \text{ year}}$	This work	

TABLE 7

Previously published estimates of Angle between line of nodes & periastron of AB-C system (degrees)

$\omega_{AB-C}$	Source	Notes/Comments
$\omega_{\text{Algol C}} = 313^\circ$	Hill et al. (1971)	Richards, M. T. (1993) p. 257, Table 1-A
$\omega^{(o)} \text{ AB-C } 125 \pm 4$	Soderhjelm, S. (1980) p. 110	
$130.29(8)^\circ$ (outer binary)	Molnar & Mutel (1998), p. 17	Possible Misquote of Pan et al. (1993)
$\omega_{\text{Algol C}} = 313^\circ$	Hill et al. (1971), Table 5, p. 450	
$\omega_{AB-C} = 310^\circ.29 + 0.08$	Pan, X. et al. (1993), p. L129	
$\text{Periastron}_{AB-C} = 125^\circ$	Lestrade et al. (1993) p. 809, Table 1-B	
$\omega_{AB-C} \omega_C = 133^\circ$ for the epoch of Hill et al. (1971) data	This work	
$\omega_{AB} = 133^\circ$	Hill et al. (1971) Table 6, p. 451	Appears to be in conflict with his $\omega_{AB} 313^\circ$ entry
$\omega_{AB} = 313^\circ$	Hill et al. (1971) p. 450, middle of the page	Appears to be in conflict with his Table 6 entry

TABLE 8

Previously published estimates of Rate in Change of  $\omega_{AB}$  with time (degrees/day)  
(aka  $d\omega_{AB}/dt$ , or  $\dot{\omega}$ )

$\Delta\omega_{A-B}/\Delta t = \dot{\omega}$	Source	Notes/Comments
$\Delta\omega_{A-B}/\Delta t = 0.03079$ Degrees/day or equivalently, 32 years for one revolution	Hill et al. (1971), p.454	Estimated from Figure 4 (360 degrees per 32 years)
$\dot{\omega}_{A-B} = .03080$ for Hill date	This work	

TABLE 9

Previously published estimates of semi-amplitude of A with respect to A-B system CM,  
 $K_A$  (km/s)

$K_A$	Source	Notes/Comments
$K_A = 44$ km/s	This work	
$K$ ( $\text{Kms}^{-1}$ ) $44 \pm 0.4$ (Algol A)	Hill et al. (1971)	Richards, M. T. (1993), p. 257

TABLE 10

Previously published estimates of semi-amplitude of B with respect to A-B system CM,  
 $K_B$  (km/s)

$K_B$	Source	Notes/Comments
$K$ ( $\text{Kms}^{-1}$ ) $201 \pm 6$ (Algol B)	Tomkin, J. & Lambert, D. (1978)	Richards, M. T. (1993), p. 257
$201 \pm 6 \text{ km}^{-1}$	Tomkin, J. & Lambert, D. (1978), p. L119	

TABLE 11

Previously published estimates of semi-amplitude of C with respect to AB-C system CM,  $K_C$  (km/s)

$K_C$	Source	Notes/Comments
$K$ ( $\text{Kms}^{-1}$ ) $31.6 \pm 2$ (Algol C)	Hill et al. (1971), p. 450	Richards, M.T. (1993), p. 257
$K_c = 33.6 \pm 0.2$ km/sec	Ebbighausen (1958), p. 600	

TABLE 12

Previously published estimates of semi-amplitude of AB with respect to AB-C ( $K_{AB-C}$ ) system CM (km/s) – Should follow the equality:  $M_c/(M_a+M_b+M_c) = K_{AB-C}/K_C \sim .27$

$K_{AB-C}$	Source	Notes/Comments
$K$ ( $\text{Kms}^{-1}$ ) $12.0 \pm 0.4$ (Algol AB)	Hill et al. (1971), p. 451	Richards, M. T. (1993), p. 257
Algol AB 9.7 km/s 10.6 km/s	McLaughlin (1937) Eggen (1948)	Ebbighausen, E. G. (1958), p. 600

TABLE 13

Previously published estimates of time of Periastron passage of A-B System – Time of maximum positive radial velocity

$T_{A-B}$	Source	Notes/Comments
2,445,639.2146 days	Gillet et al., p.228	p. 419, 1st paragraph
2,428,482.7390	Hill et al. (1971), p. 451	

TABLE 14

Previously published estimates of Periastron passage of AB-C System (day) – Time of positive radial velocity

$T_{AB-C}$	Source	Notes/Comments
$T = JD\ 2.446.931.4 \pm 1.5$	Pan, X. et al. (1993), p. L129	
Periastron Passage = 2,434,009 days	Lestrade et al (1993), p. 809 Table 1-B	
2,434,022.8500 days	This work	Calculated from 1952.05, then adjusted by eye for Hill data
$1952.007 \pm 0.015$	Ebbighausen (1958)	Hill et al. (1971), p. 450 Appears that error is .005 greater than Ebbighausen tabulated value.
2421780.3	Hill et al. (1971), p. 444 (footnote)	
1952.05	Hill et al. (197), p. 451	His final solution
$1952.007 \pm 0.010$	Ebbighausen (1958) p. 600, Table 2	

TABLE 16

Previously published estimates of light elements (a.k.a. ephemeris, or epoch of primary minimum) (usually in days or equivalently JD)

Pr.Min	Source	Notes/Comments
HJD 2,441,773.894 + $2^d.8673285E$	Kim et al. (1989), p. 1061	
JD = 2440953.4657 + $2^d.8673075E$	Ashbrook (1976)	Al-Naimiy, H.M.K. et al, (1984), p. 1
$\beta$ per epoch = 2434705.5493 Period = 2.86732973	Frieboes-Conde et al. (1970)	Nha, I.S. & Jeong, J. H. (1979), p. 82, Table II
JD 2378497.7588 + $2^d.86731077E$	J. Hellerich (1919) (He derived the extension JD).	From Eggen, O. J. (1948), p. 2
JD 2378497.756 + $2^d.87631085E$	K. Ferrare (1934)	
JD (Hel) 2441934.0796 Pd. of $2^d.86733$	Chen, K-Y et al. (1977), p. 68	
HJD 2445641.5135	Al-Naimiy et al., 1984	



TABLE 16A

Previously published estimates of rate of mass loss  $dm/dT$  solar mass per year.

$M_{\odot}/\text{yr}$	Source	Notes/Comments
$(10^{-11}-10^{-7}) M_{\odot}/\text{year}^{-1}$	Richardson, M. T. (2001), p. 276	(Classical Algols are typically in a slow stage of mass transfer)
$ \dot{M}  (M_{\odot}/\text{year}) \geq 10^{-7}$	Soderhjelm (1980)	Sarna, M.J. (1993) p. 535, Table 1
$\dot{M} = 10^{-8} M_{\odot}/\text{year}$	Cugier, H. (1982) p. 393	
$\dot{M} \approx 10^{10} M_{\odot}/\text{year}^{-1}$	Harnden et al. (1977)	
$\dot{M} \approx 10^{14} M_{\odot}/\text{year}$ (for September 1989 data only)	This work	
$10^{-13} M_{\odot}/\text{year}^{-1}$	Cugier & Chen (1977)	

TABLE 18

Previously published estimates of Full Width at Half Maximum (FWHM)  $\text{\AA}$ . (Specify the ion and the lab wavelength in  $\text{\AA}$ .)

FWHM		Source	Notes/Comments	
Light Curve FWHR ( $\text{\AA}$ )	Wavelength ( $\text{\AA}$ )		# of Datapts.	Comparison Star
260	1920.2	Eaton (1975)	53	-----
100	4350.0	Wilson et al. (1972)	700	$\pi$ Per
180	4861.3	Guinan et al. (1976)	203	$\gamma$ Per
900	5500.0	Wilson et al. (1972)	700	$\pi$ Per
295	6562.8	Guinan et al. (1976)	214	$\gamma$ Per
410	12000.0	Chen & Reuning (1966)	848	$\kappa$ Per
				Richards, M. T. et al. (1988), p. 328, Table II
FWHM	Mg II Lines	Cugier, H. (1979), p.569		
1.60 $\text{\AA}$ at	$\lambda 2795.5 \text{\AA}$			
1.24 $\text{\AA}$ for	$\lambda 2802.7 \text{\AA}$			
1.10 $\text{\AA}$ for	$\lambda 2795.5 \text{\AA}$			
.86 $\text{\AA}$ for	$\lambda 2802.7 \text{\AA}$			

TABLE 19

Previously published estimates of radial velocity,  $V_{\text{rad}}$  (or  $V_r$ ), km/s. (Specify the ion and the Lab wavelength in Å and phase.)

$V_{\text{rad}}$	Source	Notes/Comments
Journal of radial velocities (huge)	Hill, G. et al. (1993) p. 581, Table 1	
Table of Radial Velocity Si IV range from + 29 to + 4 (kms <sup>-1</sup> )	Brandi, E. et al (1989) p. 332, Table I	
*See Table 2 – Radial Velocities for ( $\beta$ Persei) with ions	Sahade, J. & Hernandez, C.A. 1985) pp. 260-261	
Radial Velocity of (C) was –13 km/sec (on Sept. 1956)	Ebbighausen, E. G. Predicted	Struve, O. & Sahade, J. (1957) p. 41

TABLE 20

Previously published estimates of the orbital inclination  $i_{A-B}$ .

Inclination $i_{A-B}$	Source	Notes/Comments
80.2 81.6 ± 0.2 82.42 ± 0.04 81.4 ± 0.1 82.4 81.5, 81.1 81.5 ± 0.5 81.2 81 ± 4 82.3 ± 0.3 81.4 ± 0.2	Chen and Reuning (1966) Hill & Hutchings (1970) Wilson et al. (1972) Grygar & Horak (1974) Eaton (1972) Guinan et al. (1976) Al-Naimiy & Budding (1977) Chen et al (1977) Rudy & Kemp (1978) Soderhjelm (1980)	Richards et al. (1988) p. 335, Table IV
$i$ 82.3 degrees	Borkovits et al. (2003) p. 1096, Table I	Hill et al. (1971)
$i$ 82.31 degrees	Mukherjee et al. (1996), p. 620	
$i$ 82.2 degrees	Palubek, G. (1998), p.22 See Moden description, p. 19	
$i$ [deg]81.4 ± 0.2 degrees	Richards et al. (1998) and Soderhjelm (1980)	Sarna, M.J. (1993) p. 535, Table I
81.4 ± 0.2 degrees	Tomkin & Tan (1985)	Richards, M.T. (1993) p. 257, Table 1-A
82.°.3	Lestrade et al. (1993) p. 809, Table 1-B	
81.2	Koch, Plavec & Wood (1970)	Sahade J. & Hernandez, C.A. (1985), p. 257
82.3 ± 0.3	Soderhjelm, S. (1980) p. 110 (original)	
$i = 57$	Frieboes-Conde et al. (1970)	Bonneau (1979)

TABLE 21

Previously published estimates of the orbital inclination of the AB-C ( $i_{AB-C}$ ).

$i_{AB-C}$	Source	Notes/Comments
$i$ [deg] $83 \pm 2$ degrees	Richards et al. (1988) and Soderhjelm (1980)	Sarna, M. J. (1993) p. 535, Table 1
$i_{abc}$ $83 \pm 3$ degrees	Soderhjelm (1980)	Richards, M. T. (1993), p. 257
$i_{abc}$ $83^\circ.98 \pm 0^\circ.09$	Pan, X et al. (1993) p. L129	
$i$ $83^\circ$	Lestrade et al. (1993) p. 809, Table 1-B	
$i$ $83 \pm 2$	Soderhjelm, S. (1980), p. 110	
$i = 79$	Soderhjelm, S. (1975)	Bonneau, D. (1979), p. L11
ab-c $i = 78.5^\circ \pm 3.0^\circ$	Bonneau, D. (1979), p. L12	

TABLE 22

Previously published estimates of  $V_{rot} \sin i$  (Rotational Velocity).

$V \sin i$	Source	Notes/Comments
$\beta$ per $V_{eq} \sin i = 51.9 \pm 1.6$ $V_{syn} \sin i = 49.9 \pm 0.5$	Mukherjee et al. (1996) p. 623, Table 4	See Table 4 for Rotation Values for various methods
$V \sin i$ ( $\text{kms}^{-1}$ ) Algol A = $53 \pm 3$ Nothing for B Algol C = $46 \pm 10$	Richards, M. T. (1993) p. 257	Also cites: Rucinski (1979) Tomkin & Tan (1985)
Algol A = $50 \pm 5 \text{ kms}^{-1}$ $55 \pm 4 \text{ kms}^{-1}$ synchronous values is = $51 \text{ kms}^{-1}$	Heuvel (1970) Hill et al. (1971) Soderhjelm (1980), p. 103	Soderhjelm, S. (1980), p. 103

TABLE 23

Previously published estimates of a sin  $i$  (km)

a sin $i$	Source	Notes/Comments
a sin $i$ (kms) A = $1.73 \times 10^6$ B = $7.93 \times 10^6$ C = $2.88 \times 10^8$ AB = $1.09 \times 10^8$	Hill et al. (1971) Tomkin & Lambert (1978) Hill et al. (1971) Hill et al. (1971)	Richards, M. T. (1993), p. 257
a sin $i$ AB = $88 \times 10^6$ km AB = $87 \times 10^6$ km C = $307 \times 10^6$ km	McLaughlin (1937) Eggen (1948) Ebbighausen (1958)	Ebbighausen, E. G. (1958) p. 600, Table 2
a sin $i = 0.13867 \pm 71.10^{-5} = 24$ AE	Pavel, F. (1949), p. 59	
a sin $i = 37 \times 10^8$ km	Eggen, O. J. (1948), p. 1	

TABLE 24

Previously published estimates of mass of Algol A ( $M_A$ )

$M_A$	Source	Notes/Comments
M 3.7 3.6 3.8	Hill et al. (1971) Soderhjelm (1980) Kim et al. (1989) Present Study	Kim et al. (1989) p. 1067, Table 4
( $M_1$ ) 3.7	Soderhjelm (1980) Lestrade et al. (1993)	Borkovits et al. (2003) p. 1096, Table 1
$M_{\odot} 3.7 \pm 0.30$	Kim (1989) Richard et al. (1988) Tomkin & Lambert (1978)	Sarna, M. J. (1993) p. 535, Table 1
M ( $M_{\odot}$ ) $3.7 \pm 0.3$	Tomkin & Lambert (1978)	Richards, M. T. (1993) p. 257, 1-B
$M_{AB} = 3.98 \pm 0.38 M_{\odot}$	Pan, X. et al. (1993) p. L131, Table 2	Mass of A+B Together
$M_A = 3.6 M_{\odot}$	Soderhjelm (1980) & Kim (1989)	Lestrade et al. (1993)
$M_A = 3.7 M_{\odot}$	Guinan, E. F. (1989), p. 37	
$M_A = 3.7 \pm 0.2 M_{\odot}$	Soderhjelm (1980), p. 100	
$M_A = 3.6 \pm 0.1 M_{\odot}$	Soderhjelm (1980), p. 101	After adjustments
$M_A = 3.7 \pm 0.3$	Tomkin & Lambert (1978) p. L119	
Mass of AB $5.3 M_{\odot}$	Bachmann & Hershey (1975) p. 836	Combining elements independent of the parallax
$3.7 M_{\odot}$	Hill et al. (1971) 459	
Mass 1 = 5.8	Eggen, O. J. (1948), p.1	

TABLE 25

Previously published estimates of mass of Algol B ( $M_B$ )

$M_B$	Source	Notes/Comments
0.8	Hill et al. (1971)	Kim et al. (1989) p. 1067, Table 4
0.79 0.82	Soderhjelm (1980) (Present Study) Kim et al. (1989)	Kim et al. (1989) p. 1067, Table 4
( $M_2$ ) 0.8	Soderhjelm (1980) Lestrade et al. (1993)	Borkovits et al. (2003) p. 1096, Table 1
$M_\odot$ $0.81 \pm 0.05$	Kim (1989) Richards et al. (1988) Tomkin & Lambert (1978)	Sarna, M. J. (1993) p. 535, Table 1
$M$ ( $M_\odot$ ) $0.81 \pm 0.05$	Tomkin & Lambert (1978)	Richards, M. T. (1993) p. 257, 1-B
$M_B = 0.79 M_\odot$	Soderhjelm (1980); Kim (1989)	Lestrade et al. (1993) p. 809, Table 1
$M_B = 0.8 M_\odot$	Guinan, E. F. (1989), p. 37	
$M_B = 0.80 \pm 0.03 M_\odot$	Soderhjelm, S. (1980), p. 100	To be corrected by him
$M_B = 0.7980 \pm 0.01 (M_\odot)$	Soderhjelm, S. (1980), p.101	
$M_B = 0.81 \pm 0.05$	Tomkin & Lambert (1978) p. L119	
$0.8 M_\odot$	Hill et al. (1971), p. 459	
Mass 2 = $1.0_\odot$	Eggen, O. J. (1948), p.1	

TABLE 26

Previously published estimates of mass of Algol C ( $M_C$ )

$M_C$	Source	Notes/Comments
1.7 1.6 1.8	Hill et al. (1971) Soderhjelm (1980) Kim et al. (1989) Present Study	Kim et al. (1989) p. 1067, Table 4
$M_\odot .8$	Richards et al. (1988) Kim (1989)	Drake (2003) p. 497, Table 1
$M_\odot 1.70 \pm 0.2$	Kim (1989) Richards et al. (1988); Tomkin & Lambert (1978)	Sarna, J. J. (1993) p. 535, Table 1
$M (M_\odot) 1.6 \pm 0.1$	Hill et al. (1971) Tomkin & Lambert (1978) Soderhjelm (1980)	Richards, M. T. (1993) p. 257, 1-B
$M(M_\odot) 1.5 \pm 0.11 M_\odot$	Pan, X. et al (1993) p. L129	
$M_c = 1.6 M_\odot$	Soderhjelm (1980) & Kim (1989)	Lestrade et al. (1993) p. 809, Table 1
$M_c = 1.6 \pm 0.1 M_\odot$	Soderhjelm (1980), p. 101	
$M_c(M_\odot) = 1.6 \pm 0.2$	Bonneau, D. (1979), p. L12	
$M_c = 1.7 \pm 0.2 M_\odot$	Tomkin & Lambert (1978) p. L119	
Mass C $1.8 M_\odot$	Bachman & Hershey (1975) p. 836	
$1.7 M_\odot$	Hill et al. (1971), p. 459	
Mass 3 = $1.2_\odot$ Mass 4 = $3.8_\odot$	Eggen, O. J. (1948), p.1	

TABLE 27

Previously published estimates of Radius ( $R_{\odot}$ ) A.

$R_A$	Source	Notes/Comments
3.0 3.22 2.89 2.88	Hill et al. (1971) Eaton (1975) Soderhjelm (1980) Kim et al. (1989) Present study	Kim et al. (1989) P. 1067, Table 4
Stellar $R_{\odot}$ 2.9, 3.5	Richards (1993)	Richards (2003) Chart 338
$R_1/A = .204$	Mukherjee et al. (1996) p. 620, Table 2	
$R_{\odot} = 2.90 \pm 0.04$	Kim (1989) and Richards et al. (1988)	Sarna, M. J. (1993) p. 535, Table 1
$R(R_{\odot}) 2.9 \pm 0.04$	Tomkin & Tan (1985)	Richards, M. T. (1993) p. 257, 1-B
$R_A 2.89 R_{\odot}$	Soderhjelm (1980) & Kim (1989)	Lestrade et al. (1993), p. 809
Unperturbed fractional Radius $R_A = .188$	Gillet, D. et al. (1989) p. 222, Table 3	
RA ( $R_{\odot}$ ) 2.90 $\pm$ 0.04 Roche 3.08 Roche 3.2 $\pm$ 0.2 Russell-Merrile 3.0 Roche 2.89 Roche	Richards (1986) Wilson et al (1972) Eaton (1975) Hill (1971) Soderhjelm (1980)	Richards, M. T. et al. (1988) p. 335, Table VIII
2.89 $\pm$ 0.04	Soderhjelm (1980) p. 110, Table 9	
Radii of Algol A = 3.2	Eaton (1975)	Cugier & Chen (1977), p. 169
3.0 $R_{\odot}$	Hill et al. (1971), p. 459	
Semiaxes of Algol A $a_A$ .188 $b_A$ .188 $c_A$ .187	Gillet, D. (1989) p. 222, Table 3	
$R_A = r_s 0.201 - 0.209$ at 3428 Å	Chen, K. -Y. et al. (1977) Table III	In terms of fraction of separation
$R_A = r_s 0.205$ at 3700 Å	Herczeg (1959)	Chen, K.-Y. et al. (1977) Table III ( in terms of fraction of separation.)
$R_A = r_s 0.224$ at 2980 Å	Eaton (1975)	Chen, K.-Y. et al (1977) Table III (in terms of fraction of separation)

TABLE 28

Previously published estimates of Radius ( $R_{\odot}$ ) B.

$R_B$	Source	Notes/Comments
3.4 3.57 3.53 3.54	Hill et al. (1971) Eaton (1975) Soderhjelm (1980)  Kim et al. (1989), Present Study	Kim et al. (1989) P. 1067, Table 4
3.5	Richards (1993)	Ness et al. (2002), p. 913
$R_{\odot} = 3.50 \pm 0.10$	Kim (1989) and Richards et al. (1988)	Sarna, M. J. (1993) p. 535, Table 1
$R(R_{\odot}) 3.5 \pm 0.1$	Tomkin & Tan (1985)	Richards, M. T. (1993) p. 257, 1-B
$R_B(R_{\odot})3.4$	Credited to Soderhjelm (1980) & Kim (1989)	Lestrade et al. (1993), p. 809
$R_B 3.53 R_{\odot}$	Soderhjelm (1980) and Kim (1989)	Lestrade et al. (1993) p. 809, Table 1-A
$R_B(R_{\odot}) 3.4$ Roche 3.6 $\pm$ 0.2 Russell-Merrille 3.23 Roche 3.53 Roche 3.5 $\pm$ 0.1 Roche	Hill et al. (1971) Eaton (1975) Wilson et al (1972) Soderhjelm (1980) Richards (1986)	Richards, M. T. et al. (1988) p. 335, Table VIII
3.5 $\pm$ 0.04	Soderhjelm (1980) p. 110, Table 9	
3.6	Eaton (1975)	Cugier & Chen (1977) p.169
3.4*	Hill et al. (1971), p. 459	*derived from the polars values R & TagTe
Semiaxes of Algol B $a_B.291$ $b_B.258$ $c_B.244$	Gillet, D. (1989) p. 222, Table 3	
$R_B = r_g 0.248-0.253$ at 3428 Å	Chen, K. -Y. et al. (1977) p. 73, Table III	
$R_B = r_g 0.262$ at 3700 Å $R_B = r_g 0.244$ at 2980 Å	Herczeg (1959) Eaton (1975)	Chen, K.-Y. et al. (1977) p. 73, Table III (in terms of fraction of separation.)



TABLE 29

Previously published estimates of Radius ( $R_{\odot}$ ) C

$R_C$	Source	Notes/Comments
1.5 1.56 1.5 1.7	Hill et al. (1971) Eaton (1975) Soderhjelm (1980) Kim et al. (1989), Present Study	Kim et al. (1989) P. 1067, Table 4
$R_{\odot} = 1.60 \pm 0.2$	Kim (1989) and Richards et al. (1988)	Sarna, M. J. (1993) p. 535, Table 1
$R(R_{\odot}) 1.4 \pm 0.1$	Tomkin & Tan (1985)	Richards, M. T. (1993) p. 257, 1-B
$R_C 1.5 R_{\odot}$	Soderhjelm (1980) & Kim (1989)	Lestrade et al. (1993), p. 809
$1.5 \pm 0.1 R_{\odot}$	Soderhjelm, S. (1980) p. 110, Table 9	
$1.5 R_{\odot}$	Hill et al. (1971), p. 459	

TABLE 30

Previously published estimates of Temp  $T_A$ 

$T_A$	Source	Notes/Comments
$T_{eff}^{pol}$ (Algol A) = 1300 K	Polubek, G. (1998), p. 22	See Figure 2, p. 21 See model description, p. 19
Ti(K) = 12000 K	Mukherjee et al. (1996) p. 620, Table 2	See Table 2, p. 620 For other comparison
$T_{eff}$ (K) 12500 $\pm$ 500	Eaton (1975) Kim (1989) Richards (1988)	Sarna, M. J. p. 535, Table 1
T (K) 13,000 $\pm$ 500	Cugier & Molaro (1983)	Richards, M. T. (1993) p. 257, 1-B
$T_A$ (eq) 12,500 $T_A$ (Pol) 12550	Guinan et al. (1976) using Wood's (1972) WINK computer model	Gillet D. et al. (1989) p. 222, Table 3
$T_A$ 12500 K	Flower (1977) Bohm-Vetense (1981)	Richards, M. T. et al. (1988) p. 328, Table 1
$T = 10^4$ K	Cugier, H. (1992), p. 393	
$T_{eff}$ (K) 12,500 $\pm$ 500	Soderhjelm, S. (1980) p. 110, Table 9	
$T_{eff}$ 12000 K	Cugier, H. (1979), p. 549	
Te 12,000 K	Chen, K.-Y. et al. (1977), p. 71	
Te 12,000 K	Kurucz (1969) Carbon & Gingerich (1969)	Chen, K.-Y. et al. (1977), p. 72
log Te 4.03	Hill et al. (1971), p. 459	

TABLE 31

Previously published estimates of Temp  $T_B$ 

$T_B$	Source	Notes/Comments
(K) $4500 \pm 300$	Richards et al. (1988)	
B (Algol B)	Eaton (1975) Kim (1989)	
$T_{eff}^{pole}$ (Algol B) = 5000 K	Polubek, G. (1998)	See Figure 2, p. 21 See model description, p. 19
$T_2(K) = 4888$ K	Mukherjee et al. (1996) p. 620, Table 2	
$T_{eff}(K) 4500 \pm 300$	Eaton (1975) Kim (1989) Richards et al. (1988)	Sarna, M. J. p. 535, Table 1
T (K) $4500 \pm 300$	Hill et al. (1971)	Richards, M. T. (1993) p. 257, 1-B
$T_B$ (eq) 5330 $T_B$ (Pol) 5590	Guinan et al. (1976) using Wood's (1972) WINK computer model	Gillet, D. et al. (1989) p. 222, Table 3
$T_B$ 5000 K	Soderhjelm (1980)	Richards, M. T. et al. (1988) p. 328, Table 1
$T_B(K)$ 5080 4700 $5330 \pm 180$ $4600 \pm 800$ 5300 5000 $5250 \pm 250$ $4500 \pm 300$ $5000 \pm 500$	Chen & Reuning (1966) Hill & Hutchings (1970) Wilson et al. (1972) Eaton (1975) Al-Naimiy & Budding (1977) Chen et al. (1977) Murad & Budding (1984) Richards (1986) Soderhjelm (1980)	Richards, M. T. et al. (1988) p. 336, Table IX
$5000 \pm 500$ K	Soderhjelm (1980) p. 110, Table 9 primary (original)	
log Te 3.66	Hill et al. (1971) p. 459	

TABLE 32

Previously published estimates of Temp  $T_C$ 

$T_C$	Source	Notes/Comments
$T_{eff}^{pole}$ (Algol C) = 7000 K	Polubek, G. (1998) p. 22	See Figure 2, p. 21 See model description, p. 19
$T_{eff}$ (K) $8000 \pm 700$	Eaton (1975) Kim (1989) Richards et al. (1988)	Sarna, M. J. p. 535, Table 1
T (K) $7000 \pm 200$	Richards, M. T. (1993) p. 257, 1-B	
$T_{eff}$ (K) $8400 \pm 500$	Soderhjelm, S. (1980) p. 110, Table 9	
8500 K	Chen et al. (1977) p. 71	
8500 K	Kurucz (1969) & Carbon & Gingerich (1969)	Chen, K.-Y. et al. (1977), p. 72
log Te 3.92	Hill et al. (1971) p. 459	

TABLE 33

Previously published estimates of log of surface gravity, log g of Algol A

Log $g_A$	Source	Notes/Comments
(log) 4.03 4.11 4.10 4.08	Hill et al. (1971) Eaton (1975) Soderhjelm (1980) Kim et al. (1989)	Kim et al. (1989) p. 1067, Table 4
log g 4.08	Richards et al. (1988) Tomkin & Lambert (1978)	Richards, M. T. (1993) p. 257, Table 1-B
log $g_A = 4.0$	Flower (1977) Bohm-Vilense (1981)	Richards, M. T. et al. (1988) p. 328, Table 1
log $g_A = 4.0$	Chen, K.-Y. et al. (1977) p. 71	
log $g_A = 4.0$	Kurucz (1969) Carbon & Gingerich (1969)	Chen, K.-Y. et al. (1977)

TABLE 34

Previously published estimates of log of surface gravity, log g of Algol B

Log g <sub>B</sub>	Source	Notes/Comments
(log) 3.66 3.66 3.70 3.69	Hill et al. (1971) Eaton (1975) Soderhjelm Kim et al. (1989)	Kim et al. (1989) p. 1067, Table 4
Log g 3.2	Tomkin & Tan (1985) Tomkin & Lambert (1978)	Richards, M. T. (1993) p. 257, Table 1-B
Log g <sub>B</sub> = 3.0	Soderhjelm (1980)	Richards, M. T. et al. (1988) p. 328, Table 1
Log g <sub>B</sub> = 3.0	Chen, K.-Y. et al. (1977) p. 71	

TABLE 35

Previously published estimates of log of surface gravity, log g of Algol C

Log g <sub>C</sub>	Source	Notes/Comments
(log) 3.92 3.94 3.92 3.93	Hill et al. (1971) Eaton (1975) Soderhjelm (1980) Kim et al. (1989)	Kim et al. (1989) p. 1067, Table 4
Log g 4.4	Tomkin & Tan (1985)	Richards, M. T. (1993) p. 257, Table 1-B
Log g 4.0	Chen, K.-Y. et al. (1977) p. 71	
Log g 4.0	Kurucz (1969) Carbon & Gingerich (1969)	Chen, K.-Y. et al. (1977) p. 72

TABLE 36

Previously published estimates of distance to Algol AB-C system (parasecs)

Distance, d	Source	Notes/Comments
pc $28.5 \pm 0.8$	ESA (1997)	Richards et al. (2003) p. 338, Chart
pc 29.0	Perryman et al. (1997)	Drake (2003) p. 497 (chart), Table 1
d/pc 28.0	Perryman et al. (1977)	Ness et al (2002) p. 913
$(31 \pm 3)$ pc	Richards cites Labeyrie et al. (1974)	Richards et al. (1996), p. 249
d (pc) $31 \pm 3$	Bachmann & Hershey (1975) Labeyrie et al. (1974)	Richards, M. T. (1993) p. 257, Table 1-B
d (pc) $28.2 \pm 0.8$ pc	Pan, X. et al. (1993) p. L129	
$\sim 25$ pc	Gillet, D. et al. (1989), p. 219	
30 pc $\sim$ cf	Cugier, H. (1979), p. 550	

TABLE 37

Previously published estimates of spectral Type Algol A

Spectral Type	Source	Notes/Comments
B8	Kim et al. (1989), p. 1062	
B8 V + K2IV = 2.8673	Richards, M. T. (2001) p. 287, Table 2	
B8 V	Mutel et al. (1998), p. 371	
B8 V	Richards cites Batten (1989) Richards (1993) Antunes, Nagase & White (1994) Ottman (1994) Morgan (1935)	Richards et al. (1996), p. 249 Richards, M. T. (1993) p. 257, Table 1
B8 V	Gimenez, A. (1996), p. 23; #2 Case of Algol	
Algol A B8 V	Sarna, M. J. (1993) p. 1 (intro)	
B8 V	Pan, X. et al. (1993), p. L129	
B8 V	Lestrade et al. (1993), p. 808	
B8 V	Guinan, E. F. (1989), p. 37	
B8 V	Gillet, D. et al. (1989), p. 219	
B8 V	Sahade, J. & Hernandez, C.A. (1985), p. 257	
B8 V	Cugier, H. & Molaro, P. (1985) p. 105	
B8 V	Soderhjelm, S. (1980), p. 100	
B8 V	Cugier, H. (1979), p. 549	
B8 V	Tomkin & Lambert (1978) p. 119	
B8 V	Cugier & Chen (1977), p. 169	
B8 V	Frieboes-Conde, H. et al. (1970) p. 78	
B8	Struve, O. & Sahade, J. (1957) p. 41	

TABLE 38

Previously published estimates of spectral Type Algol B

Spectral Type	Source	Notes/Comments
KO	Kim et al. (1989), p. 1062	
SecondaySpec Type K4	Zavala et al. (2002), p. 456	
K2 IV	Ness et al. (2002)	
K21V	Mutel et al. (1998), p. 371	
K2 subgiant	Batten (1989) Richards (1993) Antunes, Nagase & White (1994) Ottman (1994)	Richards et al. (1996), p. 249
KO – 2IV	Gimenez, A. (1996), p. 23 #2 The Case of Algol	
K2IV	Richards, M. T. (1993) p. 257, Table 1	
KIV	Pan, X. et al. (1993), p. L129	
KO – 3IV	Lestrade et al. (1993), p. 808	
K2-3 IV	Guinan, E. F. (1989), p. 37	
Type G5 – KOIV	Gillet, D. et al. (1989), p. 219	
Late B or early K Subgiant	Tomkin & Lambert (1978)	Sahade, J. & Hernandez, C. A. (1985), p. 257
Late G or K type star	Cugier, H. & Molaro, P. (1985) p. 105	
G-type of sub-giant	Soderhjelm, S. (1980), p. 100	
Type K star	Cugier, H. (1979), p. 549	
(B) Cool mass subgiant 1.2 mag deep on V	Tomkin & Lambert (1978) p. L119	
G-K range	Cugier & Chens (1977), p. 169	
Late type G or Early K	Frieboes-Conde, H. et al. (1970)	



TABLE 39

Previously published estimates of spectral Type Algol C

Spectral Type	Source	Notes/Comments
A7M <sup>a</sup>	Kim et al. (1989), p. 1062	
F2V Tertiary	Batten (1989) Richards (1993) Antunes, Nagase & White (1994) Ottman (1994)	Richards et al. (1996), p. 249
A9 / FO V	Gimenez, A. (1996), p. 23 #2 Case of Algol	
Late A or Early F Luminosity class V	Sarna, M. J. (1993) p. 1 (intro.)	
F1 V	Richards et al. (1988)	Richards, M. T. (1993) p. 257, Table 1
A7m	Lestrade et al. (1993), 808	
A5-9	Guinan, E. F. (1989), p. 37	
AM type star	Gillet, D. et al. (1989), p. 219	
AM star	Huang (1957)	Sahade, J. & Hernandez, C.A. (1985), p. 257
Late spectral A	Cugier, H. & Molaro, P. (1984) p. 105	
Late spectral A	Cugier, H. (1979), p. 550	
Late (A or F) luminosity Class IV or V	Struve & Sahade (1957)	Tomkin & Lambert (1978) p. L119
A – metallic star	Fletcher (1964)	Frieboes-Conde, H. et al. (1970)
Metallic line – A star	Struve, O. & Sahade, J. (1957) p. 41	

TABLE 40

Previously published estimates of mass ratio of Algol A-B system  $q = m_B/m_A$

$q = M_B/M_A$	Source	Notes/Comments
Superhumps $q = M_{\text{donor}}/M_{\text{receiver}} = 0.29 \pm 0.01$  Assuming that the observed peak out $\sim 3$ days is a true superhump, the mass ratio of the binary system of $\beta$ per can be estimated from the superhump period excess over the orbital pd. about (6%, §§ 1-2)	Osaki (1985)	Retter et al. (2005), p. 423 (3.2)
Permitted range for superhumps Binary mass ratio of $\beta$ per $q = 0.217 \pm 0.03$ $q = 0.22 \pm 0.03$ $q = M_S/M_P 0.22$	Hill et al. (1988) Tomkin & Lambert (1978)  Richards et al. (1988)	Retter et al. (2005), p. 423 (3.2)
$q = M_2/M_1 0.227$	Richards et al. (2003) p. 338, Chart	
$q = 0.22$	Mukherjee et al. (1996) p. 620, Table 2	
Mass ratio $M_A/M_B = \sim 4.5$ days	Gimenez, A. (1996), p. 23 Last paragraph	
$q = .217$	Lestrade et al. (1993), 809 Paragraph 1	
$q = .22$	Gillet, D. et al. (1989) p. 222, Table 3	
Mass ratio $M_A/M_B = 4.6 \pm 0.1$ Mass ratio $M_A/M_B = 4.6 \pm 0.1$	Tomkin & Lambert (1978) p. L119 abstract their original	Richards, M. T. et al. (1988) p. 328, Table 1
Mass ratio $M_A/M_B = 4.6$ Mass ratio 4.6	Hill et al. (1971) Hill et al. (1971), p. 443 original	Soderhjelm, S. (1980)  Cugier & Chen (1977) p. 169

TABLE 40 (A)

Previously published estimates of mass ratio of AB-C system  $q = M_{AB}/M_C$

$q = M_{AB}/M_C$	Source	Notes/Comments
$M_{AB}/M_C = 2.63 \pm 0.20$	Hill et al. (1971), p. 443	

TABLE 41

Previously published estimates of separation ( $R_{\odot}$ ) of center of A to center of B  
Sep. ab ( $R_{\odot}$ )

sep. AB	Source	Notes/Comments
Sep. radius $R_{\odot} 14.0$	Richards et al. (2003) p. 338, Chart	
Separation ( $10^6$ km)		
$\sim 0.03$ binary separation	Bonneau (1979)	Richards et al. (1996), p. 249
$14 R_{\odot}$	Gillet, D. et al. (1989), p. 219	
$1 \times 10^{12}$ CM = approx. $14 R_{\odot}$	Cugier & Chen (1977), p. 169	
$A/R_{\odot} 13.99$	Mukherjee et al. (1996) p. 620, Table 2	
$14.03 R_{\odot}$	Chung et al. (2004) p. 1193, Figure 10	

TABLE 42

Previously published estimates of separation of center of AB system to center of C  
(astronomical units AU)

sep. AB-C	Source	Notes/Comments
$a = 2.67 \pm 0.08$ AU	Pan, X. et al. (1993) p. L131, Table 2	
$a = 2.71$ au $\pm 0.003$ au	Bonneau, D. (1979), p. L12	

TABLE 43

Previously published estimates of  $\Omega$  omega A-B system

$\Omega_{A-B}$	Source	Notes/Comments
$\Omega 52$	Soderhjelm (1980) Lestrade et al. (1993)	Borkovits et al. (2003) p. 1096, Table 1
$\Omega 1 = 5.151$	Mukherjee et al. (1996) p. 620, Table 2	

TABLE 43 (A)

Previously published estimates of  $\Omega$  omega of AB-C system

$\Omega_{AB-C}$	Source	Notes/Comments
$\Omega_2 = 2.299$	Mukherjee et al. (1996) p. 620, Table 2	
$\Omega = 312^\circ.26 \pm 0.13$	Pan, X. et al (1993) p. L129	
$\Omega = 313^\circ \pm 5^\circ$	Bonneau, D. (1979), p. L12	
$\text{Node}_{AB-C} = 132^\circ$	Lestrade et al. (1993) p. 809, Table 1-B	

TABLE 44

Previously published estimates of mass function of AB system  $f(m)$  AB

$f(m)_{A-B}$	Source	Notes/Comments
$f(m) (M_\odot)$ Algol A $0.0254 \pm 0.0008$ B $2.42 \pm 0.22$ C $2.05 \pm 0.20$	Hill et al. (1971)	Richards, M. T. (1993) p. 257, Table 1-A

TABLE 45

Previously published estimates of rotational velocity ( $V_{rot}$ ) (km/s)

$V_{rot}$	Source	Notes/Comments
$V_{rot} 55 \text{ km s}^{-1}$	Cugier, H. & Molaro, P. (1984) p. 111 in discussion	
Rotational Velocity Algol A = $55 \pm 4 \text{ km s}^{-1}$	Hill et al. (1971), p. 443	

TABLE 46

Previously published estimates of Roche Lobe (fill out factor)  $F_A$  or ratio of Algol A

$F_A$	Source	Notes/Comments
$F_A = 0.5$	Richards, M. T. et al. (1988) p. 328, Table 1	

TABLE 47

Previously published estimates of Roche Lobe (fill out factor)  $F_B$  or ratio of Algol B

$F_B$	Source	Notes/Comments
$F_B = 1.0$	Richards, M. T. et al. (1988) p. 328, Table 1	

TABLE 48

Previously published estimates of  $\beta_A$ , Beta gravity darkening exponent or coefficient for Algol A

$\beta_A$	Source	Notes/Comments
$\beta_A = .25$	Guinan et al. (1976) using Wood's 1972 WINK computer model	Gillet, D. et al. (1989) p. 222, Table 3
$\beta_A = 0.25$	Von Zeipel (1924); Lucy (1967)	Richards, M. T. et al. (1988) p. 328, Table 1

TABLE 49

Previously published estimates of  $\beta_B$ , Beta gravity darkening exponent or coefficient for Algol B

$\beta_B$	Source	Notes/Comments
$\beta_B = .25$	Guinan et al. (1976) using Wood's 1972 WINK computer model	Gillet, D. et al. (1989) p. 222, Table 3
$\beta_B = 0.08$	Lucy (1967)	Richards, M. T. et al. (1988) p. 328, Table 1

TABLE 50

Previously published estimates of bolometric Albedo (or reflection coefficient) for Algol A

$A_A$	Source	Notes/Comments
$A_A = 1.0$	Rucinski (1969) Milne (1926)	Richards, M. T. et al. (1988) p. 328, Table 1
$W_A = 1.0$	Guinan et al. (1976) using Wood's 1972 WINK computer model	Gillet, D. (1989) p. 222, Table 3

TABLE 51

Previously published estimates of bolometric Albedo (or reflection coefficient) for Algol B

$A_B$	Source	Notes/Comments
$A_B = 0.5$	Rucinski (1969) Milne (1926)	Richards, M. T. et al. (1988) p. 328, Table 1
$W_B = 0.4$	Guinan et al. (1976) using Wood's 1972 WINK computer model	Gillet, D. (1989) p. 222, Table 3

TABLE 52

Previously published estimates of Luminosity of A

$L_A$	Source	Notes/Comments
(log $L/L_\odot$ ) 2.41	Eaton (1975)	Kim et al.(1989) p. 1067, Table 4
(log $L/L_\odot$ ) 2.26	Soderhjelm (1980)	
(log $L/L_\odot$ ) 2.19	Kim et al. (1989)	
$L_\chi = 1.4 \times 10^{31}$ erg/s	Ness et al. (2002), p. 1045	Total luminosity sited in a phases b/w 0.74 to 1.06 of LETGS observations. See conclusions, starting p. 1045
log ( $L/L_\odot$ ) $2.265 \pm 0.075$	Sarna, M. J. (1993) p. 535, Table 1	Calculated
$2.2 \leq V \leq 3.5$	Gillet, D. et al. (1989), p. 219	
x-ray luminosity prob. Varies in the range $L_\chi \approx 10^{31} - 10^{33}$ ergs/s	Sahade, J. & Hernandez, C.A. (1985), p. 258	
Lg ( $L/L_\odot$ ) $2.26 \pm 0.07$	Soderhjelm, S. (1980) p. 110, Table 9	
X-ray is $\sim 2 \times 10^{30}$ ergs/s <sup>-1</sup>	Harnden, F. R., Jr., et al. (1989) p. 418	
$L_A = L_s$ 0.839 - 0.839 at 3428 Å $L_A = L_s$ 0.888 at 3700 Å $L_A = L_s$ 0.93 at 2980 Å	Chen, K.-Y. et al. (1977)  Herczeg (1959)  Eaton (1975)	In terms of fraction of total luminosity of AB-C system. (g is the greater star, Algol B) Chen, K.-Y. et al. (1977) p. 73, Table III; (s is the smaller star.)
$L_A = .734$ fractional luminosity	Guinan et al. (1976), using Wood's 1972 WINK computer model	

TABLE 53

Previously published estimates of luminosity of B

$L_B$	Source	Notes/Comments
(log $L/L_\odot$ ) 0.68	Eaton (1975) from	Kim et al. (1989) p. 1067, Table 4
(log $L/L_\odot$ ) 0.84	Soderhjelm (1980)	
(log $L/L_\odot$ ) 0.81	Kim et al. p. (1989)	
log ( $L/L_\odot$ ) $0.65 \pm 0.14$	Sarna, M. J. (1993)	Calculated
log ( $L/L_\odot$ ) $0.84 \pm 0.16$	Soderhjelm, S. (1980) p. 110, Table 9	
$L_B = L_g$ 0.061–0.063 at 3428 Å	Chen, K.-Y. et al. (1977)	Chen, K.-Y. et al. (1977) p. 73, Table III In terms of fraction of total luminosity of AB-C system. (g is the greater star, Algol B)
$L_B = L_g$ 0.077 at 3700 Å	Herczeg (1959)	
$L_B = L_g$ 0.03 at 2980 Å	Eaton (1975)	
$L_B = .136$ fractional luminosity	Guinan et al. (1976) using Wood's 1972 WINK computer model	Gillet, D. et al (1989) p. 222, Table 3

TABLE 54

Previously published estimates of luminosity C

$L_C$	Source	Notes/Comments
(log $L/L_\odot$ ) 1.11	Eaton (1975) from	Kim et al. (1989) p. 1067, Table 4
(log $L/L_\odot$ ) 1.00	Soderhjelm (1980)	
(log $L/L_\odot$ ) 1.15	Kim et al. (1989)	
Log ( $L/L_\odot$ ) $0.97 \pm 0.17$	Sarna, M. J. (1993) p. 535, Table I	Calculated
Log ( $L/L_\odot$ ) $1.00 \pm 0.12$	Soderhjelm, S. (1980) p. 110, Table 9	



TABLE 55

Previously published estimates of limb darkening coefficient (1<sup>st</sup> order) for Algol A ( $\mu_{1A}$ )

$\mu_{1A}$	Source	Notes/Comments
$\mu_{1A} = .35$	Guinan et al. (1976) using Wood's 1972 WINK computer model	Gillet, D. et al (1989) p. 222, Table 3
$\chi_s = 0.4$ at 3428 Å $\chi_s = 0.5$ at 3700 Å $\chi_s = 0.7$ at 2980 Å	Chen, K.-Y. et al. (1977) Herczeg (1959) Eaton (1975)	Chen, K.-Y. et al. (1977) p. (1977), Table III $\chi$ in this paper is the 1 <sup>st</sup> order; s is the smaller star Algol A.

TABLE 56

Previously published estimates of limb darkening coefficient (2<sup>nd</sup> order) for Algol A

$\mu_{2A}$	Source	Notes/Comments
$[\mu_1, \mu_2]_A = 1.000; -0.096$ at 1920 Å; $T_A = 12,500$ K	Richards, M. T. et al. (1988) p. 328, Table 1-B	

TABLE 57

Previously published estimates of limb darkening coefficient (1<sup>st</sup> order) for Algol B

$\mu_{1B}$	Source	Notes/Comments
$\mu_B = .60^*$ fixed par.	Guinan et al. (1976), using Woods (1972) Computer model	Gillet et. al. (1989) p. 222, Table 3
$\chi_g = 1.0$ at 3428 Å	Chen, K.-Y. et al. (1977) p. 73, Table 111	$\chi$ in this paper is 1 <sup>st</sup> order; g is the greater, meaning Algol B.

TABLE 58

Previously published estimates of limb darkening coefficient (2<sup>nd</sup> order) of Algol B

$\mu_{2B}$	Source	Notes/Comments
$[\mu_1, \mu_2]_B = 1.199; -0.343$ at 1920 Å; $T_B = 5,000$ K	Richards, M.T. et al. (1988) p. 328, Table 1 (B)	

TABLE 59

Previously published estimates of position angle of the nodal point between 0° and 180°  
Also the position angle of the line of nodes

$\Omega$	Source	Notes/Comments
$\Omega^\circ ABC = 132 \pm 2$ $\Omega^\circ AB = 132 \pm 4$	Soderhjelm, S. (1980) p. 110, Table 8	

## APPENDIX B

### Algol Timeline

Date	Milestone / Event	Reference
Ancient times	Inhabitants of Arabian peninsula gave the second brightest star in the constellation of Perseus the name, Al Ghul, meaning “changing spirit.”	(2), p. 3, paragraph 3
Ancient times	The Hebrews knew Algol as Rōsh-ha-Satan (Satan’s head).	(2), p. 12, bibliographic note No. 12
Ancient times	The Chinese gave it the title Tseih She (the Piled-up Corpses)!	(2), p. 12, bibliographic note No. 12
205 B.C. - 25 A.D.	“The Chinese had related the observed brightness changes of Tsi-chi. (There are some Chinese character in parentheses) or Algol with death of the population or good or bad fortune recorded in <u>Hsing Ching</u> .	(1), p. 131
2 <sup>nd</sup> Century A.D. (127-141 A.D.)	The term “double star” was used by Ptolemy, and this is not necessarily a binary system.	(2), p. 1, paragraph 2 (7), p. xi, paragraph 3
1850s	Father Angelo Secchi and astronomers discovered an unknown element which was named Helium after Helios, the Greek sun god. This discovery was made while studying the body of the sun and cataloguing the chemicals in the sun’s spectral bands. These bands also revealed hydrogen, calcium, and iron.	(3)
1609	Galileo first pointed a telescope in the sky and instantly recorded the first scientific milestone – sunspots.	(3)
1650 circa	The first double star which we know to form a binary system, ζ Ursae Majoris discovered by Father Jean Baptista Riccioli.	(2), p. 1, 2 <sup>nd</sup> paragraph (7), p. 1
1669	Geminiano Montanari recorded that Algol’s light varied at times.	(1), pp. 130-131

## APPENDIX B

### Algol Timeline continued

1670 Nov. 8	The first known recorded minimum of Algol's light, though its hour or minute is unknown.	(2), p. 3, last paragraph, and p. 13, bibliographic note No. 13
1695	Maraldi confirmed the variability of Algol.	(2), p. 3, last paragraph
1761	Lambert published a brief in which it is maintained that the stars are suns and are accompanied by retinues of planets.	(7), p. 2, paragraph 2
1767	Reverend John Michell gave the first scientific argument that probably many double stars, then known, were the result of a physical rather than optical association.	(2), p. 2, paragraph 1
1767	Michell used a probability argument to conclude that it is highly probable in particular and next to certainty in general that such double stars, etc., as appear to consist of two or more stars placed very close together do really consist of stars, placed near together.	(4), p. 7, paragraph 1
1779	Herschel conceived the idea of utilizing double stars to test a method of measuring stellar parallax suggested long before by Galileo in early 1600s.	(7), p. 5, paragraph 1
1783	John Goodricke <ol style="list-style-type: none"> <li>1) discovered that Algol's variability was periodic, thus he discovered the first short-period variable ever known.</li> <li>2) estimated its period to be two days, 20 hours, and 45 minutes.</li> <li>3) reasoned that Algol was an eclipsing binary.</li> </ol>	(2), p. 4
1783	Goodricke suggested, "The periodic passage between us and the star of a dark object."	(1), p. 2, paragraph 3 (5), p. 4, paragraph 2
1784	Goodricke discovered that $\beta$ Lyrae was an eclipsing variable.	(1), p. 2, paragraph 3

## APPENDIX B

### Algol Timeline continued

1802	The term “binary star” was first used by Sir William Herschel.	(2), p. 1, 1 <sup>st</sup> sentence, paragraph 2
1802	William Herschel, in collaboration with his sister, Caroline, published observations over 40 years attempting to establish distances between double stars via the inverse-square law of light propagation.	(4), p. 7, paragraph 1
1827	The mathematical method required to determine the geometry of the relative orbit of one component with respect to its companion from a set of observations of position angle and separation was first developed by Savary.	(4), p. 8, paragraph 2
1850s	Father Angelo Secchi, the Vatican’s chief astronomer, pioneered the branch of science called spectroscopy. Spectroscopy revealed a complexity of the sun, activity around the edges of the sun.	(3)
1857	Mizar (Ursae Majoris) first double star to be observed photographically measurable images being secured by G. P. Bond at the Harvard Observatory.	(7), p. 1, paragraph 1
1862	Father Secchi found that the sun must also be a star since the stars and the sun were composed of the same chemicals as revealed through spectroscopy.	(3)
1889	ζ Ursae Majoris’ principal component was recognized as the first spectroscopic binary by E. C. Pickering	(2), p. 1, 2 <sup>nd</sup> paragraph
1889	Vogel’s spectroscopic observations confirmed that Algol was an eclipsing binary.	(2), p. 5, paragraph 2
1890	Vogel was first to prove the star Algol was indeed a binary star, by demonstrating that the primary star was receding from the observer before primary eclipse, and approaching the observer after primary eclipse.	(4), p. 10, paragraph 2
1893	Belopolsky found that the radial velocities of the H <sub>β</sub> emission of β Lyrae gave a velocity curve opposite in phase to, and with smaller amplitude than that from the stellar absorption lines.	(1), p. 6, paragraph 6

## APPENDIX B

### Algol Timeline continued

1893	Dr. Kristian Birkeland, a Norwegian Scientist, drew his own conclusions about the sun. Birkeland's hunch was that the magnetic storms accompanying the Northern Lights (Aurora) were caused by a stream of electrically charged particles buffeting the earth's magnetic field. (His ideas were never taken.)	(3)
1896	Pickering reported Bailey's discovery of the variation in line intensities of $\mu^1$ scorpis – the lines of one of the components are weaker when its velocities are of recession.	(1), p. 2, paragraph 1
1898	Pickering (1904) and Wendell (1909) independently observed a strange increase of brightness immediately after primary on the light curve of R Canis Majoris.	(1), p. 5, last paragraph
1898	Myers proposed the existence of a gaseous envelope around the system of $\beta$ Lyrae.	(1), pp. 6-7
1907-1912	Schlessinger detected narrow lines near the primary minimum. Later attributed to Algol C by Pearce and Meltzer.	(1), p. 131 (1), p. 131 (11), (12)
1908	Curtiss reported variations of the velocity of the center of mass of the eclipsing pair of Algol.	(1), p. 131
1908	Barr's analysis of the available orbits and radial velocity curves of spectroscopic binaries found that: A) very often, the velocity curves were unsymmetrical, B) these asymmetries with only a few exceptions, were similar, in the sense that the "ascending branch of the curve" was of greater length than the "descending branch," and C) a logical consequence of A and B, that the values of the longitude of Periastron ( $\omega$ ) did not show a random distribution, but rather were concentrated in the first quadrant. This peculiar distribution of the curves, known as the Barr effect in spectroscopic binaries, already suggested as Barr himself pointed out, that the "observed radial velocities" were contaminated by some extraneous effect that, at that time, was difficult to access.	(1), p. 2, paragraph 6
1908 & 1911	Dugan & Stebbins independently discovered the reflection effect.	(1), p. 2, paragraph 5

## APPENDIX B

### Algol Timeline continued

1908 (June)	Hale, while studying absorption lines of the sun's surface, discovered that sunspots were caused by magnetic distortion. These distortions were 4,000 times greater than the earth's magnetic field.	(3)
1910	"Primitive use of photoelectric effects."	(1), p. 2, paragraph 4
1910	Stebbins detected Algol's shallow secondary minimum and variations of light between eclipses, using a selenium conductive cell.	(1), p. 131
1912	Hans Geitel & Julius Elster in Germany, and Jakob Kunz in Illinois marked the first use of photoelectric photometry, using a potassium hydride cell.	(8)
1912	Norris Russel published a general solution of light curves. (The scatter in the data due to the lower precision at that time covered up the transient changes in observed brightness of components now known to interact.) "Instrumental difficulties were such that unusual variations were rarely attributed to the star itself." Astronomers were biased toward periodic unchanging light curves.	(1), pp. 2-3, Quote reference is: (1), p. 5, paragraph 3
1918	Maggini obtained the first two-color light curves for Algol at 6450 Å and 4120 Å using a wedge photometer and filters.	(1), p. 131
1921	Stebbins obtained the first complete photoelectric light curve for Algol, and he found fluctuations of the period of Algol using light minima from 1852 through 1887.	(1), p. 131
1922	Shapley noted a difference in the appearance of the ionized calcium lines on the leading and following sides of the brighter component of $\beta$ Aurigae.	(1), p. 6, paragraph 2
1922	The first suggestion of a third body in the Algol system by Stebbins studying period variations.	(1), p. 131
1922	Hellerich presented spectroscopic elements of Algol.	(1), p. 131
1924	McLaughlin computed absolute dimensions of Algol.	(1), p. 131
1924	Rossiter discovered the rotation effect.	Rossiter (1924)
1924	Dugan, after comparing his observations with earlier work regarding the strange increase in brightness after primary of R Canis Majoris concluded that it was a real but transient feature of the light curve.	(1), p. 5, last paragraph

## APPENDIX B

### Algol Timeline continued

1931	Struve & Elvey were first to observe the doubling of Mg II 4481 (confirmed in 1935 by Morgan).	Article
1935	Morgan confirmed double lines of Mg II, 4481 Å found near center of primary of Algol.	(1), p. 134 Morgan (1935)
1937	Dugan and Wright presented the first general study of periodic changes in eclipsing systems and found relatively sudden period changes with no periodic pattern unaccountable for by rotation of the aps or third body effects. (no explanation offered)	(1), p. 6, paragraph 5
1937	McLaughlin suggested that earlier periods of motion for Algol C found spectroscopically must be ruled out due to systematic errors in reductions.	(13), p. 598 paragraph 2
1939	Hall's precise times of minimum in two colors was probably the first strong evidence against the Tikhoff-Nordmann effect, which is "the alleged phenomenon whereby the time of minimum light is a function of the wavelength."	(1), p. 130, (14) p. 460
1940s	Algol Paradox noted by astronomers. Term used to describe a discrepancy in our theories of stellar evolution.	(6), p. 25, paragraph 2
1940s (late)	Rockets discovered fringes of space scorched by radiation from x-rays, gamma rays, and ultraviolet light which had to be coming from the sun. The rays didn't penetrate the earth's atmosphere.	(3)
1941	Struve postulated a gas stream in $\beta$ Lyrae. This may be the first time that a gas stream was suggested in a close binary system.)	(1), p. 7 paragraph 5
1941	Struve postulated the existence of gaseous streams between the components of $\beta$ Lyrae and of an ultra expanding general gaseous envelope.	(1), p. 7, paragraph 5
1942	Discovery by A. H. Joy that the double H emissions of RW Tauri undergo eclipses as well, and therefore must arise from a gaseous ring around the primary component.	(1), p. 7, paragraph 6 (5), p. 1, paragraph 5
1947	Ludwig Biermann calculated that something more than pressure from sunlight pushed the tails of comets ( <i>assumed earlier by Chinese astronomers</i> ). Biermann called it "solar corpuscular radiation" (solar wind). His idea was immediately rejected.	(3)



## APPENDIX B

### Algol Timeline continued

1948	Eggen found photometrically that the value of the period of Motion of Algol C was satisfied by a period 1.873 years, the value determined by McLaughlin in 1937, spectroscopically.	(13)
1948	Eggen suggested the Algol system has four components, the fourth component with an orbital period 188.4 years.	Eggen (1948), p. 1, abstract
1948	Sidney Chapman, a physicist, scorned Biermann's solar wind theory and felt that the corona of the sun extended far beyond where it appeared during a solar eclipse, yet still thought the corona was firmly bound to the sun.	(3)
1950	Wood was the first to try to explain period changes in a number of eclipsing systems probably indicative of mass loss.	(1) p. 8, paragraph 7 (5), p. 1, paragraph 6
1950s (late)	Eugene Parker worked on resolving the Biermann/Chapman contradiction in their two theories and found them both to be right. He took it further and found that the only answer would be a supersonic solar wind. He calculated that the sun's corona did have enough thermal energy to escape the sun's gravity stream out into space at 500 km/sec. He published his findings in 1958. (They were thought to be absurd.)	(3)
1954	Walker and Herbig suggested the existence of a "hot spot" in the nebular ring around the hot component in UX Ursae Majoris.	(5), p. 1 (Intro.), paragraph 7
1955	J. A. Crawford and Z. Kopal, independently suggested an explanation of the Algol paradox in terms of post-main sequence evolution.	(1), p. 8, paragraph 2 (5), p. 1, paragraph 6
1957	Struve and Sahade interpreted emission features near phase .75 as gas streaming.	(1), p. 134
1959	Kopal defines a "close binary system" as those whose separation is comparable to dimensions of the components lending well to their discovery by spectroscopy.	(2), p. 3
1960	Herczeg with a photometric solution suggested systematic changes in the depths of primary eclipse of Algol.	(1), p. 133

## APPENDIX B

### Algol Timeline continued

1962	R. Giacconi and his collaborators discovered the first x-ray sources outside our solar system. This discovery began the field now known as X-ray astronomy – The first point x-ray source discovered was an x-ray binary, known as Sco X-1.	(1), p. 13, paragraph 2, (9)
1962	Mariner II's probe to Venus found that space was awash with solar wind, exceeding Eugene Parkers expectations (1958). The probe detected winds of 300-800 kms/sec. These electrically charged hurricanes are ferocious and relentless. The violent gusts break free at times from the sun's gravitational and magnetic forces. These were the flares and coronal mass ejections first witnessed by Skylab in 1970s.	(3)
1964	Fletcher deduced presence of circumstellar helium around Algol A, which was not distributed symmetrically around the line of centers.	(1), p. 134
1966	Algol is the first eclipsing system to have a light curve observed in the infrared, and the orange spectral regions. Chen and Reuning, 1966	(1), p. 130
1966	Paczynski & Plavec independently coined the term "interacting binaries."	(5), p. 1 (Intro.), paragraph 3
1967	Glushneva & Esipov detected Algol B spectrographically.	(1), p. 131, (16)
1967	Plavec and Paczyński independently were the first to suggest a change in the way close binary is defined by taking the evolutionary history into account.	(1), p. 1, paragraph 2
1967	International colloquium considering evolution of double stars.	(1), p. 12, paragraph 2
1968	Lucy assumes a common convective envelope for W Ursae Majoris systems.	(1), p. 36
1970	Frieboes-Conde, Herczeg & Hog determined that only three components are needed to explain the phenomena of Algol	(1), p. 130 (17), p. 1
1970	Frieboes-Conde et al. confirmed Algol to be three components only.	(1), p. 132 (17), p. 1

## APPENDIX B

### Algol Timeline continued

1971	<p>Concept of hot spot</p> <ul style="list-style-type: none"> <li>▪ Warner and Nather</li> <li>▪ Photoelectric (Krzemiński and Smak)</li> </ul> <p>Warner &amp; Nather, and Krzemiński &amp; Smak almost simultaneously developed the concept of “hot spots.” Warner &amp; Nather believed that hot spots were created by ejected matter falling on a disk surrounding the secondary star. Krzemiński &amp; Smak suggested that the hot spots on the disk surrounding the primary, white dwarf star are the source of the S-wave emission lines.</p>	(1), p. 13 pp. 104 – 105
1971	Hill et al. confirmed the 32-year periodicity of Algol’s $\omega$ to be apsidal.	(1), p. 132
1971	Paczyński proposed specific application of the term “close” to such interacting binary systems.	(19), p. 242
1972	Wade and Hjellming detected Algol as a quiescent radio source.	(1), p. 134
1972	Algol’s radio flare activity observed by Hjellming, Wade, and Webster might be correlated with optical spectrum variations observed by Bolton.	(1), p. 134
1972	Wilson and Devinney introduced their method for determining “accurate close binary light curves” which is an improvement over the Russel Method for “binaries exhibiting even modest proximity effects.”	(1), p. 133, (18)
1973	Skylab, the first solar space laboratory, was launched beyond earth’s atmosphere. This was when the most extensive period of solar observation in history began. Sunspots, networks, filaments, and solar flares were clearly detected.	(3)
1973	Skylab astronauts discovered coronal mass ejections, huge outbursts of material on a scale much greater than solar flares.	(3)
1973	Rule & Elsmore used speckle interferometry and accurately located to barycentre of Algol	(19), p. 244
1974	Labegrie et al. observed Algol C as an astrometric binary, believing they resolved it by speckle interferometry.	(1), p. 131

## APPENDIX B

### Algol Timeline continued

1975	Eaton published far ultraviolet (UV) observations of Algol from the orbiting astronomical observatory (OAO-2) taken August 1969 and July 1972. The wavelengths are 2930 Å, 1920 Å, and 1550 Å.	(1), p. 135, paragraph 2
1975	The SAS-3 satellite detected x-ray emission from Algol. Schnopper et al., 1976. The intensity equaled $1.6 \times 10^{31}$ ergs/s	(1), p. 82, p. 130 (5) p. 80, paragraph 4.3
1975	Soft x-rays were detected from Algol in the range .15-2 KeV to 2 KeV by Harnden et al., indicating a mass loss rate approximately equal to $10^{-10} M_{\odot}$ /year.	Harnden (1977) p. 422
1975	Longmore & Jameson found that IR excess was attributed to gas stream.	(19), p. 244
1975	Bachmann & Hershey, with inclusion of accurate astrometry, had more confident element specification.	(19), p. 244
1975	Gibson et al., through radio observations (1400, 2695, 6000, and 8085 MHz), detected a large flare from Algol.	(19), p. 244
1975 & 1976	Chen and Wood obtained UV observations of Algol taken on September 7th, 8th, and 9th, 1973, and January 4, 1974, from the Copernicus satellite. They observed that the Mg II resonance lines near 2800Å appeared to be doubled.	(1), p. 135
1976	Algol itself was first detected as an x-ray source by Schnopper et al. (1976).	(1), p. 130 (5), p. 80, paragraph 4.3
1976	Guinan et al. estimates the extent of circumstellar material in Algol for H <sub>A</sub> and H <sub>B</sub> light curves to be approximately 2.6 R <sub>A</sub> ( <i>I have to check that number because there was an incorrect unit of measure in there.</i> )	(1), p. 134
1977	Kondo et al. used UV observations of Algol taken on October 9 <sup>th</sup> through 10 <sup>th</sup> , 1974, from a balloon-borne spectrometer. The Mg II lines gave evidence of mass flow.	(1), pp. 135-136
1978	Tomkin & Lambert used Reticon spectroscopy and detected Na II lines of Algol's secondary.	(19), p. 244
1979	Bonneau, using speckle interferometry, revised absolute elements of the triple system of Algol.	(19), p. 244

## APPENDIX B

### Algol Timeline continued

1979	White et al. through x-ray spectrometry found no eclipses. An active corona of Algol's subgiant was inferred.	(19), p. 244
1979	Cugier, using UV spectrometry, found high resolution Mg II line profiles which allowed detailed modeling.	(19), p. 244
1981	Chen et al., using UV spectrometry, found high resolution Mg II line profiles, like Cugier in 1979, allowing detailed modeling.	(19), p. 244
1983	Kemp et al. (1983) pointed out the Chandrasekhar Effect from their intensive polarization studies of $\beta$ Per	(19), p. 242
1988	Lestrade et al. observed $\beta$ per at 2.3 and 8.4 GHz with the Very Large Array. The brightness temperature of the radio source varies from $3 - 50 \times 10^8$ K and is indicative of gyrosynchrotron emission of mildly relativistic electrons in an active coronal region with magnetic fields of about 30 Gauss at unit optical depth. The size of the source is estimated to be about three cool radii. Two outbursts occurred. One was a high brightness ( $\approx 1.5 \times 10^{10}$ K), broadband burst, and the other was a short ( $\approx 15$ minutes) outburst at 1.66 GHz with a brightness temperature of about $3 \times 10^{10}$ K and a magnetic field of approximately 300 Gauss. Both of these are very likely associated with coronal loops.	(1), p. 130 (5), p. 45, paragraph 1
1999	Kempner & Richards (1999) were the first to calculate UV difference profiles for an Algol-type system (U Sge).	(10)

**References:** (1) Sahade and Wood (1978); (2) Kopal (1959); (3) "The Planets" (DVD); (4) Hilditch (2001); (5) Sahade/McCluskey/Kondo (1993); (6) Pringle & Wade (1985); (7) "The Binary Stars" Robert Grant Aitken, McGraw-Hill, N. Y. (1935); (8) <http://www.phys-astro.sonoma.edu/people/faculty/tenn/asphistory/1994.html>. The Astronomical Society of the Pacific "106<sup>th</sup> Annual Meeting" History Sessions: presented by ASP History Committee History II: Historic & Prehistoric Astronomy Tuesday, 28 June 1994, North ArizUniv. Flagstaff, AZ, Invited lecture 1:30p Photoelectric photometry: The First Fifty Years – John B. Hearnshaw, University of Canterbury; (9) [online document <http://lheawww.gsfc.nasa.gov/users/white/xrb.html>] Cited: 3/13/06, High energy Astrophysics Learning Center: x-ray binaries; (10) Kempner & Richards (1999); (11) Struve and Sahade (1957b); (12) I. Barney (1923);

(13) Ebbighausen (1958); (14) Hall (1939); (15) Eggen (1948); (16) Frieboes-Conde et al. (1970); (17) Hill et al. (1971); (18) Wilson & Devinney, 1971, ApJ. 166:605-619; (19) Budding (1985)

# APPENDIX C

## IONIZATION FRACTIONS

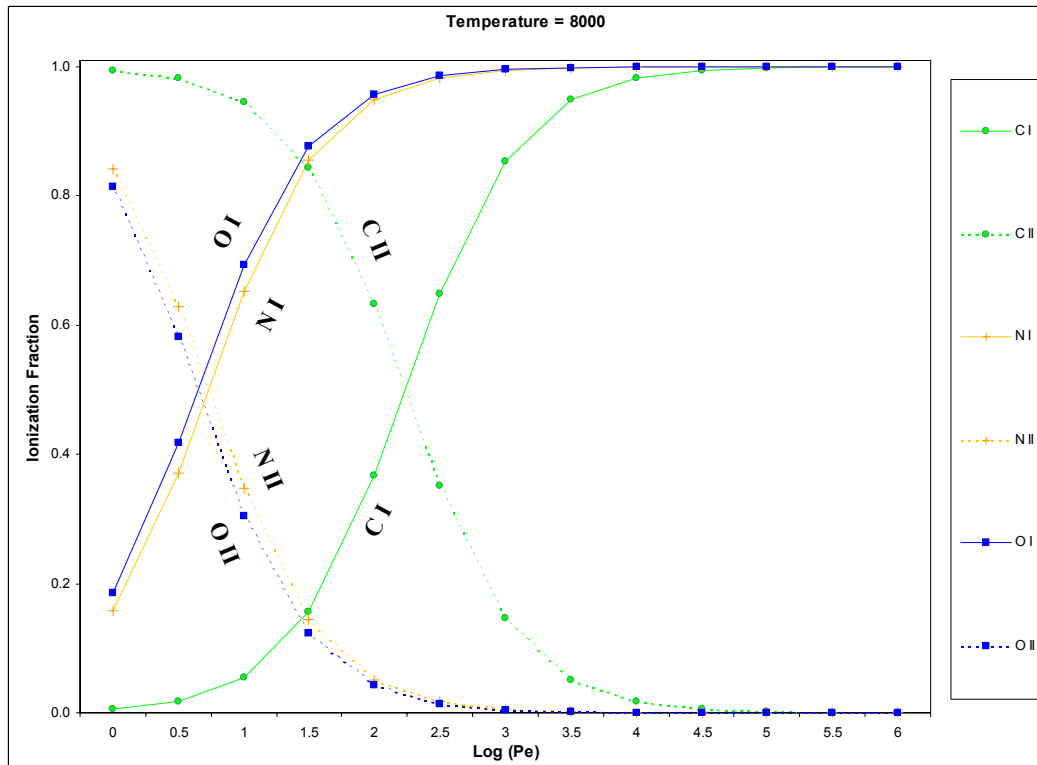


FIG. C.1 - Ionization Fraction of Carbon, Nitrogen, and Oxygen at 8,000 K

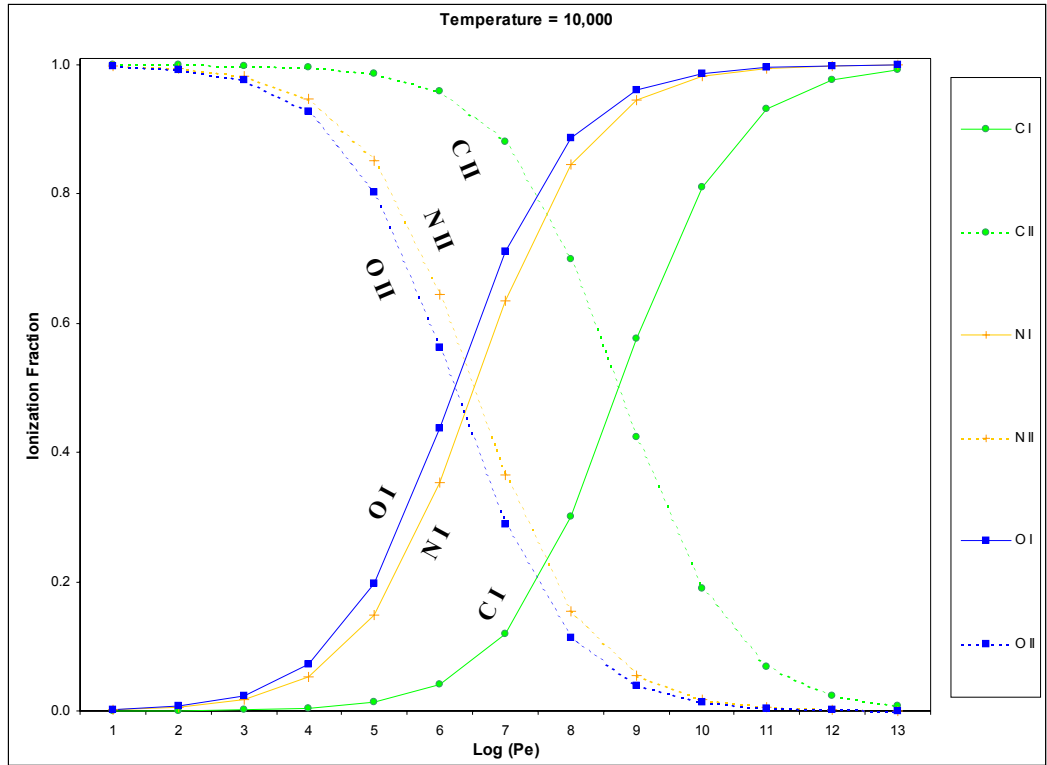


FIG. C.2 - Ionization Fraction of Carbon, Nitrogen, and Oxygen at 10,000 K

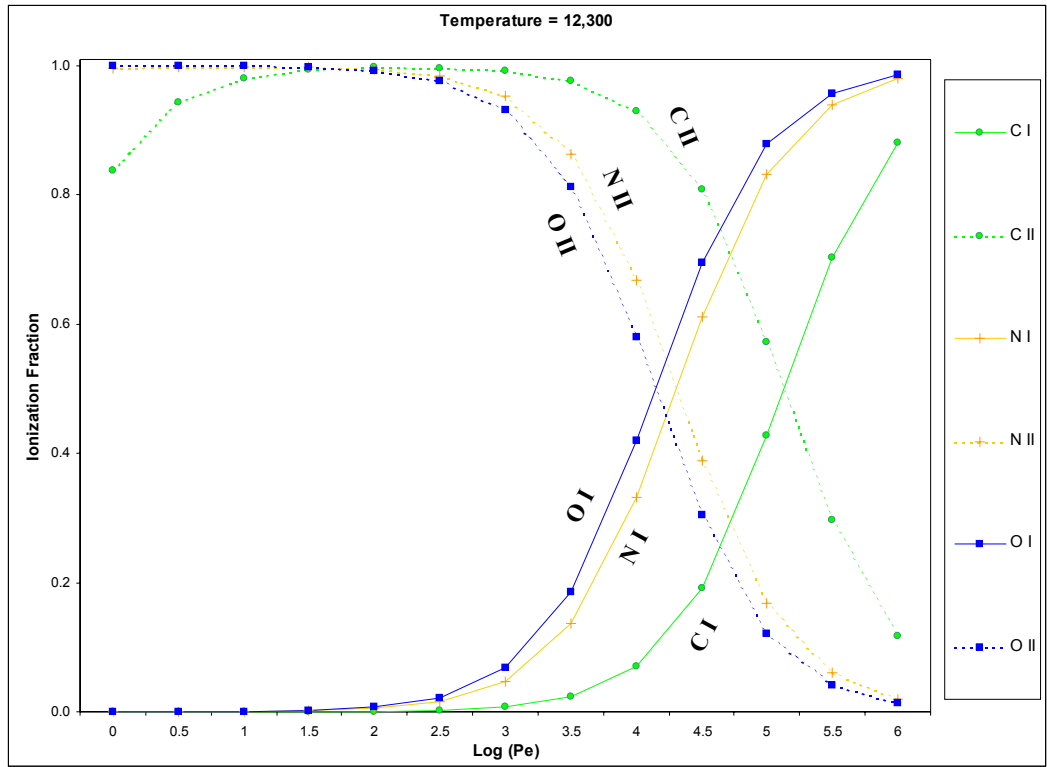


FIG. C.3 - Ionization Fraction of Carbon, Nitrogen, and Oxygen at 12,300 K



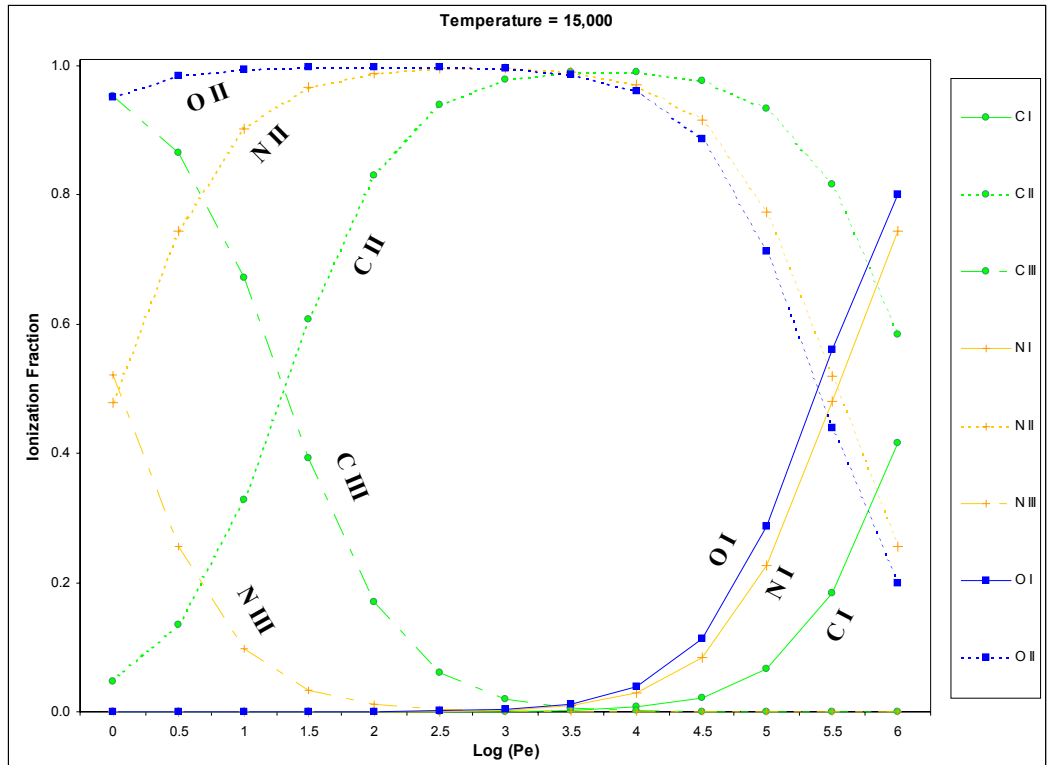


FIG. C.4 - Ionization Fraction of Carbon, Nitrogen, and Oxygen at 15,000 K

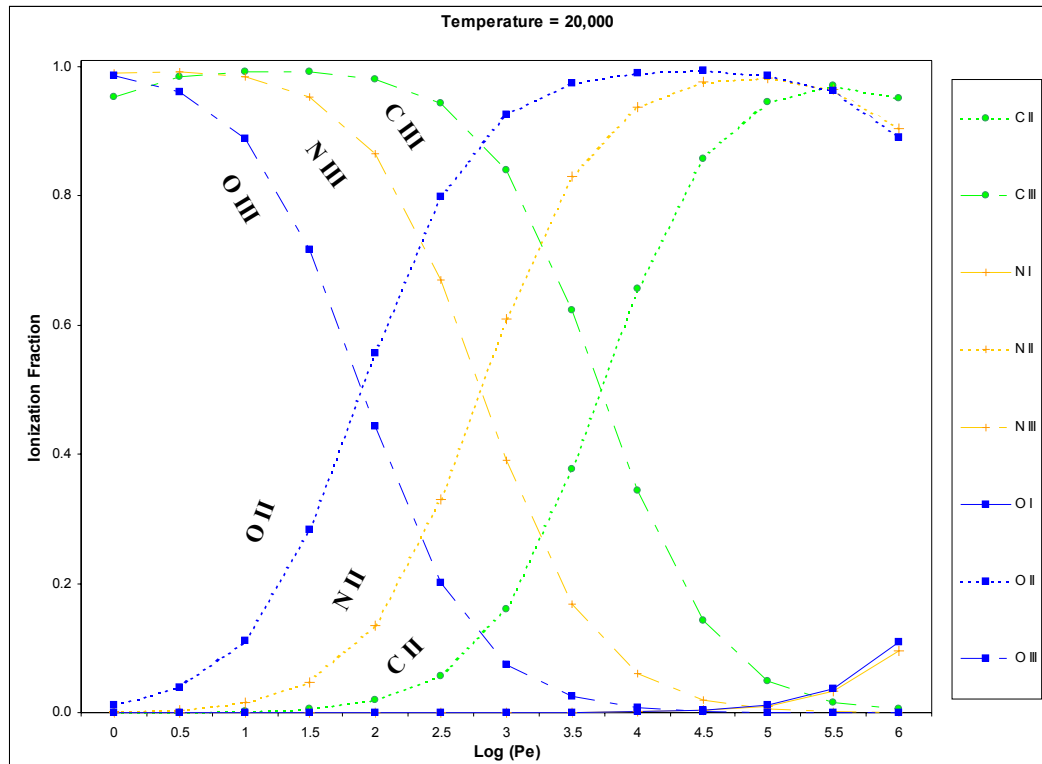


FIG. C.5 - Ionization Fraction of Carbon, Nitrogen, and Oxygen at 20,000 K

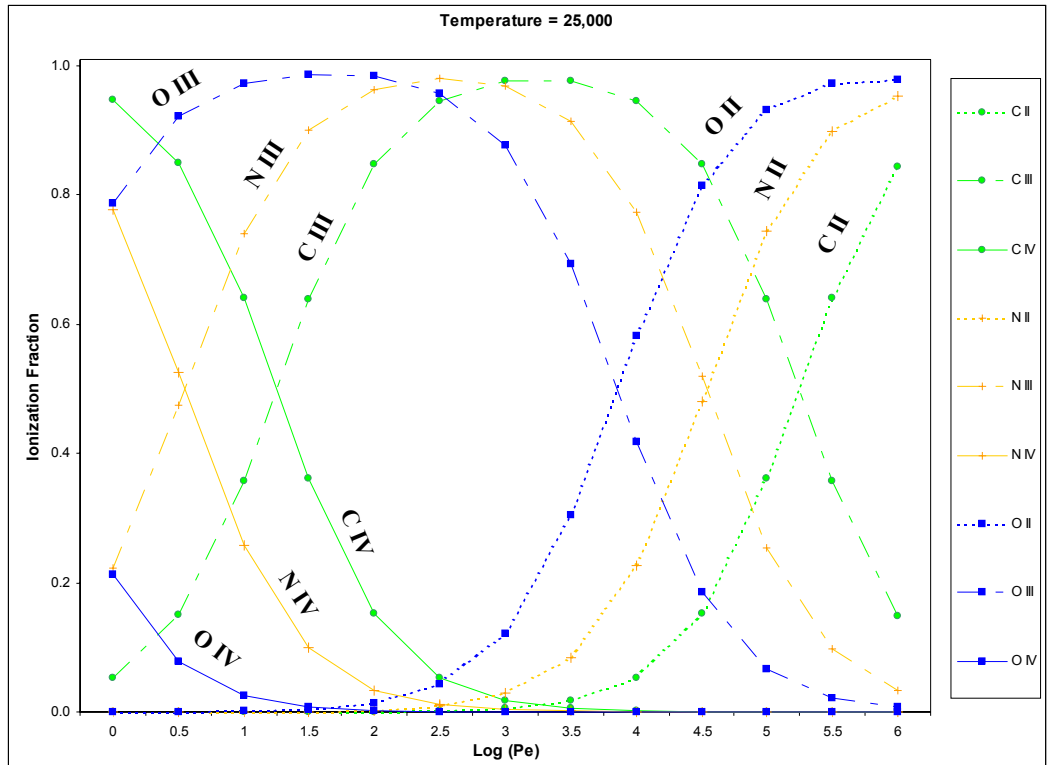


FIG. C.5- Ionization Fraction of Carbon, Nitrogen, and Oxygen at 25,000 K

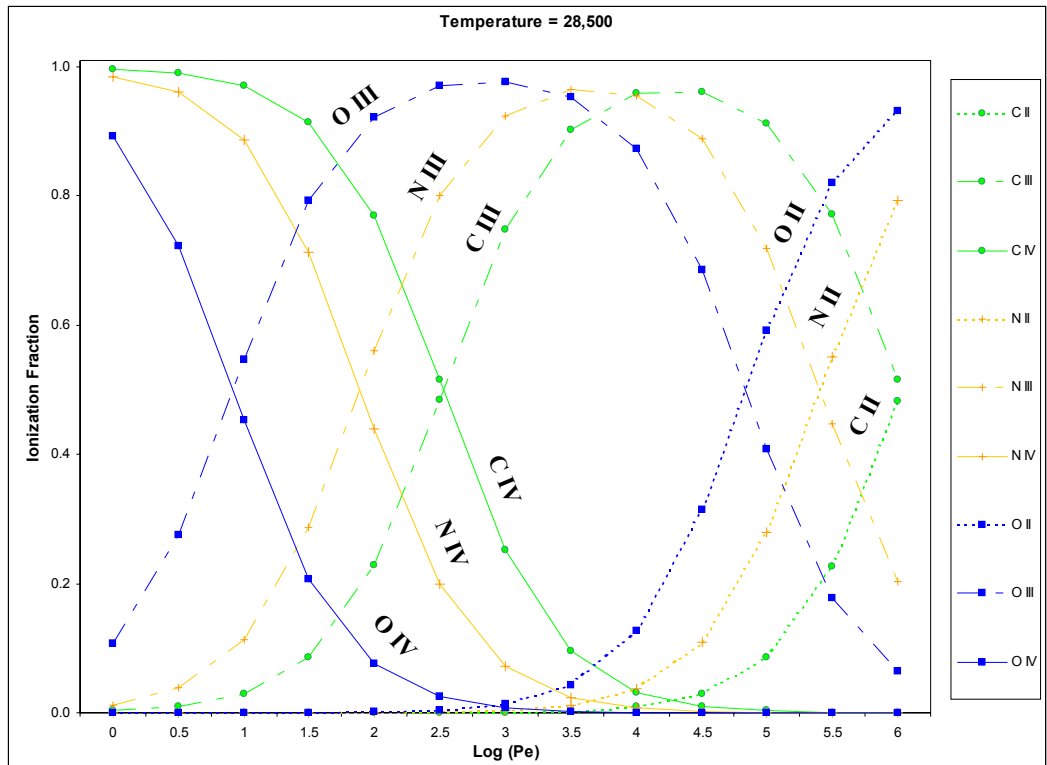


FIG. C.6 - Ionization Fraction of Carbon, Nitrogen, and Oxygen at 28,500 K

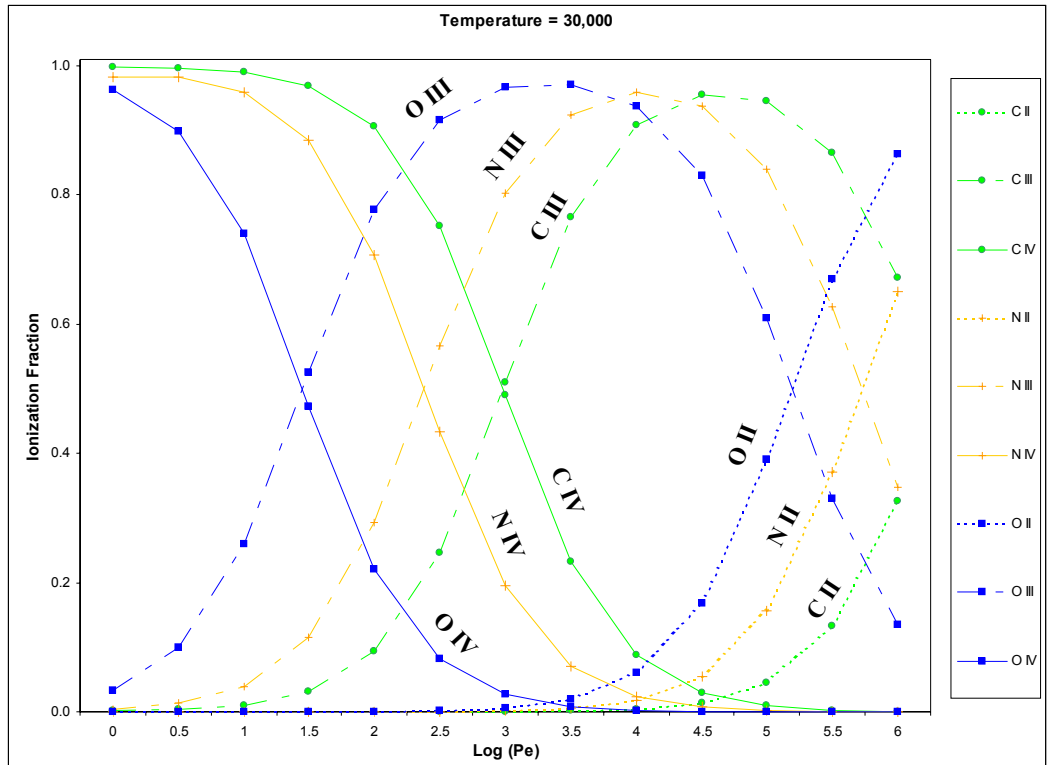


FIG. C.7 - Ionization Fraction of Carbon, Nitrogen, and Oxygen at 30,000 K

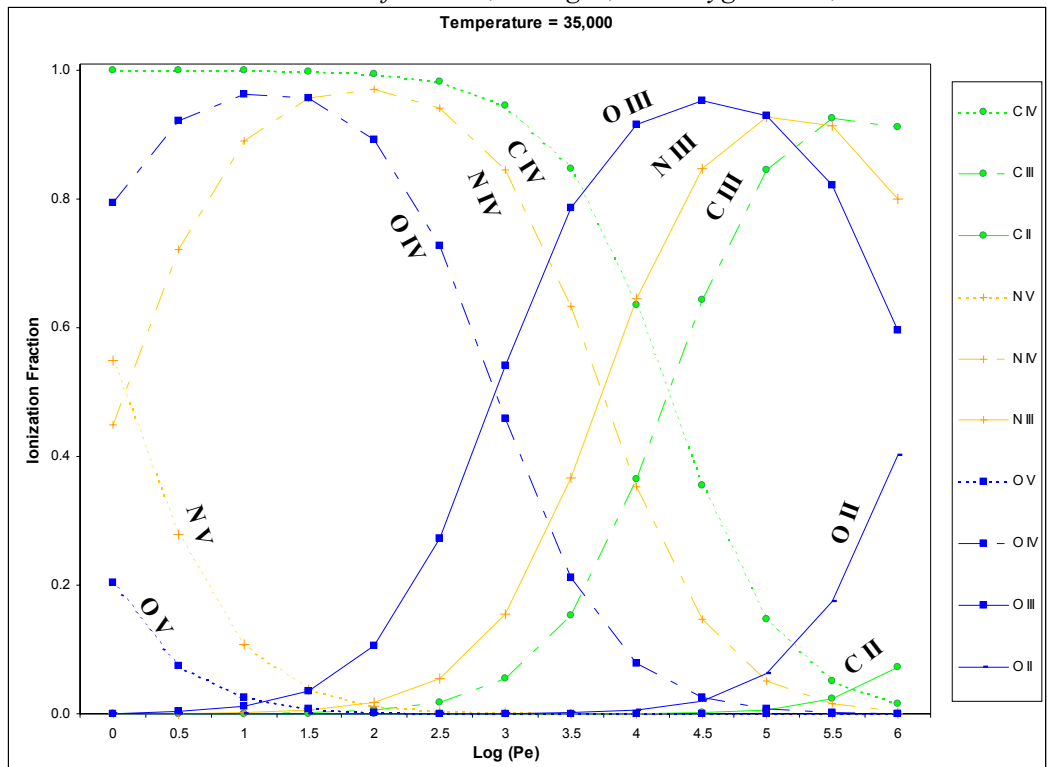


FIG. C.8 - Ionization Fraction of Carbon, Nitrogen, and Oxygen at 35,000 K

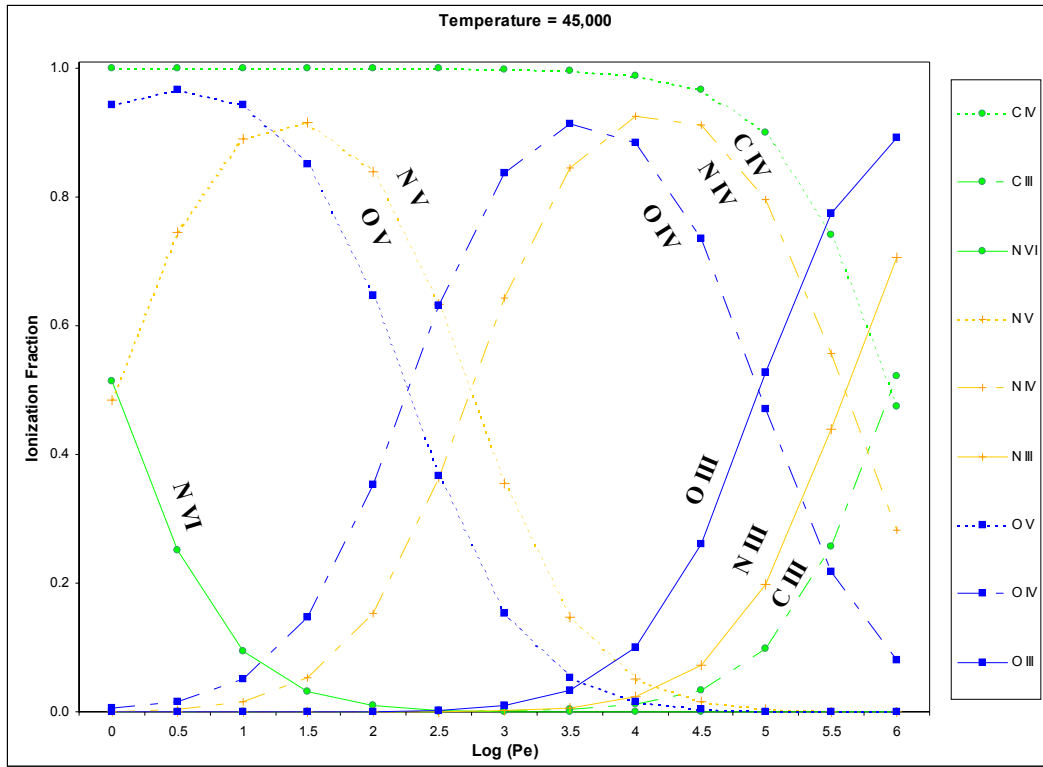


FIG. C.9 - Ionization Fraction of Carbon, Nitrogen, and Oxygen at 45,000 K

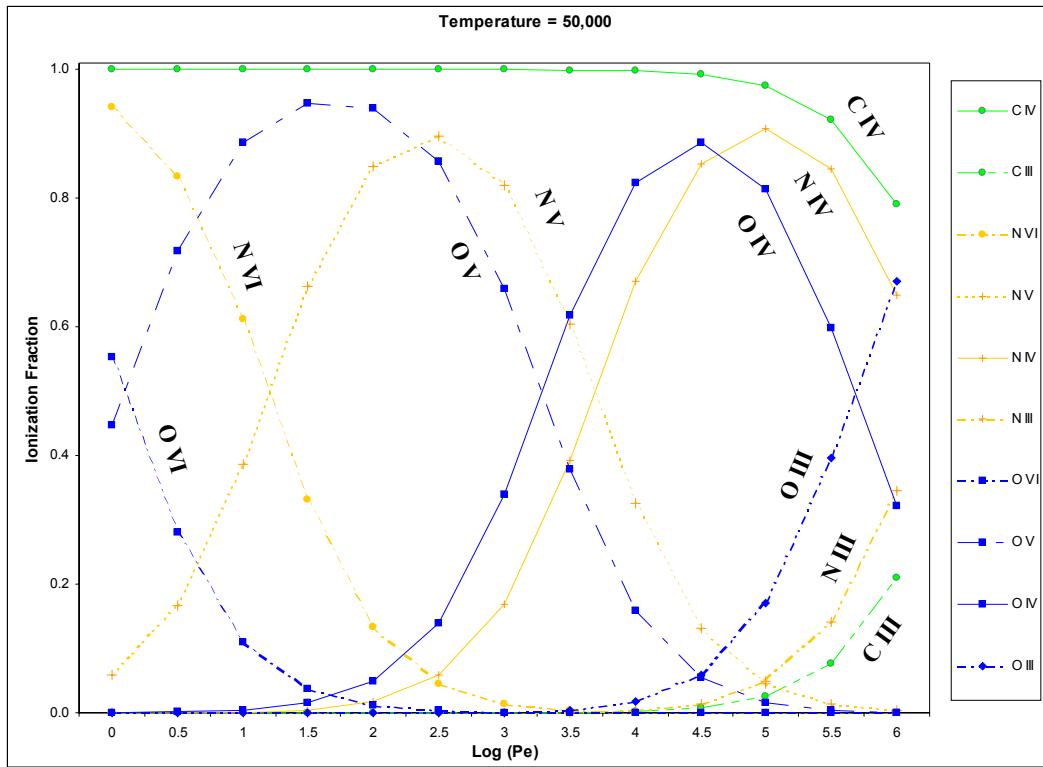


FIG. C.10 - Ionization Fraction of Carbon, Nitrogen, and Oxygen at 50,000 K

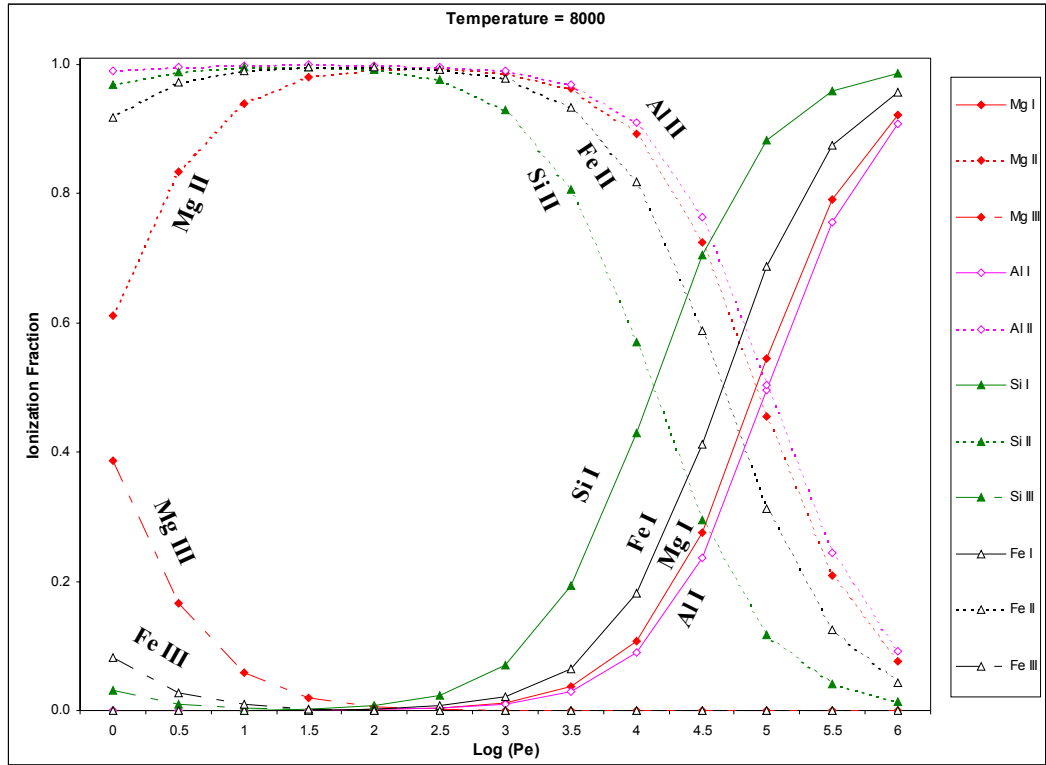


FIG. C.11 - Ionization Fraction of Mg, Al, Si, and Fe at 8,000 K

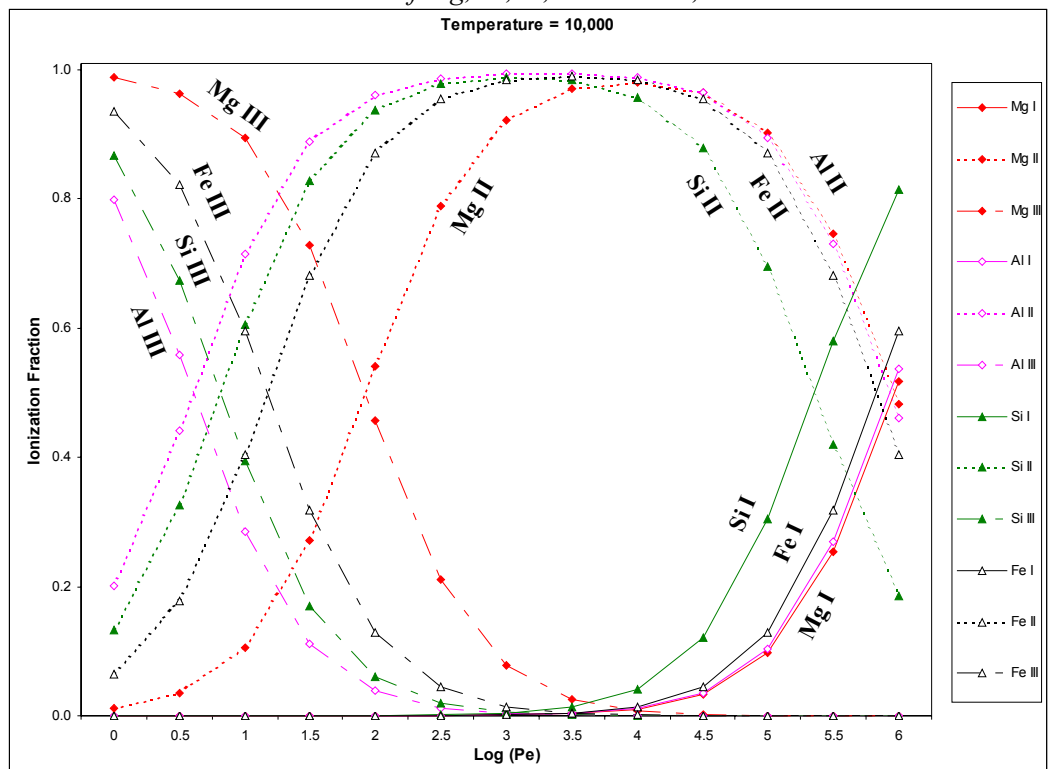


FIG. C.12 - Ionization Fraction of Mg, Al, Si, and Fe at 10,000 K

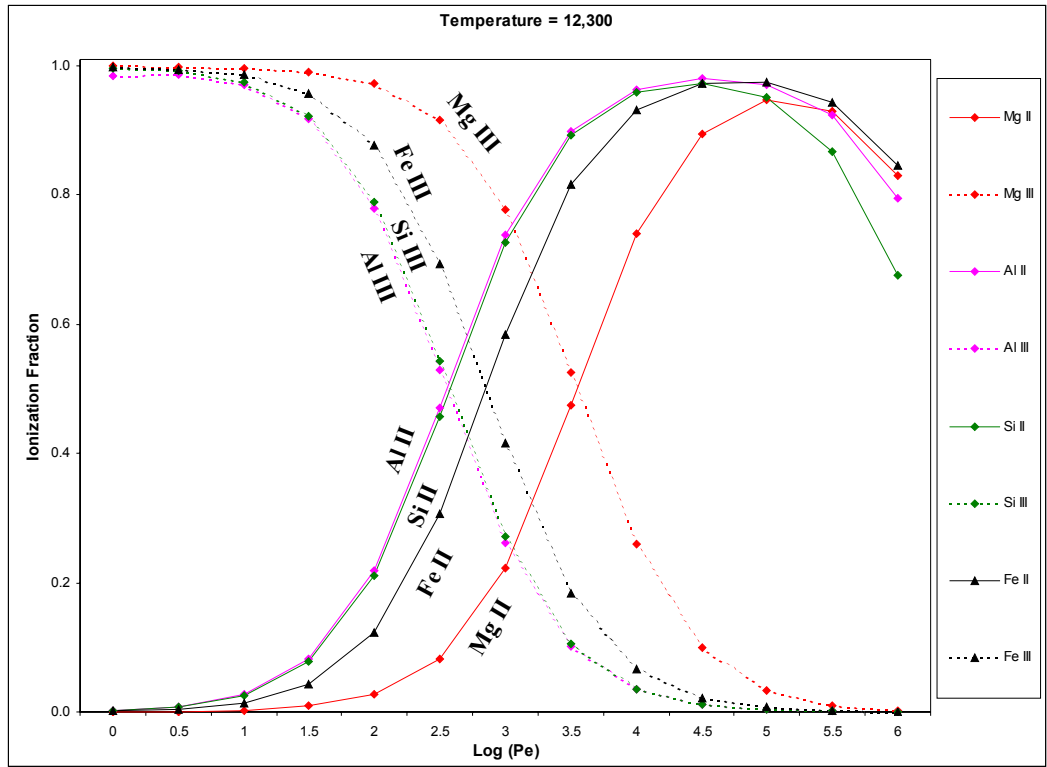


FIG. C.13 - Ionization Fraction of Mg, Al, Si, and Fe at 12,300 K

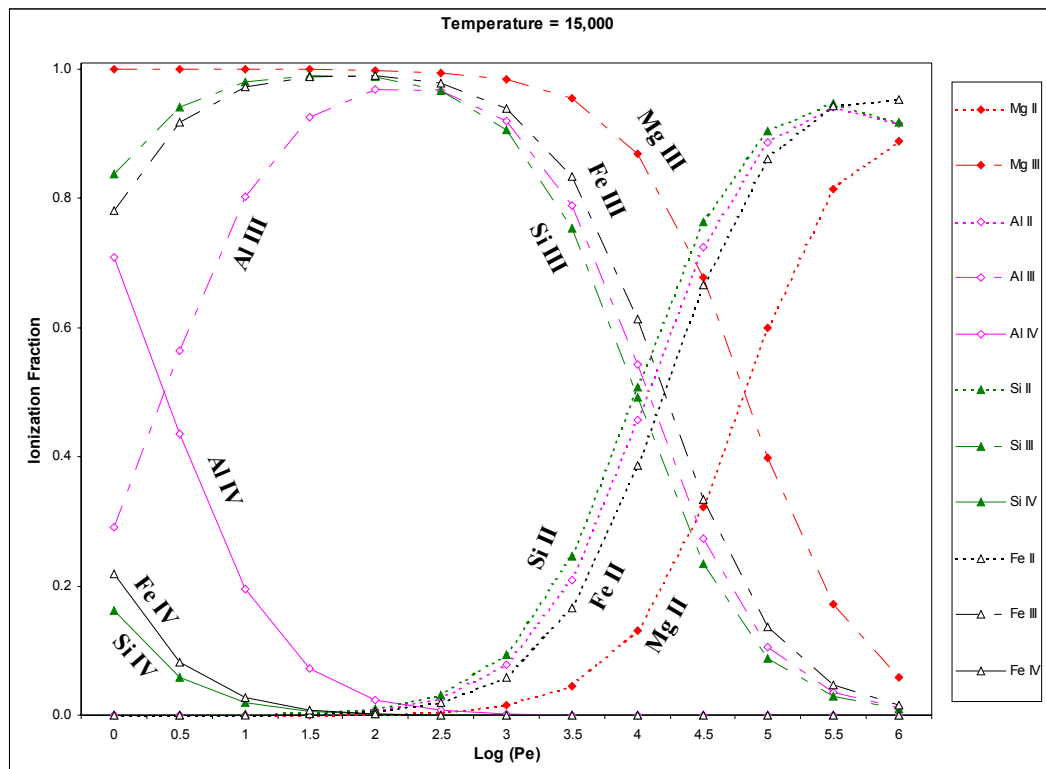


FIG. C.14 - Ionization Fraction of Mg, Al, Si, and Fe at 15,000 K

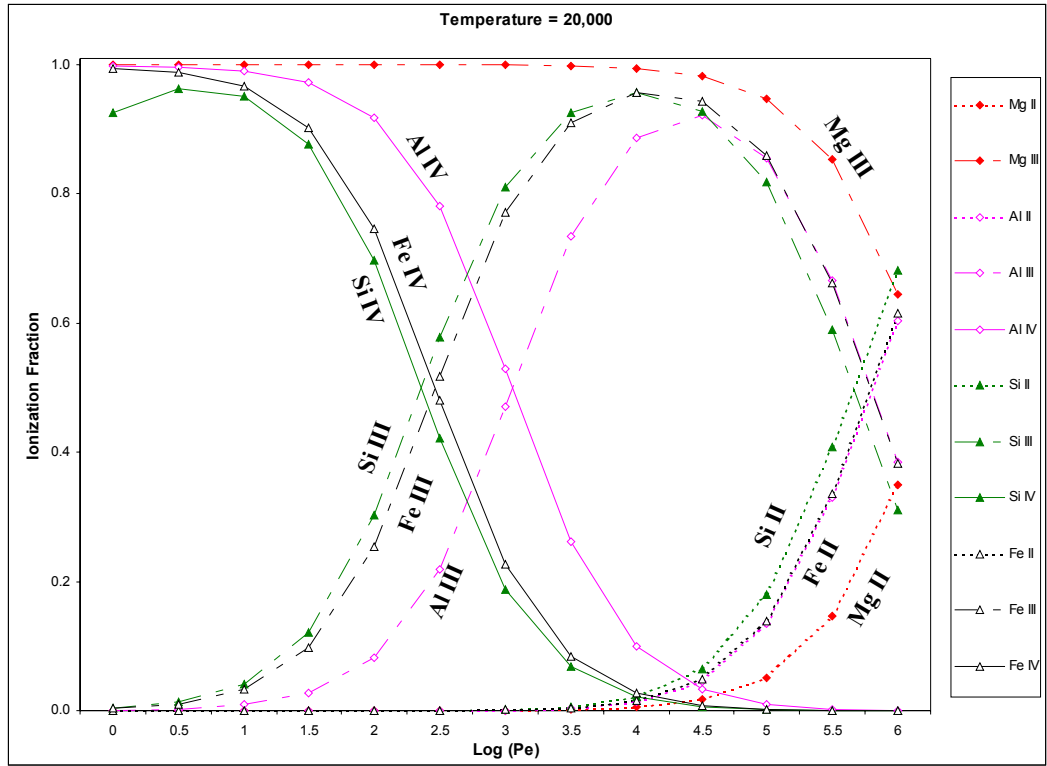


FIG. C.15 - Ionization Fraction of Mg, Al, Si, and Fe at 20,000 K

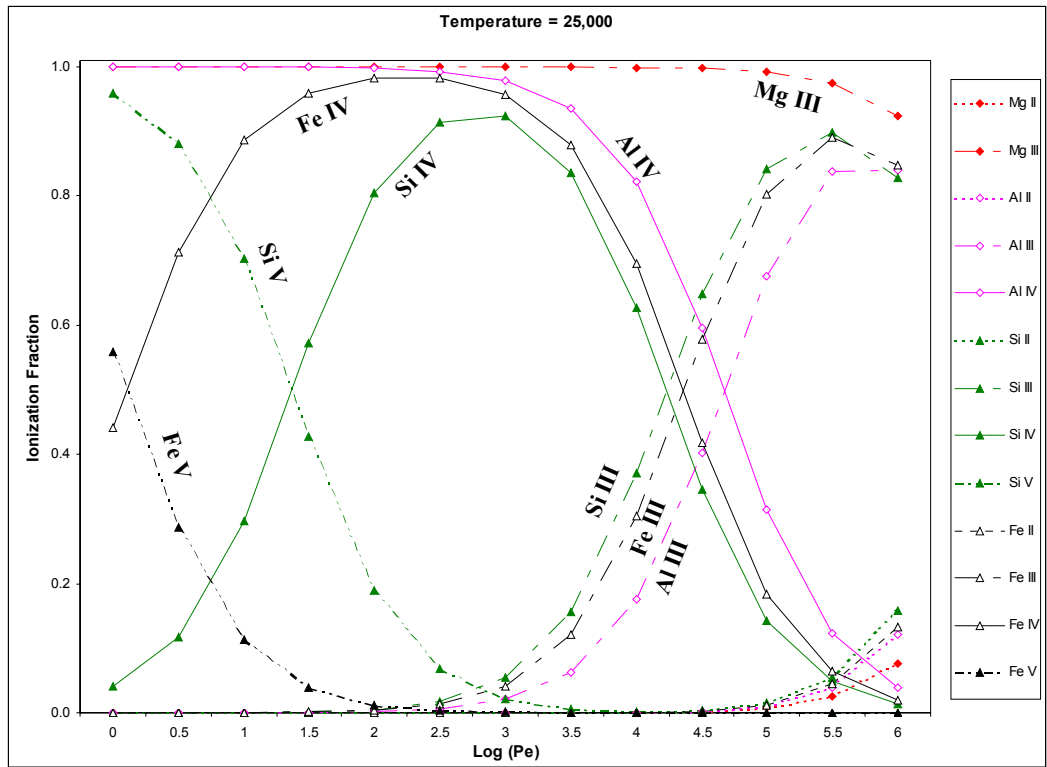


FIG. C.16 - Ionization Fraction of Mg, Al, Si, and Fe at 25,000 K

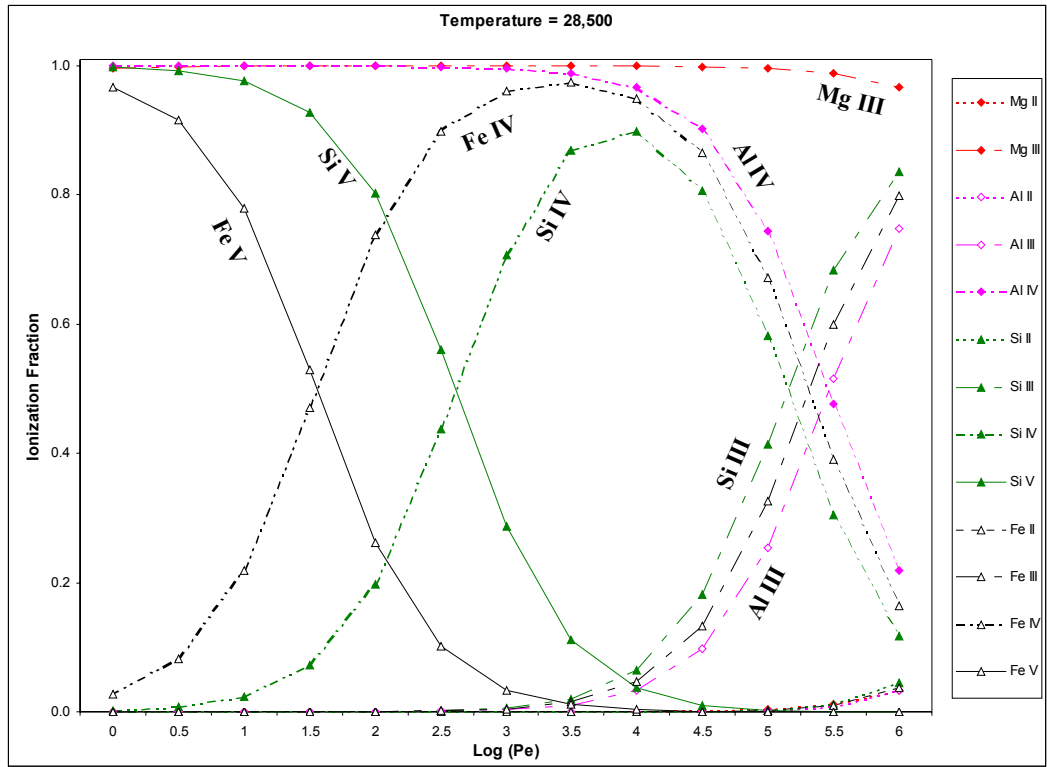


FIG. C.17 - Ionization Fraction of Mg, Al, Si, and Fe at 28,500 K

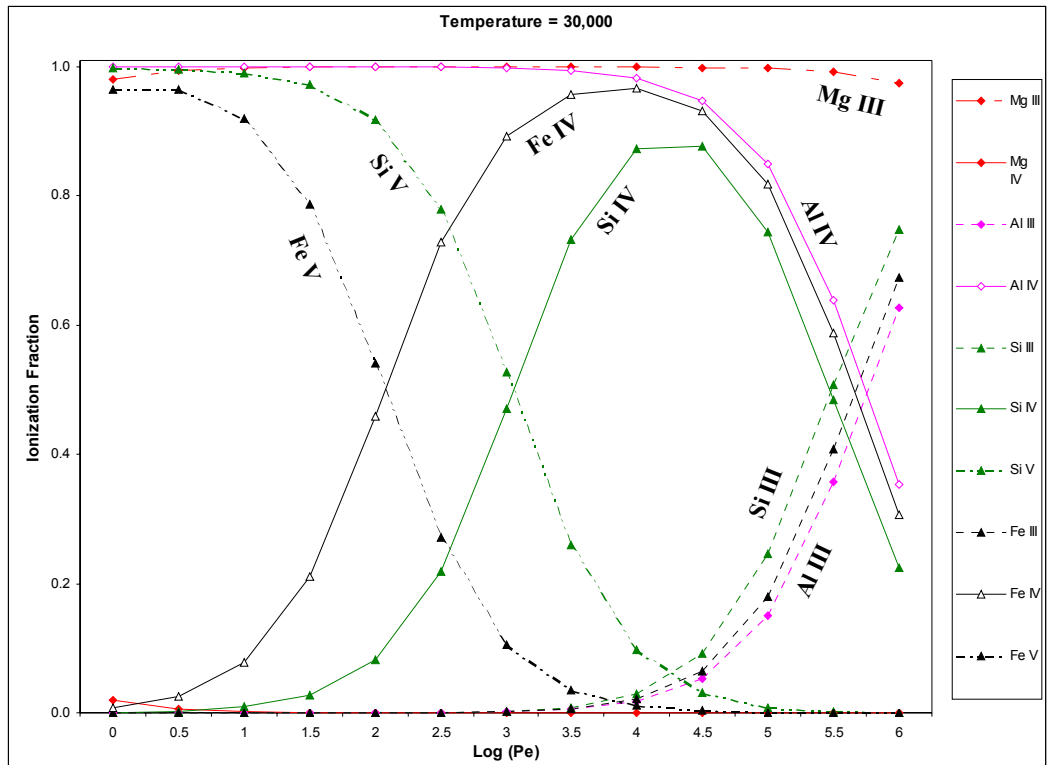


FIG. C.18 - Ionization Fraction of Mg, Al, Si, and Fe at 30,000 K



# APPENDIX D.1

## Continuum Flux

TABLE D.1.1.  
Large Aperture SWP Continuum Flux Measurements ( $\times 10E-10$ ) (ergs/cm<sup>2</sup>/s/Å)

SWP Graph ID	Aper Phase	1194 Å	1243 Å	1263 Å	1308 Å	1350- 1400 Å	1400- 1450 Å	1450- 1500 Å	1500- 1550 Å	1550- 1600 Å	1600- 1650 Å	1650- 1700 Å	1700- 1750 Å	1750- 1800 Å	1800- 1850 Å	1850- 1900 Å	1900- 1950 Å	1950- 2000 Å	
3	L	0.0052	1.95	4.90	7.50	8.65	8.49	8.60	7.90	7.50	7.01	6.60	6.40	6.29	5.99	6.15	6.13	6.00	5.60
5	L	0.0141	3.50	6.85	8.92	10.27	10.20	10.10	10.00	9.80	9.00	9.00	8.40	8.00	7.40	7.50	7.10	7.30	6.80
7	L	0.0204	3.53	8.18	11.50	13.10	12.90	13.00	12.10	11.00	10.30	9.60	9.48	9.00	8.50	8.70	8.60	8.49	8.00
8	L	0.0378	4.80	12.90	19.10	22.17	20.79	22.00	19.60	19.50	17.40	16.40	15.90	15.50	14.00	14.70	14.40	14.20	13.00
10	L	0.0855	12.00	23.40	31.20	33.60	31.90	33.30	31.40	30.80	28.00	27.50	26.40	24.60	23.00	23.40	22.70	22.30	20.30
11	L	0.1317	13.00	23.90	30.70	34.97	31.90	34.30	32.20	31.20	28.30	27.80	26.50	24.50	23.40	23.80	22.60	22.20	20.50
12	L	0.1538	13.00	21.60	29.90	34.54	31.90	32.90	31.90	30.80	27.80	26.90	26.30	24.00	22.40	22.10	22.30	22.30	20.00
13	L	0.1625	10.60	20.60	27.80	31.50	31.80	32.00	30.80	30.70	27.90	26.50	26.50	23.60	21.90	21.80	21.80	21.80	18.80
14	L	0.1889	9.29	22.80	31.20	34.80	34.00	35.00	31.90	30.90	27.80	26.00	25.60	23.30	23.00	23.30	22.60	22.10	19.90
15	L	0.3209	13.00	24.00	30.80	34.22	32.20	33.80	32.00	30.60	28.90	28.00	27.20	24.50	23.40	23.90	22.80	22.70	20.60
17	L	0.4790	9.00	22.70	31.90	34.90	32.80	33.90	32.10	30.40	27.49	26.00	24.90	23.00	22.50	22.20	22.80	22.30	19.70
19	L	0.5454	9.70	23.00	30.70	34.90	33.80	33.90	32.00	29.80	26.90	25.70	24.90	24.00	22.50	22.80	22.60	22.40	20.30
20	L	0.6326	12.00	23.00	33.30	33.00	34.10	34.90	32.30	30.40	27.00	25.50	25.20	23.60	22.40	22.50	22.70	22.00	20.00
22	L	0.6452	14.00	23.80	32.70	34.67	34.10	35.80	32.80	31.50	27.20	26.80	25.00	23.40	22.30	22.80	22.30	22.30	20.30
23	L	0.6522	15.00	23.70	31.20	34.81	32.60	32.90	31.80	31.40	28.30	27.90	26.30	24.50	23.60	23.30	22.80	22.70	21.20
24	L	0.6595	12.90	22.70	31.60	34.36	34.50	34.90	32.90	31.70	27.80	26.50	25.20	24.20	22.60	22.60	22.10	22.40	20.90
25	L	0.6704	12.00	22.00	31.90	34.97	34.80	34.90	33.00	32.00	27.70	26.80	25.50	23.80	23.40	23.00	22.60	22.40	20.90
26	L	0.6772	10.70	21.00	32.40	34.77	34.10	34.90	32.90	32.20	27.70	26.50	25.00	23.90	23.00	22.60	22.90	22.30	20.50
28	L	0.7784	10.10	23.00	33.00	34.90	33.40	34.20	31.90	32.20	26.80	25.90	24.50	23.00	22.80	22.80	22.10	22.50	20.00
29	L	0.7869	13.80	24.00	32.40	33.90	33.00	33.40	32.30	31.40	28.90	27.30	26.90	24.00	23.60	23.60	22.80	22.40	20.80

TABLE  
D.1.1 -continued

SWP Graph ID	Aper	Phase	1194 Å	1243 Å	1263 Å	1308 Å	1350- 1400 Å	1400- 1450 Å	1450- 1500 Å	1500- 1550 Å	1550- 1600 Å	1600- 1650 Å	1650- 1700 Å	1700- 1750 Å	1750- 1800 Å	1800- 1850 Å	1850- 1900 Å	1900- 1950 Å	1950- 2000 Å
30	L	0.8005	13.00	22.80	31.10	32.90	34.40	34.00	32.90	32.00	27.90	26.50	25.10	23.80	22.90	23.50	22.40	22.40	20.10
31	L	0.8075	14.00	24.00	31.90	33.47	33.50	33.70	32.10	31.50	28.70	28.00	26.90	24.70	24.00	24.00	23.00	22.70	21.00
32	L	0.8813	8.20	21.70	31.20	34.90	33.20	34.00	31.90	31.00	26.00	25.40	24.10	22.50	22.90	22.80	22.30	22.60	20.50
33	L	0.8866	13.00	22.70	30.40	33.80	31.70	31.80	30.90	30.90	27.50	27.20	25.00	23.30	22.60	22.00	21.30	21.60	20.20
34	L	0.8904	11.90	19.50	29.00	26.50	28.50	29.50	29.70	29.50	25.60	25.10	23.90	20.60	21.90	21.50	21.30	20.50	19.60
35	L	0.9009	14.00	21.90	30.00	34.20	31.00	32.00	31.00	30.90	27.90	27.00	26.50	23.40	22.10	22.40	21.70	21.30	19.80
36	L	0.9070	13.30	21.70	29.90	32.80	30.20	32.10	31.10	29.80	26.50	26.40	24.90	22.50	22.10	21.70	21.80	21.00	20.30
37	L	0.9149	12.90	23.00	30.10	34.10	31.30	33.00	31.90	31.60	28.90	28.00	26.50	23.60	22.80	22.60	21.90	21.90	20.50
38	L	0.9217	11.30	20.90	28.30	31.20	30.30	32.00	31.90	30.90	27.90	27.00	26.00	23.30	22.70	22.30	21.90	21.60	20.40
39	L	0.9218	12.00	21.90	29.90	33.20	31.60	32.30	31.80	30.30	26.90	26.80	25.90	23.40	22.60	22.30	22.20	21.50	20.90
40	L	0.9247	9.50	21.20	28.90	32.20	30.30	32.00	31.90	30.60	27.30	26.90	25.80	23.50	23.00	22.50	22.60	22.00	20.50
41	L	0.9299	12.90	22.60	30.80	33.90	31.30	32.90	32.00	30.70	27.80	27.20	26.10	22.90	22.40	22.00	21.90	22.00	20.40
42	L	0.9358	11.80	21.00	27.90	32.70	31.00	31.50	30.80	29.70	27.10	25.80	25.50	22.80	22.00	22.00	21.90	21.60	19.90
43	L	0.9388	9.63	19.10	28.00	29.10	28.60	30.30	29.80	28.70	25.30	24.50	23.00	21.60	21.20	20.70	20.40	20.50	18.90
44	L	0.9397	11.00	20.90	28.40	31.80	29.60	31.50	30.00	30.00	27.20	26.20	25.60	23.00	21.80	22.10	22.10	21.00	19.60
45	L	0.9471	11.00	20.60	28.20	31.40	28.90	30.30	29.30	29.30	25.70	25.20	24.50	22.10	21.50	20.80	20.40	19.90	19.40
46	L	0.9571	8.48	16.00	21.70	24.60	23.00	24.10	23.30	23.60	20.60	20.90	20.00	18.30	17.30	16.70	16.80	16.50	15.60
47	L	0.9573	9.00	16.70	23.00	26.20	24.30	26.40	24.70	24.70	21.90	21.60	20.30	18.90	18.00	17.60	17.40	17.30	16.20
48	L	0.9636	10.00	15.90	21.90	24.50	23.00	23.90	23.10	22.60	20.30	19.90	19.40	17.40	16.90	16.00	16.20	15.90	14.90
50	L	0.9712	5.40	10.60	14.90	17.00	15.70	16.50	16.30	16.30	14.40	14.30	13.30	12.50	12.00	12.10	12.00	11.70	11.00
51	L	0.9777	4.73	9.22	13.00	15.10	14.00	15.20	14.90	14.50	12.90	12.90	12.40	11.60	10.80	11.00	10.80	10.80	9.80
53	L	0.9791	5.90	10.20	14.20	16.30	15.10	15.70	15.00	15.30	14.00	13.40	12.70	11.60	11.10	10.90	10.60	10.60	10.30
54	L	0.9797	3.90	7.60	12.00	12.40	11.90	12.60	12.10	12.00	11.10	10.80	10.70	9.40	9.30	9.20	8.80	8.70	8.50
58	L	0.9947	1.60	5.40	7.73	9.10	8.60	9.00	8.60	8.70	7.80	7.80	7.30	6.90	6.60	6.70	6.57	6.50	6.10

TABLE D.1.2  
Small Aperture SWP Continuum Flux Measurements (ergs/cm<sup>2</sup>/s/Å)

SWP Graph ID	1194 Å	1243 Å	1263 Å	1308 Å	1350-1400 Å	1400-1450 Å	1450-1500 Å	1500-1550 Å	1550-1600 Å	1600-1650 Å	1650-1700 Å	1700-1750 Å	1750-1800 Å	1800-1850 Å	1850-1900 Å	1900-1950-2000 Å	
S 0.0015	1.46	2.75	4.34	4.55	4.71	4.94	4.73	4.72	4.34	4.19	4.04	3.88	3.84	3.59	3.67	3.66	3.56
S 0.0031	0.92	1.86	2.81	3.14	3.09	3.23	3.30	3.29	2.89	2.65	2.60	2.41	2.45	2.37	2.34	2.38	2.35
S 0.0053	0.59	1.17	1.89	2.16	2.12	2.14	2.09	2.12	1.89	1.83	1.77	1.66	1.67	1.59	1.59	1.65	1.59
S 0.0183	0.60	1.14	1.73	1.94	1.92	1.99	1.92	1.95	1.74	1.68	1.67	1.54	1.52	1.49	1.49	1.52	1.47
S 0.0816	6.38	12.66	16.92	17.46	16.98	17.22	16.81	16.35	14.90	14.39	13.95	12.92	12.64	12.41	12.52	12.82	11.86
S 0.3297	5.10	9.72	14.70	16.15	15.54	15.80	14.93	14.82	13.63	12.66	12.76	11.20	11.23	10.42	10.86	11.27	10.23
S 0.4927	4.19	7.61	10.95	11.79	11.44	12.00	11.33	11.28	10.27	9.79	9.42	8.61	8.35	8.17	8.09	8.21	7.59
S 0.6361	7.02	12.54	18.16	17.72	20.26	21.20	19.76	20.34	17.56	17.52	16.69	15.23	15.09	14.22	14.92	14.40	13.49
S 0.7674	6.51	11.78	17.82	17.65	18.01	18.87	17.38	17.42	15.88	15.42	14.66	13.55	12.95	12.53	12.96	12.67	12.54
S 0.9669	1.72	3.18	4.43	4.53	4.64	4.91	4.76	4.81	4.23	4.07	3.96	3.59	3.63	3.44	3.56	3.60	3.47
S 0.9791	1.43	3.29	4.76	5.56	5.35	5.78	5.51	5.59	4.99	4.78	4.68	4.14	4.32	4.03	4.13	4.16	4.09
S 0.9874	1.21	2.55	3.81	4.40	4.41	4.65	4.53	4.58	3.97	3.88	3.73	3.42	3.54	3.36	3.47	3.50	3.41
S 0.9880	1.28	2.67	4.32	4.65	4.79	5.10	4.74	4.87	4.32	4.31	4.10	3.72	3.80	3.64	3.78	3.65	3.59
S 0.9915	0.43	0.80	1.18	1.34	1.34	1.41	1.36	1.32	1.23	1.15	1.06	0.97	1.00	0.96	0.95	0.97	0.92
S 0.9951	0.92	2.28	3.25	3.75	3.81	3.95	3.78	3.95	3.48	3.32	3.28	2.96	3.10	3.00	3.02	2.99	2.89

TABLE D.1.3  
Large APERTURE SWP Normalized Continuum Flux Measurements (ergs/cm<sup>2</sup>/s/Å)

SWP Graph ID	Aper Phase	1194 Å	1243 Å	1263 Å	1308 Å	1350- 1400 Å	1400- 1450 Å	1400- 1450 Å	1450- 1500 Å	1500- 1550 Å	1550- 1600 Å	1600- 1650 Å	1650- 1700 Å	1700- 1750 Å	1750- 1800 Å	1800- 1850 Å	1850- 1900 Å	1900- 1950 Å	1950- 2000 Å
3	L	0.0052	0.15	0.21	0.24	0.25	0.25	0.25	0.24	0.25	0.24	0.25	0.25	0.26	0.26	0.27	0.27	0.27	0.28
5	L	0.0141	0.27	0.29	0.29	0.30	0.30	0.31	0.32	0.32	0.32	0.32	0.32	0.33	0.32	0.32	0.32	0.33	0.33
7	L	0.0204	0.27	0.35	0.37	0.38	0.39	0.38	0.36	0.37	0.35	0.37	0.36	0.37	0.37	0.38	0.38	0.38	0.39
8	L	0.0378	0.38	0.55	0.61	0.64	0.62	0.64	0.63	0.62	0.59	0.61	0.61	0.64	0.61	0.62	0.64	0.64	0.64
10	L	0.0855	1.02	1.00	1.00	0.94	0.96	0.98	1.00	1.01	1.01	1.01	1.01	1.02	1.00	0.99	1.00	1.00	1.00
11	L	0.1317	1.03	1.02	0.99	1.01	0.95	1.01	1.00	1.01	1.01	1.01	1.01	1.01	1.01	1.01	1.00	1.00	1.01
12	L	0.1538	1.00	0.92	0.96	1.00	0.95	0.96	0.99	1.00	0.98	1.01	1.01	0.99	0.97	0.94	0.98	1.00	0.98
13	L	0.1625	0.83	0.86	0.89	0.92	0.95	0.94	0.98	0.99	0.97	1.01	0.98	0.95	0.92	0.95	0.98	0.98	0.93
14	L	0.1889	0.72	0.99	1.00	1.00	1.02	1.01	0.99	0.99	0.95	0.98	0.97	1.00	0.99	1.00	0.99	0.99	0.98
15	L	0.3209	1.02	1.02	0.98	0.99	0.99	0.98	0.99	1.03	1.03	1.04	1.01	1.01	1.01	1.01	1.01	1.02	1.01
17	L	0.4790	0.71	0.96	1.02	1.00	1.01	0.99	0.99	0.98	0.95	0.96	0.95	0.97	0.95	1.00	1.00	0.97	0.97
19	L	0.5454	0.78	0.98	0.99	1.02	1.00	0.99	0.96	0.96	0.93	0.96	0.96	0.99	0.97	1.00	1.01	0.99	0.99
20	L	0.6326	0.95	0.99	1.04	0.96	1.02	1.01	0.98	0.97	0.93	0.96	0.96	0.98	0.97	1.00	0.98	0.98	0.98
22	L	0.6452	1.10	1.00	1.06	1.01	1.03	1.04	1.02	1.02	0.97	0.96	0.96	0.98	0.96	0.98	1.00	0.99	0.99
23	L	0.6522	1.18	1.00	1.00	1.01	0.98	0.96	1.01	1.02	1.01	1.02	1.01	1.01	0.99	1.00	1.02	1.04	1.04
24	L	0.6595	1.00	0.96	1.01	0.99	1.03	1.01	1.02	1.03	0.97	0.97	0.97	1.00	0.98	0.96	1.01	1.01	1.01
25	L	0.6704	0.90	0.93	1.02	1.01	1.04	1.01	1.02	1.03	0.97	0.97	0.97	0.99	1.01	0.97	1.00	1.01	1.02
26	L	0.6772	0.84	0.90	1.05	1.00	1.02	1.02	1.04	0.99	0.97	0.97	0.97	0.99	0.96	1.01	1.00	1.00	1.00
28	L	0.7784	0.78	0.98	1.03	1.01	1.00	1.00	0.97	0.96	0.95	0.94	0.96	0.97	0.97	0.98	1.01	0.99	0.99
29	L	0.7869	1.08	1.02	1.04	0.98	0.99	0.98	1.01	1.03	1.00	1.02	1.00	1.00	1.02	1.00	1.00	1.01	1.01
30	L	0.8005	0.98	0.98	0.99	0.95	1.03	0.99	1.03	1.00	0.97	0.97	0.97	0.99	0.99	0.99	1.01	0.98	0.98
31	L	0.8075	1.09	1.03	1.02	0.96	1.00	0.98	1.02	1.02	1.03	1.03	1.03	1.03	1.04	1.02	1.01	1.02	1.03
32	L	0.8813	0.66	0.93	1.01	1.01	1.00	0.99	1.00	0.93	0.93	0.93	0.93	0.94	0.98	0.97	0.98	1.01	1.00
33	L	0.8866	1.04	0.96	0.98	0.97	0.95	0.94	0.99	0.99	0.99	0.97	0.96	0.97	0.94	0.94	0.94	0.97	0.99
34	L	0.8904	0.94	0.82	0.95	0.77	0.85	0.86	0.92	0.94	0.92	0.91	0.85	0.94	0.90	0.94	0.94	0.92	0.96
35	L	0.9009	1.06	0.94	0.98	0.99	0.91	0.93	0.97	0.98	1.00	0.99	1.01	0.97	0.96	0.96	0.96	0.97	0.97
36	L	0.9070	1.01	0.92	0.96	0.90	0.91	0.93	0.97	0.96	0.95	0.96	0.96	0.93	0.96	0.92	0.96	0.95	0.99
37	L	0.9149	1.01	0.99	0.97	0.99	0.94	0.96	0.98	1.02	1.02	1.02	1.02	0.98	0.99	0.95	0.97	0.99	1.00
38	L	0.9217	0.90	0.89	0.91	0.90	0.91	0.94	0.99	0.99	0.99	0.99	0.99	0.96	0.98	0.95	0.96	0.97	1.00

TABLE D.1.3 - *continued*

SWP Graph ID	Aper Phase	1194 Å	1243 Å	1263 Å	1308 Å	1350-1400 Å	1400-1450 Å	1450-1500 Å	1500-1550 Å	1550-1600 Å	1600-1650 Å	1650-1700 Å	1700-1750 Å	1750-1800 Å	1800-1850 Å	1850-1900 Å	1900-1950 Å	1950-2000 Å
39	L	0.9218	0.87	0.92	0.96	0.97	0.95	0.94	0.99	0.98	0.96	0.98	0.99	0.97	0.95	0.98	0.97	1.02
40	L	0.9247	0.76	0.91	0.93	0.94	0.91	0.94	0.99	0.97	0.98	0.99	0.97	0.99	0.96	1.00	0.99	1.00
41	L	0.9299	0.99	0.96	0.99	0.98	0.94	0.95	0.99	1.00	0.99	1.00	0.95	0.97	0.93	0.97	0.99	1.00
42	L	0.9358	0.90	0.88	0.90	0.94	0.93	0.91	0.95	0.97	0.94	0.97	0.95	0.96	0.93	0.97	0.97	0.97
43	L	0.9388	0.76	0.81	0.90	0.84	0.85	0.88	0.92	0.91	0.89	0.89	0.90	0.91	0.88	0.89	0.92	0.93
44	L	0.9397	0.87	0.88	0.92	0.92	0.89	0.92	0.94	0.97	0.96	0.97	0.96	0.94	0.94	0.97	0.95	0.96
45	L	0.9471	0.87	0.88	0.91	0.90	0.86	0.89	0.91	0.94	0.92	0.94	0.92	0.92	0.88	0.90	0.90	0.95
46	L	0.9571	0.65	0.68	0.70	0.71	0.69	0.70	0.72	0.76	0.75	0.76	0.76	0.74	0.71	0.74	0.74	0.76
47	L	0.9573	0.72	0.71	0.74	0.76	0.73	0.77	0.77	0.80	0.79	0.78	0.78	0.78	0.75	0.77	0.78	0.79
48	L	0.9636	0.77	0.68	0.70	0.71	0.69	0.70	0.72	0.73	0.72	0.74	0.72	0.72	0.68	0.72	0.72	0.73
50	L	0.9712	0.42	0.45	0.48	0.49	0.47	0.48	0.51	0.52	0.52	0.51	0.52	0.52	0.51	0.53	0.52	0.53
51	L	0.9777	0.37	0.39	0.42	0.43	0.42	0.45	0.46	0.47	0.47	0.48	0.48	0.47	0.47	0.48	0.49	0.48
53	L	0.9791	0.47	0.43	0.46	0.47	0.45	0.46	0.50	0.50	0.49	0.49	0.48	0.48	0.47	0.47	0.48	0.50
54	L	0.9797	0.30	0.32	0.36	0.36	0.36	0.37	0.38	0.40	0.40	0.41	0.39	0.40	0.39	0.39	0.39	0.42
58	L	0.9947	0.19	0.23	0.25	0.27	0.26	0.26	0.27	0.28	0.29	0.28	0.29	0.29	0.28	0.29	0.29	0.30

TABLE D.1.4  
Large APERTURE LWP/LWR Continuum Flux Measurements (ergs/cm<sup>2</sup>/s/Å)

LWPR Graph ID	Aper	Phase	1850- 1900 Å	1900- 1950 Å	1950- 2000 Å	2000- 2050 Å	2050- 2075 Å	2075- 2125 Å	2125- 2175 Å	2175- 2225 Å	2225- 2275 Å	2275- 2325 Å	2325- 2375 Å	2375- 2425 Å	2425- 2475 Å	...
2	L	0.0034	5.25	4.95	5.35	5.58	5.58	5.60	5.03	4.59	4.51	4.38	3.77	3.61	3.61	
6	L	0.0220	6.13	7.50	8.10	7.96	8.58	8.38	7.55	6.98	6.59	6.37	5.52	5.21	5.37	
7	L	0.0390	15.00	16.30	15.30	15.08	14.41	14.02	12.40	10.98	10.20	9.90	8.40	8.10	8.00	
9	L	0.0867	20.25	18.80	19.70	20.60	20.45	19.90	18.20	16.59	15.95	15.80	13.30	12.75	12.70	
10	L	0.1303	23.00	22.13	21.20	20.94	20.81	19.37	17.70	15.80	15.10	14.50	12.90	12.20	12.30	
11	L	0.1547	23.50	20.98	20.15	21.12	20.50	20.78	19.30	17.80	16.30	16.50	13.85	12.70	12.75	
12	L	0.1903	16.50	19.00	19.40	20.22	20.91	19.82	18.20	16.98	16.30	16.10	13.83	13.22	13.10	
13	L	0.3196	18.00	18.10	20.10	21.21	20.99	20.18	18.70	17.12	15.95	16.75	13.50	13.12	13.15	
16	L	0.4778	19.25	16.90	19.30	19.14	19.80	19.90	17.60	16.59	15.60	15.30	13.40	12.65	13.00	
18	L	0.5463	19.35	18.50	20.35	20.83	20.62	20.21	18.80	17.38	16.00	16.15	13.95	13.20	13.28	
19	L	0.6343	17.50	20.10	20.80	21.20	20.48	20.25	19.00	17.11	16.15	16.05	13.75	13.00	12.95	
22	L	0.7798	17.50	18.40	20.00	20.19	20.71	20.22	18.60	17.20	16.05	15.95	13.25	12.75	12.95	
23	L	0.7884	17.25	18.50	20.25	19.99	19.63	19.12	18.05	16.80	15.95	15.70	13.20	12.50	12.45	
24	L	0.8825	19.30	19.85	20.20	20.37	20.60	20.69	18.45	17.35	16.20	15.90	13.40	12.55	12.80	
25	L	0.8878	14.70	18.50	19.30	19.33	19.89	19.51	18.20	16.99	16.50	16.05	13.63	12.45	12.40	
26	L	0.8915	16.60	18.00	19.95	20.87	20.59	20.82	19.75	16.90	17.95	17.10	13.83	13.20	12.35	
27	L	0.9018	16.95	17.85	19.95	19.14	19.33	19.30	18.20	16.50	16.10	15.20	12.80	12.40	12.50	
28	L	0.9082	16.13	18.10	19.90	21.13	20.72	21.51	19.82	17.50	17.20	17.10	13.40	13.60	13.60	
29	L	0.9166	19.13	19.80	20.15	19.95	19.90	19.75	18.70	16.59	16.10	16.00	13.15	11.90	12.40	
30	L	0.9227	16.60	16.85	19.00	20.04	19.80	20.81	18.80	16.65	16.00	16.70	12.85	13.05	13.15	
31	L	0.9259	18.50	17.00	19.30	20.22	20.67	20.51	18.70	17.20	15.85	15.75	12.70	12.10	12.45	
32	L	0.9323	18.70	17.40	19.70	19.31	18.86	19.00	18.00	16.89	15.85	15.00	12.65	11.60	12.10	
33	L	0.9367	15.90	16.30	18.25	19.13	18.79	19.90	18.07	16.45	15.85	15.60	12.30	11.85	12.70	
34	L	0.9409	24.25	24.60	22.70	21.67	21.23	19.81	17.60	15.80	14.65	13.90	12.13	11.10	12.05	
35	L	0.9488	15.05	16.50	18.05	17.90	18.19	17.79	16.20	15.58	14.45	13.95	11.45	10.50	10.90	
36	L	0.9581	14.05	14.00	13.95	14.39	14.31	14.89	13.50	12.01	11.50	11.45	9.25	8.80	9.65	
37	L	0.9590	20.00	19.65	18.00	17.57	17.62	16.81	14.55	13.10	11.30	11.30	9.70	9.00	9.40	
38	L	0.9650	12.50	14.50	14.25	14.48	14.45	14.28	13.08	11.98	11.30	11.30	9.50	8.40	8.65	
40	L	0.9721	7.00	8.50	9.80	10.34	10.46	10.80	9.80	8.59	8.45	8.50	6.64	6.50	6.79	
41	L	0.9794	8.13	8.70	9.60	9.54	9.49	9.60	8.40	7.80	7.30	6.90	5.95	5.45	5.86	
42	L	0.9801	7.60	8.50	9.70	9.35	9.44	9.35	8.90	8.08	7.80	7.35	6.10	5.78	5.90	

TABLE D.1.4 - continued

LWPR ID	Graph	Aper	Phase	2475- 2525 Å	2525- 2575 Å	2575- 2625 Å	2625- 2675 Å	2675- 2725 Å	2725- 2775 Å	2775- 2825 Å	2825- 2875 Å	2875- 2925 Å	2925- 2975 Å	2975- 3025 Å	3025- 3075 Å	3075- 3125 Å	3125- 3175 Å	3175- 3225 Å	3225- 3275 Å
2	L	0.0034		3.74	3.65	3.84	3.82	3.65	3.38	3.43	3.25	3.12	3.02	3.01	2.85	2.77	2.42	2.07	1.45
6	L	0.0220		5.50	5.46	5.70	5.63	5.27	5.01	4.84	4.60	4.40	4.33	4.19	4.05	3.82	3.50	3.00	2.18
7	L	0.0390		8.55	8.60	8.95	8.80	8.29	7.90	7.90	7.30	6.95	6.90	6.62	6.42	6.98	5.19	4.25	2.38
9	L	0.0867		13.40	12.90	13.30	13.10	12.40	11.70	11.40	10.80	10.15	9.90	9.80	9.50	9.00	7.85	6.60	4.90
10	L	0.1303		12.35	12.80	12.90	13.05	12.50	12.00	11.90	11.05	10.60	10.40	10.10	9.70	9.10	7.90	6.60	4.10
11	L	0.1547		12.95	12.55	12.80	13.00	12.30	11.70	11.60	10.80	10.50	10.30	9.80	9.60	9.10	7.75	5.40	2.40
12	L	0.1903		13.83	13.30	13.55	13.20	12.50	11.85	11.70	10.95	10.50	10.00	10.00	9.50	9.05	7.95	6.85	5.10
13	L	0.3196		13.92	13.40	13.60	13.29	12.70	12.05	12.00	11.05	10.60	10.20	10.00	9.65	9.25	8.00	6.90	5.00
16	L	0.4778		13.00	13.00	13.10	12.70	12.30	11.50	11.50	10.65	10.30	10.00	9.65	9.30	8.80	7.90	7.20	4.80
18	L	0.5463		14.15	13.25	13.50	13.20	12.70	11.80	11.65	11.10	10.40	10.20	9.95	9.60	9.25	7.95	6.70	4.80
19	L	0.6343		13.82	13.30	13.40	13.30	12.70	12.30	11.80	11.30	10.60	10.55	9.93	9.55	9.30	8.10	6.55	4.60
22	L	0.7798		13.40	13.20	13.20	13.05	12.45	11.80	11.70	10.70	10.60	10.10	9.90	9.55	9.25	8.05	6.80	5.55
23	L	0.7884		13.25	12.90	12.80	13.00	12.20	11.45	11.40	10.80	10.40	10.20	9.75	9.55	8.85	8.00	6.55	4.75
24	L	0.8825		13.50	13.10	13.20	13.20	12.70	11.70	11.80	10.80	10.55	10.30	10.00	9.70	9.20	8.30	6.80	5.00
25	L	0.8878		12.80	12.30	12.45	12.70	12.30	11.35	11.00	10.50	10.30	9.95	9.55	9.20	8.60	7.80	5.50	3.40
26	L	0.8915		12.70	12.15	12.90	12.75	11.90	11.00	10.70	10.45	10.35	10.00	9.55	9.20	8.70	7.80	5.40	3.10
27	L	0.9018		13.10	12.58	12.55	12.60	12.10	11.60	11.25	10.65	10.30	9.90	9.55	9.20	8.80	7.45	5.90	3.10
28	L	0.9082		13.35	12.60	13.10	13.05	11.90	11.70	11.80	10.70	10.40	10.10	9.85	9.20	9.00	7.90	6.70	4.80
29	L	0.9166		12.65	12.65	12.45	12.50	12.20	11.30	11.50	10.65	10.20	9.90	9.65	9.35	8.55	7.45	5.75	2.75
30	L	0.9227		13.15	13.00	13.20	13.20	12.70	11.70	11.70	10.90	10.50	10.20	10.00	9.30	8.85	8.00	5.80	4.35
31	L	0.9259		13.00	12.60	13.00	12.70	12.40	11.30	11.60	10.75	10.10	10.10	9.75	9.60	8.80	7.95	6.45	4.90
32	L	0.9323		12.45	11.90	12.30	12.20	11.80	11.10	10.80	10.45	10.10	9.70	9.55	9.20	8.35	7.20	5.35	3.10
33	L	0.9367		12.75	12.30	12.60	12.60	12.00	11.00	11.10	10.50	10.00	9.60	9.60	8.85	8.75	7.35	5.50	3.85
34	L	0.9409		12.15	12.05	12.60	12.30	11.89	11.00	11.25	10.25	9.85	9.90	9.55	9.30	8.65	7.75	6.00	3.90
35	L	0.9488		11.55	11.30	11.30	11.40	11.00	10.20	10.00	9.50	9.10	8.90	8.70	7.90	7.90	6.55	5.70	3.30
36	L	0.9581		9.50	9.10	9.20	9.35	9.15	8.30	8.35	7.80	7.55	7.30	7.18	6.75	6.65	5.40	3.83	2.45
37	L	0.9590		9.65	9.60	9.90	9.90	9.70	8.70	8.95	8.30	8.10	7.89	7.65	7.40	6.85	6.20	4.56	2.90
38	L	0.9650		8.90	8.55	8.70	8.90	8.50	7.90	7.95	7.42	7.15	7.08	6.95	6.60	6.00	5.14	3.88	2.40
40	L	0.9721		6.84	6.70	6.70	6.79	6.55	6.03	6.00	5.68	5.60	5.31	5.31	4.89	4.69	4.19	3.38	2.39
41	L	0.9794		6.18	5.94	6.10	5.95	5.88	5.26	5.50	5.08	4.95	4.86	4.82	4.51	4.27	3.65	2.90	2.23
42	L	0.9801		6.14	5.95	6.14	6.11	6.01	5.46	5.53	5.23	5.18	5.02	4.83	4.62	4.30	3.70	2.90	2.10

TABLE D.1.5  
Small APERTURE LWP/LWR Continuum Flux Measurements (ergs/cm<sup>2</sup>/s/Å)

LWPR Graph ID	Aper Phase	1850- 1900 Å	1900- 1950 Å	1950- 2000 Å	2000- 2050 Å	2050- 2075 Å	2075- 2125 Å	2125- 2175 Å	2175- 2225 Å	2225- 2275 Å	2275- 2325 Å	2325- 2375 Å	2375- 2425 Å	2425- 2475 Å	2475- 2525 Å	2525- 2575 Å	...
1	S	0.0030	3.25	2.78	3.00	3.04	2.99	3.00	2.81	2.57	2.36	2.39	2.07	2.04	2.05	2.09	2.02
3	S	0.0034	2.08	1.81	1.84	1.87	1.81	1.78	1.80	1.61	1.55	1.56	1.28	1.30	1.33	1.35	1.26
4	S	0.0049	3.01	2.50	2.82	2.84	2.84	2.81	2.69	2.35	2.09	2.28	1.86	1.70	1.83	1.88	1.76
5	S	0.0165	0.83	0.65	0.69	0.65	0.59	0.58	0.54	0.46	0.45	0.47	0.40	0.42	0.43	0.42	0.41
8	S	0.0801	10.95	8.75	9.30	9.72	9.26	9.51	9.05	7.91	7.65	6.85	5.90	6.09	6.07	6.01	5.92
14	S	0.3200	9.50	8.25	8.60	8.41	8.24	8.52	7.90	7.10	6.81	6.67	5.78	5.77	5.83	5.69	5.34
15	S	0.3280	10.50	8.95	9.60	9.63	9.49	9.71	8.95	8.11	7.85	7.56	6.59	6.55	6.57	6.40	6.40
17	S	0.4939	12.90	9.95	10.90	11.34	10.80	11.41	10.95	9.45	9.10	8.75	7.65	7.60	7.20	7.25	7.03
20	S	0.6520	13.95	12.00	11.20	12.56	11.55	12.60	12.10	10.84	10.20	9.90	8.70	8.50	8.40	8.65	8.30
21	S	0.7685	12.70	10.15	10.95	11.27	10.90	11.21	10.55	9.30	8.75	8.20	7.13	7.30	6.70	7.05	6.90
39	S	0.9683	5.13	4.30	4.84	4.77	4.62	4.87	4.58	3.98	3.78	3.74	3.05	3.17	3.03	3.22	3.12
43	S	0.9895	3.08	2.60	2.84	2.98	2.92	3.10	2.82	2.53	2.45	2.44	2.14	2.07	2.08	2.12	2.20
44	S	0.9901	0.74	0.37	0.35	0.44	0.45	0.51	0.51	0.51	0.54	0.50	0.42	0.37	0.41	0.41	0.40

TABLE D.1.5 - continued

LWPR Graph ID	Aper Phase	2575-2625 Å	2625- 2675 Å	2675- 2725 Å	2725- 2775 Å	2775- 2825 Å	2825- 2875 Å	2875- 2885 Å	2885-292 Å	2925- 2975 Å	2975- 3025 Å	3025- 3075 Å	3075- 3125 Å	3125- 3175 Å	3175- 3225 Å	3225- 3275 Å
1	S	0.0030	1.99	2.08	1.91	1.90	1.84	1.74	1.73	1.62	1.61	1.59	1.62	1.56	1.33	1.40
3	S	0.0034	1.27	1.33	1.26	1.16	1.20	1.12	1.11	1.06	1.06	1.06	1.06	1.03	0.97	1.19
4	S	0.0049	1.81	1.86	1.79	1.66	1.68	1.63	1.62	1.53	1.54	1.54	1.56	1.47	1.43	1.48
5	S	0.0165	0.40	0.42	0.38	0.36	0.34	0.32	0.32	0.32	0.30	0.30	0.30	0.29	0.33	0.38
8	S	0.0801	5.90	6.11	5.71	5.55	5.45	5.05	5.01	4.85	4.69	4.62	4.73	4.52	4.15	4.40
14	S	0.3200	5.05	5.47	4.99	4.91	4.98	4.60	4.58	4.28	4.28	4.11	4.12	3.94	3.55	4.02
15	S	0.3280	6.30	6.36	5.81	5.71	5.80	5.21	5.21	5.00	4.89	4.68	4.80	4.52	3.99	4.12
17	S	0.4939	6.88	7.10	6.68	6.58	6.40	5.89	5.78	5.55	5.52	5.37	5.30	5.39	5.05	5.25
20	S	0.6520	8.05	8.25	7.70	7.70	7.60	6.85	6.80	6.51	6.37	6.28	6.15	5.85	5.90	5.80
21	S	0.7685	6.74	6.83	6.48	6.22	6.20	5.75	5.61	5.35	5.35	5.17	5.18	5.15	4.49	5.35
39	S	0.9683	3.14	3.14	3.02	2.88	2.94	2.67	2.72	2.59	2.60	2.56	2.55	2.51	2.37	2.42
43	S	0.9895	1.96	2.05	1.90	1.86	1.86	1.69	1.66	1.62	1.59	1.56	1.54	1.48	1.34	1.41
44	S	0.9901	0.40	0.39	0.38	0.37	0.36	0.36	0.34	0.33	0.32	0.34	0.36	0.40	0.41	0.61



TABLE D.1.6  
Large APERTURE LWP/LWR Normalized Continuum Flux Measurements (ergs/cm<sup>2</sup>/s/Å)

LWPR Graph ID	Aper	Phase	1850- 1900 Å	1900- 1950 Å	1950- 2000 Å	2000- 2050 Å	2050- 2075 Å	2075- 2125 Å	2125- 2175 Å	2175- 2225 Å	2225- 2275 Å	2275- 2325 Å	2325- 2375 Å	2375- 2425 Å	2425- 2475 Å	2475- 2525 Å	2525- 2575 Å	...
2	L	0.0034	0.29	0.27	0.26	0.27	0.27	0.28	0.27	0.27	0.28	0.27	0.28	0.28	0.28	0.27	0.28	
6	L	0.0220	0.33	0.41	0.40	0.38	0.41	0.41	0.41	0.41	0.41	0.39	0.41	0.40	0.41	0.40	0.41	
7	L	0.0390	0.82	0.88	0.76	0.73	0.69	0.69	0.67	0.64	0.64	0.61	0.62	0.62	0.62	0.62	0.65	
9	L	0.0867	1.10	1.02	0.97	0.99	0.99	0.99	0.98	0.97	1.00	0.98	0.98	0.98	0.98	0.97	0.97	
10	L	0.1303	1.25	1.20	1.05	1.01	1.00	0.96	0.95	0.92	0.94	0.90	0.95	0.94	0.95	0.89	0.97	
11	L	0.1547	1.28	1.13	1.00	1.02	0.99	1.03	1.04	1.04	1.02	1.02	1.02	0.98	0.98	0.94	0.95	
12	L	0.1903	0.90	1.03	0.96	0.97	1.01	0.98	0.98	0.99	1.02	1.00	1.02	1.02	1.01	1.00	1.00	
13	L	0.3196	0.98	0.98	0.99	1.02	1.01	1.00	1.01	1.00	1.00	1.04	0.99	1.01	1.01	1.01	1.01	
16	L	0.4778	1.05	0.91	0.95	0.92	0.95	0.99	0.95	0.97	0.98	0.95	0.99	0.97	1.00	0.94	0.98	
18	L	0.5463	1.05	1.00	1.00	1.00	0.99	1.00	1.01	1.02	1.00	1.00	1.03	1.02	1.02	1.03	1.00	
19	L	0.6343	0.95	1.09	1.03	1.02	0.99	1.00	1.02	1.00	1.01	0.99	1.01	1.00	1.00	1.00	1.00	
22	L	0.7798	0.95	0.99	0.99	0.97	1.00	1.00	1.00	1.01	1.00	0.99	0.97	0.98	1.00	0.97	1.00	
23	L	0.7884	0.94	1.00	1.00	0.96	0.95	0.95	0.97	0.98	1.00	0.97	0.97	0.96	0.96	0.96	0.97	
24	L	0.8825	1.05	1.07	1.00	0.98	0.99	1.02	0.99	1.01	1.01	0.99	0.99	0.97	0.98	0.98	0.99	
25	L	0.8878	0.80	1.00	0.95	0.93	0.96	0.97	0.98	0.99	1.03	0.99	1.00	0.96	0.95	0.93	0.93	
26	L	0.8915	0.90	0.97	0.99	1.01	0.99	1.03	1.06	0.99	1.12	1.06	1.02	1.02	0.95	0.92	0.92	
27	L	0.9018	0.92	0.96	0.99	0.92	0.93	0.96	0.98	0.96	1.01	0.94	0.94	0.95	0.96	0.95	0.95	
28	L	0.9082	0.88	0.98	0.98	1.02	1.00	1.06	1.07	1.02	1.08	1.06	0.99	1.05	1.05	0.97	0.95	
29	L	0.9166	1.04	1.07	1.00	0.96	0.96	0.98	1.01	0.97	1.01	0.99	0.97	0.92	0.95	0.92	0.96	
30	L	0.9227	0.90	0.91	0.94	0.97	0.95	1.03	1.01	0.97	1.00	1.04	0.94	1.00	1.01	0.95	0.98	
31	L	0.9259	1.01	0.92	0.95	0.97	1.00	1.02	1.01	1.01	0.99	0.98	0.93	0.93	0.96	0.94	0.95	
32	L	0.9323	1.02	0.94	0.97	0.93	0.91	0.94	0.97	0.99	0.99	0.93	0.93	0.89	0.93	0.90	0.90	
33	L	0.9367	0.86	0.88	0.90	0.92	0.91	0.99	0.97	0.96	0.99	0.97	0.90	0.91	0.98	0.92	0.93	
34	L	0.9409	1.32	1.33	1.12	1.04	1.02	0.98	0.95	0.92	0.92	0.86	0.89	0.85	0.93	0.88	0.91	
35	L	0.9488	0.82	0.89	0.89	0.86	0.88	0.88	0.87	0.91	0.90	0.86	0.84	0.81	0.84	0.84	0.85	
36	L	0.9581	0.76	0.76	0.69	0.69	0.69	0.74	0.73	0.70	0.72	0.71	0.68	0.68	0.74	0.69	0.69	
37	L	0.9590	1.09	1.06	0.89	0.85	0.85	0.83	0.78	0.77	0.71	0.70	0.71	0.69	0.72	0.70	0.73	
38	L	0.9650	0.68	0.78	0.70	0.70	0.70	0.71	0.70	0.70	0.71	0.70	0.70	0.65	0.67	0.64	0.65	
40	L	0.9721	0.38	0.46	0.48	0.50	0.50	0.53	0.53	0.50	0.53	0.53	0.49	0.50	0.52	0.50	0.51	
41	L	0.9794	0.44	0.47	0.47	0.46	0.46	0.48	0.45	0.46	0.46	0.43	0.44	0.42	0.45	0.45	0.45	
42	L	0.9801	0.41	0.46	0.48	0.45	0.45	0.46	0.48	0.47	0.49	0.46	0.45	0.44	0.45	0.44	0.45	

TABLE D.1.6 -continued

LWPR Graph ID	Aper	Phase	2575- 2625 Å	2625- 2675 Å	2675- 2725 Å	2725- 2775 Å	2775- 2825 Å	2825- 2875 Å	2875- 292 Å5	2925- 2975 Å	2975- 3025 Å	3025- 3075 Å	3075- 3125 Å	3125- 3175 Å	3175- 3225 Å	3225- 3275 Å
2	L	0.0034	0.29	0.29	0.29	0.28	0.29	0.29	0.30	0.29	0.30	0.30	0.30	0.30	0.30	0.30
6	L	0.0220	0.42	0.43	0.42	0.42	0.41	0.42	0.42	0.42	0.42	0.42	0.42	0.44	0.44	0.44
7	L	0.0390	0.67	0.67	0.66	0.66	0.66	0.66	0.66	0.67	0.67	0.67	0.76	0.65	0.63	0.49
9	L	0.0867	0.99	0.99	0.99	0.98	0.96	0.98	0.97	0.97	0.99	0.99	0.98	0.98	0.97	1.00
10	L	0.1303	0.96	0.99	1.00	1.01	1.00	1.00	1.01	1.02	1.02	1.01	1.00	0.99	0.97	0.84
11	L	0.1547	0.95	0.98	0.98	0.98	0.97	0.98	1.00	1.01	0.99	1.00	1.00	0.97	0.79	0.49
12	L	0.1903	1.01	1.00	1.00	0.99	0.98	0.99	1.00	0.98	1.01	0.99	0.99	0.99	1.01	1.04
13	L	0.3196	1.01	1.01	1.01	1.01	1.01	1.00	1.01	1.00	1.01	1.01	1.01	1.00	1.01	1.02
16	L	0.4778	0.97	0.96	0.98	0.96	0.97	0.96	0.98	0.98	0.97	0.97	0.96	0.99	1.06	0.98
18	L	0.5463	1.00	1.00	1.01	0.99	0.98	1.00	0.99	1.00	1.01	1.00	1.01	0.99	0.99	0.98
19	L	0.6343	1.00	1.01	1.01	1.03	0.99	1.02	1.01	1.03	1.00	0.99	1.02	1.01	0.96	0.94
22	L	0.7798	0.98	0.99	0.99	0.99	0.98	0.97	1.01	0.99	1.00	0.99	1.01	1.01	1.00	1.13
23	L	0.7884	0.95	0.98	0.97	0.96	0.96	0.98	0.99	1.00	0.98	0.99	0.97	1.00	0.96	0.97
24	L	0.8825	0.98	1.00	1.01	0.98	0.99	0.98	1.01	1.01	1.01	1.01	1.01	1.04	1.00	1.02
25	L	0.8878	0.93	0.96	0.98	0.95	0.92	0.95	0.98	0.97	0.96	0.96	0.94	0.98	0.81	0.69
26	L	0.8915	0.96	0.97	0.95	0.92	0.90	0.95	0.99	0.98	0.96	0.96	0.95	0.98	0.99	1.10
27	L	0.9018	0.93	0.95	0.96	0.97	0.95	0.96	0.98	0.97	0.96	0.96	0.96	0.93	0.87	0.63
28	L	0.9082	0.97	0.99	0.95	0.98	0.99	0.97	0.99	0.99	0.99	0.96	0.98	0.99	0.99	0.98
29	L	0.9166	0.93	0.95	0.97	0.95	0.97	0.96	0.98	0.97	0.97	0.97	0.94	0.93	0.85	0.56
30	L	0.9227	0.98	1.00	1.01	0.98	0.98	0.99	1.00	1.00	1.01	0.97	0.97	1.00	0.85	0.89
31	L	0.9259	0.97	0.96	0.99	0.95	0.97	0.97	0.99	0.99	0.98	1.00	0.96	0.99	0.95	1.00
32	L	0.9323	0.92	0.92	0.94	0.93	0.91	0.95	0.97	0.95	0.96	0.96	0.91	0.90	0.79	0.63
33	L	0.9367	0.94	0.95	0.96	0.92	0.93	0.95	0.96	0.94	0.97	0.92	0.96	0.92	0.81	0.79
34	L	0.9409	0.94	0.93	0.95	0.92	0.95	0.93	0.94	0.97	0.96	0.97	0.95	0.97	0.88	0.80
35	L	0.9488	0.84	0.86	0.88	0.86	0.84	0.86	0.87	0.87	0.88	0.89	0.86	0.82	0.84	0.67
36	L	0.9581	0.68	0.71	0.73	0.70	0.70	0.71	0.72	0.71	0.72	0.70	0.73	0.68	0.56	0.50
37	L	0.9590	0.74	0.75	0.77	0.73	0.75	0.75	0.77	0.77	0.77	0.77	0.77	0.78	0.67	0.59
38	L	0.9650	0.65	0.67	0.68	0.66	0.67	0.67	0.68	0.69	0.70	0.69	0.66	0.64	0.57	0.49
40	L	0.9721	0.50	0.51	0.52	0.51	0.50	0.51	0.54	0.52	0.54	0.51	0.51	0.52	0.50	0.49
41	L	0.9794	0.45	0.45	0.47	0.44	0.46	0.46	0.47	0.47	0.49	0.47	0.47	0.46	0.43	0.46
42	L	0.9801	0.46	0.46	0.48	0.46	0.46	0.47	0.50	0.49	0.49	0.48	0.47	0.46	0.43	0.43

## APPENDIX D.2

### Radial Velocities

TABLE D.2.1  
OBSERVED SWP RADIAL VELOCITIES (km/s)

SWP Graph	Al II	Al III	*Al III	C II	C II	C IV
ID	1670.7867	1854.716	1862.7895	1334.5323	1335.7077	1548.185
1	1.49	0.65	-12.79	3.98	-19.68	-10.65
2	-3.00	11.96	-3.14	3.98	-15.19	6.78
3	-9.28	-15.52	-28.89	-9.50	-26.42	-33.89
4	-11.97	-25.22	-32.11	-7.26	-19.68	2.90
5	-8.38	-15.52	-25.67	-7.26	-35.39	-22.27
6	-19.15	-28.45	-36.94	-11.75	-35.39	-35.82
7	-24.53	-31.68	-36.94	-20.73	-44.37	-24.21
8	-24.53	-28.45	-33.72	-27.47	-39.88	-39.70
9	-19.15	-12.28	-14.40	-16.24	-35.39	-8.71
10	-25.43	-25.22	-29.69	-18.49	-42.13	-35.82
11	-38.88	-34.91	-43.37	-36.46	-53.35	-4.84
12	-35.29	-34.91	-41.76	-38.71	-51.11	-45.51
13	-65.80	-67.24	-65.90	-52.18	-82.53	-74.55
14	-50.55	-46.23	-54.64	-40.95	-60.08	-66.81
15	-33.50	-38.15	-51.42	-22.98	-48.86	-31.95
16	-22.73	-26.83	-33.72	-16.24	-44.37	-45.51
17	-10.17	-12.28	-27.28	-11.75	-24.17	-39.70
18	5.98	8.73	-6.36	8.47	-12.95	-12.59
19	5.98	2.26	-9.58	-0.52	-8.46	-16.46
20	43.66	36.21	29.05	44.41	16.23	8.71
21	31.99	29.74	27.44	24.19	16.23	-2.90
22	40.07	36.21	33.88	38.80	22.96	6.78
23	45.45	32.97	33.88	44.41	11.74	12.59
24	48.14	32.97	33.88	46.66	25.21	6.78
25	45.45	36.21	33.07	39.92	22.96	2.90
26	49.04	42.67	41.92	42.17	27.45	6.78
27	56.22	55.60	49.97	46.66	38.67	20.33
28	38.27	39.44	22.61	41.04	31.94	10.65
29	49.04	45.91	43.53	51.15	25.21	26.14
30	49.04	45.91	41.92	48.90	34.18	16.46
31	43.66	45.91	38.71	51.15	34.18	26.14
32	27.51	23.28	16.98	26.44	11.74	-0.97
33	29.30	23.28	14.56	21.95	11.74	-4.84
34	22.12	23.28	27.44	19.70	9.49	-10.65
35	20.33	11.96	8.13	3.98	5.01	-0.97

TABLE D.2.1 - *continued*

SWP	AI	AI	*AI	C	C	C
Graph	II	III	III	II	II	IV
ID	1670.7867	1854.716	1862.7895	1334.5323	1335.7077	1548.185
36	7.77	11.96	8.13	8.47	-1.73	-4.84
37	20.33	21.66	6.52	8.47	2.76	22.27
38	31.10	42.67	32.27	36.55	11.74	-4.84
39	13.15	15.19	1.69	8.47	-1.73	22.27
40	20.33	28.13	17.78	21.95	2.76	24.21
41	16.74	16.81	8.13	11.84	5.01	12.59
42	9.56	2.26	-6.36	3.98	-1.73	-10.65
43	-1.20	29.74	17.78	-0.52	-10.71	26.14
44	16.74	16.81	11.35	12.96	0.52	22.27
45	14.05	10.34	-3.14	-0.52	-6.22	-8.71
46	16.74	16.81	8.13	12.96	-3.97	-0.97
47	23.92	18.43	12.96	17.45	-3.97	10.65
48	21.23	11.96	3.30	-0.52	-3.97	2.90
49	33.79	53.99	49.97	33.18	11.74	18.40
50	14.95	8.73	1.69	15.21	0.52	2.90
51	18.54	21.66	8.13	3.98	-8.46	10.65
52	16.74	42.67	33.88	28.69	9.49	26.14
53	14.95	20.04	1.69	-0.52	0.52	6.78
54	10.46	8.73	-3.14	12.96	0.52	-10.65
55	5.98	26.51	27.44	17.45	-6.22	14.52
56	15.84	18.43	11.35	19.70	9.49	0.97
57	4.18	13.58	1.69	8.47	15.11	0.97
58	5.98	3.88	-14.40	-2.76	-12.95	18.40
59	2.39	23.28	17.78	10.72	-19.68	45.51

TABLE D.2.2  
OBSERVED SWP RADIAL VELOCITIES (km/s)

SWP	Fe	Fe	Fe	Fe	Fe	Fe	Fe
Graph	III	III	III	II	II	II	II
ID	1895.456	1914.056	1926.304	1608.45106	1635.401	1639.40124	1640.15205
1	18.03	5.33	-3.74	7.26	-0.18	5.26	1.45
2	14.87	-11.90	-19.30	9.12	16.31	8.92	-7.69
3	3.80	0.63	-22.41	-13.24	-13.02	-17.60	-7.69
4	10.12	-24.43	-6.85	12.85	-1.10	-2.06	-2.20
5	-2.53	-30.70	-30.19	-13.24	-9.35	-18.51	-9.51
6	-0.95	-21.30	-25.52	-9.52	-20.35	-16.68	-10.43
7	-9.65	-36.96	-38.75	-30.02	-33.18	-36.80	-31.45
8	-21.51	-35.40	-37.97	-26.29	-35.01	-33.14	-27.79
9	-4.90	-18.17	-23.97	-11.38	-11.18	-18.51	-10.43
10	-13.60	-26.78	-34.86	-24.43	-16.68	-16.68	-22.31
11	-27.84	-38.53	-49.65	-43.07	-38.68	-36.80	-33.28
12	-29.42	-33.83	-45.76	-39.34	-35.01	-25.83	-45.16
13	-61.84	-58.89	-73.77	-71.02	-69.84	-61.49	-68.00
14	-35.75	-44.80	-71.43	-48.66	-38.68	-56.92	-51.55
15	-19.93	-35.40	-64.43	-29.09	-31.35	-34.97	-42.41
16	-16.77	-32.27	-37.97	-16.97	-24.01	-18.51	-24.14
17	3.01	-13.47	-27.08	-0.20	-11.18	-17.60	-27.79
18	18.03	8.46	0.16	8.19	16.31	16.23	6.94
19	11.70	3.76	-8.40	-3.93	-3.85	-5.71	-4.03
20	55.99	46.05	28.95	31.49	45.65	34.52	27.04
21	51.25	40.17	24.28	31.49	38.31	36.35	30.70
22	48.08	31.95	35.95	31.49	40.15	36.35	50.80
23	48.08	37.43	18.05	26.83	36.48	45.49	45.32
24	57.57	40.57	24.28	31.49	43.81	41.83	39.84
25	55.20	42.92	27.39	34.28	41.98	45.49	38.01
26	55.99	42.13	32.06	37.08	47.48	39.09	48.98
27	70.22	46.05	38.29	65.04	56.64	50.98	48.98
28	57.57	35.08	24.28	30.56	43.81	30.86	45.32
29	56.78	44.48	49.18	33.35	45.65	50.98	39.84
30	54.41	36.65	32.84	31.49	38.31	39.09	48.98
31	55.99	43.70	35.17	33.35	51.14	47.32	45.32
32	38.59	36.65	24.28	10.99	35.56	16.23	14.25
33	35.43	17.86	18.05	12.85	30.98	32.69	27.04
34	39.54	30.39	16.50	18.44	18.15	16.23	17.90
35	26.73	10.02	7.16	14.71	19.98	3.43	8.76
36	22.78	9.24	4.82	-2.06	1.65	3.43	-4.03
37	24.36	17.86	17.28	9.12	23.65	25.37	10.59
38	43.34	35.08	33.62	20.30	38.31	32.69	27.04
39	19.61	13.94	14.47	9.12	-0.18	6.17	6.94
40	32.27	22.55	25.83	10.99	10.82	14.40	30.70
41	30.68	16.29	13.38	5.39	12.65	18.06	6.94
42	22.78	7.67	8.72	-0.20	-0.18	-1.14	-4.03
43	11.70	7.67	1.71	-7.65	-0.18	-0.23	-11.34
44	29.10	19.42	12.61	9.12	16.31	18.06	7.85
45	21.98	6.11	-9.18	-0.20	8.98	12.57	-4.03
46	22.78	16.29	7.16	12.85	14.48	9.83	5.11

TABLE D.2.2 - *continued*

SWP	Fe	Fe	Fe	Fe	Fe	Fe	Fe
Graph	III	III	III	II	II	II	II
ID	1895.456	1914.056	1926.304	1608.45106	1635.401	1639.40124	1640.15205
47	33.85	30.39	10.27	16.58	21.81	17.15	28.87
48	25.94	19.42	10.27	14.71	18.15	16.23	10.59
49	46.50	50.75	39.84	37.08	49.31	41.83	39.84
50	27.52	11.59	3.27	14.71	16.31	14.40	10.59
51	33.85	25.69	18.05	12.85	16.31	18.06	27.04
52	46.50	46.83	32.06	33.35	34.65	29.03	27.04
53	27.52	16.29	-9.96	24.03	23.65	19.89	17.90
54	23.57	8.46	8.72	1.67	5.32	7.09	7.85
55	29.10	36.65	25.83	26.83	23.65	14.40	25.21
56	32.27	24.12	13.38	14.71	43.81	21.72	27.04
57	25.94	24.12	13.38	25.90	21.81	54.63	19.73
58	18.82	11.59	-14.63	5.39	19.06	14.40	6.94
59	22.78	-0.94	-6.85	18.44	18.15	2.52	14.25

TABLE D.2.3  
OBSERVED SWP RADIAL VELOCITIES (km/s)

SWP Graph	Si II	Si II	*Si II	Si II	Si II	Si II	Si II	*Si II	*Si II
ID	1260.4212	1264.7374	1304.37	1305.59	1309.2769	1526.7076	1533.432	1808.0117	1816.9796
1	-10.99	5.36	66.65	5.74	30.48	4.40	1.56	-5.26	38.84
2	-22.88	10.10	36.77	-9.18	19.03	-1.49	-10.17	-26.81	23.17
3	-10.99	16.02	64.35	4.59	21.32	-5.42	-10.17	-26.81	28.12
4	-16.93	0.62	50.56	-4.59	23.61	-3.46	-4.30	-11.89	36.36
5	-28.83	0.62	62.06	0.00	16.74	-11.31	-17.99	-25.15	18.22
6	-19.31	5.36	36.77	-9.18	9.87	-19.17	-17.99	-19.35	23.17
7	-34.77	0.62	60.91	-12.63	-3.87	-21.13	-27.76	-28.47	5.02
8	-28.83	-6.49	32.18	-25.26	-1.58	-19.17	-29.72	-31.79	11.62
9	-40.72	-7.68	27.58	-14.93	-1.58	-15.24	-25.81	-21.84	19.87
10	-25.85	-12.42	36.77	-16.07	-6.16	-21.13	-29.72	-16.03	9.97
11	-52.61	-23.09	25.28	-39.27	-24.48	-28.98	-51.22	-28.47	1.72
12	-31.21	-23.09	26.43	-9.18	-8.45	-30.95	-39.49	-40.91	19.87
13	-57.37	-57.46	-9.19	-58.55	-47.38	-62.37	-74.68	-61.63	-13.13
14	-40.72	-33.75	16.09	-40.18	-31.35	-44.69	-57.09	-41.74	-13.13
15	-25.85	-18.35	27.58	-41.33	-6.16	-32.91	-14.08	-40.08	-3.23
16	-28.83	-10.05	25.28	-47.07	0.71	-21.13	-25.81	-30.13	26.47
17	-25.85	5.36	63.21	0.00	12.16	-11.31	-14.08	-18.52	19.87
18	3.88	19.58	64.35	5.74	21.32	8.33	9.38	17.96	53.69
19	-16.93	18.39	71.25	10.33	19.03	-1.49	-4.30	6.35	51.21
20	42.53	52.76	94.23	39.04	67.11	37.78	32.84	44.49	79.26
21	18.74	45.65	91.93	32.15	48.79	35.82	25.02	37.86	99.06
22	40.15	61.06	97.68	29.85	69.40	37.78	36.75	47.80	85.86
23	37.77	44.47	109.17	48.22	64.82	43.67	36.75	42.83	77.61
24	30.64	55.14	104.58	43.63	64.82	39.74	36.75	54.44	77.61
25	61.56	57.51	105.73	27.55	67.11	41.71	40.66	39.51	87.51
26	54.42	52.76	112.62	48.22	71.69	41.71	40.66	51.12	82.56
27	42.53	52.76	110.32	47.07	83.14	53.49	50.44	61.07	95.76
28	33.61	52.76	103.43	49.37	62.53	37.78	36.75	34.54	82.56
29	52.04	55.14	113.77	66.59	64.82	39.74	42.62	46.15	85.86
30	42.53	57.51	103.43	50.52	71.69	39.74	42.62	41.17	71.01
31	48.47	52.76	99.98	55.11	71.69	39.74	34.80	49.46	82.56
32	23.50	52.76	87.34	41.33	69.40	24.04	25.02	22.93	64.41
33	18.74	21.95	91.93	34.44	41.93	24.04	17.20	4.69	62.76
34	13.99	38.54	82.74	34.44	37.35	24.04	17.20	14.64	61.11
35	3.88	16.02	77.00	36.74	39.64	20.11	11.34	9.67	64.41
36	-5.04	21.95	66.65	18.37	23.61	8.33	5.47	3.03	52.86
37	2.09	18.39	74.70	36.74	37.35	18.14	13.29	14.64	54.51
38	33.61	39.73	85.04	29.85	53.37	24.04	17.20	34.54	59.46
39	6.85	24.32	68.95	32.15	30.48	12.25	9.38	-5.26	36.36
40	24.69	38.54	87.34	40.18	41.93	18.14	19.16	19.62	57.81
41	-5.04	19.58	78.14	24.11	32.77	22.07	15.25	-0.28	42.96
42	6.85	19.58	80.44	33.30	28.19	10.29	9.38	-1.94	38.01
43	-7.42	14.84	48.27	9.18	12.16	-3.46	-6.26	11.33	38.01
44	4.47	24.32	80.44	34.44	32.77	16.18	5.47	11.33	56.16
45	4.47	23.14	64.35	27.55	30.48	12.25	9.38	-1.94	33.06

TABLE D.2.3 - *continued*

SWP Graph	Si II	Si II	*Si II	Si II	Si II	Si II	Si II	*Si II	*Si II
ID	1260.4212	1264.7374	1304.37	1305.59	1309.2769	1526.7076	1533.432	1808.0117	1816.9796
46	3.88	29.06	85.04	35.59	28.19	12.25	15.25	14.64	51.21
47	6.85	33.80	80.44	41.33	39.64	22.07	15.25	30.39	62.76
48	-5.04	13.65	73.55	28.70	28.19	14.22	15.25	4.69	42.96
49	18.74	52.76	96.53	24.80	48.79	33.85	28.93	41.17	69.36
50	4.47	24.32	72.40	29.85	25.90	10.29	11.34	-0.28	42.96
51	13.99	26.69	80.44	43.63	32.77	14.22	11.34	27.91	67.71
52	27.07	36.17	78.14	18.37	39.64	27.96	21.11	22.93	66.06
53	11.61	13.65	78.14	39.04	28.19	20.11	17.20	11.33	44.61
54	4.47	13.65	73.55	20.67	23.61	8.33	-4.30	-1.94	44.61
55	30.64	26.69	71.25	13.78	32.77	14.22	9.38	14.64	59.46
56	27.07	21.95	72.40	6.89	48.79	22.07	19.16	22.93	61.11
57	6.85	40.91	56.31	18.37	46.50	14.22	3.52	27.91	49.56
58	3.88	16.02	58.61	16.07	30.48	4.40	1.56	6.35	57.81
59	-5.04	14.84	51.71	4.59	23.61	6.36	1.56	1.38	41.31



TABLE D.2.4 - OBSERVED SWP RADIAL VELOCITIES (km/s)

SWP Graph	Si III	Si III	Si III	Si III	Si III	Si III	Si IV	extra comp.	Si IV	extra comp
ID	1294.545	1296.726	1298.96	1301.149	1302.2	1303.323	1393.755		1402.77	
1	2.32	-6.01	-32.31	-13.59	-4.60	-0.69	-34.42		-10.69	
2	1.16	-3.70	-20.77	-18.20	-16.12	-12.19	-23.66		27.78	
3	1.16	-24.51	-33.47	-22.81	-29.93	-19.09	-15.06		2.14	
4	4.63	-15.26	-25.39	-27.42	-4.60	-21.39	-39.79		-49.15	
5	-15.05	-31.44	-41.54	-33.18	-31.08	-25.99	-23.66		2.14	
6	-15.05	-24.51	-36.93	-28.57	-3.45	-24.84	-46.25		-47.02	
7	-19.68	-41.85	-47.31	-34.33	-44.89	-42.09	-30.11		-32.06	
8	-22.00	-33.75	-48.47	-38.94	-39.14	-30.59	-33.34		-35.26	
9	-17.37	-33.75	-36.93	-35.48	-27.63	-29.44	-21.51		-3.21	
10	-22.00	-38.38	-47.31	-34.33	-35.68	-29.44	-29.04		-27.78	
11	-33.58	-48.78	-56.54	-48.15	-54.10	-51.29	-44.09		-23.51	
12	-28.95	-47.63	-62.31	-48.15	-55.25	-51.29	-37.64		-37.40	
13	-59.05	-74.21	-92.32	-75.80	-79.43	-76.60	-66.68		-68.39	
14	-45.16	-58.03	-76.16	-50.46	-57.55	-62.80	-44.09		-47.02	
15	-38.21	-54.56	-65.78	-52.76	-43.74	-51.29	-41.94		-36.33	
16	-26.63	-36.07	-60.01	-38.94	-40.29	-38.64	-41.94		-23.51	
17	-5.79	-17.57	-41.54	-22.81	-31.08	-30.59	-29.04		0.00	
18	12.74	-1.39	-24.23	-28.57	-9.21	-6.44	3.23		51.29	
19	-3.47	-10.63	-21.93	-6.68	-11.51	-8.74	-11.83		36.33	
20	54.42	33.29	16.16	23.27	17.27	29.21	35.49		68.39	
21	26.63	12.48	5.77	16.36	13.81	10.81	24.74		81.21	
22	52.11	35.60	18.46	26.73	16.12	22.31	37.64		57.70	
23	52.11	37.92	16.16	11.75	11.51	20.01	41.94		55.57	
24	45.16	30.98	23.08	32.49	19.57	22.31	44.09		47.02	
25	42.84	33.29	19.62	47.46	18.42	26.91	39.79		66.25	
26	55.58	35.60	20.77	30.18	18.42	31.51	50.55		91.90	
27	59.05	42.54	25.39	46.31	16.12	36.11	59.15		102.58	
28	54.42	28.67	13.85	25.58	12.66	24.61	33.34		27.78	
29	56.74	37.92	27.70	47.46	13.81	38.41	48.40		51.29	
30	44.00	30.98	20.77	41.70	6.91	43.01	41.94		37.40	
31	47.47	26.36	20.77	41.70	12.66	17.71	48.40		44.88	
32	28.95	5.55	6.92	12.90	0.00	24.61	39.79		38.47	
33	33.58	3.24	-6.92	7.14	2.30	-5.29	27.96		28.85	
34	24.32	14.80	0.00	0.23	4.60	22.31	22.59		0.00	
35	28.95		-3.46	2.53	-3.45	1.61	13.98		10.69	
36	13.89	-6.01	-20.77	-6.68	-10.36	-4.14	11.83		12.82	
37	15.05	7.86	0.00	0.23	0.00	-9.89	25.81		23.51	
38	38.21	28.67	-4.62	10.60	18.42	10.81	37.64		38.47	
39	12.74	-3.70	-16.16	-3.23	-9.21	-1.84	10.75		14.96	
40	45.16	-1.39	-13.85	12.90	1.15	3.91	10.75		38.47	
41	19.68	5.55	-9.23	0.23	-9.21	-4.14	22.59		19.23	
42	12.74	-4.86	-15.00	-4.38	-13.81	-8.74	5.38		11.75	
43	4.63	-15.26	-32.31	-10.14	-23.02	-8.74	5.38		19.23	
44	13.89	0.92	-12.69	-0.92	-2.30	6.21	16.13		12.82	
45	19.68	5.55	0.00	2.53	-13.81	-7.59	9.68		17.10	

TABLE D.2.4 - *continued*

SWP Graph	Si III	Si III	Si III	Si III	Si III	Si III	Si IV	extra comp.	Si IV	extra comp
ID	1294.545	1296.726	1298.96	1301.149	1302.2	1303.323	1393.755		1402.77	
46	23.16	3.24	-11.54	-3.23	2.30	7.36	16.13		19.23	
47	32.42	11.33	-13.85	5.99	0.00	10.81	-2.15		14.96	
48	17.37	3.24	8.08	4.84	-6.91	-4.14	8.60		14.96	
49	49.79	21.73	-9.23	11.75	23.02	38.41	30.11	100.02	57.70	
50	22.00	7.86	-13.85	-4.38	-9.21	3.91	21.51		19.23	
51	3.47	14.80	-9.23	4.84	-6.91	11.96	1.08		25.65	
52	35.90	14.80	6.92	11.75	9.21	16.56	23.02	94.64	47.02	
53	24.32	12.48	-3.46	7.14	-8.06	-5.29	-2.15		11.75	
54	17.37	4.39	-21.93	0.23	-11.51	1.61	-1.08		16.03	
55	31.26	10.17	-5.77	16.36	0.00	10.81	13.98	90.34	0.00	82.28
56	26.63	17.11	-5.77	0.23	4.60	8.51	23.66		38.47	
57	23.16	5.55	-8.08	-18.20	9.21	37.26	22.59		47.02	
58	5.79	0.92	-23.08	-6.68	-18.42	-6.44	-2.15		19.23	
59	24.32	0.92	-11.54	-5.53	-12.66	2.76	7.53	100.02	-17.10	82.28

TABLE D.2.5- OBSERVED LWP/LWR RADIAL VELOCITIES (km/s)

LWP/LWR	Fe	Fe	Fe	Fe	Mg	Mg	*Mg	Mg
Graph	II	II	II	II	II	II	II	II
ID	2586.65	2599.147	2600.173	2750.13	2791.6	2796.352	2798.823	2803.531
1	-4.64	-11.19	0.81	-20.71	-4.30	-2.89	-12.43	-2.25
2	-5.79	-3.11	6.57	-3.27	-2.15	5.15	-1.72	15.93
3	-15.07	-4.27	-5.53	-20.71	-15.03	-5.57	-31.17	-3.31
4	-4.64	-7.73	4.27	-20.71	-25.77	2.47	-17.79	-3.31
5	-4.06	-18.11	-28.59	-41.42	-35.44	-61.86	-44.56	-1.18
6	-24.34	-29.30	-22.25	-22.89	-22.55	-16.30	-23.14	-7.59
7	-19.70	-29.64	-21.10	-19.62	-22.02	-15.01	-23.14	-18.29
8	-5.22	-15.80	-7.26	-31.61	-23.63	-15.01	-28.50	-17.22
9	-18.54	-23.30	-17.64	-21.80	-19.33	-15.01	-21.86	-11.87
10	-24.34	-18.11	-18.79	-18.53	-27.92	-16.30	-23.14	-16.15
11	-38.25	-39.45	-45.31	-35.97	-42.96	-51.14	-52.60	-40.74
12	-31.29	-49.25	-34.94	-32.70	-37.59	-27.02	-25.82	-34.33
13	-41.72	-50.40	-45.31	-42.51	-49.94	-45.78	-44.56	-41.81
14	-27.82	-51.56	-36.09	-37.06	-57.99	-43.10	-60.63	-28.98
15	-37.09	-52.13	-38.39	-39.24	-53.70	-37.74	-44.56	-28.98
16	-3.48	-4.84	4.27	-2.18	-4.30	2.47	-1.72	9.52
17	4.64	7.27	22.71	5.45	3.22	7.83	10.28	12.73
18	19.70	17.07	26.17	25.07	22.02	23.91	22.38	38.39
19	31.29	20.53	34.24	39.24	31.14	26.59	30.42	30.90
20	26.66	19.95	19.25	9.81	21.48	18.55	14.35	22.35
21	42.30	48.79	50.96	46.87	48.33	37.31	42.41	29.83
22	39.41	46.48	43.47	54.51	46.18	39.99	43.81	45.87
23	52.15	49.94	46.93	54.51	52.62	48.03	62.55	49.08
24	46.36	40.14	40.01	46.87	45.10	45.35	41.13	46.94
25	30.71	23.41	26.75	27.25	22.55	26.59	25.06	33.04
26	17.62					26.59		28.77
27	17.38	19.95	21.56	19.62	20.40	15.87	14.35	26.63
28	15.07					26.59	22.38	27.70
29	20.28	17.65	23.87	25.07	17.18	26.59	18.63	35.18
30	17.38	11.30	21.56	20.71	18.26	26.59	17.03	28.77
31	23.18	23.41	26.17	28.34	23.63	27.87	30.42	31.97
32	18.54	17.07	22.71	17.44	10.74	23.91	17.03	31.97
33	15.65	9.92	15.80	19.62	18.26	21.23	14.35	31.97
34	26.66	18.80	26.17	23.98	23.63	27.87	22.38	39.46
35	16.23	7.84	14.64	16.35	10.74	13.19	8.99	22.35
36	24.34	19.38	23.87	21.80	22.55	26.05	19.70	28.77
37	26.08	30.91	28.48	27.25	19.33	26.59	19.70	34.11
38	21.44	18.22	20.41	20.71	15.03	15.87	19.70	26.63
39	19.70	28.60	28.48	8.72	23.63	26.59	27.74	18.07
40	24.92	19.95	23.87	21.80	24.70	17.15	19.70	26.63
41	28.40	19.38	25.60	29.43	19.33	18.55	19.70	28.77
42	23.18	16.49	16.95	15.81	15.03	7.83	25.06	22.35
43	13.91	16.49	15.80	10.90	21.48	5.15	17.03	11.66
44	-6.95	15.92	19.25	18.53	23.63	2.47	-1.72	7.38

## APPENDIX D.3

### Line Widths

TABLE D.3.1— SWP FWHM (Å) Al II, Al III

SWP Graph ID	Phase	Exposure ID	Time Group Labels	Al II 1670	Al III 1862			Al III 1854		
					Short ward Width	FWHM net	Long ward Width	Short ward Width	FWHM net	Long ward Width
2	0.0031	SWP03262	Sep-Nov'78	1.00	...	1.30	0.00	...	1.64	...
9	0.0816	SWP03303		0.86	...	1.24	0.00	...	1.22	0.24
21	0.6361	SWP02643		0.80	...	0.90	...	...	0.68	0.00
49	0.9669	SWP03298		1.10	...	1.36	0.42	...	1.27	0.13
52	0.9791	SWP03259		1.00	...	1.40	0.00	...	1.44	0.30
55	0.9874	SWP03260		0.98	...	1.42	0.46	...	1.54	0.50
59	0.9951	SWP03261		0.96	...	1.44	0.37	...	1.38	0.22
1	0.0015	SWP03772	Dec'78-Jan'79	0.92	0.18	0.85	...	0.21	0.91	...
16	0.3297	SWP03752		0.80	...	0.94	...	...	0.86	...
18	0.4927	SWP03818		0.73	...	0.84	...	...	0.66	...
27	0.7674	SWP03794		0.90	...	0.74	...	...	0.67	...
56	0.9880	SWP03771		0.82	0.19	0.93	...	...	1.72	...
4	0.0053	SWP07111	Nov'79	0.87	0.26	1.00	...	0.51	1.41	...
6	0.0183	SWP07112		0.97	...	1.04	...	...	0.96	...
57	0.9915	SWP07110		0.86	...	0.97	...	...	0.84	...
34	0.8904	SWP21452	Nov'83	0.90	...	0.44	...	...	0.81	...
36	0.9070	SWP21453		0.85	...	0.54	...	...	0.74	...
39	0.9218	SWP21454		0.85	0.11	0.73	...	...	0.85	...
42	0.9358	SWP21455		0.92	0.20	0.98	...	...	0.90	...
46	0.9571	SWP21456		0.98	0.19	0.99	...	...	0.82	...
50	0.9712	SWP21457		1.04	0.14	0.90	...	...	0.90	...
54	0.9797	SWP21458		1.14	0.13	0.93	...	...	0.92	...
12	0.1538	SWP22417	Mar'84	0.85	...	0.68	0.00	...	0.84	...
13	0.1625	SWP22418		0.81	...	0.72	0.00	...	0.80	...
38	0.9217	SWP22411		1.02	...	1.36	0.18	...	1.55	0.25
43	0.9388	SWP22439		1.02	...	1.56	0.32	...	1.65	0.55

TABLE D.3.1— (continued)

SWP Graph ID	Phase	Exposure ID	Time Group Labels	Al III 1862			Al III 1854			
				Al II 1670	Short ward Width	FWHM net	Long ward Width	Short ward Width	FWHM net	Long ward Width
33	0.8866	SWP26472	Jul'85	0.80	...	0.85	...	...	0.73	...
35	0.9009	SWP26473		0.85	...	0.98	...	...	0.82	...
37	0.9149	SWP26474		0.85	...	0.85	...	...	0.80	...
41	0.9299	SWP26475		0.84	0.07	0.93	...	...	0.92	...
45	0.9471	SWP26476		0.98	0.15	1.05	...	0.21	0.95	...
48	0.9636	SWP26477		0.93	0.21	0.95	...	0.23	0.97	...
53	0.9791	SWP26478		1.02	0.17	0.95	...	0.22	0.90	...
20	0.6326	SWP27781	Feb-Mar'86	0.88	...	1.22	...	0.25	1.09	...
22	0.6452	SWP27782		0.83	...	0.94	...	...	1.02	...
23	0.6522	SWP27783		0.85	...	0.98	...	...	1.17	...
24	0.6595	SWP27784		0.94	...	0.96	...	...	1.00	...
25	0.6704	SWP27785		0.88	...	1.04	...	...	1.06	...
26	0.6772	SWP27786		0.82	0.08	0.98	...	...	0.97	...
29	0.7869	SWP27830		0.82	0.18	1.12	...	0.19	1.19	...
30	0.8005	SWP27831		0.91	...	1.12	...	...	1.32	...
31	0.8075	SWP27832		0.91	0.09	0.99	...	...	1.30	...
3	0.0052	SWP36983	Sep'89	0.88	...	0.94	...	0.11	0.85	...
5	0.0141	SWP37019		0.82	...	0.82	...	...	0.74	...
7	0.0204	SWP36984		0.81	...	0.84	...	...	0.90	...
8	0.0378	SWP36985		0.87	...	0.84	...	...	0.80	...
10	0.0855	SWP37021		0.80	...	0.90	...	...	0.84	...
11	0.1317	SWP36989		0.76	...	0.76	...	...	0.76	...
14	0.1889	SWP36992		0.82	0.09	0.79	...	...	0.80	...
15	0.3209	SWP36996		0.81	...	0.84	...	...	0.80	...
17	0.4790	SWP37001		0.73	...	0.86	...	...	0.74	...
19	0.5454	SWP37003		0.74	...	0.84	...	...	0.74	...
28	0.7784	SWP37011		0.76	0.12	0.92	...	0.08	0.74	...
32	0.8813	SWP37014		0.86	0.25	1.10	...	0.30	1.14	...
40	0.9247	SWP37016		0.96	...	1.28	0.16	...	1.20	...
44	0.9397	SWP36979		1.03	...	1.20	...	...	1.14	...
47	0.9573	SWP36980		1.07	...	1.20	...	...	1.15	...
51	0.9777	SWP36981		1.05	...	1.21	0.11	...	1.18	...
58	0.9947	SWP36982		0.93	0.13	0.90	...	...	0.94	...

TABLE D.3.2— SWP FWHM (Å), C II, Fe II, Fe III, Si II, Si III

SWP Graph ID	Phase	Exposure ID	Time Group Labels	C II 1334	C II 1335	Fe II 1608	Fe III 1926	Si II 1533	Si III 1294
2	0.0031	SWP03262	Sep-Nov'78	0.80	1.44	0.45	0.85	1.12	0.56
9	0.0816	SWP03303		0.98	1.32	0.35	0.92	0.82	0.55
21	0.6361	SWP02643		0.76	1.04	0.45	0.96	0.64	0.56
49	0.9669	SWP03298		0.84	1.40	0.47	1.16	0.96	0.57
52	0.9791	SWP03259		0.88	1.30	0.37	1.00	0.93	0.61
55	0.9874	SWP03260		0.90	1.30	0.46	1.24	0.88	0.56
59	0.9951	SWP03261		0.88	1.35	0.44	0.93	1.01	0.58
1	0.0015	SWP03772	Dec'78-Jan'79	0.80	1.06	0.43	0.80	0.80	0.51
16	0.3297	SWP03752		0.88	1.02	0.42	0.96	0.68	0.44
18	0.4927	SWP03818		0.74	1.10	0.50	0.75	0.69	0.44
27	0.7674	SWP03794		0.80	1.08	0.59	0.80	0.72	0.50
56	0.9880	SWP03771		0.76	1.05	0.36	0.87	0.74	0.54
4	0.0053	SWP07111	Nov'79	0.88	0.94	0.40	1.00	0.88	0.46
6	0.0183	SWP07112		0.90	1.08	0.49	0.90	0.97	0.48
57	0.9915	SWP07110		0.94	0.92	0.55	0.92	0.98	0.55
34	0.8904	SWP21452	Nov'83	0.70	0.96	0.53	0.63	0.75	0.48
36	0.9070	SWP21453		0.82	0.94	0.49	0.80	0.76	0.51
39	0.9218	SWP21454		0.80	1.02	0.48	0.79	0.77	0.50
42	0.9358	SWP21455		0.94	1.04	0.57	0.84	0.82	0.50
46	0.9571	SWP21456		0.81	1.06	0.45	0.81	0.78	0.46
50	0.9712	SWP21457		0.88	1.14	0.41	0.84	0.90	0.48
54	0.9797	SWP21458		0.90	1.09	0.46	0.87	0.94	0.51
12	0.1538	SWP22417	Mar'84	0.92	1.02	0.47	0.78	0.77	0.44
13	0.1625	SWP22418		0.97	1.10	0.61	0.82	0.76	0.48
38	0.9217	SWP22411		0.92	1.37	0.60	1.00	0.94	0.54
43	0.9388	SWP22439		1.01	1.53	0.61	1.06	1.06	0.55

TABLE D.3.2— (continued)

SWP Graph ID	Phase	Exposure ID	Time Group Labels	C II 1334	C II 1335	Fe II 1608	Fe III 1926	Si II 1533	Si III 1294
33	0.8866	SWP26472	Jul'85	0.88	1.00	0.52	0.69	0.70	0.44
35	0.9009	SWP26473		0.74	0.98	0.49	0.82	0.84	0.50
37	0.9149	SWP26474		0.82	1.00	0.49	0.69	0.75	0.47
41	0.9299	SWP26475		0.84	1.05	0.60	1.00	0.84	0.47
45	0.9471	SWP26476		0.79	1.06	0.58	0.91	0.82	0.48
48	0.9636	SWP26477		0.72	1.11	0.41	0.83	0.74	0.52
53	0.9791	SWP26478		0.80	1.08	0.40	0.82	0.91	0.46
20	0.6326	SWP27781	Feb-Mar'86	0.92	1.00	0.61	0.73	0.69	0.53
22	0.6452	SWP27782		0.97	0.96	0.58	0.93	0.72	0.45
23	0.6522	SWP27783		0.80	1.20	0.55	0.80	0.77	0.51
24	0.6595	SWP27784		0.84	1.03	0.58	0.69	0.70	0.47
25	0.6704	SWP27785		0.68	1.18	0.68	0.91	0.78	0.48
26	0.6772	SWP27786		0.84	1.07	0.44	0.70	0.78	0.50
29	0.7869	SWP27830		1.05	1.12	0.40	0.93	0.76	0.49
30	0.8005	SWP27831		0.88	1.10	0.50	0.77	0.81	0.52
31	0.8075	SWP27832		1.04	1.14	0.45	0.86	0.77	0.51
3	0.0052	SWP36983	Sep'89	0.79	0.94	0.59	0.70	0.80	0.43
5	0.0141	SWP37019		0.84	0.95	0.49	0.71	0.90	0.40
7	0.0204	SWP36984		0.82	1.00	0.48	0.64	0.79	0.45
8	0.0378	SWP36985		0.82	1.00	0.47	0.69	0.76	0.47
10	0.0855	SWP37021		0.88	1.02	0.57	0.82	0.72	0.45
11	0.1317	SWP36989		0.94	0.94	0.45	0.86	0.76	0.47
14	0.1889	SWP36992		0.94	1.05	0.61	0.76	0.72	0.39
15	0.3209	SWP36996		0.90	0.98	0.70	0.71	0.66	0.53
17	0.4790	SWP37001		0.82	0.95	0.50	0.94	0.72	0.45
19	0.5454	SWP37003		0.72	1.04	0.57	1.06	0.64	0.46
28	0.7784	SWP37011		0.87	1.01	0.69	0.64	0.77	0.46
32	0.8813	SWP37014		0.84	1.20	0.50	1.01	0.81	0.54
40	0.9247	SWP37016		0.90	1.23	0.64	1.00	0.88	0.62
44	0.9397	SWP36979		0.86	1.24	0.50	0.91	0.95	0.48
47	0.9573	SWP36980		0.86	1.14	0.55	0.90	1.00	0.61
51	0.9777	SWP36981		0.80	1.20	0.52	0.84	0.82	0.54
58	0.9947	SWP36982		0.84	1.00	0.58	0.92	0.82	0.55

TABLE D.3.3— SWP FWHM (Å) Si IV

SWP Graph ID	Phase	Exposure ID	Time Group Labels	Si IV 1393			Si IV 1402		
				Short ward Width	FWHM net	Long ward Width	Short ward Width	FWHM net	Long ward Width
2	0.0031	SWP03262	Sep-Nov'78	...	1.43	...	...	1.35	...
9	0.0816	SWP03303		...	1.00	0.19	...	1.03	0.16
21	0.6361	SWP02643		...	0.62	...	...	0.84	...
49	0.9669	SWP03298		...	1.17	0.25	...	1.23	0.21
52	0.9791	SWP03259		...	1.57	0.36	...	1.32	0.22
55	0.9874	SWP03260		...	1.73	0.27	...	0.62	0.25
59	0.9951	SWP03261		...	1.42	0.21	...	0.64	0.18
1	0.0015	SWP03772	Dec'78-Jan'79	...	1.00	...	...	0.93	...
16	0.3297	SWP03752		...	0.90	...	...	0.66	0.12
18	0.4927	SWP03818		...	0.71	...	...	0.90	...
27	0.7674	SWP03794		...	0.48	...	...	0.61	...
56	0.9880	SWP03771		0.31	0.79	...	...	0.82	...
4	0.0053	SWP07111	Nov'79	...	0.96	...	...	0.91	...
6	0.0183	SWP07112		...	0.93	...	...	0.79	0.15
57	0.9915	SWP07110		...	1.25	...	...	0.85	...
34	0.8904	SWP21452	Nov'83	...	0.46	...	...	#N/A	...
36	0.9070	SWP21453		0.14	0.72	...	...	0.48	...
39	0.9218	SWP21454		...	0.65	...	...	0.54	...
42	0.9358	SWP21455		0.19	0.91	...	...	0.65	...
46	0.9571	SWP21456		...	0.78	...	...	0.70	...
50	0.9712	SWP21457		0.24	0.76	...	...	0.62	...
54	0.9797	SWP21458		0.29	0.99	...	...	0.75	...
12	0.1538	SWP22417	Mar'84	...	0.73	...	...	0.54	...
13	0.1625	SWP22418		0.10	0.71	...	...	0.60	0.10
38	0.9217	SWP22411		...	1.15	...	...	0.96	...
43	0.9388	SWP22439		...	1.85	0.54	...	1.86	0.65



TABLE D.3.3— (continued)

SWP Graph ID	Phase	Exposure ID	Time Group Labels	Si IV 1393			Si IV 1402		
				Short ward Width	FWHM net	Long ward Width	Short ward Width	FWHM net	Long ward Width
33	0.8866	SWP26472	Jul'85	...	0.66	...	...	0.67	...
35	0.9009	SWP26473		0.11	0.67	...	...	0.63	...
37	0.9149	SWP26474		0.11	0.69	...	...	0.62	...
41	0.9299	SWP26475		0.06	0.86	...	...	0.74	...
45	0.9471	SWP26476		0.23	0.81	...	0.15	0.77	...
48	0.9636	SWP26477		0.12	0.75	...	...	0.75	...
53	0.9791	SWP26478		...	0.80	...	...	0.66	...
20	0.6326	SWP27781	Feb-Mar'86	...	1.00	...	...	1.19	...
22	0.6452	SWP27782		0.11	0.85	...	...	1.00	...
23	0.6522	SWP27783		...	1.08	...	...	1.00	...
24	0.6595	SWP27784		...	0.90	...	...	0.95	...
25	0.6704	SWP27785		...	0.92	...	...	0.96	...
26	0.6772	SWP27786		...	0.93	...	...	0.89	...
29	0.7869	SWP27830		...	0.92	...	...	0.85	...
30	0.8005	SWP27831		...	1.00	...	...	0.79	0.17
31	0.8075	SWP27832		...	0.96	...	...	0.90	...
3	0.0052	SWP36983	Sep'89	...	0.76	...	...	0.95	...
5	0.0141	SWP37019		0.12	0.82	...	...	0.94	...
7	0.0204	SWP36984		0.15	0.69	...	...	0.81	0.15
8	0.0378	SWP36985		...	0.53	...	...	0.59	0.14
10	0.0855	SWP37021		...	0.68	...	...	0.65	0.07
11	0.1317	SWP36989		...	0.58	...	...	0.84	...
14	0.1889	SWP36992		...	0.82	...	...	0.66	0.12
15	0.3209	SWP36996		...	0.45	...	...	0.73	0.13
17	0.4790	SWP37001		0.09	0.60	...	...	0.60	...
19	0.5454	SWP37003		...	0.62	...	...	0.84	...
28	0.7784	SWP37011		...	0.68	...	...	0.60	...
32	0.8813	SWP37014		0.34	0.91	...	...	1.14	...
40	0.9247	SWP37016		...	1.26	...	...	1.21	...
44	0.9397	SWP36979		...	1.37	...	...	0.94	0.24
47	0.9573	SWP36980		...	1.34	...	...	1.07	0.38
51	0.9777	SWP36981		...	1.23	...	...	1.19	0.19
58	0.9947	SWP36982		0.15	0.83	...	...	1.20	...

TABLE D.3.4— LWP/LWR FWHM (Å) Mg II  $\lambda$ 2791, Mg II  $\lambda$ 2796

LWP/ LWR ID	Phase	Exposure ID	Time Group Labels	Mg II 2791				Mg II 2796		
				Fe II 2600 FWHM net	Short ward Width	FWHM net	Long ward Width	Short ward Width	FWHM net	Long ward Width
4	0.0049	LWR02856	Sep-Nov'78	0.95	...	1.16	...	0.42	1.39	...
8	0.0801	LWR02911		0.89	...	1.06	...	...	1.40	...
20	0.6520	LWR02345		0.91	...	1.10	...	...	1.08	...
39	0.9683	LWR02906		0.98	...	1.14	...	...	1.48	0.47
1	0.0030	LWR03350	Dec'78-Jan'79	1.17	...	1.26	0.20	0.41	1.21	...
14	0.3200	LWR03328		0.84	...	0.87	0.49	...	1.30	0.10
15	0.3280	LWR03329		1.13	...	1.30	...	...	1.35	...
17	0.4939	LWR03398		0.83	...	1.13	...	...	1.03	...
21	0.7685	LWR03374		0.95	...	1.00	...	...	1.23	0.18
43	0.9895	LWR03349		0.88	0.28	0.88	...	...	1.20	...
3	0.0034	LWR06047	Nov'79	0.83	...	1.00	...	0.53	1.38	...
5	0.0165	LWR06048		1.11	...	0.84	...	...	1.79	0.34
44	0.9901	LWR06046		0.45	...	0.80	...	0.18	0.98	...
26	0.8915	LWP02226	Nov'83	...	...	...	...	...	1.00	...
28	0.9082	LWP02227		...	...	...	...	...	1.10	...
30	0.9227	LWP02228		0.89	...	0.92	0.12	...	1.30	...
33	0.9367	LWP02229		0.95	...	0.98	...	...	1.53	...
36	0.9581	LWP02230		0.86	...	0.86	...	...	1.50	...
40	0.9721	LWP02231		0.83	0.07	0.89	...	...	1.60	...
11	0.1547	LWP02895	Mar'84	0.91	...	0.93	0.16	...	1.23	0.28
25	0.8878	LWP06484	Jul'85	0.82	...	0.94	...	...	1.28	...
27	0.9018	LWP06485		0.85	...	1.00	...	...	1.20	...
29	0.9166	LWP06486		0.73	0.14	0.80	...	...	1.25	...
32	0.9323	LWP06487		0.78	0.25	1.05	...	...	1.38	...
35	0.9488	LWP06488		0.89	0.16	1.02	...	...	1.40	...
38	0.9650	LWP06489		0.74	0.15	0.79	...	...	1.45	...
42	0.9801	LWP06490		0.82	0.18	0.82	...	0.25	1.70	...

TABLE D.3.4—(continued)

LWP/ LWR ID	Phase	Exposure ID	Time Group Labels	Fe II 2600 FWHM net	Mg II 2791			Mg II 2796		
					Short ward Width	FWHM net	Long ward Width	Short ward Width	FWHM net	Long ward Width
19	0.6343	LWP07717	Feb-Mar'86	0.78	...	0.84	...	...	1.20	...
23	0.7884	LWP07738		0.80	...	0.80	...	...	1.32	0.32
2	0.0034	LWP16323	Sep'89	1.00	...	0.90	...	0.33	1.28	...
6	0.0220	LWP16324		0.91	...	0.80	...	...	1.50	...
7	0.0390	LWP16325		0.90	...	0.67	...	...	1.48	...
9	0.0867	LWP16356		0.99	...	0.90	...	...	1.35	...
10	0.1303	LWP16327		0.75	...	0.70	...	...	1.33	...
12	0.1903	LWP16329		0.98	0.19	0.93	...	...	1.30	0.30
13	0.3196	LWP16333		0.85	0.28	0.90	...	...	1.26	0.16
16	0.4778	LWP16338		0.80	...	1.00	...	...	1.18	...
18	0.5463	LWP16340		0.75	...	0.98	...	...	1.05	...
22	0.7798	LWP16347		0.73	...	0.86	0.22	...	1.20	0.20
24	0.8825	LWP16350		0.80	...	1.02	0.32	...	1.35	...
31	0.9259	LWP16352		0.88	...	1.14	...	...	1.50	...
34	0.9409	LWP16320		0.86	...	1.00	...	...	1.53	...
37	0.9590	LWP16321		0.76	...	0.88	...	...	1.50	...
41	0.9794	LWP16322		0.95	0.12	0.96	...	...	1.68	0.15

TABLE D.3.5— LWP/LWR FWHM (Å) Mg II  $\lambda$ 2798, Mg II  $\lambda$ 2803

LWP/ LWR ID	Phase	Exposure ID	Time Group Labels	Mg II 2798			Mg II 2803		
				Short ward Width	FWHM net	Long ward Width	Short ward Width	FWHM net	Long ward Width
4	0.0049	LWR02856	Sep-Nov'78	...	0.70	...	0.24	1.35	...
8	0.0801	LWR02911		...	0.75	...	...	1.43	...
20	0.6520	LWR02345		...	0.60	...	...	0.91	...
39	0.9683	LWR02906		...	0.80	...	...	1.63	0.27
1	0.0030	LWR03350	Dec'78-Jan'79	0.13	0.83	...	0.10	1.27	...
14	0.3200	LWR03328		...	0.85	0.35	...	1.28	...
15	0.3280	LWR03329		...	0.71	...	...	1.41	...
17	0.4939	LWR03398		...	0.65	...	...	0.97	...
21	0.7685	LWR03374		...	0.73	...	...	1.15	0.50
43	0.9895	LWR03349		...	0.68	...	...	1.02	...
3	0.0034	LWR06047	Nov'79	...	0.91	...	0.37	1.33	...
5	0.0165	LWR06048		...	0.89	0.19	0.21	0.93	...
44	0.9901	LWR06046		...	0.45	...	0.08	0.38	...
26	0.8915	LWP02226	Nov'83	...	...	...	...	1.05	...
28	0.9082	LWP02227		...	0.65	...	...	1.05	...
30	0.9227	LWP02228		...	0.90	...	...	1.06	...
33	0.9367	LWP02229		...	0.93	...	0.23	1.35	...
36	0.9581	LWP02230		...	0.80	...	...	1.35	...
40	0.9721	LWP02231		...	0.79	...	...	1.38	...
11	0.1547	LWP02895	Mar'84	...	0.77	0.06	...	1.24	0.16
25	0.8878	LWP06484	Jul'85	...	0.85	...	...	0.94	...
27	0.9018	LWP06485		...	0.90	...	...	1.13	...
29	0.9166	LWP06486		...	0.73	...	...	1.02	...
32	0.9323	LWP06487		...	0.87	...	...	1.13	...
35	0.9488	LWP06488		...	0.95	...	0.06	1.21	...
38	0.9650	LWP06489		...	0.80	...	...	1.31	...
42	0.9801	LWP06490		0.20	0.80	...	0.25	1.56	...

TABLE D.3.5—(continued)

LWP/ LWR ID	Phase	Exposure ID	Time Group Labels	Mg II 2798			Mg II 2803		
				Short ward Width	FWHM net	Long ward Width	Short ward Width	FWHM net	Long ward Width
19	0.6343	LWP07717	Feb-Mar'86	...	0.90	...	...	0.99	0.29
23	0.7884	LWP07738		...	0.75	...	...	1.17	0.33
2	0.0034	LWP16323	Sep'89	...	0.85	...	...	1.20	...
6	0.0220	LWP16324		...	0.71	...	...	1.40	...
7	0.0390	LWP16325		...	0.70	...	...	1.21	0.25
9	0.0867	LWP16356		...	0.80	...	...	1.18	0.18
10	0.1303	LWP16327		...	0.70	...	...	1.13	0.18
12	0.1903	LWP16329		...	1.00	...	...	1.17	0.29
13	0.3196	LWP16333		...	0.80	...	...	1.15	0.21
16	0.4778	LWP16338		...	0.98	...	...	1.10	...
18	0.5463	LWP16340		...	0.91	...	...	0.90	...
22	0.7798	LWP16347		...	0.75	...	...	0.92	0.16
24	0.8825	LWP16350		...	1.03	...	...	1.15	...
31	0.9259	LWP16352		...	1.10	...	...	1.17	...
34	0.9409	LWP16320		...	1.18	...	0.15	1.35	...
37	0.9590	LWP16321		...	0.95	...	...	1.42	...
41	0.9794	LWP16322		...	0.93	...	...	1.32	...

# APPENDIX D.4

## Residual Intensities

TABLE D.4.1 - SWP Residual Intensities

SWP Graph ID	Phase	Time Group Labels	Al II 1670	Al III 1862	Al III 1854	C II 1334	C II 1335	Fe III 1926	Si II 1533	Si III 1294	Si IV 1393	Si IV 1402
2	0.0031	Sep-Nov'78	-0.01	0.38	0.33	0.18	0.19	0.50	0.23	0.47	0.35	0.50
9	0.0816		0.07	0.28	0.21	0.20	0.18	0.46	0.18	0.35	0.28	0.35
21	0.6361		0.09	0.55	0.46	0.21	0.16	0.67	0.21	0.39	0.69	0.80
49	0.9669		-0.03	0.25	0.21	0.15	0.16	0.34	0.09	0.37	0.25	0.33
52	0.9791		0.03	0.34	0.27	0.18	0.17	0.45	0.15	0.37	0.30	0.40
55	0.9874		0.08	0.38	0.34	0.16	0.16	0.49	0.12	0.42	0.37	0.49
59	0.9951		0.03	0.41	0.32	0.26	0.18	0.50	0.16	0.45	0.43	0.53
1	0.0015	Dec'78-Jan'79	0.08	0.48	0.42	0.19	0.15	0.61	0.13	0.46	0.49	0.72
16	0.3297		0.13	0.54	0.44	0.25	0.22	0.63	0.18	0.42	0.56	0.72
18	0.4927		0.13	0.52	0.47	0.18	0.18	0.64	0.18	0.45	0.59	0.79
27	0.7674		0.18	0.55	0.47	0.19	0.16	0.62	0.18	0.41	0.58	0.80
56	0.9880		0.09	0.46	0.44	0.19	0.17	0.61	0.12	0.45	0.55	0.78
4	0.0053	Nov'79	0.11	0.43	0.57	0.22	0.19	0.58	0.10	0.35	0.43	0.58
6	0.0183		0.03	0.35	0.27	0.20	0.20	0.53	0.15	0.37	0.32	0.43
57	0.9915		0.00	0.38	0.41	0.23	0.19	0.41	0.16	0.39	0.48	0.55
34	0.8904	Nov'83	0.04	0.64	0.22	0.19	0.16	0.54	0.13	0.37	0.39	1.00
36	0.9070		0.08	0.44	0.27	0.19	0.15	0.50	0.16	0.32	0.32	0.44
39	0.9218		0.03	0.34	0.27	0.18	0.15	0.49	0.14	0.34	0.32	0.41
42	0.9358		0.03	0.30	0.21	0.20	0.14	0.48	0.13	0.33	0.29	0.39
46	0.9571		0.00	0.29	0.20	0.16	0.13	0.50	0.10	0.34	0.26	0.39
50	0.9712		0.02	0.28	0.22	0.15	0.14	0.48	0.11	0.34	0.30	0.40
54	0.9797		0.06	0.31	0.23	0.15	0.13	0.53	0.14	0.39	0.30	0.43
12	0.1538	Mar'84	0.08	0.39	0.30	0.19	0.17	0.55	0.17	0.40	0.39	0.46
13	0.1625		0.10	0.46	0.27	0.20	0.18	0.60	0.21	0.36	0.42	0.54
38	0.9217		0.03	0.22	0.19	0.18	0.15	0.41	0.17	0.36	0.19	0.33
43	0.9388		0.02	0.23	0.16	0.20	0.16	0.40	0.16	0.34	0.25	0.29
33	0.8866	Jul'85	0.08	0.35	0.25	0.17	0.16	0.53	0.19	0.40	0.35	0.47
35	0.9009		0.01	0.31	0.26	0.16	0.13	0.55	0.19	0.43	0.33	0.42
37	0.9149		0.04	0.29	0.22	0.14	0.12	0.48	0.18	0.39	0.30	0.44
41	0.9299		0.03	0.27	0.22	0.14	0.11	0.47	0.16	0.36	0.31	0.39
45	0.9471		0.05	0.24	0.18	0.15	0.13	0.48	0.16	0.40	0.28	0.37
48	0.9636		0.03	0.23	0.15	0.15	0.11	0.45	0.10	0.33	0.24	0.30
53	0.9791		0.02	0.21	0.16	0.16	0.13	0.46	0.16	0.37	0.24	0.30
20	0.6326	Feb-Mar'86	0.12	0.51	0.44	0.27	0.20	0.57	0.12	0.48	0.51	0.62
22	0.6452		0.11	0.46	0.39	0.24	0.19	0.61	0.17	0.47	0.45	0.65
23	0.6522		0.17	0.46	0.41	0.23	0.21	0.67	0.23	0.43	0.50	0.62
24	0.6595		0.14	0.43	0.39	0.24	0.18	0.56	0.13	0.39	0.47	0.59
25	0.6704		0.09	0.45	0.38	0.26	0.20	0.59	0.17	0.45	0.45	0.60

TABLE D.4.1 - *continued*

SWP Graph ID	Phase Time Group Labels	Al II 1670	Al III 1862	Al III 1854	C II 1334	C II 1335	Fe III 1926	Si II 1533	Si III 1294	Si IV 1393	Si IV 1402
26	0.6772	0.11	0.41	0.39	0.24	0.19	0.65	0.16	0.42	0.48	0.59
29	0.7869	0.13	0.37	0.31	0.21	0.17	0.48	0.20	0.41	0.38	0.46
30	0.8005	0.14	0.30	0.28	0.21	0.18	0.45	0.17	0.41	0.34	0.43
31	0.8075	0.14	0.30	0.26	0.22	0.17	0.50	0.18	0.41	0.37	0.41
3	0.0052 Sep'89	-0.02	0.41	0.28	0.19	0.16	0.56	0.08	0.35	0.43	0.54
5	0.0141	0.05	0.43	0.35	0.14	0.13	0.56	0.17	0.30	0.51	0.62
7	0.0204	-0.05	0.30	0.24	0.18	0.14	0.55	0.07	0.39	0.39	0.50
8	0.0378	-0.03	0.26	0.19	0.16	0.13	0.48	0.02	0.29	0.25	0.45
10	0.0855	0.08	0.33	0.24	0.13	0.13	0.52	0.13	0.37	0.35	0.45
11	0.1317	0.07	0.45	0.35	0.18	0.15	0.63	0.17	0.31	0.51	0.63
14	0.1889	0.08	0.50	0.44	0.20	0.17	0.66	0.10	0.36	0.62	0.67
15	0.3209	0.09	0.52	0.46	0.19	0.15	0.63	0.21	0.34	0.67	0.70
17	0.4790	0.09	0.52	0.44	0.18	0.15	0.63	0.11	0.39	0.65	0.72
19	0.5454	0.09	0.49	0.44	0.17	0.13	0.69	0.10	0.40	0.61	0.76
28	0.7784	0.13	0.52	0.42	0.22	0.18	0.57	0.12	0.44	0.66	0.72
32	0.8813	0.03	0.29	0.24	0.16	0.16	0.47	0.08	0.39	0.37	0.40
40	0.9247	0.08	0.32	0.25	0.14	0.12	0.50	0.18	0.37	0.34	0.39
44	0.9397	0.07	0.31	0.24	0.13	0.15	0.43	0.17	0.36	0.29	0.36
47	0.9573	0.04	0.30	0.22	0.14	0.13	0.46	0.14	0.31	0.28	0.35
51	0.9777	0.03	0.33	0.25	0.15	0.13	0.48	0.10	0.37	0.30	0.42
58	0.9947	0.06	0.39	0.31	0.13	0.12	0.61	0.15	0.37	0.39	0.49

TABLE D.4.2  
LWP/LWR Residual Intensities

LWPR Graph ID	Phase	Time Group Labels	Mg II 2790	Mg II 2795	Mg II 2797	Mg II 2802
4	0.0049	Sep-Nov'78	0.52	0.92	0.63	0.26
8	0.0801		0.53	0.23	0.62	0.26
20	0.6520		0.62	0.30	0.68	0.36
39	0.9683		0.52	0.16	0.63	0.18
1	0.0030	Dec'78-Jan'79	0.60	0.23	0.73	0.29
14	0.3200		0.70	0.37	0.70	0.43
15	0.3280		0.59	0.40	0.71	0.43
17	0.4939		0.61	0.31	0.66	0.40
21	0.7685		0.62	0.34	0.73	0.45
43	0.9895		0.63	0.25	0.61	0.30
3	0.0034	Nov'79	0.66	0.27	0.75	0.28
5	0.0165		0.57	0.15	0.56	0.24
44	0.9901		0.67	0.11	0.61	0.38
26	0.8915	Nov'83	1.00	0.19	1.00	0.18
28	0.9082		1.00	0.18	0.64	0.18
30	0.9227		0.59	0.15	0.57	0.17
33	0.9367		0.61	0.13	0.59	0.14
36	0.9581		0.59	0.14	0.56	0.10
40	0.9721		0.56	0.15	0.56	0.13
11	0.1547	Mar'84	0.73	0.27	0.67	0.25
25	0.8878	Jul'85	0.77	0.19	0.64	0.17
27	0.9018		0.72	0.18	0.62	0.23
29	0.9166		0.65	0.15	0.59	0.13
32	0.9323		0.67	0.14	0.59	0.14
35	0.9488		0.68	0.12	0.57	0.12
38	0.9650		0.60	0.09	0.51	0.11
42	0.9801		0.59	0.12	0.55	0.11
19	0.6343	Feb-Mar'86	0.74	0.58	0.65	0.39
23	0.7884		0.67	0.28	0.63	0.41
2	0.0034	Sep'89	0.67	0.25	0.61	0.32
6	0.0220		0.65	0.22	0.53	0.30
7	0.0390		0.62	0.22	0.54	0.21
9	0.0867		0.69	0.18	0.55	0.21
10	0.1303		0.66	0.33	0.66	0.34
12	0.1903		0.70	0.39	0.72	0.45
13	0.3196		0.74	0.37	0.68	0.43
16	0.4778		0.69	0.36	0.66	0.44
18	0.5463		0.73	0.28	0.65	0.40
22	0.7798		0.71	0.33	0.66	0.42
24	0.8825		0.64	0.20	0.60	0.28
31	0.9259		0.66	0.16	0.56	0.26
34	0.9409		0.63	0.16	0.55	0.22
37	0.9590		0.62	0.15	0.57	0.20
41	0.9794		0.62	0.19	0.57	0.26



## APPENDIX D.5

### Equivalent Widths

TABLE D.5.1— SWP EQUIVALENT WIDTHS

SWP ID	Phase	Exposure ID	Time Group Labels	Al II 1670	Al III 1862	Al III 1854	C II 1334	C II 1335	Fe II 1608	Fe III 1926	Si II 1533	Si III 1294	Si IV 1393	Si IV 1402
2	0.0031	SWP03262	Sep—	1.07	0.86	1.17	0.70	1.24	0.21	0.46	0.92	0.32	0.98	0.72
9	0.0816	SWP03303	Nov'78	0.85	0.95	1.03	0.83	1.16	0.15	0.53	0.72	0.38	0.77	0.71
21	0.6361	SWP02643		0.78	0.43	0.39	0.64	0.93	0.17	0.33	0.54	0.37	0.21	0.18
49	0.9669	SWP03298		1.21	1.09	1.07	0.76	1.25	0.25	0.81	0.93	0.38	0.94	0.88
52	0.9791	SWP03259		1.04	0.99	1.12	0.76	1.15	0.20	0.59	0.84	0.41	1.16	0.84
55	0.9874	SWP03260		0.96	0.94	1.08	0.80	1.16	0.22	0.68	0.83	0.35	1.16	0.55
59	0.9951	SWP03261		0.99	0.91	1.00	0.69	1.18	0.22	0.49	0.90	0.34	0.86	0.47
1	0.0015	SWP03772	Dec'78—	0.91	0.47	0.56	0.69	0.96	0.18	0.34	0.74	0.29	0.54	0.28
16	0.3297	SWP03752	Jan'79	0.74	0.46	0.51	0.70	0.85	0.16	0.38	0.60	0.27	0.42	0.19
18	0.4927	SWP03818		0.68	0.43	0.38	0.64	0.96	0.21	0.29	0.60	0.26	0.31	0.20
27	0.7674	SWP03794		0.78	0.36	0.38	0.69	0.97	0.26	0.32	0.63	0.31	0.21	0.13
56	0.9880	SWP03771		0.79	0.53	1.02	0.65	0.93	0.17	0.37	0.70	0.31	0.38	0.19
4	0.0053	SWP07111	Nov'79	0.82	0.61	0.65	0.73	0.81	0.16	0.45	0.84	0.32	0.58	0.41
6	0.0183	SWP07112		1.00	0.72	0.74	0.76	0.92	0.19	0.45	0.88	0.32	0.68	0.48
57	0.9915	SWP07110		0.91	0.64	0.53	0.77	0.79	0.27	0.58	0.88	0.36	0.69	0.41
34	0.8904	SWP21452	Nov'83	0.92	0.17	0.67	0.60	0.86	0.23	0.31	0.69	0.32	0.30	...
36	0.9070	SWP21453		0.83	0.32	0.58	0.70	0.85	0.24	0.42	0.68	0.37	0.52	0.28
39	0.9218	SWP21454		0.87	0.51	0.66	0.70	0.92	0.24	0.43	0.70	0.35	0.47	0.34
42	0.9358	SWP21455		0.95	0.73	0.76	0.80	0.95	0.29	0.47	0.76	0.36	0.69	0.42
46	0.9571	SWP21456		1.04	0.75	0.70	0.72	0.99	0.24	0.43	0.75	0.33	0.61	0.46
50	0.9712	SWP21457		1.09	0.69	0.75	0.80	1.05	0.22	0.47	0.85	0.34	0.57	0.40
54	0.9797	SWP21458		1.14	0.68	0.75	0.81	1.00	0.24	0.44	0.86	0.33	0.74	0.46
12	0.1538	SWP22417	Mar'84	0.83	0.44	0.62	0.79	0.90	0.20	0.37	0.68	0.28	0.47	0.31
13	0.1625	SWP22418		0.78	0.41	0.63	0.82	0.96	0.26	0.35	0.64	0.33	0.44	0.30
38	0.9217	SWP22411		1.05	1.13	1.33	0.80	1.24	0.27	0.63	0.83	0.37	0.99	0.68
43	0.9388	SWP22439		1.07	1.28	1.48	0.86	1.37	0.31	0.67	0.95	0.38	1.47	1.40
33	0.8866	SWP26472	Jul'85	0.79	0.59	0.59	0.78	0.89	0.20	0.35	0.60	0.28	0.45	0.38
35	0.9009	SWP26473		0.90	0.72	0.65	0.66	0.90	0.21	0.39	0.72	0.30	0.48	0.39
37	0.9149	SWP26474		0.87	0.65	0.66	0.75	0.94	0.21	0.38	0.66	0.30	0.51	0.37
41	0.9299	SWP26475		0.86	0.72	0.76	0.77	0.99	0.27	0.56	0.75	0.32	0.63	0.48
45	0.9471	SWP26476		0.99	0.85	0.83	0.71	0.99	0.26	0.50	0.74	0.30	0.61	0.52
48	0.9636	SWP26477		0.96	0.78	0.87	0.65	1.05	0.23	0.49	0.71	0.37	0.60	0.55
53	0.9791	SWP26478		1.06	0.80	0.80	0.71	1.00	0.21	0.47	0.81	0.31	0.64	0.49

TABLE D.5.1— (continued)

SWP ID	Phase	Exposure ID	Time Group Labels	Al II 1670	Al III 1862	Al III 1854	C II 1334	C II 1335	Fe II 1608	Fe III 1926	Si II 1533	Si III 1294	Si IV 1393	Si IV 1402
20	0.6326	SWP27781	Feb—	0.83	0.64	0.65	0.72	0.85	0.28	0.33	0.65	0.29	0.52	0.49
22	0.6452	SWP27782	Mar'86	0.79	0.54	0.66	0.79	0.82	0.22	0.39	0.64	0.26	0.50	0.37
23	0.6522	SWP27783		0.75	0.57	0.73	0.66	1.01	0.20	0.28	0.63	0.31	0.57	0.41
24	0.6595	SWP27784		0.86	0.58	0.65	0.68	0.89	0.25	0.32	0.65	0.30	0.51	0.42
25	0.6704	SWP27785		0.85	0.61	0.70	0.54	1.00	0.35	0.40	0.69	0.28	0.54	0.40
26	0.6772	SWP27786		0.78	0.62	0.63	0.68	0.92	0.19	0.26	0.69	0.31	0.51	0.39
29	0.7869	SWP27830		0.76	0.75	0.88	0.88	0.99	0.15	0.52	0.65	0.31	0.61	0.49
30	0.8005	SWP27831		0.83	0.83	1.01	0.74	0.96	0.24	0.45	0.72	0.33	0.71	0.48
31	0.8075	SWP27832		0.83	0.73	1.03	0.87	1.00	0.18	0.46	0.67	0.32	0.64	0.57
3	0.0052	SWP36983	Sep'89	0.95	0.59	0.65	0.68	0.84	0.29	0.33	0.79	0.30	0.46	0.47
5	0.0141	SWP37019		0.83	0.50	0.51	0.77	0.88	0.23	0.33	0.80	0.30	0.43	0.38
7	0.0204	SWP36984		0.91	0.62	0.73	0.72	0.91	0.27	0.30	0.78	0.29	0.44	0.43
8	0.0378	SWP36985		0.96	0.66	0.69	0.73	0.93	0.31	0.38	0.80	0.36	0.43	0.35
10	0.0855	SWP37021		0.79	0.64	0.68	0.81	0.95	0.29	0.42	0.67	0.30	0.47	0.38
11	0.1317	SWP36989		0.75	0.45	0.53	0.82	0.85	0.20	0.34	0.67	0.35	0.31	0.33
14	0.1889	SWP36992		0.81	0.42	0.47	0.80	0.93	0.26	0.27	0.69	0.27	0.33	0.23
15	0.3209	SWP36996		0.78	0.43	0.46	0.77	0.89	0.27	0.28	0.55	0.37	0.16	0.23
17	0.4790	SWP37001		0.71	0.44	0.44	0.71	0.86	0.21	0.37	0.68	0.29	0.22	0.18
19	0.5454	SWP37003		0.71	0.46	0.44	0.64	0.96	0.34	0.35	0.61	0.29	0.26	0.22
28	0.7784	SWP37011		0.70	0.47	0.45	0.72	0.89	0.33	0.29	0.72	0.28	0.25	0.18
32	0.8813	SWP37014		0.88	0.83	0.93	0.75	1.07	0.30	0.57	0.79	0.35	0.61	0.73
40	0.9247	SWP37016		0.94	0.93	0.96	0.82	1.15	0.29	0.54	0.77	0.42	0.88	0.79
44	0.9397	SWP36979		1.02	0.88	0.92	0.79	1.13	0.25	0.55	0.84	0.33	1.04	0.63
47	0.9573	SWP36980		1.09	0.89	0.95	0.78	1.06	0.29	0.52	0.91	0.45	1.03	0.73
51	0.9777	SWP36981		1.09	0.86	0.94	0.72	1.12	0.27	0.47	0.78	0.36	0.91	0.74
58	0.9947	SWP36982		0.93	0.58	0.69	0.77	0.94	0.28	0.38	0.74	0.37	0.54	0.65

TABLE D.5.2— LWP/LWR EQUIVALENT WIDTHS

LWP/ LWR ID	Phase	Exposure ID	Time Group Labels	Fe II 2600	Mg II 2791	Mg II 2796	Mg II 2798	Mg II 2803
4	0.0049	LWR02856	Sep-Nov'78	0.63	0.59	1.18	0.28	1.06
8	0.0801	LWR02911		0.54	0.53	1.15	0.30	1.14
20	0.6520	LWR02345		0.49	0.44	0.80	0.21	0.62
39	0.9683	LWR02906		0.65	0.59	1.32	0.32	1.43
1	0.0030	LWR03350	Dec'78-Jan'79	0.68	0.53	0.99	0.24	0.97
14	0.3200	LWR03328		0.33	0.28	0.87	0.27	0.78
15	0.3280	LWR03329		0.54	0.57	0.87	0.22	0.86
17	0.4939	LWR03398		0.45	0.46	0.75	0.23	0.62
21	0.7685	LWR03374		0.53	0.40	0.86	0.21	0.67
43	0.9895	LWR03349		0.49	0.35	0.96	0.28	0.76
3	0.0034	LWR06047	Nov'79	0.46	0.37	1.07	0.25	1.02
5	0.0165	LWR06048		0.66	0.39	1.62	0.41	1.40
44	0.9901	LWR06046		0.29	0.59	0.93	0.19	0.79
26	0.8915	LWP02226	Nov'83	...	...	0.86	...	0.92
28	0.9082	LWP02227		...	...	0.96	0.25	0.92
30	0.9227	LWP02228		0.56	0.41	1.17	0.41	0.93
33	0.9367	LWP02229		0.65	0.41	1.40	0.40	1.24
36	0.9581	LWP02230		0.60	0.37	1.37	0.38	1.29
40	0.9721	LWP02231		0.58	0.45	1.45	0.37	1.27
11	0.1547	LWP02895	Mar'84	0.44	0.26	0.95	0.27	0.98
25	0.8878	LWP06484	Jul'85	0.45	0.23	1.09	0.33	0.83
27	0.9018	LWP06485		0.50	0.29	1.04	0.36	0.92
29	0.9166	LWP06486		0.43	0.30	1.13	0.31	0.94
32	0.9323	LWP06487		0.49	0.37	1.26	0.38	1.04
35	0.9488	LWP06488		0.54	0.34	1.31	0.43	1.14
38	0.9650	LWP06489		0.51	0.36	1.41	0.41	1.24
42	0.9801	LWP06490		0.57	0.36	1.60	0.39	1.48
19	0.6343	LWP07717	Feb-Mar'86	0.36	0.23	0.84	0.33	0.65
23	0.7884	LWP07738		0.40	0.28	1.01	0.30	0.74
2	0.0034	LWP16323	Sep'89	0.54	0.32	1.02	0.36	0.88
6	0.0220	LWP16324		0.56	0.30	1.24	0.36	1.05
7	0.0390	LWP16325		0.55	0.27	1.22	0.34	1.02
9	0.0867	LWP16356		0.59	0.30	1.18	0.38	1.00
10	0.1303	LWP16327		0.38	0.25	0.95	0.26	0.80
12	0.1903	LWP16329		0.44	0.29	0.85	0.30	0.69
13	0.3196	LWP16333		0.40	0.24	0.84	0.28	0.70
16	0.4778	LWP16338		0.38	0.33	0.81	0.36	0.65
18	0.5463	LWP16340		0.41	0.28	0.80	0.34	0.57
22	0.7798	LWP16347		0.37	0.27	0.86	0.27	0.56
24	0.8825	LWP16350		0.49	0.39	1.15	0.44	0.88
31	0.9259	LWP16352		0.53	0.41	1.33	0.51	0.93
34	0.9409	LWP16320		0.57	0.39	1.37	0.57	1.12
37	0.9590	LWP16321		0.48	0.36	1.35	0.43	1.21
41	0.9794	LWP16322		0.61	0.41	1.45	0.42	1.04

## APPENDIX D.6

### Difference Spectra Results and Ion Column Densities

TABLE D.6.1

Line	$f_{ik}$	Lab Wavelength
Mg II 2796	6.08E-01	2796.352
Mg II 2803	3.03E-01	2803.531

TABLE D.6.2 - Mg II 2796

Pair ID	far Left A	FWHM	Depth	Eq. Width	Ni, atoms along l.o.s	Vrad	Left Width (km/s)	Right Width (km/s)	Inner Left B	FWHM	Depth	Eq. Width	Ni, atoms along l.o.s	Vrad	Left Width (km/s)	Right Width (km/s)
1	2794.72	0.40	0.250	0.21	4.90E+12	-175.0	61.6	21.4	2795.45	0.70	0.365	0.27	6.46E+12	-96.7	37.5	37.5
2									2795.43	0.65	0.199	0.14	3.27E+12	-98.8	34.8	34.8
3	2794.82	0.59	0.355	0.39	9.29E+12	-164.2	79.3	31.6	2795.67	0.78	0.400	0.33	7.89E+12	-73.1	41.8	41.8
4	2794.53	0.60	0.360	0.44	1.06E+13	-195.3	92.2	32.2	2795.44	1.00	0.460	0.49	1.16E+13	-97.8	53.6	53.6
5	2794.92	0.25	0.400	0.24	5.72E+12	-153.5	47.2	13.4	2795.48	0.85	0.575	0.52	1.24E+13	-93.5	45.6	45.6
6									2795.64	0.70	0.285	0.21	5.05E+12	-76.3	37.5	37.5
7									2795.78	0.70	0.230	0.17	4.07E+12	-61.3	37.5	37.5
8									2795.77	0.75	0.260	0.27	6.41E+12	-62.4	64.3	40.2
9									2796.00	0.60	0.115	0.07	1.75E+12	-37.7	32.2	32.2
10									2796.35	0.00	0.00	0.00	0.00E+00	0.0	0.0	0.0
11									2795.62	0.80	0.162	0.14	3.28E+12	-78.5	42.9	42.9
12									2796.35	0.00	0.00	0.00	0.00E+00	0.0	0.0	0.0
13									2796.35	0.00	0.00	0.00	0.00E+00	0.0	0.0	0.0
14									2795.58	0.60	0.180	0.11	2.73E+12	-82.8	32.2	32.2
15									2795.44	0.70	0.230	0.17	4.07E+12	-97.8	37.5	37.5
16									2796.35	0.00	0.00	0.00	0.00E+00	0.0	0.0	0.0
17									2796.35	0.00	0.00	0.00	0.00E+00	0.0	0.0	0.0
18									2796.35	0.00	0.00	0.00	0.00E+00	0.0	0.0	0.0
19									2796.35	0.00	0.00	0.00	0.00E+00	0.0	0.0	0.0
20									2795.60	0.79	0.172	0.14	3.44E+12	-80.6	42.3	42.3
21									2795.73	0.59	0.108	0.07	1.61E+12	-66.7	31.6	31.6
22									2796.35	0.00	0.00	0.00	0.00E+00	0.0	0.0	0.0
23									2796.35	0.00	0.00	0.00	0.00E+00	0.0	0.0	0.0
24									2795.49	0.5	0.110	0.06	1.39E+12	-92.4	26.8	26.8
25									2796.10	0.55	0.060	0.04	8.35E+11	-27.0	29.5	29.5
26																
27									2796.06	0.64	0.098	0.07	1.59E+12	-31.3	34.3	34.3
28																
29									2795.58	0.49	0.105	0.05	1.30E+12	-82.8	26.3	26.3
30									2795.42	0.7	0.162	0.12	2.87E+12	-99.9	37.5	37.5
31									2795.6	0.63	0.210	0.14	3.35E+12	-80.6	33.8	33.8
32									2795.46	0.9	0.215	0.21	4.89E+12	-95.6	48.2	48.2
33									2795.58	0.9	0.200	0.19	4.55E+12	-82.8	48.2	48.2
34									2795.38	0.93	0.230	0.23	5.41E+12	-	49.9	49.9
35									2795.5	0.83	0.230	0.20	4.83E+12	-91.3	44.5	44.5
36									2795.32	0.73	0.145	0.11	2.68E+12	-	39.1	39.1
37									2795.38	1	0.240	0.26	6.07E+12	-	53.6	53.6
38									2795.42	0.95	0.251	0.25	6.03E+12	-99.9	50.9	50.9
39									2795.6	0.65	0.260	0.29	7.00E+12	-80.6	79.3	34.8
40									2795.3	1.1	0.265	0.31	7.37E+12	-	59.0	59.0
41									2795.3	1.08	0.242	0.28	6.61E+12	-	57.9	57.9
42									2795.5	1	0.310	0.33	7.84E+12	-91.3	53.6	53.6
43									2795.11	1.3	0.202	0.28	6.64E+12	-	69.7	69.7
44									2795.48	1.15	0.330	0.40	9.60E+12	-93.5	61.6	61.6

TABLE D.6.3 - Mg II 2796

Pair ID	Extra Width L or R	far Left A	FWHM	Depth	Eq. Width	Ni, atoms along l.o.s	Vrad w	Extra Width L or R	Inner Left B	FWHM	Depth	Eq. Width	Ni, atoms along l.o.s	Vrad w
1	L	2794.15	1.15	0.250	0.31	7.27E+12	-236.6	n						
2	n							n						
3	L	2794.08	1.48	0.355	0.56	1.33E+13	-243.6	n						
4	L	2793.67	1.72	0.360	0.66	1.57E+13	-287.5	n						
5	L	2794.48	0.88	0.400	0.37	8.90E+12	-200.7	n						
6	n							n						
7	n							n						
8	n							L	2795.17	1.2	0.260	0.33	7.89E+12	-126.7
9	n							n						
10	n							n						
11	n							n						
12	n							n						
13	n							n						
14	n							n						
15	n							n						
16	n							n						
17	n							n						
18	n							n						
19	n							n						
20	n							n						
21	n							n						
22	n							n						
23	n							n						
24	n							n						
25	n							n						
26	n							n						
27	n							n						
28	n							n						
29	n							n						
30	n							n						
31	n							n						
32	n							n						
33	n							n						
34	n							n						
35	n							n						
36	n							n						
37	n							n						
38	n							n						
39	n							L	2794.86	1.48	0.260	0.41	9.73E+12	-159.954
40	n							n						
41	n							n						
42	n							n						
43	n							n						
44	n							n						

TABLE D.6.4 - Mg II 2796

Pair ID	Inner Right C	FWHM	Depth	Eq. Width	Ni, atoms along l.o.s	Vrad	Left Width (km/s)	Right Width (km/s)	Far Right D	FWHM	Depth	Eq. Width	Ni, atoms along l.o.s	Vrad	Left Width (km/s)	Right Width (km/s)
1	2797.02	0.38	0.152	0.06	1.46E+12	71.6	20.4	20.4								
2	2796.85	0.58	0.17	0.10	2.42E+12	53.4	31.1	31.1								
3	2797.50	1.00	0.19	0.20	4.81E+12	123.1	53.6	53.6								
4	2797.23	1.20	0.270	0.45	1.06E+13	94.1	64.3	101.8								
5	2797.02	0.84	0.13	0.15	3.60E+12	71.6	45.0	72.4								
6	2796.80	0.64	0.19	0.13	3.04E+12	48.0	34.3	34.3								
7	2796.82	0.56	0.21	0.13	2.97E+12	50.2	30.0	30.0								
8	2796.80	0.60	0.198	0.19	4.48E+12	48.0	32.2	63.8								
9	2796.86	0.62	0.270	0.18	4.23E+12	54.5	33.2	33.2								
10	2796.90	0.41	0.230	0.10	2.38E+12	58.7	22.0	22.0								
11	2796.99	0.44	0.155	0.07	1.72E+12	68.4	23.6	23.6								
12	2796.94	0.37	0.17	0.07	1.61E+12	63.0	19.8	19.8								
13	2796.91	0.30	0.180	0.06	1.37E+12	59.8	16.1	16.1								
14	2796.74	0.27	0.110	0.03	7.51E+11	41.6	14.5	14.5								
15	2796.71	0.28	0.080	0.02	5.67E+11	38.4	15.0	15.0								
16	2796.35	0.00	0.00	0.00	0.00E+00	0.0	0.0	0.0								
17	2796.35	0.00	0.00	0.00	0.00E+00	0.0	0.0	0.0								
18	2796.35	0.00	0.00	0.00	0.00E+00	0.0	0.0	0.0								
19	2796.35	0.00	0.00	0.00	0.00E+00	0.0	0.0	0.0								
20	2797.28	0.62	0.108	0.07	1.69E+12	99.5	33.2	33.2								
21	2796.35	0.00	0.00	0.00	0.00E+00	0.0	0.0	0.0								
22	2796.35	0.00	0.00	0.00	0.00E+00	0.0	0.0	0.0								
23	2797.08	0.7	0.185	0.14	3.28E+12	78.0	37.5	37.5								
24	2796.9	0.65	0.298	0.21	4.90E+12	58.7	34.8	34.8								
25	2796.87	0.60	0.215	0.14	3.26E+12	55.5	32.2	32.2								
26																
27	2796.84	0.83	0.148	0.13	3.11E+12	52.3	44.5	44.5								
28																
29	2796.8	0.73	0.298	0.23	5.50E+12	48.0	39.1	39.1								
30	2796.83	0.9	0.318	0.30	7.24E+12	51.2	48.2	48.2								
31	2796.99	0.93	0.295	0.29	6.94E+12	68.4	49.9	49.9								
32	2796.89	0.82	0.338	0.30	7.01E+12	57.7	44.0	44.0								
33	2796.92	0.98	0.35	0.37	8.67E+12	60.9	52.5	52.5								
34	2797.02	1.02	0.37	0.40	9.54E+12	71.6	54.7	54.7								
35	2796.83	0.95	0.28	0.28	6.73E+12	51.2	50.9	50.9								
36	2797.02	0.93	0.412	0.41	9.69E+12	71.6	49.9	49.9								
37	2797.1	1.03	0.385	0.42	1.00E+13	80.2	55.2	55.2								
38	2796.98	1.05	0.375	0.42	9.96E+12	67.3	56.3	56.3								
39	2797	0.84	0.37	0.50	1.19E+13	69.5	45.0	91.1								
40	2797.1	1.1	0.408	0.48	1.14E+13	80.2	59.0	59.0								
41	2797.2	1.2	0.385	0.49	1.17E+13	90.9	64.3	64.3								
42	2796.93	0.93	0.388	0.38	9.13E+12	62.0	49.9	49.9								
43	2796.98	0.52	0.15	0.08	1.97E+12	67.3	27.9	27.9								
44	2797.5	1.23	0.385	0.50	1.20E+13	123.1	65.9	65.9								

TABLE D.6.5 - Mg II 2796

Pair ID	Extra Width L or R	Inner Right C	FWHM	Depth	Eq. Width	Ni, atoms along l.o.s	Vrad w	Extra Width L or R	Far Right D	FWHM	Depth	Eq. Width	Ni, atoms along l.o.s	Vrad w
1	n							n						
2	n							n						
3	n							n						
4	R	2798.18	1.9	0.270	0.55	1.30E+13	196.0	n						
5	R	2797.70	1.35	0.130	0.19	4.44E+12	144.0	n						
6	n							n						
7	n							n						
8	R	2797.40	1.19	0.198	0.25	5.96E+12	111.8	n						
9	n							n						
10	n							n						
11	n							n						
12	n							n						
13	n							n						
14	n							n						
15	n							n						
16	n							n						
17	n							n						
18	n							n						
19	n							n						
20	n							n						
21	n							n						
22	n							n						
23	n							n						
24	n							n						
25	n							n						
26	n							n						
27	n							n						
28	n							n						
29	n							n						
30	n							n						
31	n							n						
32	n							n						
33	n							n						
34	n							n						
35	n							n						
36	n							n						
37	n							n						
38	n							n						
39	R	2797.85	1.7	0.370	0.67	1.59E+13	160.6	n						
40	n							n						
41	n							n						
42	n							n						
43	n							n						
44	n							n						



TABLE D.6.6 - Mg II 2796

Pair ID	Ni Total Blue	Ni Total Red
1	1.14E+13	1.46E+12
2	3.27E+12	2.42E+12
3	1.72E+13	4.81E+12
4	2.22E+13	1.06E+13
5	1.81E+13	3.60E+12
6	5.05E+12	3.04E+12
7	4.07E+12	2.97E+12
8	6.41E+12	4.48E+12
9	1.75E+12	4.23E+12
10	0.00E+00	2.38E+12
11	3.28E+12	1.72E+12
12	0.00E+00	1.61E+12
13	0.00E+00	1.37E+12
14	2.73E+12	7.51E+11
15	4.07E+12	5.67E+11
16	0.00E+00	0.00E+00
17	0.00E+00	0.00E+00
18	0.00E+00	0.00E+00
19	0.00E+00	0.00E+00
20	3.44E+12	1.69E+12
21	1.61E+12	0.00E+00
22	0.00E+00	0.00E+00
23	0.00E+00	3.28E+12
24	1.39E+12	4.90E+12
25	8.35E+11	3.26E+12
26		
27	1.59E+12	3.11E+12
28		
29	1.30E+12	5.50E+12
30	2.87E+12	7.24E+12
31	3.35E+12	6.94E+12
32	4.89E+12	7.01E+12
33	4.55E+12	8.67E+12
34	5.41E+12	9.54E+12
35	4.83E+12	6.73E+12
36	2.68E+12	9.69E+12
37	6.07E+12	1.00E+13
38	6.03E+12	9.96E+12
39	7.00E+12	1.19E+13
40	7.37E+12	1.14E+13
41	6.61E+12	1.17E+13
42	7.84E+12	9.13E+12
43	6.64E+12	1.97E+12
44	9.60E+12	1.20E+13